UNIVERSITÀ
DEGLI STUDI
FIRENZE

DOTTORATO DI RICERCA
INTERNATIONAL DOCTORATE IN STRUCTURAL BIOLOGY

Expression and characterization of human proteins involved in neurological disorders

Settore Scientifico Disciplinare CHIM/03

CICLO XXXII

COORDINATOR Prof. Claudio Luchinat

PhD student
Dott. Sara Bologna

Tutor
Prof. Marco Fragai

Coordinator
Prof. Claudio Luchinat

November 2016 – 2019

This thesis has been approved by the University of Florence, the University of Frankfurt and the Utrecht University

Universiteit Utrecht

CERM Firenze

Contents

Preface

Aim of the thesis and study objectives

My PhD research project, entitled “Expression and characterization of human proteins involved in neurodegenerative diseases”, was focused on the application of molecular biology and proteomics methodologies to prepare samples of proteins involved in neurodegenerative diseases.
The target proteins were α-synuclein (α-syn) and the amyloid beta peptides (Aβ), involved in the pathogenesis of Parkinson’s disease (PD) and Alzheimer’s disease (AD), respectively.
The aim of my research activity was the optimization of the expression and purification of the neurodegeneration-associated proteins to carry out the following projects:

- “NMR analysis of the aggregation kinetics of Aβ1-40”, to reveal aggregation mechanisms of Aβ1-40 and to develop a kinetic model describing the formation of oligomeric and fibrillary species.

- “NMR analysis of the assembly of Aβ42:Aβ40 mixed fibrils”. This project is in the frame of an integrative study aimed to characterize the structure of the mixed fibrils (containing Aβ1-42 and Aβ1-40 peptides) at atomic detail.

- “Development of a protein aggregation assays for the diagnosis of synucleinopathies” This project was focused on the development of a protocol tool for the diagnosis PD, dementia with Lewy bodies (DLB) and multiple system atrophy (MSA) based on α-synuclein aggregation assays (SAA-*seeding aggregation assays*) starting from aliquots of Cerebrospinal fluid (CSF).

- Study of the interaction between alpha-synuclein and human biofluids components" This project concerned the study of the interaction of α-synuclein with lipoproteins, proteins and other constituents of CSF and plasma.

Organization of the thesis and experimental approaches

Chapter 1 (Introduction), provides a global review of Neurodegenerative disorders and their research status, with a particular focus on Parkinson's disease (PD) and Alzheimer's diseas (AD). The main part of this chapter is focused on the understanding of the role that α-synuclein and Aβ peptides have in the pathogenesis of PD and AD.

Chapter 2 (Methodological aspects), describes the materials and the methods of the projects enclosed in this thesis work. The main part of the chapter regards the analysis of the protocol for the expression of Aβ peptides and α-synuclein, dwelling on the issues and the strategies for the preparation of samples for NMR, EM and AFM microscopy analysis and ThT fluorescence experiments. In this chapter is also browsed the antibody-based analysis used for amyloids aggregates study. Finally, a short part is dedicated to the analysis of pH variations of cerebrospinal fluid (CSF) withdrawn from patients with other neurological diseases (OND) and not affected by synucleinopathies.

Chapter 3 (*Results*), shows all the achievements obtained during this PhD research period in the form of full text published articles and in preparation manuscripts. The respective supporting information follows each article.

Chapter 4 (*Conclusions and perspectives*), summarizes all the goals and outlooks of these PhD research work, making a critical analysis of the obtained results and of the improvements needed to the protocols adopted in each project.

Chapter 1

Introduction

1.1 Neurodegenerative diseases

Neurodegenerative diseases represent a large group of neurological disorders affecting specific subsets of neurons in certain functional anatomic systems. These kind of pathologies are untreatable and weakening conditions that result in progressive degeneration and/or death of nerve cells. Neurons from brain and spinal cord do not regenerate themselves: therefore when they die they can not be replaced.[1]

One of the most well grounded risk factor for developing a neurodegenerative pathology is the increasing of the age and several approved drugs do not seem to stop the progression.[2]

A common link of all these diseases is the presence of deposits of misfolded proteins in neurons and other cells or extracellularly [3],[4] Consequently, this kind of pathologies are classified as *proteinophaties*.[5]

Misfolded proteins exist in cells together with unfolded, intermediately folded, and correctly folded species. Many factors can trigger protein misfolding: mutations in the gene sequence leading to the production of a protein unable to adopt the native folding, errors on the processes of transcription or translation, failure of chaperone machinery, mistakes on the post-translational modifications, structural modification produced by environmental changes.[6],[7]

The most recurrent prospect for misfolded proteins is self-aggregation that ends with the formation of intracellular and extracellular protein deposits containing a fibrillar protein species called *amyloid*.[8] The term *amyloid* was introducted in 1854 by the German physician Rudolph Virchow who used the iodine staining of cerebra corpora amylacea in human brain tissue with an abnormal macroscopic appereance.

Virchow discovered that the corpora amylacea stained pale blue with the iodine treatment, and violet after the subsequent addition of sulfuric acid and he concluded that the abnormal substance was cellulose or starch and gave it the name *amyloid*, derived from the Latin “amylum” and the Greek “amylon”. In 1859, Friedreich and Kekule demonstrated the presence of protein insight an amyloid mass and the attention of the scientific community was shifted to the study of amyloids as a class of proteins, with a propensity to undergo conformational changes resulting in fibril formation.[9]

For this reason, neurodegenerative disorders can be also defined as *amyloid-based neurodegenerative diseases.*[10]

In *Table1,* showed below, are listed the main *amyloid-based proteinopathies*.

Table 1: Amyloid-based neurodegenerative diseases and their hallmarks

Disease	**Protein**	**Hallmarks**
Parkinson's disease (AD)	**α-synuclein**	**Intracellular aggregates (Lewy bodies)** [11]
Alzheimer's disease (AD)	**Aβ peptides**	**Extracellular amyloid deposits (“plaques”), intracellular neurofibrillary tangles** [12]
Tauopathies	**Tau**	**Cytoplasmic neurofibrillary tangles (NFTs)** [13]
Prion diseases (TSEs)	**PrPSc**	**Prion plaque** [14]
Familial amyotrophic lateral sclerosis (ALS)	**SOD1**	**Eosinophilic intraneuronal inclusions (Bunina bodies)** [15]
Polyglutamine disorders (PolyQ)	**PolyQ proteins**	**Nuclear and cytoplasmic inclusions** [16]

1.2 Alzheimer’s disease and Aβ peptides

Alzheimer's disease (AD) is one of the most frequent form of dementia.
Changes in the brain of patients with Alzheimer's disease begin years before any signs of the disorder. This time period, is referred to as preclinical Alzheimer's disease.
The stages of Alzheimer’s clinically defined, are separated into three categories: mild, moderate and severe, where people lose the ability to communicate or respond to their environment and need assistance with all activities of daily living.[17]
The major pathological hallmarks of the disorder are the accumulations of intracellular neurofibrillary tangles and extracellular amyloid plaques (Figure 1) in susceptible brain regions, as was discovered by Alois Alzheimer who described the long-term study of the female patient Auguste D., at the Frankfurt Psychiatric Hospital in November 1901.[18]

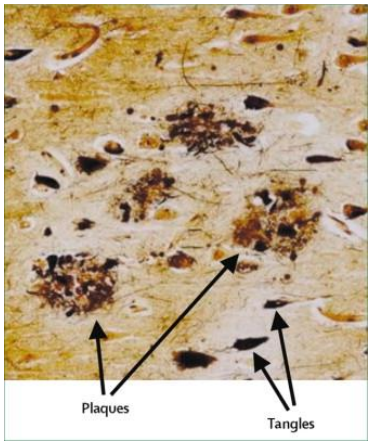

Fig. 1: Plaques and tangles in the cerebral cortex in Alzheimer's disease. Reprint from Blennow, K., de Leon, M. J. & Zetterberg, H. Alzheimer’s disease. *The Lancet* **368**, 387–403 (2006).

The main constituent of the plaques is β-amyloid (A*β*), a 39–43 amino acids long peptide, deriving from the amyloid precursor protein (APP).[19]
In humans, the gene for APP is located on chromosome 21 and mutations in critical regions of amyloid precursor protein, cause familial susceptibility to Alzheimer's disease[20].

APP undergoes extensive post-translational modifications including the proteolytic processing to generate peptide fragments. The cleavage is catalyzed by proteases of secretase family: α-secretase and β-secretase remove the whole extracellular domain to release membrane-anchored carboxy-terminal fragments that may be associated with apoptosis. Cleavage by γ-secretase adjacent to residues 42 or 43 of APP generates the Aβ species (Figure 3).[21],[22]

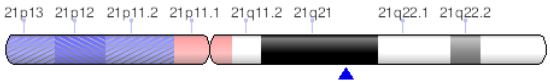

Fig. 2: APP gene
(Reprint from ClinGen Dosage Sensitivity Curation Page, id: ISCA-1095)

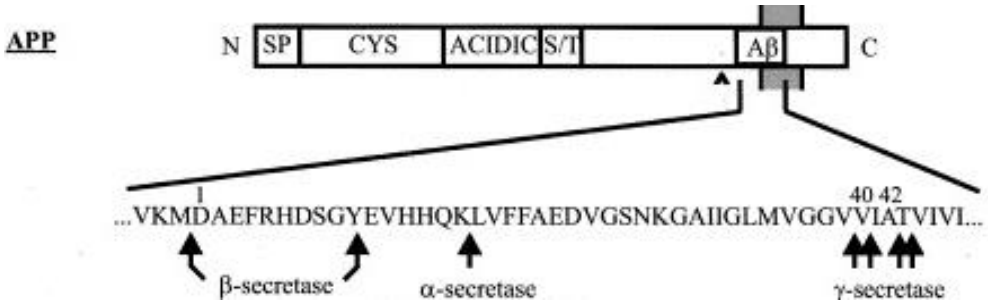

Fig. 3: APP cleavage pathway (Reprint from Nunan, J. & Small, D. H. Regulation of APP cleavage by α-, β- and γ-secretases. FEBS Letters 483, 6–10 (2000).)

At low concentrations, A*β* still has some physiological functions in the body: it can act as neurotrophic factor for neurons growth and antimicrobial peptide in innate immune system.[23]

Aβ monomer is not toxic. Only upon its aggregation it can induce the toxic effects, according to the amyloid hypothesis.

Among the toxic effects of Aβ, meaningful is the increased oxidative stress: elevated levels of Aβ1-40 and Aβ1-42 have been reported to be associated with increased levels of oxidation products from proteins, lipids and nucleic acids in AD hippocampus and cortex.[24]

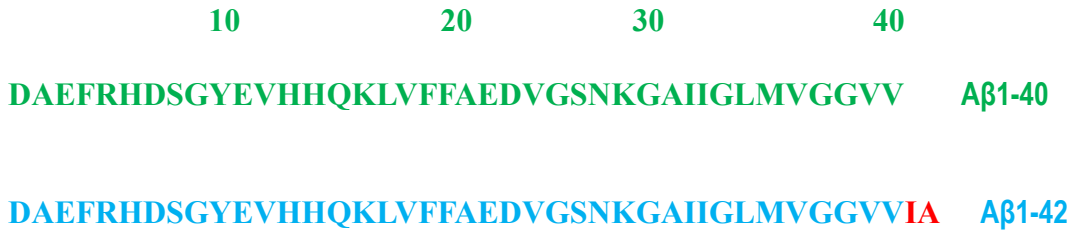

Fig. 4: Amyloid beta peptides

Both Aβ1-40 and Aβ1-42, hydrophilic amino acid residues are located in the N-terminal region, while most amino acid residues in C-terminal region are hydrophobic.

Although these two kinds of Aβ differ only in two amino acid residues, they differ significantly in their concentration, metabolism, physiological functions, toxicities, and aggregation mechanism.

While Aβ1-40 is the predominant species in unaffected individuals, the ratio of Aβ1-42:1-40 increases in Alzheimer's disease. Aβ1-42 is more amyloidogenic than Aβ1-40 in vitro and appears to be more neurotoxic and prone to generate the free-radical damage in cellular assays [(25)]. Furthermore, increased levels of Aβ1-42 correlate with familial and sporadic AD patients[(26),(27),]

Another difference between the two Aβ monomers is their aggregation process, as will be elucidated in the next paragraph.

1.3 Aβ aggregation

Because of the hydrophobic interaction, hydrogen bonding and aromatic stacking effects, Aβ oligomerization occurs via distinct intermediates, including oligomers of 3-50 Aβ monomers (soluble), protofibrils, fibrils and plaques (insoluble), as was confirmed by the analysis of in vitro aggregation pathway and by biochemical characterization of Aβ deposits from AD patients brains.[28]

Aβ aggregates have been described ranging in size from dimers up to particles of one million daltons or larger. Using the atomic force microscope analysis (AMF), prefibrillar oligomers (PFOs) are detected as spherical particles of ~3–10 nm that appear at early times of incubation and disappear as mature fibrils appear [29],[30]. At the same time, at longer times of incubation, PFOs coalesce and form curvilinear beaded strings that called protofibrils and ring-shaped, pore-like structures known as annular protofibrils (APFs)[31]. The final stage is the fibril formation, as is represented in the morphological pathway in the Figure 5.[32]

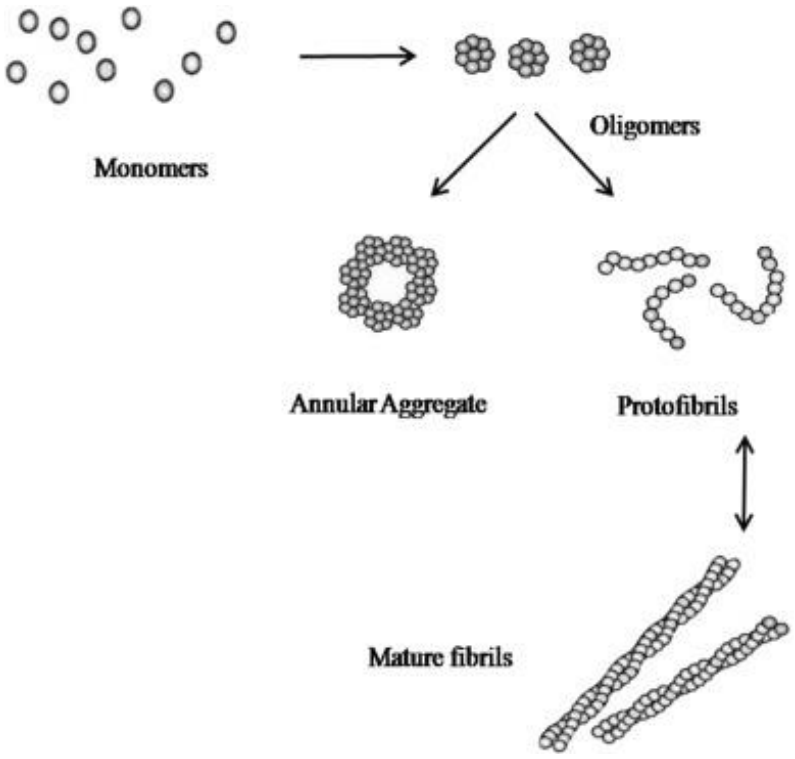

Fig. 5: Aβ fibrils formation morphological pathway (Reprint from Salahuddin, P., Fatima, M. T., Abdelhameed, A. S., Nusrat, S. & Khan, R. H. Structure of amyloid oligomers and their mechanisms of toxicities: Targeting amyloid oligomers using novel therapeutic approaches. *European Journal of Medicinal Chemistry* **114**, 41–58 (2016).)

The kinetics of amyloid formation is well represented by a sigmoidal curve with a nucleation phase (lag phase), in which monomers undergo conformational change and misfolding and associate to form oligomeric nuclei and an elongation phase (growth phase), in which the nuclei rapidly grow by further addition of monomers and form larger polymers and fibrils until saturation (plateau phase).[33],[34].

The “nucleation phase”, is thermodynamically unfavourable and occurs gradually, whereas “elongation phase”, is much more favourable process and proceeds quickly.[35]

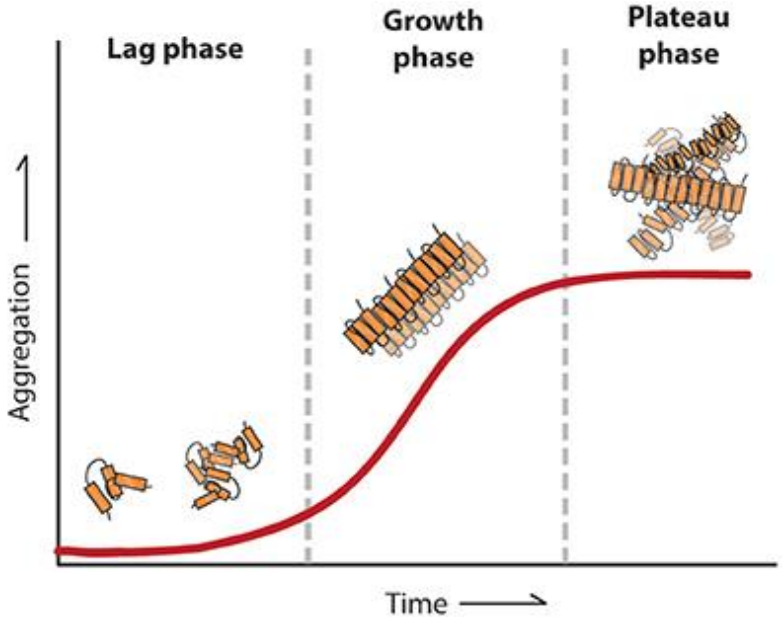

Fig. 6: Exponential curve of amyloid aggregation kinetics (Reprint from Stroo, E., Koopman, M., Nollen, E. A. A. & Mata-Cabana, A. Cellular Regulation of Amyloid Formation in Aging and Disease. *Front. Neurosci.* **11**, (2017).

The formation of molecular aggregates involves the transition of a system initially in a homogeneous solution phase, to form a new aggregated phase co-existing with a monomer solution phase.

In amyloid systems, monomers of one substance may nucleate in solution (Figure 7: primary nucleation, left) or on the surface of an already existing aggregates composed of the same kind of monomeric building block (Figure 7: monomer-dependent secondary nucleation, right).

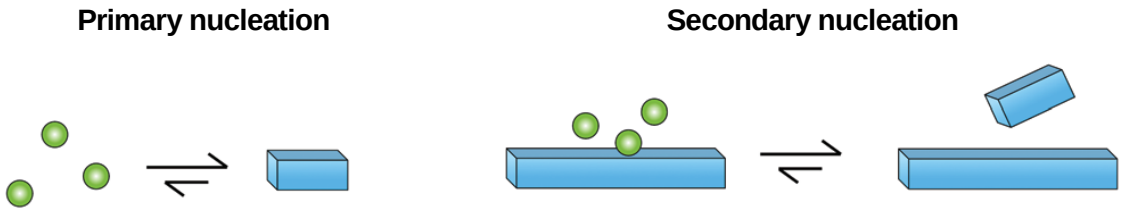

Fig. 7: Cartoon of primary and secondary nucleation reactions. Green (monomers), aggregated state (blue). (Reprint from Törnquist, M. *et al.* Secondary nucleation in amyloid formation. *Chem. Commun.* **54**, 8667–8684 (2018).)

For example, Aβ1-42, the most prone to aggregate of Aβ peptides, tends to self-assembly following a positive feedback loop that originates from the interactions between the monomeric and fibrillar forms. Once a small but critical concentration of amyloid fibrils has accumulated, the toxic oligomeric species are mainly formed from monomeric peptide molecules through a fibril-catalyzed secondary nucleation reaction, rather than through a classical mechanism of homogeneous primary nucleation.

Initially, in the absence of fibrils, all oligomers are generated through primary pathways because secondary nucleation requires the presence of fibrils. Once a critical concentration of amyloid fibrils has formed, however, secondary nucleation will overtake primary nucleation as the major source of new oligomers and further proliferation becomes exponential in nature due to positive feedback. [36-39]

In addition, monomeric Aβ1-42 cross-react with Aβ1-40 at the stage of primary nucleation.[40]

Aβ1-40 aggregation process is accelerate in presence of Aβ1-42 monomers and Aβ1-42 self-assembly is slowed down by Aβ1-40.[41]

Aβ-associated toxicity is a dynamic property and a critical equilibrium between the two Aβ species, Aβ1-40 and Aβ1-42, exists. This balance between the Aβ species determines the rate of appearance of the neurotoxic properties.

Under physiological conditions, the peptides co-exist in a 1:9 Aβ1-42:Aβ1-40 ratio. In patients with familial AD this ratio is shifted to higher percentage of Aβ1-42 and the critical value is 3:7.

In the plaques found post-mortem in AD afflicted people, the range of Aβ1-42:Aβ1-40 peptide ratio was found to be from 1:1 to 9:1.[42]

In particular, the critical ratio 3:7 Aβ1-42:Aβ1-40 is associated with an increasing of synaptotoxic intermediates production and with the reduction of the nucleation time.

For Aβ1-42:Aβ1-40 ratios higher than 3:7, instead, a plateau is reached and there are not observed significant variations in the nucleation time and in the fibril elongation time.[43],[44]

1.4 Amyloid fibrils structure

Amyloid-like fibrils of different proteins have a common structural “cross-β” spine, as was proved by the last six decades of research. In 1959 elongated, unbranched fibrils in electron micrographs of diseased tissues were observed by Cohen and Calkins[45], and in 1968 Glenner and Eanes discovered that the fibrils exhibit an X-ray diffraction signature known as the cross-β pattern.[46]

This pattern is characterized by several protofilaments, each composed of repeating units of β-sheets with hydrogen bonds along the length of the fibre. The β-sheet units are parallel to the fibril axis with their strands perpendicular to this axis (Figure 8).

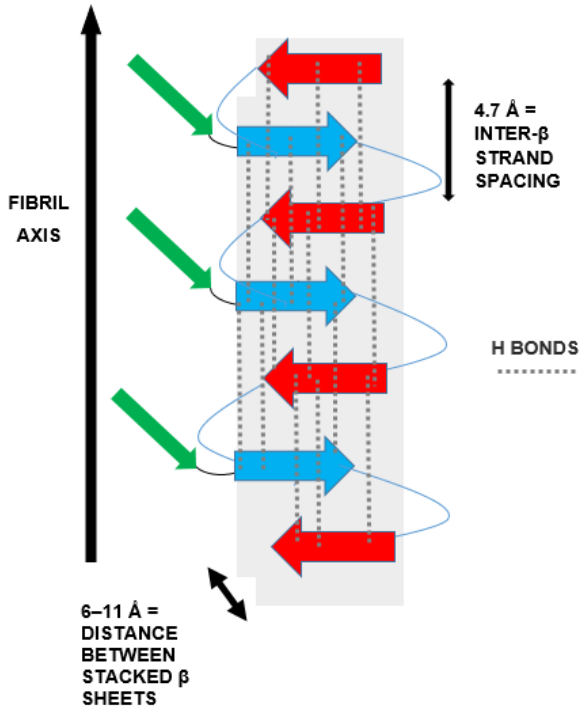

Fig. 8: Cross-β sheet diagram.

The hypothesis of a common molecular organization was supported by the finding that amyloid fibrils from six different neurodegenerative disease-associated proteins, showed similar cross-β diffraction patterns.[47-51]

An important point regarding the structural determination of amlyloid fibrils is that is not easy to obtain experimentally a high-resolution molecular structure using the

most common biophysical techniques. This is because amyloid fibrils are non-crystalline solid materials and are not compatible with X-ray christallography.

On the other hand, these fibrils are insoluble, which makes it difficult to use solution state NMR for structure determination. For this reason, solid-state NMR (SSNMR) spectroscopy has been realized to be a valuable method to gain insight into the structure of the amyloid fibril.[52]

Concerning the amyloid-β fibrils characterization by SSNMR, the Aβ1-40 alloform was extensively characterized by SSNMR in the past several years[53-57] and all the Aβ1–40 species resolved by NMR, share a U-shaped motif, while the Aβ1-42 fibrils structure was only recently well resolved as an S-shaped fibrillar species.[57-60]

Furthermore, recent advances in single-particle cryo-EM have enabled the structure determination of amyloid fibrils, proving that cryo-EM technique allows near-atomic characterization of amyloid filaments from post-mortem human brain tissue.[61]

In vitro, the amyloid fibrils are easily and readily detected by using benzothiazole salt Thioflavin T (ThT), a commonly used probe to monitor their formation. In particular, the binding of ThT to amyloid fibrils, induces a shift in excitation maximum (385 nm to 450 nm) and emission maximum (445 nm to 482 nm) [62],[63], as is shown in the spectrum in the Figure 9.

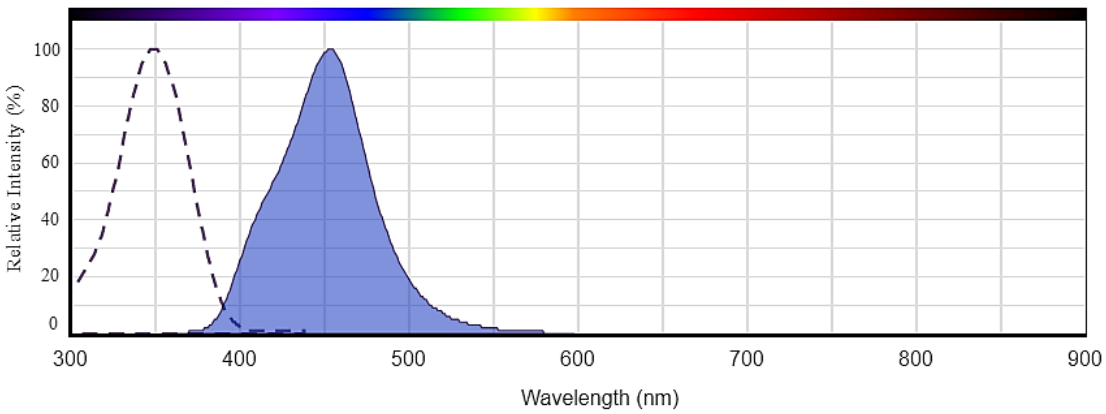

Fig.9: Excitation/emission spectrum of the fluorophore ThT (Reprint from AAT Bioquest's interactive Spectrum Viewer tool)

The mechanism of ThT strong fluorescence signal at 482 nm has been associated with the rotational immobilization of the central C–C bond connecting the

benzothiazole and aniline rings (Figure 10). The target sites of ThT-fibrils interaction are the side chain channels along the long axis of amyloid filaments and the minimal binding site on the fibre surface has been suggested to extend across three or four consecutive β-strands.[64],[65]

ThT dye is also called Basic Yellow 1 or CI 49005 and is used to visualize plaques composed of β-amyloid found in the brains of Alzheimer's disease patients.

The reagent binds rapidly and specifically to the anti-parallel beta-sheet fibrils but does not bind to monomer or oligomeric intermediates. In addition, the binding of ThT does not interfere with the aggregation of beta-amyloid peptide into amyloid fibrils.

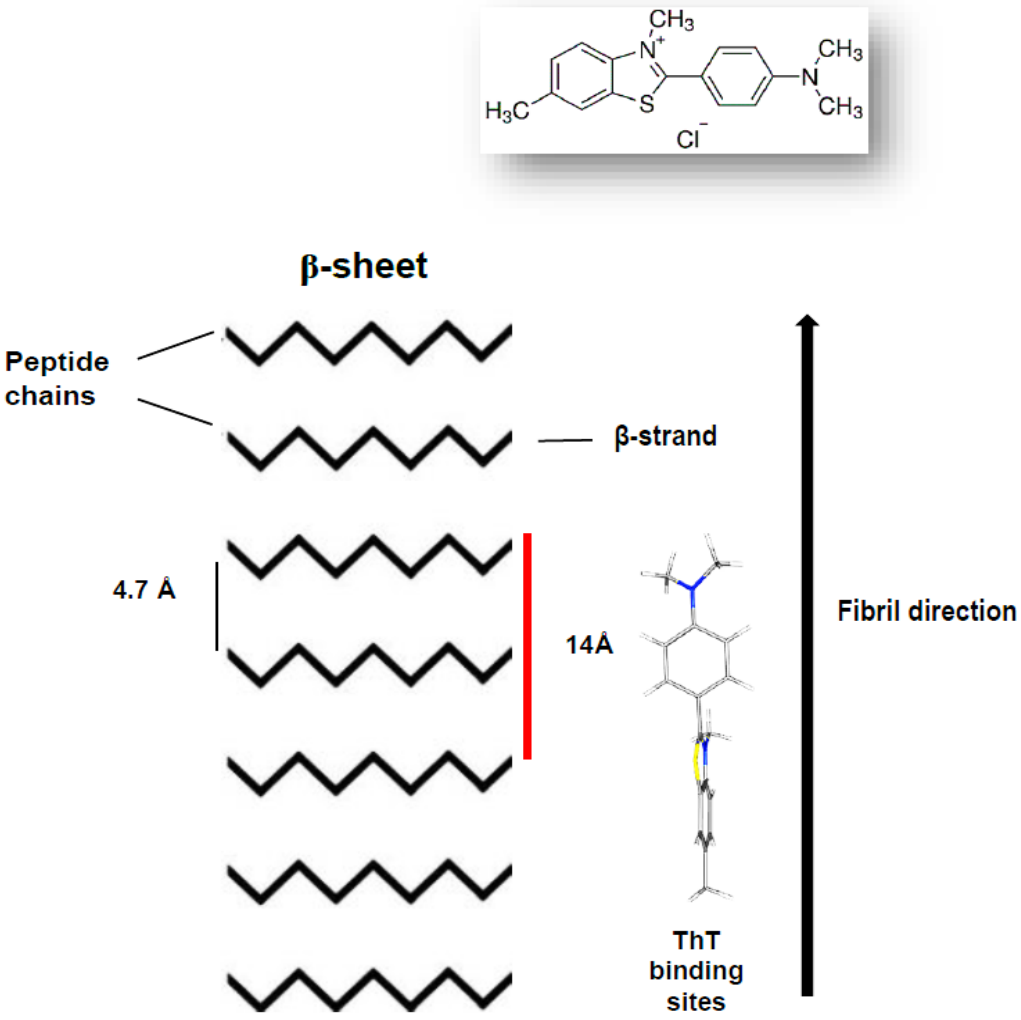

Fig. 10: Schematic illustration of Thioflavin T oriented with its long axis parallel to the long axis of the fibril.The minimal binding site on the fibre surface is extended across three consecutive β-strands (14Å).

1.5 Parkinson's disease and α-synuclein

Parkinson's disease (PD), first described by James Parkinson in 1817 with the term "Shaking Palsy (Paralysis Agitans)"[66], is the second most common neurogenic disorder after Alzheimer disease, affecting approximately 1% of the population over age 50. This proteinopathy is clinically characterized by parkinsonism (resting tremor, bradykinesia, rigidity and postural instability) and pathologically by the loss of dopaminergic neurons in the *substantia nigra pars compacta,* in association with the presence of ubiquitinated protein deposits in the cytoplasm of neurons (Lewy bodies).[67],[68]

Hence, restorative dopaminergic therapies are the main treatment. Monoamine oxidase inhibitors are initially used to prevent endogenous dopamine catabolism; alternatively, L-DOPA, the metabolic precursor of dopamine, or dopamine agonists are used.[69]

Nowadays, many groups are working on new therapies, not only symptomatic, through the development of drugs able to inhibit oligomer accumulation, neuronal degeneration, and disease progression.[70]

Genetically speaking, PD is a heterogeneous and most likely, complex disorder.

In 1996, was mapped and subsequent identified the first mutations responsible for Parkinson's disease (PD) that showed PD may be hereditary.[71]

The protein involved in the pathogenesis of PD is α-synuclein (α-synuclein).

The encoding gene is SNCA (cytogenetic location: 4q22.1) and its mutations are related to pathological phenotype of autosomal dominant Parkinson disease 1, Parkinson disease 4 and Lewy body dementia.

Other two members of Synuclein family are two homologous proteins, *β (SNCB)* and *γ* synucleins (SNCC). *Γ* Synuclein, forms fibrils much more slowly than α synuclein, and *β* synuclein does not form fibrils under typical in vitro or in vivo conditions.[72]

Inside the cellular environment, this protein is involved in regulating of presynaptic function and in neurotransmitter release (dopamine) and plays also a role in the movement of microtubules and in the binding of fatty acids [73] Several factors like post-translational modifications, oxidative stress, fatty acids concentration, proteolysis, phospholipids and metal ions can promote the misfolding of a-syn with the consequent formation of oligomers and amyloid-like fibrils[74],[75].

A-synuclein is a 14kDa highly soluble cytosolic protein. Is classified as an *intrinsically disordered protein* (IDP), as well as Aβ peptides. The term “disordered” indicate a lack of a specific stable three-dimensional structure and the structural disorder in IDPs can be placed in one or more separate regions along the chain, or it may span the entire length of the protein.[76]

The monomer of α-synuclein is composed of three distinct regions: an amphipathic α-helical domain in the N-terminus which mediates binding to phospholipid membranes, a central hydrophobic region, called NAC (non-Aβ component), having the β-sheet potential, and a C-terminus that is highly negatively charged, and is prone to be unstructured [77] (Figure 11)

MDVFMKGLSKAKEGVVAAAEKTKQGVAEAAGKTKEGVLYVGSKTKEGVVHGVATVAEKTK

EQVTNVGGAVVTGVTAVAQKTVEGAGSIAAATGFVKKDQLGKNEEGAPQEGILEDMPVDP

DNEAYEMPSEEGYQDYEPEA

Fig. 11: α-synuclein regions. BLUE:N-term domain (1-60), RED: NAC domain (61-95), GREEN: C-term domain (96-140).

1.6 α-synuclein as biomarker of Parkinson's disease

The study of of Parkinson's disease biomarkers is a large and expanding field.[78-81] The development of early diagnostic biomarkers for PD is necessary to intervene at the onset of disease and to monitor the progress of therapeutic interventions that may slow or stop the course of the disease.
Several biofluids have the potential role to serve as sources of PD biomarkers, including, cerebrospinal fluid (CSF), blood (including whole blood and all blood compartments), saliva, and urine. Three of the most important aspects to take into account during a PD biomarker-based screening are the biological-compartments accessibility, low costs and reliability/reproducibility. Up to now, research on biomarkers for PD has made significant progress and an increasing number of candidate biomarkers for PD have been found (Table 2).

Table 2: Biochemical markers of Parkinson's disease

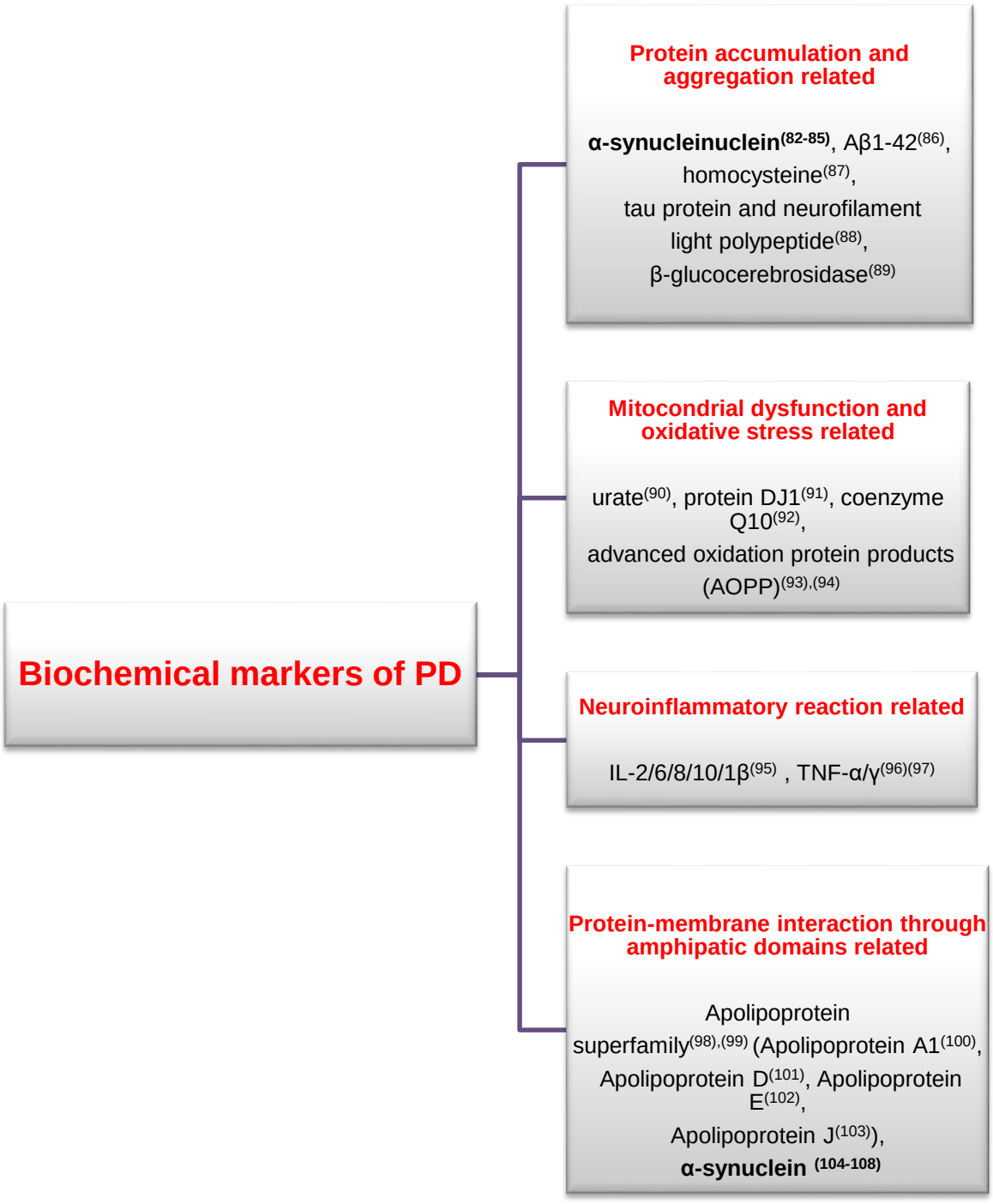

In the past few years, it is catching on the hypothesis that alpha-synuclein could act as biomarker of PD in biological fluids. (82-85),(104-108)

Results obtained by El-Agnaf and coworkers, detected the existence of an extracellular form of alpha-synuclein, in cerebrospinal fluid (CSF) and in plasma.[109]

Outside the cell, this protein, according to The Braak hypothesis of Lewy pathology progression in Parkinson's disease, can be spread out through an exocytotic mechanism under stress conditions, and endocytic uptake occurs in nearby cells.[110]

A recent theory formulated in 2011 by several studies of Steiner and coworkers describes the spreading mechanism of alpha-synuclein. Small amount of α-synuclein are released from neuronal cells by unconventional exocytosis, and this extracellular alpha-synuclein contributes to the major pathological features of Lewy body dementia (LBD).[111]

This evidence suggests that neuronal cells normally secrete α-synuclein into the surrounding media in the brain: this protein could circulate to the CSF and then to the blood, putting forward an interesting possibility of the potential use of α-synuclein or its derivatives in biological fluids as a biomarker for PD and related disorders.

The final goal of α-synuclein based-screening in biological fluids is the development of methods for the diagnosis of this pathology at a pre-clinical stage.

1.7 SAA (seeding aggregation assays)

Many Parkinson's disease preclinical diagnostic techniques, together with ELISA test [112-116], are under development in numerous laboratories of the world. These tests are based on the SAA (seeding aggregation assays) approach.[117-122]

Behind the word "seeding" there is a self-amplification process (nucleation-dependent) of pathogenic aggregated species in which the formed "seeds" act as template for the recruitment of other soluble monomers to form highly ordered insoluble protein with β-sheet structure. The seeding mechanism, was first described for prion protein (PrP) [123-127] and later this paradigm was extended to β-amyloid (Aβ) to explain the conversion of soluble proteins to amyloid fibrils in vitro.[128-130]

An analogous process was recently reported for α-synuclein, where the addition of α-synuclein preformed fibrils (PFFs) acts as a seed and drives the aggregation of soluble monomers. This seeding effect determine the reduction of the lag phase followed by the rapid formation of α-synuclein fibrils.[131-137]

The real-time monitoring of of α-synuclein seeding activity is an expanding field due to its capability to individuate subjects that will be prone to develop synucleinopathies through the detection of misfolded α-synuclein in brain homogenates and cerebrospinal fluid, strengthening the diagnostic and prognostic role of the preclinical screening in PD.

Nowadays, three are the most growing tests that use the SAA approach for the diagnosis of sinucleinopathies: PMCA, RT-QuIC ("α-synuclein Protein Misfolding Cyclic Amplification" and "Real-Time Quaking-Induced Conversion")[138-142] and HANABI ("HANdai Amyloid Burst Inducer").[143] In all these techniques, the formation of amyloid is monitored instantly using the dye Thioflavin T.

In particular, PMCA and RT-QuIC protocols, conceptually analogous to DNA amplification by PCR, are based on the enlargement of a preformed quantity of aggregated protein (seed) present in biological fluids or tissue samples. In these experiments, seeds samples incubated at a specific temperature in a buffer solution containing the monomeric substrate, act as template of polymerization.

By introducing in the protocol shaking/sonication steps, the aggregates are fragmented to form more polymerization points.

At the end of the procedure, the initial amount of seed is exponentially amplified with the loss of the monomer present in solution.[144] (Figure 12).

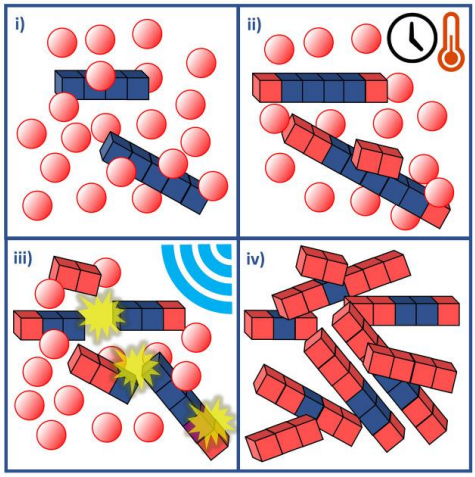

Fig. 12: PMCA assay description. i) monomer (red spheres) is incubated with seeds (blue cubes). ii) Seeds undergo elongation at their extremities and catalyze the formation of new nuclei of polymerization on their surfaces. iii) Sonication or shaking cycles increase the number of points of polymerization. Steps ii) and iii) are repeated several times, depending on the protocol adopted. iv) End point of the procedure in which the initial quantity of protein is exponentially amplified.
(Reprint from Paciotti, Silvia et al. "Are We Ready for Detecting α-synuclein Prone to Aggregation in Patients? The Case of "Protein-Misfolding Cyclic Amplification" and "Real-Time Quaking-Induced Conversion" as Diagnostic Tools." *Front. Neurol.* (2018).)

The first PMCA protocol was developed by Soto's group in 2001 to detect the misfolded prion protein (PrP^{Sc})[145], but only recently the PMCA and RT-QuIC techniques have been applied for the amplification and detection of aggregates of misfolded α-synuclein. The positive results obtained from different studies confirm the sensitivity and specificity of these assays for α-synuclein aggregates detection in CSF samples, suggesting their possible use as diagnostic tools.

1.8 References

1. https://www.neurodegenerationresearch.eu/about/what/

2. Casey, D. A., Antimisiaris, D. & O'Brien, J. Drugs for Alzheimer's Disease: Are They Effective? *P T* **35**, 208–211 (2010).

3. Taylor, J. P., Hardy, J. & Fischbeck, K. H. Toxic proteins in neurodegenerative disease. *Science* **296**, 1991–1995 (2002).

4. Selkoe, D. J. Folding proteins in fatal ways. *Nature* **426**, 900–904 (2003).

5. Bayer, T. A. Proteinopathies, a core concept for understanding and ultimately treating degenerative disorders? *Eur Neuro psychopharmacol* **25**, 713–724 (2015).

6. Moreno-Gonzalez, I. & Soto, C. Misfolded Protein Aggregates: Mechanisms, Structures and Potential for Disease Transmission. *Semin Cell Dev Biol* **22**, 482–487 (2011).

7. Sweeney, P. *et al.* Protein misfolding in neurodegenerative diseases: implications and strategies. *Transl Neurodegener* **6**, (2017).

8. Treusch, S., Cyr, D. M. & Lindquist, S. Amyloid deposits. *Cell Cycle* **8**, 1668–1674 (2009).

9. Sipe, J. D. & Cohen, A. S. Review: History of the Amyloid Fibril. *Journal of Structural Biology* **130**, 88–98 (2000).

10. Ow, S.-Y. & Dunstan, D. E. A brief overview of amyloids and Alzheimer's disease. *Protein Sci* **23**, 1315–1331 (2014).

11. Spillantini, M. G. *et al.* α-synuclein in Lewy bodies. *Nature* **388**, 839–840 (1997).

12. Alzheimer A. Über eine eigenartige Erkrankung der Hirnrinde. Allgemeine Zeitschrift fur Psychiatrie und Psychisch-gerichtliche Medizin, 64:146-8. (1907)

13. Michael-Titus, A., Revest, P. & Shortland, P.- DEMENTIA. in *The Nervous System (Second Edition)* (eds. Michael-Titus, A., Revest, P. & Shortland, P.) 251–266 (Churchill Livingstone, 2010).

14. Eghiaian, F. *et al.* Insight into the PrPC-->PrPSc conversion from the structures of antibody-bound ovine prion scrapie-susceptibility variants. *Proc. Natl. Acad. Sci. U.S.A.* **101**, 10254–10259 (2004).

15. Okamoto, K., Mizuno, Y. & Fujita, Y. Bunina bodies in amyotrophic lateral sclerosis. *Neuropathology* **28**, 109–115 (2008).

16. Rubinsztein, D., Wyttenbach, A. & Rankin, J. Intracellular inclusions, pathological markers in diseases caused by expanded polyglutamine tracts? *J Med Genet* **36**, 265–270 (1999).

17. Stages of Alzheimer's. *Alzheimer's Disease and Dementia* Available at: https://alz.org/alzheimers-dementia/stages.

18. Hippius, H. & Neundörfer, G. The discovery of Alzheimer's disease. *Dialogues Clin Neurosci* **5**, 101–108 (2003).

19. Kang, J. *et al.* The precursor of Alzheimer's disease amyloid A4 protein resembles a cell-surface receptor. *Nature* **325**, 733–736 (1987).

20. Jonsson, T. *et al.* A mutation in APP protects against Alzheimer's disease and age-related cognitive decline. *Nature* **488**, 96 (2012).

21. Zheng, H. & Koo, E. H. The amyloid precursor protein: beyond amyloid. *Molecular Neurodegeneration* **1**, 5 (2006).

22. Nunan, J. & Small, D. H. Regulation of APP cleavage by α-, β- and γ-secretases. *FEBS Letters* **483**, 6–10 (2000).

23. Qiu, T., Liu, Q., Chen, Y.-X., Zhao, Y.-F. & Li, Y.-M. Aβ42 and Aβ40: similarities and differences. *Journal of Peptide Science* **21**, 522–529 (2015).

24. Blennow, K., de Leon, M. J. & Zetterberg, H. Alzheimer's disease. *The Lancet* 368, 387–403 (2006).

25. Cheignon, C. *et al.* Oxidative stress and the amyloid beta peptide in Alzheimer's disease. *Redox Biol* **14**, 450–464 (2018).

26. Lista, S. *et al.* Biomarkers in Sporadic and Familial Alzheimer's Disease. *Journal of Alzheimer's Disease* **47**, 291–317 (2015).

27. Pauwels, K. *et al.* Structural Basis for Increased Toxicity of Pathological Aβ42:Aβ40 Ratios in Alzheimer Disease. *J Biol Chem* **287**, 5650–5660 (2012).

28. Di Carlo, M. Beta amyloid peptide: from different aggregation forms to the activation of different biochemical pathways. *Eur. Biophys. J.* **39**, 877–888 (2010).

29. Finder, V. H. & Glockshuber, R. Amyloid-beta aggregation. *Neurodegener Dis* **4**, 13–27 (2007).

30. Lashuel, H. A., Hartley, D., Petre, B. M., Walz, T. & Lansbury, P. T. Amyloid pores from pathogenic mutations. *Nature* **418**, 291–291 (2002).

31. Walsh, D. M., Lomakin, A., Benedek, G. B., Condron, M. M. & Teplow, D. B. Amyloid β-Protein Fibrillogenesis DETECTION OF A PROTOFIBRILLAR INTERMEDIATE. *J. Biol. Chem.* **272**, 22364–22372 (1997).

32. Lasagna-Reeves, C. A., Glabe, C. G. & Kayed, R. Amyloid-β Annular Protofibrils Evade Fibrillar Fate in Alzheimer Disease Brain. *J. Biol. Chem.* **286**, 22122–22130 (2011).

33. Salahuddin, P., Fatima, M. T., Abdelhameed, A. S., Nusrat, S. & Khan, R. H. Structure of amyloid oligomers and their mechanisms of toxicities: Targeting amyloid oligomers using novel therapeutic approaches. *European Journal of Medicinal Chemistry* **114**, 41–58 (2016).

34. Bruggink, K. A., Müller, M., Kuiperij, H. B. & Verbeek, M. M. Methods for analysis of amyloid-β aggregates. *J. Alzheimers Dis.* **28**, 735–758 (2012).

35. Stroo, E., Koopman, M., Nollen, E. A. A. & Mata-Cabana, A. Cellular Regulation of Amyloid Formation in Aging and Disease. *Front. Neurosci.* **11**, (2017).

36. Kumar, S. & Walter, J. Phosphorylation of amyloid beta (Aβ) peptides – A trigger for formation of toxic aggregates in Alzheimer's disease. *Aging (Albany NY)* **3**, 803–812 (2011).

37. Törnquist, M. *et al.* Secondary nucleation in amyloid formation. *Chem. Commun.* **54**, 8667–8684 (2018).

38. Linse, S. Monomer-dependent secondary nucleation in amyloid formation. *Biophys Rev* **9**, 329–338 (2017).

39. Cohen, S. I. A. *et al.* Proliferation of amyloid-β42 aggregates occurs through a secondary nucleation mechanism. *Proc. Natl. Acad. Sci. U.S.A.* **110**, 9758–9763 (2013).

40. Buell, A. K. *et al.* Detailed Analysis of the Energy Barriers for Amyloid Fibril Growth. *Angewandte Chemie International Edition* **51**, 5247–5251 (2012).

41. Cukalevski, R. *et al.* The Aβ40 and Aβ42 peptides self-assemble into separate homomolecular fibrils in binary mixtures but cross-react during primary nucleation. *Chem. Sci.* **6,** 4215–4233 (2015).

42. Pauwels, K. *et al.* Structural Basis for Increased Toxicity of Pathological Aβ42:Aβ40 Ratios in Alzheimer Disease. *J Biol Chem* **287,** 5650–5660 (2012).

43. Roher, A. E. *et al.* beta-Amyloid-(1-42) is a major component of cerebrovascular amyloid deposits: implications for the pathology of Alzheimer disease. *Proc Natl Acad Sci U S A* **90**, 10836–10840 (1993).

44. Kuperstein, I. *et al.* Neurotoxicity of Alzheimer's disease Aβ peptides is induced by small changes in the Aβ42 to Aβ40 ratio. *EMBO J* **29**, 3408–3420 (2010).

45. COHEN, A. S. & CALKINS, E. Electron Microscopic Observations on a Fibrous Component in Amyloid of Diverse Origins. *Nature* **183**, 1202–1203 (1959).

46. EANES, E. D. & GLENNER, G. G. X-RAY DIFFRACTION STUDIES ON AMYLOID FILAMENTS. *J Histochem Cytochem.* **16**, 673–677 (1968).

47. Nelson, R. *et al.* Structure of the cross-β spine of amyloid-like fibrils. *Nature* **435**, 773–778 (2005).

48. Sunde, M. *et al.* Common core structure of amyloid fibrils by synchrotron X-ray diffraction11Edited by F. E. Cohen. *Journal of Molecular Biology* **273**, 729–739 (1997).

49. Greenwald, J. & Riek, R. Biology of Amyloid: Structure, Function, and Regulation. *Structure* **18**, 1244–1260 (2010).

50. Astbury, W. T., Dickinson, S. & Bailey, K. The X-ray interpretation of denaturation and the structure of the seed globulins. *Biochemical Journal* **29**, 2351-2360.1 (1935).

51. Sunde, M. *et al.* Common core structure of amyloid fibrils by synchrotron X-ray diffraction11Edited by F. E. Cohen. *Journal of Molecular Biology* **273**, 729–739 (1997).

52. Naito, A. & Kawamura, I. Solid-state NMR as a method to reveal structure and membrane-interaction of amyloidogenic proteins and peptides. *Biochimica et Biophysica Acta (BBA) - Biomembranes* **1768**, 1900–1912 (2007).

53. Petkova, A. T. *et al.* A structural model for Alzheimer's beta -amyloid fibrils based on experimental constraints from solid state NMR. *Proc. Natl. Acad. Sci. U.S.A.* **99**, 16742–16747 (2002).

54. Bertini, I. *et al.* Formation kinetics and structural features of Beta-amyloid aggregates by sedimented solute NMR. *Chembiochem* **14**, 1891–1897 (2013).

55. Bera, S. *et al.* Biophysical insights into the membrane interaction of the core amyloid-forming Aβ40 fragment K16-K28 and its role in the pathogenesis of Alzheimer's disease. *Phys Chem Chem Phys* **18**, 16890–16901 (2016).

56. Bertini, I., Gonnelli, L., Luchinat, C., Mao, J. & Nesi, A. A new structural model of Aβ40 fibrils. *J. Am. Chem. Soc.* **133**, 16013–16022 (2011).

57. Grasso, G. *et al.* Conformational Dynamics and Stability of U-Shaped and S-Shaped Amyloid β Assemblies. *Int J Mol Sci* **19**, (2018).

58. Wälti, M. A. *et al.* Atomic-resolution structure of a disease-relevant Aβ1-42 amyloid fibril. *Proc. Natl. Acad. Sci. U.S.A.* **113**, E4976-4984 (2016).

59. Colvin, M. T. *et al.* High Resolution Structural Characterization of Aβ42 Amyloid Fibrils by Magic Angle Spinning NMR. *J. Am. Chem. Soc.* **137**, 7509–7518 (2015).

60. Xiao, Y. *et al.* Aβ(1–42) fibril structure illuminates self-recognition and replication of amyloid in Alzheimer's disease. *Nature Structural &Amp; Molecular Biology* **22**, 499 (2015).

61. Fitzpatrick, A. W. & Saibil, H. R. Cryo-EM of amyloid fibrils and cellular aggregates. *Current Opinion in Structural Biology* **58**, 34–42 (2019).

62. Biancalana, M. & Koide, S. Molecular mechanism of Thioflavin-T binding to amyloid fibrils. *Biochim. Biophys. Acta* **1804**, 1405–1412 (2010).

63. Xue, C., Lin, T. Y., Chang, D. & Guo, Z. Thioflavin T as an amyloid dye: fibril quantification, optimal concentration and effect on aggregation. *Royal Society Open Science* **4**, (2017).

64. Lindberg, D. J. *et al.* Binding of Thioflavin-T to Amyloid Fibrils Leads to Fluorescence Self-Quenching and Fibril Compaction. *Biochemistry* **56**, 2170–2174 (2017).

65. Wu, C., Biancalana, M., Koide, S. & Shea, J.-E. Binding Modes of Thioflavin-T to the Single-Layer β-Sheet of the Peptide Self-Assembly Mimics. *Journal of Molecular Biology* **394**, 627–633 (2009).

66. Parkinson, J. An Essay on the Shaking Palsy. *JNP* **14**, 223–236 (2002).

67. Jankovic, J. Parkinson's disease: clinical features and diagnosis. *Journal of Neurology, Neurosurgery & Psychiatry* **79**, 368–376 (2008).

68. Spillantini, M. G., Crowther, R. A., Jakes, R., Hasegawa, M. & Goedert, M. alpha-Synuclein in filamentous inclusions of Lewy bodies from Parkinson's disease and dementia with lewy bodies. *Proc. Natl. Acad. Sci. U.S.A.* **95**, 6469–6473 (1998).

69. Lees, A. J. Drugs for Parkinson's disease. *Journal of Neurology, Neurosurgery & Psychiatry* **73**, 607–610 (2002).

70. Wagner, J. *et al.* Anle138b: a novel oligomer modulator for disease-modifying therapy of neurodegenerative diseases such as prion and Parkinson's disease. *Acta Neuropathol* **125**, 795–813 (2013).

71. Polymeropoulos, M. H. *et al.* Mutation in the alpha-synuclein gene identified in families with Parkinson's disease. *Science* **276**, 2045–2047 (1997).

72. Lavedan, C. The Synuclein Family. *Genome Res.* **8**, 871–880 (1998).

73. Venda, L. L., Cragg, S. J., Buchman, V. L. & Wade-Martins, R. α-synuclein and dopamine at the crossroads of Parkinson's disease. Trends Neurosci. 33, 559–568 (2010).

74. Wallin, S. Intrinsically disordered proteins: structural and functional dynamics. *Research and Reports in Biology* (2017).

75. Hashimoto, M. *et al.* Oxidative stress induces amyloid-like aggregate formation of NACP/alpha-synuclein in vitro. *Neuroreport* **10**, 717–721 (1999).

76. Fink, A. L. The Aggregation and Fibrillation of α-synuclein. *Acc. Chem. Res.* **39**, 628–634 (2006).

77. Fusco, G. *et al.* Direct observation of the three regions in α-synuclein that determine its membrane-bound behaviour. *Nature Communications* **5**, 3827 (2014).

78. Emamzadeh, F. N. & Surguchov, A. Parkinson's Disease: Biomarkers, Treatment, and Risk Factors. *Frontiers in Neuroscience* **12**, (2018).

79. He, R. *et al.* Recent Advances in Biomarkers for Parkinson's Disease. *Front Aging Neurosci* **10**, (2018).

80. Parnetti, L. *et al.* Cerebrospinal fluid biomarkers in Parkinson disease. *Nature Reviews Neurology* **9**, 131–140 (2013).

81. Parnetti, L. *et al.* CSF and blood biomarkers for Parkinson's disease. *Lancet Neurol* **18**, 573–586 (2019).

82. Atik, A., Stewart, T. & Zhang, J. Alpha-Synuclein as a Biomarker for Parkinson's Disease. *Brain Pathol.* **26**, 410–418 (2016).

83. Tokuda, T. *et al.* Detection of elevated levels of α-synuclein oligomers in CSF from patients with Parkinson disease. *Neurology* **75**, 1766–1772 (2010).

84.Tian, C. *et al.* Erythrocytic α-synuclein as a potential biomarker for Parkinson's disease. *Translational Neurodegeneration* **8**, 15 (2019).

85. Fayyad, M. *et al.* Parkinson's disease biomarkers based on α-synuclein. *Journal of Neurochemistry* (2019). doi:10.1111/jnc.14809

86. Berlyand, Y. *et al.* An Alzheimer's Disease-Derived Biomarker Signature Identifies Parkinson's Disease Patients with Dementia. *PLOS ONE* **11**, e0147319 (2016).

87. Doherty, G. H. Homocysteine and Parkinson's Disease: A Complex Relationship. *Journal of Neurological Disorders* **01**, (2013).

88. Constantinescu, R., Rosengren, L., Eriksson, B., Blennow, K. & Axelsson, M. Cerebrospinal fluid neurofilament light and tau protein as mortality biomarkers in parkinsonism. *Acta Neurol. Scand.* **140**, 147–156 (2019).

89. Parnetti, L. *et al.* Cerebrospinal fluid β-glucocerebrosidase activity is reduced in parkinson's disease patients. *Mov. Disord.* **32**, 1423–1431 (2017).

90. Cipriani, S., Chen, X. & Schwarzschild, M. A. Urate: a novel biomarker of Parkinson's disease risk, diagnosis and prognosis. *Biomark Med* **4**, 701–712 (2010).

91. Hong, Z. *et al.* DJ-1 and α-synuclein in human cerebrospinal fluid as biomarkers of Parkinson's disease. *Brain* **133**, 713–726 (2010).

92. Mischley, L. K., Allen, J. & Bradley, R. Coenzyme Q10 Deficiency in Patients with Parkinson's Disease. *J Neurol Sci* **318**, 72–75 (2012).

93. Medeiros, M. S. *et al.* Iron and Oxidative Stress in Parkinson's Disease: An Observational Study of Injury Biomarkers. *PLoS ONE* **11**, e0146129 (2016).

94. Franco, R., Doorn, J. A. & Rochet, J.-C. *Oxidative Stress and Redox Signalling in Parkinson's Disease*. (Royal Society of Chemistry, 2017).

95. Leal, M. C., Casabona, J. C., Puntel, M. & Pitossi, F. Interleukin-1β and tumor necrosis factor-α: reliable targets for protective therapies in Parkinson's Disease? *Front. Cell. Neurosci.* **7**, (2013).

96. Hall, S. *et al.* Cerebrospinal fluid concentrations of inflammatory markers in Parkinson's disease and atypical parkinsonian disorders. *Scientific Reports* **8**, 1–9 (2018).

97. Eidson, L. N. *et al.* Candidate inflammatory biomarkers display unique relationships with alpha-synuclein and correlate with measures of disease severity in subjects with Parkinson's disease. *J Neuroinflammation* **14**, (2017).

98. Emamzadeh, F. N. Role of Apolipoproteins and α-synuclein in Parkinson's Disease. *J Mol Neurosci* **62**, 344–355 (2017).

99. Li, L. *et al.* Relationship between Apolipoprotein Superfamily and Parkinson's Disease. *Chin Med J (Engl)* **130**, 2616–2623 (2017).

100. Qiang, J. K. *et al.* Plasma apolipoprotein A1 as a biomarker for Parkinson disease. *Ann. Neurol.* **74**, 119–127 (2013).

101. Waldner, A., Dassati, S., Redl, B., Smania, N. & Gandolfi, M. Apolipoprotein D Concentration in Human Plasma during Aging and in Parkinson's Disease: A Cross-Sectional Study. *Parkinsons Dis* **2018**, 3751516–3751516 (2018).

102. Paslawski, W. *et al.* α-synuclein−lipoprotein interactions and elevated ApoE level in cerebrospinal fluid from Parkinson's disease patients. *PNAS* **116**, 15226–15235 (2019).

103. Sasaki, K., Doh-ura, K., Wakisaka, Y. & Iwaki, T. Clusterin/apolipoprotein J is associated with cortical Lewy bodies: immunohistochemical study in cases with α-synucleinopathies. *Acta Neuropathol* **104**, 225–230 (2002).

104. Førland, M. G. *et al.* Evolution of cerebrospinal fluid total α-synuclein in Parkinson's disease. *Parkinsonism Relat. Disord.* **49**, 4–8 (2018).

105. Foulds, P. G. *et al.* A longitudinal study on α-synuclein in blood plasma as a biomarker for Parkinson's disease. *Sci Rep* **3**, 2540 (2013).

106. Kasuga, K., Nishizawa, M. & Ikeuchi, T. α-synuclein as CSF and Blood Biomarker of Dementia with Lewy Bodies. *Int J Alzheimers Dis* **2012**, (2012).

107. Eusebi, P. *et al.* Diagnostic utility of cerebrospinal fluid α-synuclein in Parkinson's disease: A systematic review and meta-analysis. *Mov. Disord.* **32**, 1389–1400 (2017).

108. Simonsen, A. H. *et al.* The utility of α-synuclein as biofluid marker in neurodegenerative diseases: a systematic review of the literature. *Biomarkers in Medicine* **10**, 19–34 (2015).

109. El-Agnaf, O. M. A. et al. Alpha-synuclein implicated in Parkinson's disease is present in extracellular biological fluids, including human plasma. FASEB J. Off. Publ. Fed. Am. Soc. Exp. Biol. 17, 1945–1947 (2003)

110. Braak, H. *et al.* Staging of the intracerebral inclusion body pathology associated with idiopathic Parkinson's disease (preclinical and clinical stages). *J. Neurol.* **249 Suppl 3**, III/1-5 (2002).

111. Steiner, J. A., Angot, E. & Brundin, P. A deadly spread: cellular mechanisms of α-synuclein transfer. Cell Death Differ 18, 1425–1433 (2011).

112. Majbour, N. K. *et al.* Oligomeric and phosphorylated alpha-synuclein as potential CSF biomarkers for Parkinson's disease. *Mol Neurodegener* **11**, (2016).

113. Feng, N. *et al.* Antibody biomarker for de novo Parkinson disease: attempted validation. *npj Parkinson's Disease* **4**, 28 (2018).

114. Sharon, R., Elhadi, S. A. & Grigoletto, J. Peripheral α-synuclein, determined by a lipid-elisa: A potential biomarker for Parkinson's disease. *Journal of the Neurological Sciences* **381**, 733 (2017).

115. Santos, M. C. T. dos *et al.* Evaluation of cerebrospinal fluid proteins as potential biomarkers for early stage Parkinson's disease diagnosis. *PLOS ONE* **13**, e0206536 (2018).

116. Gupta, V., Garg, R. K. & Khattri, S. Serological Analysis of Alpha-synuclein and NF-κB in Parkinson's Disease Patients. *J Clin Diagn Res* **9**, BC01–BC04 (2015).

117. Takatsuki, H. *et al.* Rapid and Quantitative Assay of Amyloid-Seeding Activity in Human Brains Affected with Prion Diseases. *PLOS ONE* **10**, e0126930 (2015).

118. Xu, Y., Martini-Stoica, H. & Zheng, H. A seeding based cellular assay of tauopathy. *Molecular Neurodegeneration* **11**, 32 (2016).

119. Colby, D. W. *et al.* Prion detection by an amyloid seeding assay. *Proc Natl Acad Sci U S A* **104**, 20914–20919 (2007).

120. Volpicelli-Daley, L. A., Luk, K. C. & Lee, V. M.-Y. Addition of exogenous α-synuclein Pre-formed fibrils to Primary Neuronal Cultures to seed recruitment of endogenous α-synuclein to Lewy body and Lewy Neurite-like aggregates. *Nat Protoc* **9**, 2135–2146 (2014)

121. Oueslati, A., Ximerakis, M. & Vekrellis, K. Protein Transmission, Seeding and Degradation: Key Steps for α-synuclein Prion-Like Propagation. *Exp Neurobiol* **23**, 324–336 (2014).

122. Walker, L. C., Diamond, M. I., Duff, K. E. & Hyman, B. T. Mechanisms of Protein Seeding in Neurodegenerative Diseases. *JAMA Neurol* **70**, (2013).

123. Weissmann, C. The state of the prion. *Nat Rev Microbiol* **2**, 861–871 (2004).

124. Barron, R. M. *et al.* PrP aggregation can be seeded by pre-formed recombinant PrP amyloid fibrils without the replication of infectious prions. *Acta Neuropathol* **132**, 611–624 (2016).

125. Takatsuki, H. *et al.* Prion-Seeding Activity Is widely Distributed in Tissues of Sporadic Creutzfeldt-Jakob Disease Patients. *EBioMedicine* **12**, 150–155 (2016).

126. Come, J. H., Fraser, P. E. & Lansbury, P. T. A kinetic model for amyloid formation in the prion diseases: importance of seeding. *Proc Natl Acad Sci U S A* **90**, 5959–5963 (1993).

127. Barria, M. A., Gonzalez-Romero, D. & Soto, C. Cyclic Amplification of Prion Protein Misfolding. *Methods Mol Biol* **849**, 199–212 (2012).

128. Jarrett, J. T. & Lansbury, P. T. Seeding 'one-dimensional crystallization' of amyloid: a αpathogenic mechanism in Alzheimer's disease and scrapie? *Cell* **73**, 1055–1058 (1993).

129. Olsson, T. T., Klementieva, O. & Gouras, G. K. Prion-like seeding and nucleation of intracellular amyloid-β. *Neurobiol. Dis.* **113**, 1–10 (2018).

130. Sowade, R. F. & Jahn, T. R. Seed-induced acceleration of amyloid-β mediated neurotoxicity in vivo. *Nat Commun* **8**, 1–12 (2017).

131. Okuzumi, A. *et al.* Rapid dissemination of alpha-synuclein seeds through neural circuits in an in-vivo prion-like seeding experiment. *Acta Neuropathologica Communications* **6**, 96 (2018).

132. Brundin, P. & Melki, R. Prying into the Prion Hypothesis for Parkinson's Disease. *J. Neurosci.* **37**, 9808–9818 (2017).

133. Kakuda, K. *et al.* Ultrasonication-based rapid amplification of α-synuclein aggregates in cerebrospinal fluid. *Scientific Reports* **9**, 6001 (2019).

134. Luk, K. C. *et al.* Exogenous α-synuclein fibrils seed the formation of Lewy body-like intracellular inclusions in cultured cells. *PNAS* 106, 20051–20056 (2009).

135. Recasens, A. & Dehay, B. Alpha-synuclein spreading in Parkinson's disease. *Front. Neuroanat.* 8, (2014).

136. Busquets, M. A., Espargaró, A., Estelrich, J. & Sabate, R. Could α-synuclein Amyloid-Like Aggregates Trigger a Prionic Neuronal Invasion? *BioMed Research International* (2015).

137. Angot, E., Steiner, J. A., Hansen, C., Li, J.-Y. & Brundin, P. Are synucleinopathies prion-like disorders? *The Lancet Neurology* 9, 1128–1138 (2010).

138. Jones, D. R. *et al.* Transmission of Soluble and Insoluble α-synuclein to Mice. *J Neuropathol Exp Neurol* 74, 1158–1169 (2015).

139. Green, A. J. E. RT-QuIC: a new test for sporadic CJD. *Practical Neurology* **19**, 49–55 (2019).

140. Groveman, B. R. *et al.* Rapid and ultra-sensitive quantitation of disease-associated α-synuclein seeds in brain and cerebrospinal fluid by αSyn RT-QuIC. *Acta Neuropathol Commun* **6**, (2018).

141. Jung, B. C. *et al.* Amplification of distinct α-synuclein fibril conformers through protein misfolding cyclic amplification. *Exp Mol Med* **49**, e314 (2017).

142. Yoshinaga, S., Yamanaka, T., Furukawa, Y. & Nukina, N. The detection of seeds alpha-synuclein using protein misfolding cyclic amplification(PMCA). *Journal of the Neurological Sciences* **381**, 972–973 (2017).

143. Paciotti, Silvia et al. “Are We Ready for Detecting α-synuclein Prone to Aggregation in Patients? The Case of “Protein-Misfolding Cyclic Amplification” and “Real-Time Quaking-Induced Conversion” as Diagnostic Tools.” *Front. Neurol.* (2018).

144. Kakuda, K. et al. Ultrasonication-based rapid amplification of α-synuclein aggregates in cerebrospinal fluid. Scientific Reports 9, 6001 (2019).

145. Soto, C., Saborio, G. P. & Anderes, L. Cyclic amplification of protein misfolding: application to prion-related disorders and beyond. *Trends Neurosci.* **25**, 390–394 (2002).

Chapter 2

Methodological aspects

2.1 Preparation of Aβ peptides with exogenous methionine

Amyloid beta monomers with an exogenous methionine (Met-0) were expressed using a pET3a plasmid (5′ cloning site NdeI -not destroyed-; 3′ cloning site BamHI-not destroyed-). The insertion of this Met-0 is essential for the production of heterologous proteins: the start codon that initiates translation process in E.Coli is ATG (Met).[1] Before using, the plasmid containing the gene was amplified and purified through Midiprep and Miniprep techniques based on alkaline lysis method, by H.C. Bimboim and J. Doly.[2],[3] The concentrations of plasmid used was 50-70 ng/µL for each 50µL of E.Coli batch.

2.1.a Expression of Aβ peptides

The E.Coli strain selected for the transformation protocol was the BL21(DE3)pLysS, competent cells providing tighter control of the expression of toxic proteins.[4] The original stocks (Lot: 3106858) worked better than the same strain of the other generations both in term of transformation efficiency and expression level. These cells are resistant to chloramphenicol that was added to the media together with ampicillin (plasmid antibiotic resistance).[5] To mantain the plasmid in the cells, avoiding satellite colonies formation, ampicillin was replaced by carbenicillin: this antibiotic is inactivated more slowly by β-lactamase enzymes, making the selection more effective.[6] The concentration of each antibiotic for liter of colture was that recommended: 100 µL/mL ampicillin/carbenicillin, 34 µL/mL chloramphenicol.

The best expression was observed using freshly transformed cells and not bacterial glycerol stocks. The growth was for performed using rich medium (Luria

Bertani, LB), minimal medium (M9) with the addition of nitrogen (ammonium sulphate) and carbon (glucose) sources, [7-9] or a combination of these two media for the expression of isotopically enriched samples (Marley method).[7]
The media were sterylized by performing an autoclave cycle (T=121°C, t=25 min). The protocol chosen for the expression was the Marley method (Figure 13) which permits to obtain a higher final monomer yield.

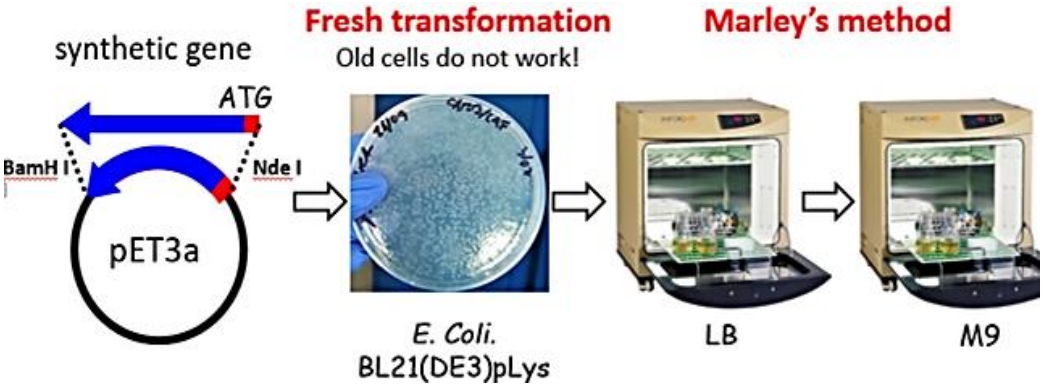

Fig. 13: Application of the method for preparing isotopically labeled recombinant proteins developed by J.Marley.

Transformed cells were grown in LB medium until OD600 value reached 0.6-0.8 (start of exponential phase of E.Coli growth) and, after a centrifugation at 3500 rpm (JA-10, Beckman Coulter), the pellet was exchanged into the M9 minimal medium containing $(^{15}NH4)_2SO_4$ 1.0 g/L and D-Glucose-$13C_6$ 4g/L as nitrogen and carbon sources for labelled samples. The expression was induced with 1.2 mM Isopropyl-β-D-thiogalactoside and, after 4 hours incubation at 39 °C, cells were harvested at 4000 rpm (JA-10,Beckman Coulter). The key point of this protocol was the expression at high temperature value (from 39°C to 42°C) which promotes the aggregation of hydrophobic Aβ peptides into insoluble inclusion bodies (IBs)[10-14], considered to be amorphous type of aggregates, devoid of any structural regularity. The IBs Aβ expression can be exploited as a strategy to recover the peptides directly from the insoluble fraction using a strong chaotropic agent (GdnHCl, Urea) at high concentration.[15],[16]

2.1.b Extraction and purification of Aβ peptides

Extraction step was performed through sonication for 35 minutes followed by IBs solubilisation through a homogenization process with Urea 8 M. Purification was performed via anion exchange chromatography in batch (according to Walsh et al.[17]) or using AKTA FPLC System through the Q-column with linear gradient of NaCl + Urea 8M buffer (GE Healthcare HiPrep™ Q HP 16/10). The last step of purification was a size-exclusion chromatography (SEC) using the preparative column Sephadex 75 HiLoad 16/60 (or 26/60) with 50 mM Ammonium acetate buffer at pH 8.5 as elution buffer.

After each step of chromatography, a column washing with NaOH was performd to remove all traces of impurities and protease contaminations. The advantage of SEC is its fractionation capability, which allows the separation of different population of oligomers (including protofibrils), as well as relatively pure populations of monomers, dimers and trimmers.[18-20]

More then one step of gel-filtration, according to the protocol reported by Hellstrand *et al.*, 2010 and Johnson *et al.*, 2011,[21],[22] was also carried out, but only when the final amount of the peptide obtained from the first SEC was enough to prepare samples with our target concentration. All the manipulations were carried out at alkaline pH which avoid protein precipitation at its isoelectric point (pI). Protein concentration was preliminary estimated using UV-VIS spectrophotometer.[23]

2.1.c Optimization of the protocol for Aβ1-40 and Aβ1-42 preparation

During this PhD project developement, an optimization of the protocol for the expression of Aβ monomers was implemented: Aβ1-40 was used as a template to solve many troubleshooting related to the expression of this monomer.

The plasmid was the first variable investigated. A comparison in terms of transformation efficiency between two plasmid (pET21a(+) and pET3a) containing the gene expressing Aβ1-40 was carried out: pET3a was confirmed as the most efficient vector.

Moreover, another screening procedure was carried out on E.Coli strains. Expression tests using C41(DE3), BL21Star(DE3), BL21(DE3)pLysS cells, corroborated that BL21(DE3)pLysS is the most eligible strain to express Aβ toxic

peptides. A satisfactory expression profile was obtained using small colture media volumes (higher S/V), according to the relationship between the oxygen levels and E.Coli growth.(Figure 14)

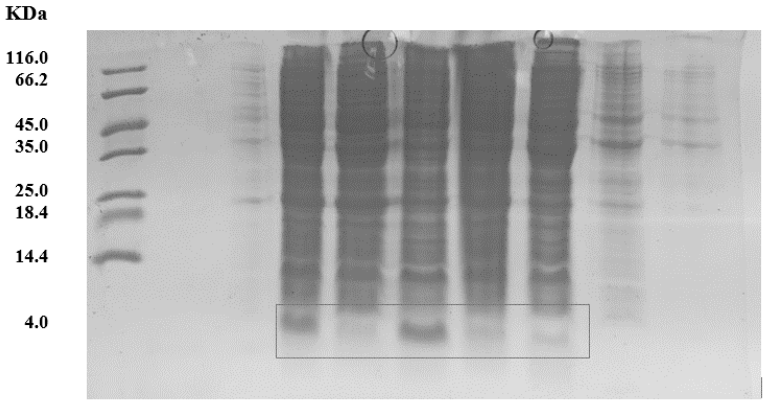

Fig.14: TRICINE SDS-PAGE. Scaling up of Aβ1-40 production using pET3a and BL21(DE3)pLysS strain.

In addition, several troubleshooting connected to the extraction and purification processes were figured out. In particular, because of Aβ1-40 is more soluble than Aβ1-42, the former protein is usually found in the soluble fraction during the extraction step through sonication.(Figure 15)

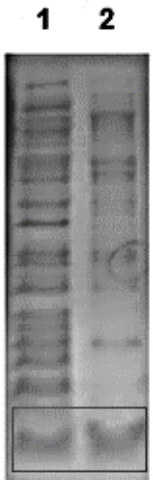

Fig. 15: Aβ1-40 in the soluble fraction. Lane 1: S1 (sample after sonication step) ; lane 2: S2 (sample after a washing step with buffer TRIS 10 mM, EDTA 1 mM, pH:8.0)

This issue was overcomed purifying the supernataint with a GE Healthcare HiPrep™ Q HP 16/10 in presence of denaturing conditions to avoid in protein aggregation inside the column.

A key step for the preparation of the recombinant Aβ protein is the purification proceure, considered extremely critical, because can influence the final yield of the sample.

Two different modalities of preliminary purification through anion-exchange were compared: column-mode and under vacuum with Büchner funnel, as was suggested by Walsh and coworkers[17].

In the under vacuum anion exchange, the diethylaminoethyl cellulose DE-52 resin (Whatman) was used and the elution was performed in 50 mL batches with increasing concentration of salt (20 mM NaCl, 50 mM NaCl, 3*125 mM NaCl, 150 mM NaCl, 200 mM NaCl, 1 M NaCl).

The advantage of the purification by Büchner funnel was that the the peptides were mantained diluted: using this strategy, Aβ aggregation, occurring when the sample is loaded in a column with a small volume, was overcomed. On the other hand, this method showed less capability of protein amount recovery after the elution.

Alternatively, GE Healthcare HiPrep™ Q HP 16/10 (CV=20 mL) or HiTrap Q FF anion exchange (CV=5 mL) with linear gradient of salt (0-50% NaCl) were used for this first step of purification and in presence of Urea at the concentration of 8M, to avoid the aggregation at the top of the column.

The Figure 16 shows the comparison on Tricine SDS-PAGE gel of the two different purification protocols via anion exchange chromatography.

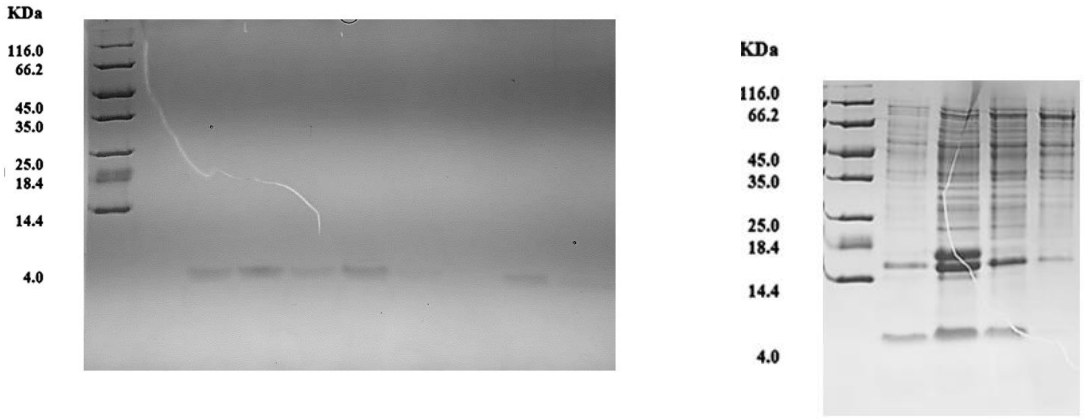

Fig.17: Batch-mode (from 50 mM to 1M NaCl) ; Column-mode (elution 0-50% NaCl)

In Figure 17, is reported the chromatogram of the anion exchange by HiTrap Q FF column.

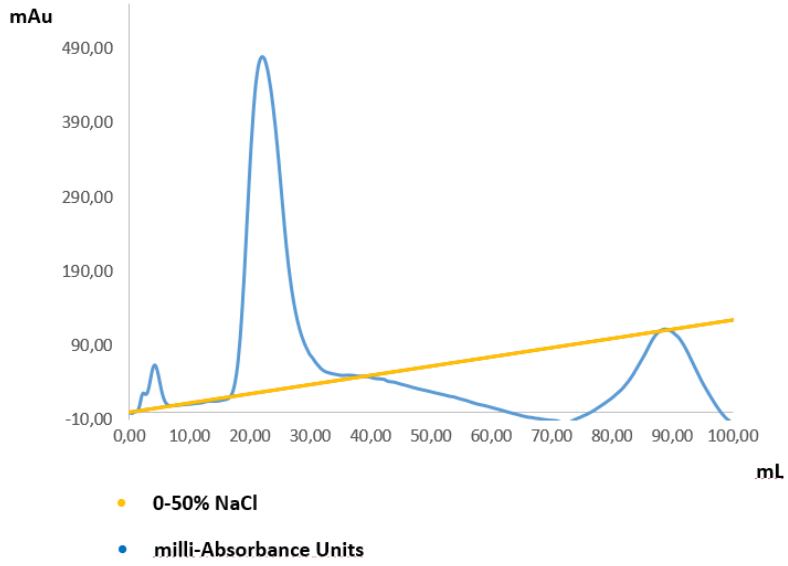

Fig. 17: anion exchange purification by HiTrap Q FF column (CV=5mL) in the presence of Urea 8M. System: AKTA FPLC.

The last step of purification was a gel-filtration (column: HiLoad 16/600 Superdex 75 pg or HiLoad 26/600 Superdex 75 pg).

When the yield was enough to inject sample again, a second size-exclusion chromatography was recommended. The chromatogram and the Tricine SDS-PAGE of the eluted fractions are shown below.

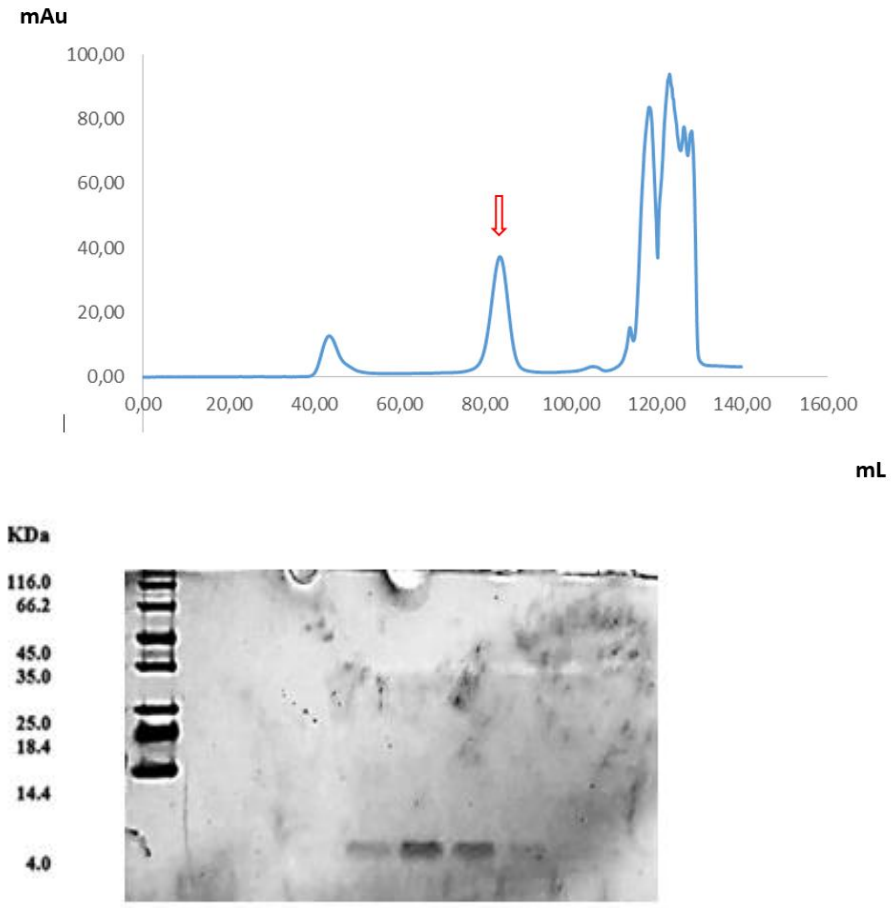

Fig. 18: gel-filtration chromatogram (HiLoad 16/600 Superdex 75 pg column) and eluted fractions.

To concentrate Aβ samples before each step of purification, two different strategies were tested. In particular, the eluate derived from anion exchange was concentrate by pressure-based method using stirred cells or lyophilized.

The freeze-drying was preferred because the dry state offers many advantages for long-term storage and because the biological activity of the protein is recovered.[25] Moreover, another critical point of the protocol was the choice of the chaotropic agent that should be added to Aβ sample to avoid the aggregation process.[26-29] The choice of the denaturant was strictly related to the applied purification protocol. After the purification by the anion exchange column, Urea (final concentration 8 M) was added to the elution buffers. Alternatively, when the the purification was carried out by anion exchange using the resin within a Büchner funnel under vacuum, the chaotropic agent was added only before the gel-filtration step. The procedure, in this last case, consisted in a freeze-drying followed by a resuspention anion exchange eluate with Guanidine hydrochloride (GdnHCl) 6 M that is a better denaturant than Urea.

Finally, to keep Aβ samples in a monomeric form, a protocol of monomerization at high pH values was adopted.[30],[31] Lyophilized Aβ samples were treated with NaOH 3.5 mM and sonicated in a ultrasonic bath to remove residual aggregates before their use for the in solution NMR experiments.

All the protocol implementations and the techniques tested for Aβ monomers purification are summarized in Scheme 1.

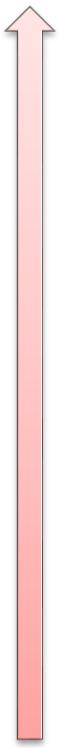

- Extraction: sonication

- Inclusion bodies (IBs) solubilization with UREA 8M

- Preliminary purification: anion exchange in column (elution buffer containing UREA 8M)

- Sample concentration by pressure-based method (stirred cells)

- Last purification: size-exclusion chromatography (SEC)

- Lyophilization

- Monomerization with NaOH 3.5 mM and sonication in a ultrasonic bath to remove residual aggregates

- Extraction: sonication

- Inclusion bodies (IBs) solubilization with UREA 8M

- Preliminary purification: anion exchange using Büchner funnel

- Lyophilization

- Resuspention of lyophilized sample with a buffer containing GdnHCl 6M

-Last purification: size-exclusion chromatography (SEC)

- Lyophilization

- Monomerization with NaOH 3.5 mM and sonication in a ultrasonic bath to remove residual aggregates

Scheme 1: Two alternative extraction and purification protocols of Aβ peptides.

2.2 NMR sample preparation of Aβ1-40 for kinetics studies

NMR samples of Aβ1-40 peptide were prepared at the concentration of 30 μM and 100 μM in 50 mM $(NH_4)OAc$ buffer,containing EDTA 1.0 mM NaN_3 0.2%, ThT 5.0 μM (only for samples which were used in parallel with fluorescence), SigmaFast Protease Inhibitor Cocktail and 10% D_2O at pH 8.5.

This value that is higher than physiological pH was chosen because it allows the formation of fibrils with with high reproducibility.[32]

These experimental conditions were selected after performing a series of screening tests to reach the best sample stability.

The experiments were recorded on a Bruker 700 MHz NMR spectrometer equipped with an automatic sample changer. The results of this screening are summarized in Table 3.

Table 3: Summary of the tests performed using a 700 MHz Bruker NMR spectrometer to find the optimal aggregation conditions.

N°	Aβ (μM)	Final state	Features of the $(NH_4)OAc$ buffer
1	40	Fast degradation	NaN_3 0.02% + inib. 10 μM ABSF
2	40	Fast degradation	-
3	40	Poor degradation w/o fibrillation	NaN_3 0.2%
4	40	Poor degradation w/o fibrillation	NaN_3 0.2% + inib. 100 μM ABSF
5	40	Poor degradation w/o fibrillation	NaN_3 0.2% + inib. 10 μM ABSF
6	40	Degradation	inib. 100 μM ABSF
7	40	Degradation	NaN_3 0.02% + inib. 100 μM ABSF
8	40	No degradation w fibrillation	NaN_3 0.02% + inib. 10 μM ABSF + 10 mM EDTA
9	40	No signal w protein precipitation	NaN_3 0.02% + inib. 10 μM ABSF + 1 mM $ZnCl_2$
10	40	Degradation w fibrillation	NaN_3 0.02% + inib. 10 μM ABSF + 100 μM EDTA
11	40	Poor degradation w fibrillation	NaN_3 0.2% + 1mM EDTA
12	40	Fast degradation	NaN_3 0.02% + inib. 10 μM ABSF + 1 μM ZnCl2
13	40	Poor degradation w/o fibrillation	NaN_3 0.02% + inib. 10 μM ABSF + 20 μM ThT
14	40	Poor degradation w fibrillation	NaN_3 0.02% + inib. 10 μM ABSF + 100 μM EDTA + 20 μM ThT
15	40	Poor degradation w fibrillation	1 mM EDTA
16	40	No degradation w fibrillation	10 mM EDTA
17	40	Degradation w fibrillation	NaN_3 0.2% + inib. 10 μM ABSF
18	40	Poor degradation w/o fibrillation	NaN_3 0.02% + inib. 10 μM ABSF (sterilized tube)
19	40	Degradation	NaN_3 0.2% + inib. 10 μM ABSF + 1 mM ZnCl2
20	100	Poor degradation w fibrillation	NaN_3 0.2% + 1 mM EDTA
21	150	No degradation w fibrillation	NaN_3 0.2% + inib. 10 μM ABSF + 1 mM EDTA

The fast degradation of the monomeric Aβ1-40 was a critical problem for the reproducibility of our kinetics analysis of the protein aggregation [33],[34].

Bacterial contamination was one of the sources for the protein degradation. Indeed, the degradation was partially abolished by the addition of sodium azide to the solution and by using sterilized NMR tube.[35]

In Figure 19 are reported the 1D ^{1}H NMR spectra collected at different time points on a sample of Aβ1-40 at the concentration of 40 μM and at a temperature of 298 K with a pH 8.5 in ammonium acetate buffer. The growth of sharp peaks near the monomer signals in the methyl region is a hallmark of degradation.[39] The degradation was then completely abolished by adding a protease inhibitor cocktail containing high concentration of EDTA, a divalent metal ions cheletors with a specific activity against metalloproteases.[36-38]

Therefore, the NMR esperiments were recorded on sample of the monomeric Aβ1-40 containing 0.2% of sodium azide , the *SigmaFast* EDTA-free complete protease inhibitor cocktail with ABSF at concentration of 10 μM and 1 mM of EDTA.

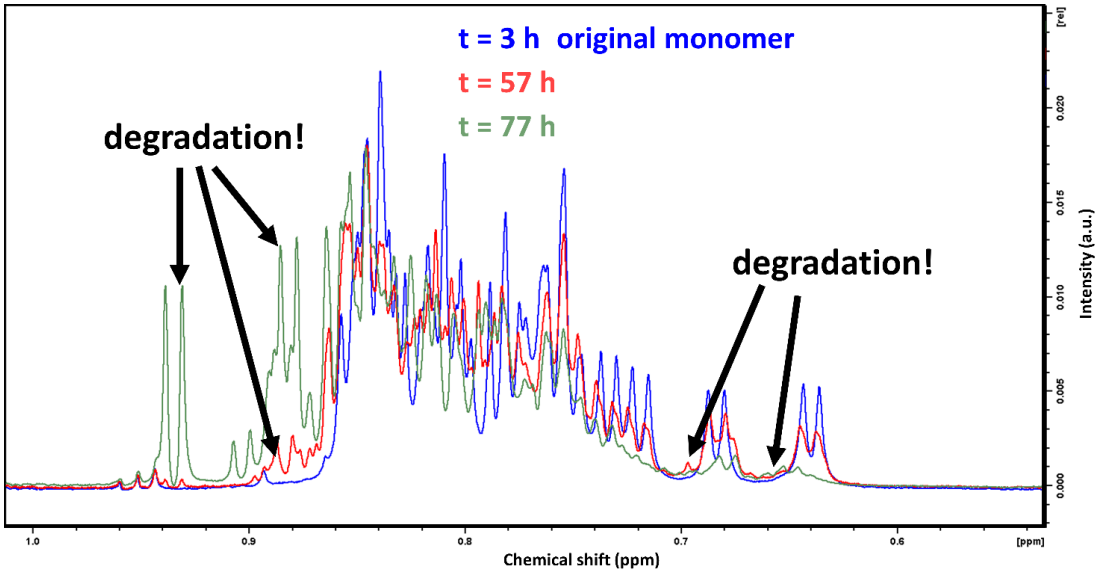

Fig. 19: 1D ^{1}H NMR spectra of a 40 μM Aβ1-40 sample in absence of EDTA 1.0 mM, NaN_3 0.2%, and SigmaFast Protease Inhibitor Cocktail. (Reprint from Supporting Information. Bellomo, G. *et al.* Aggregation kinetics of the Aβ1-40 peptide monitored by NMR. *Chem. Commun. (Camb.)* **54**, 7601–7604 (2018).)

Another aspect that affected the process of Aβ fibril formation with a dramatic effect on the aggregation kinetics, was the presence of contaminants in the NMR tubes. If the tubes are not properly cleaned, the presence of a solid impurity could promote the formation of macroscopic fibrillary nuclei at the bottom of NMR tube (Figure 20).

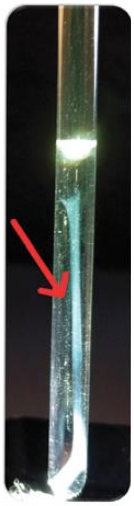

Fig. 20: agglomerate of fibrils presumably grown over the surface of an impurity present in the bottom of the NMR tube, the pale blue color resulted from the addition of 5 mM of ThT. (Reprint from Bellomo, G. *et al.* Aggregation kinetics of the Aβ1-40 peptide monitored by NMR. *Chem. Commun. (Camb.)* **54**, 7601–7604 (2018).)

2.3 Assembly of Aβ42:Aβ40 mixed fibrils revealed by SSNMR and microscopy (EM & AFM) and labelling schemes

To investigate the arrangement of the fibrils obtained by mixing Aβ1-40 and Aβ1-42 peptides, equimolar solutions of the two proteins were mixed and the resulting fibrils investigated by Solid-state NMR Spectroscopy (SSNMR).Different labeling schemes were used to record specific experiments and more recently:

- ^{15}N-uniformly enriched Aβ1-42/ ^{13}C-uniformly enriched Aβ1-40.
- ^{15}N-uniformly enriched Aβ1-42/ natural isotopic abundance Aβ1-40 (control sample).
- ^{15}N-uniformly enriched Aβ1-40/ natural isotopic abundance Aβ1-42 (control sample)

The same fibrils were investigated by for EM and AFM microscopy..
The experimental protocol to prepare the fibrils is the following:

- Sample concentration: 15 mg (for SSNMR) or 5 mg (for AFM and EM) of diluted samples in 50 mM ammonium acetate buffer (pH 8.5) of enriched ^{15}N Aβ1-42 and ^{13}C Aβ1-40 were concentrated to reach 100 μM as final concentration (measured by UV-VIS spectrophotometer, Figure 21)

- Fibrillization reaction: concentrated samples were filtered through a 0.20 μm syringe filter, put into 2mL microcentrifuge tubes (V=1 mL each), sealed with parafilm tape and incubated at 37 °C under shaking (950 rpm) for 4- 5 weeks.

In Figure 22 are reported the EM (Fig 22A) and AFM (Fig.22B) images acquired in collaboration with Max-Delbrück-Centrum für Molekulare Medizin (MDC) Berlin.

- Sample preparation for SSNMR: overnight ultracentrifugation at 60000 rpm (ca. 2.65 × 105 g) and 4 °C for 24 h. The pellet was washed with fresh and cold ultrapure water (Millipore) for three times (1 mL per time), and then wet material was packed into a 3.2 mm ZrO2 MAS rotor under 4 °C.

- Fibril samples were kept fully hydrated during all the steps.

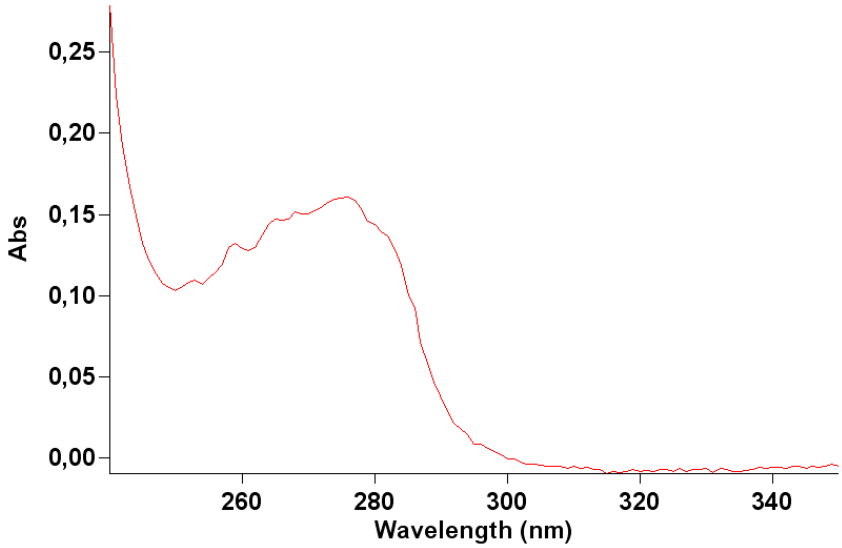

Fig. 21: Aβ monomers quantification for fibrillization reaction using Varian Cary 50 Bio UV-VISible Spectrophotometer (Beer's law).

AβM1-40 and AβM1-42 aromatic amino acids

Phe (F) 3

Trp (W) 0

Tyr (Y) 1

MW AβM1-40: 4461 Da

MW AβM1-42: 4645,2 Da

• $C = A / \varepsilon b$

• A: absorbance value (A280nm)

• ε:1490 M^{-1}/cm^{-1}

• b path length (1 cm)

• C: Concentration (M) → 100µM

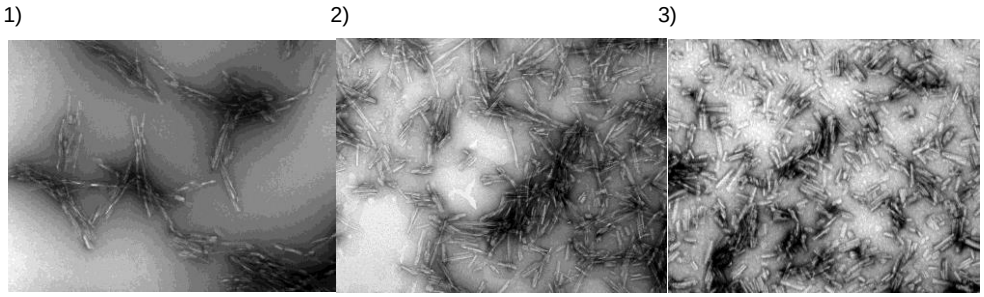

Fig. 22 A: 1) EM picture of mixed fibrils.
2) Fibrils sonicated for 5 min (fibrils are still sticking together).
3) Fibrils sonicated for 10 min (smaller fragments are produced).

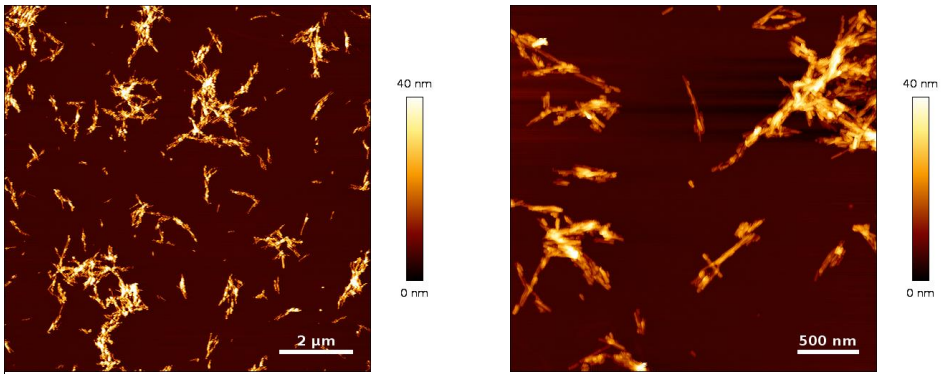

Fig. 22 B: AFM pictures.

2.4 Production of human recombinant α-synuclein

Human recombinant α-synuclein was expressed in the full-length wild-type (wt) canonical isoform (1-140) and in the His-tag (C-term and N-term) variants.
For the wt α-synuclein, a pT7-7 plasmid (5′ cloning site NdeI -not destroyed- , 3′ cloning site HindIII -not destroyed-) cloned with the gene encoding wild-type α-synuclein was used. The E.Coli strain chosen as host system for the expression was BL21(DE3)Gold.
Recombinant α-synuclein with a polyhistidine tag (six His residues) was expressed starting from BL21(DE3)Gold cells and pET-15b (N-terminal His tag) and pET21a(+) (C-terminal His tag) containing SNCA gene.
All the plasmids were genetically linked with amplicillin resistance.

2.4.a Expression and extraction of α-synuclein

BL21(DE3)Gold competent cells (50 µL) were transformed with 50-100 ng/µL of plasmid using heat shock method.
The overnight preculture of the transformed cells was diluted 100-fold in LB or M9 media (with carbon and ^{15}N-nitrogen sources for labelled samples) and induced at an OD600 value of 0.6−0.8 with 1 mM isopropyl-β-D-thiogalactoside (IPTG). After 5 h of incubation at 37 °C, the cells were harvested at 4000 rpm (JA-10, Beckman Coulter).
The extraction was carried out through osmotic shock using as lysis buffer 100 mL of the buffer Tris 30 mM, ethylenediaminetetraacetic acid (EDTA) 2 mM, and sucrose 40%, at pH 7.2, according to Shevchik et al.[40] and Huang et al.[41]. The suspension was then ultracentrifuged at 20000 rpm (Type 70 Ti rotor, Beckman Coulter) for 25 min, and the pellet was collected and resuspended with 90 mL precooled ultrapure water containing 38 µL of 1 M $MgCl_2$ and then ultracentrifuged a second time. Supernatants derived from these two centrifugation steps were combined and dialyzed against 4 L of 20 mM Tris/HCl buffer at pH 8.0.
The SDS-PAGE in Figure 23 displays the extraction profile recombinant of α-synuclein through osmotic shock technique. This lysis method exploiting osmotic shock was preferred to sonication procedure due to its mildness and the the absence of localized heating generated during the sonication process, expecially

when the sonicator is not equipped with a pre-cooling system (large-volume samples). Another advantage of this technique is that it allows the complete recovery of α-synuclein from the periplasm, the location where this protein is mostly expressed in Escherichia coli.[42],[43]

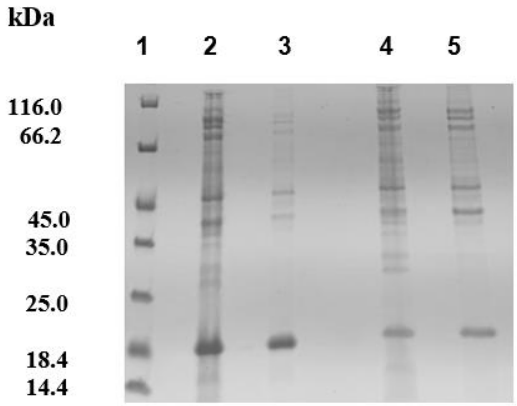

Fig. 23: SDS-PAGE α-synuclein extraction: lane 1 Thermo Scientific Unstained Protein Molecular Weight Marker, lane 2: cell pellet resuspended in lysis buffer, lane 3: collected supernatant after the first ultracentrifugation at 20000 rpm, lane 4:pellet resuspended in cold water(+38 µL $MgCl_2$) lane 5: collected supernatant after the second ultracentrifugation at 20000 rpm.

As can be observed from Figure 23, the apparent MW of α-synuclein is 18 kDa (theoretical MW: 14 kDa): this altered gel mobility can be attributable to the low binding of SDS by the highly acidic C-term sequence of the protein.[44]
Samples of α-synuclein-6xHis tag were expressed and purified using the same protocols of the wilde-type protein. The only difference was the use of a HisTrap FF column, CV= 5mL for the preliminary purification, in lieu of anion exchange.

2.4.b Purification of α-synuclein and protocol modifications

Wild-type full length recombinant α-synuclein was purified as follow:
Supernatants derived from the extraction step were combined and dialyzed against 4 L of 20 mM Tris/HCl buffer at pH 8.0. The protein was then loaded in the fast protein liquid chromatography system, and anion-exchange chromatography was carried out with 0−50% linear gradient 1 M NaCl (GE Healthcare HiPrep Q HP 16/10 Column). The collected fractions were lyophilized and resuspended in
10 mM Tris/HCl, 1 mM EDTA, and 8 M Urea at pH 8.0 for chemical denaturation.

The advantage of this protocol is that is avoided the boiling method before the column injection, adopted in many purification protocols of α-synuclein. [45],[46]
Sample heating does not affect on the structure of α-synuclein that, due to its solubility, remains in solution. Conversely, the other proteins present in solution, precipitate when exposed to the thermal denaturation.
The boiling procedure (T: 90-100°C) of α-synuclein should be avoided because it gives rise to the formation of degradation products, as reported in the literature.[41],[47],[48]
Another relevant point that should be taken into account in the preparation of sample of monomeric α-synuclein, is the aggregate removal by gel-filtration chromatography.
To eliminate the aggregates still present in solution, two size-exclusion chromatographies (HiLoad 16/600 Superdex 75 pg Column) were cerried out with 20 mM phosphate and 0.5 mM EDTA at pH 8.0 as the elution buffer (Figure 24). Purified α-synuclein was dialyzed against Milli-Q water and lyophilized in batches for long-term storage. The Roche complete protease inhibitor cocktail was added only during the extraction step in the quantity suggested by the producer.
In the Scheme 2 are reported the two tested extraction and purification procedures. The protocol providing the osmotic shock extraction and back-to-back gel-filtration purification allowed to achive better results in terms of purity of the final α-synuclein samples.

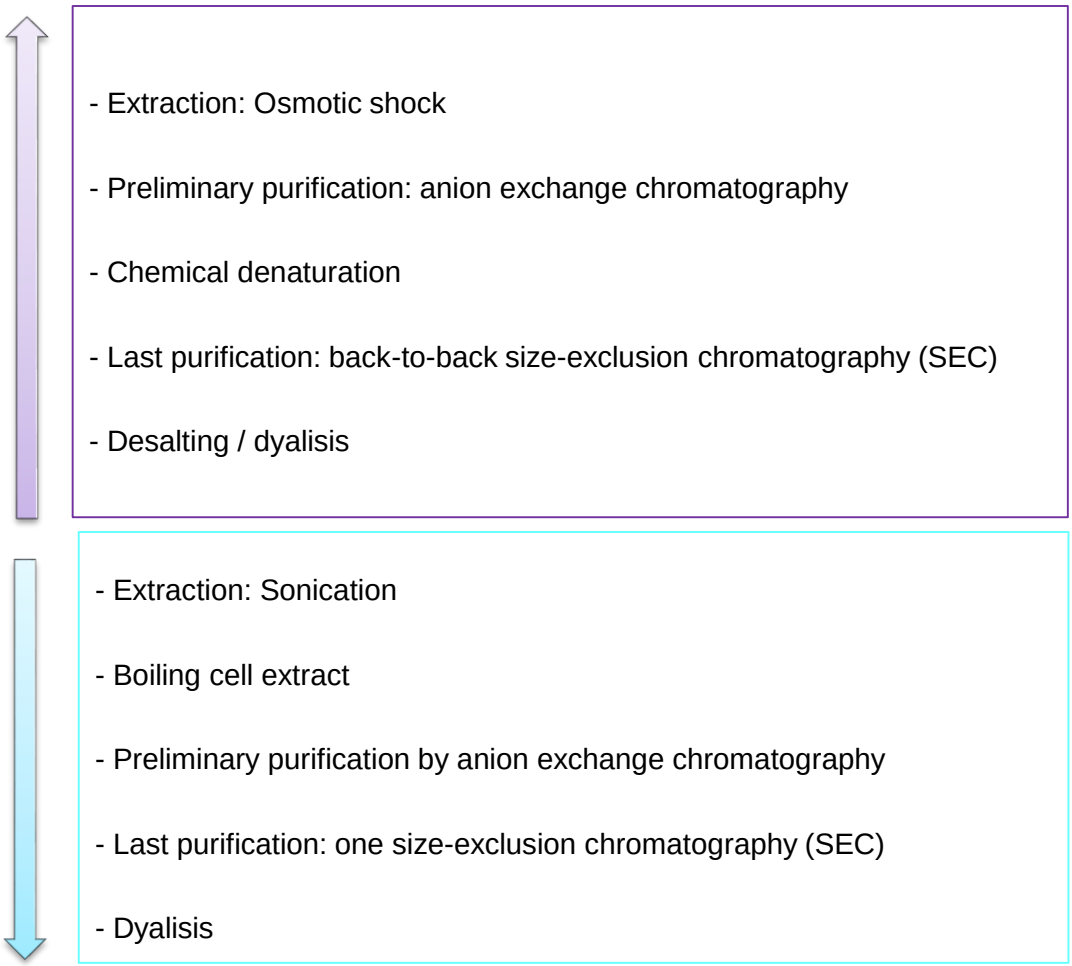

Scheme 2: Comparison between the two different extraction and purification procedures of α-synuclein.

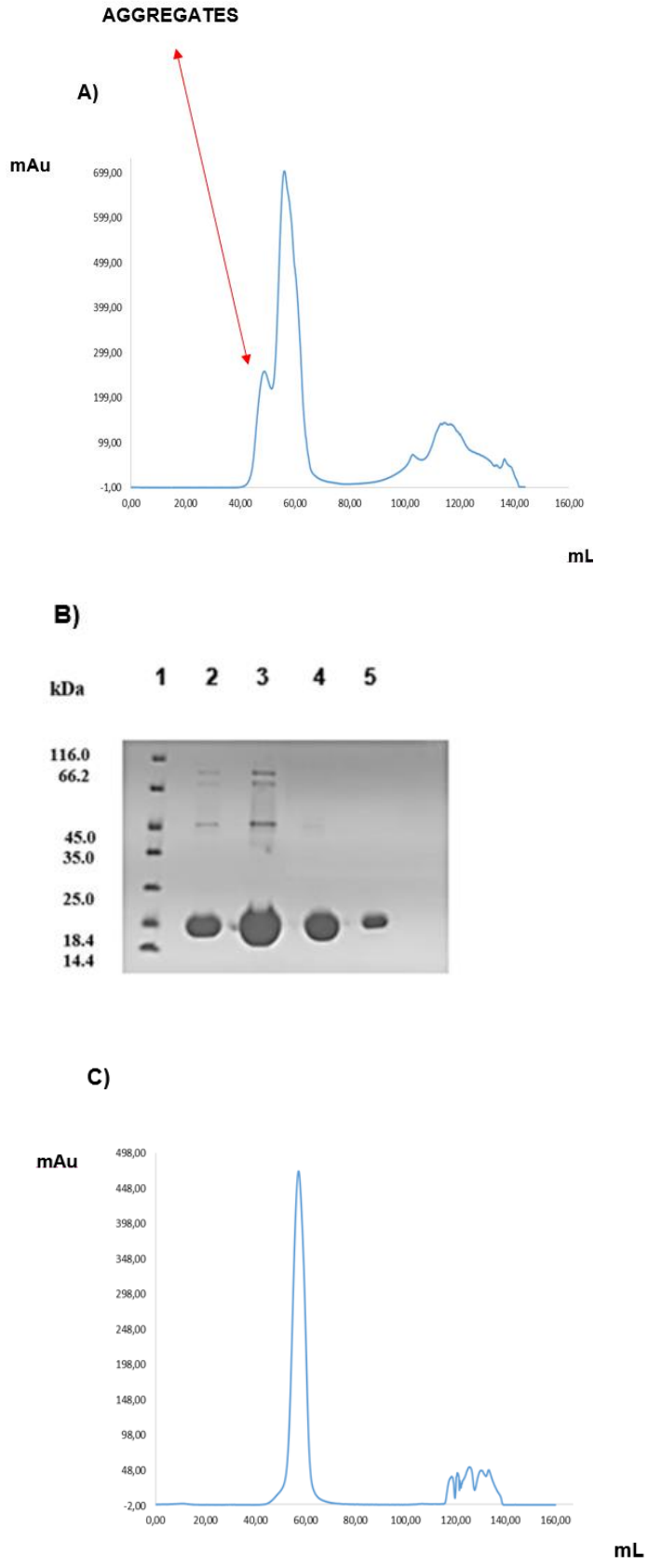

Fig. 24: A) 1st SEC purification. **B)** lane 1: Thermo Scientific Unstained Protein Molecular Weight Marker, lane 2 and 3: α-synuclein fractions after the 1st SEC purification, lane 4 and 5: α-synuclein fractions after the 2nd SEC purification. **C)** 2nd SEC purification.

It might also be noted that, a sizable difference between the purity of the α-synuclein-6xHis (purified by HisTrap FF column) and that of the wt protein (both expressed in LB medium), existed after the first purification step (Figure 25).
For the α-synuclein-6xHis the second size-exclusion of the protocol could be avoided.

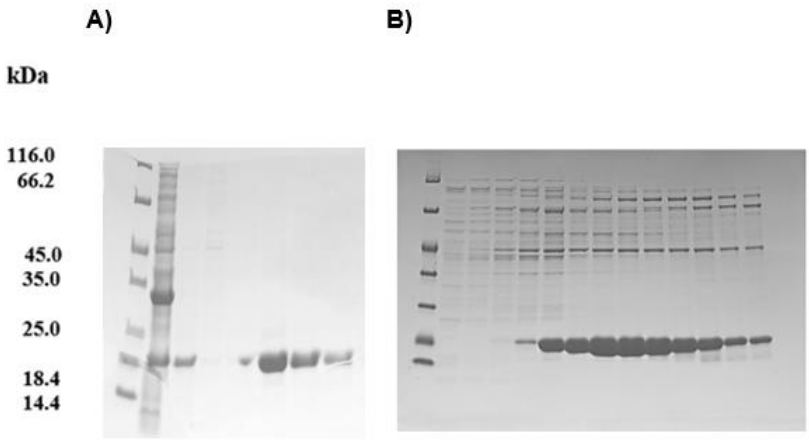

Fig. 25: A) Extraction and purification of α-synuclein-6xHis. B) Purification of wt full-length α-synuclein by anion exchange.

The removal of the Urea from the final sample was another critical step in the protocol. The presence of the denaturant was monitored by measuring spectrophotometrically the shifts of the absorbance of tyrosine and tryptophan at 287-291 nm: this increasing originates from the change in refractive index of the solvent with the concentration of the chaotropic added.[49] (Figure 26)

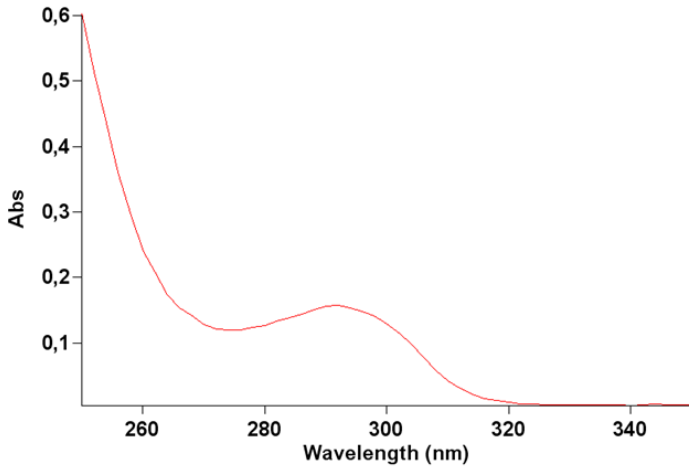

Fig. 26: Absorbance shift at 287-291 nm of aromatic residues in presence of Urea 8M (measure performed using Varian Cary 50 Bio UV-VISible Spectrophotometer).

A desalting step, followed by a dyalisis allows to remove the Urea from the α-synuclein final samples.

2.4.c α-synuclein samples quality check

To check the monomeric state of alpha-synuclein in the final sample, Western Blot (WB) assays using α-synuclein Antibody (211) and α-synuclein-O2 (immunogen: aggregated α-synuclein) were performed. At this regard, the sample alpha-synuclein prepared according the protocols described above have been analyzed and compared.

The Figure 27 shows the difference between α-synuclein samples purified using the two different protocols previously described: the former (A) was prepared without the chemical denaturation and the back-to-back SEC purification, the latter (B) was produced by means of these implementations.

The detection with α-synuclein O_2 anti-α-synuclein aggregated Antibody, confirms the efficiency of the protocol optimizations (only the band of the monomer, without degradation, was observed).

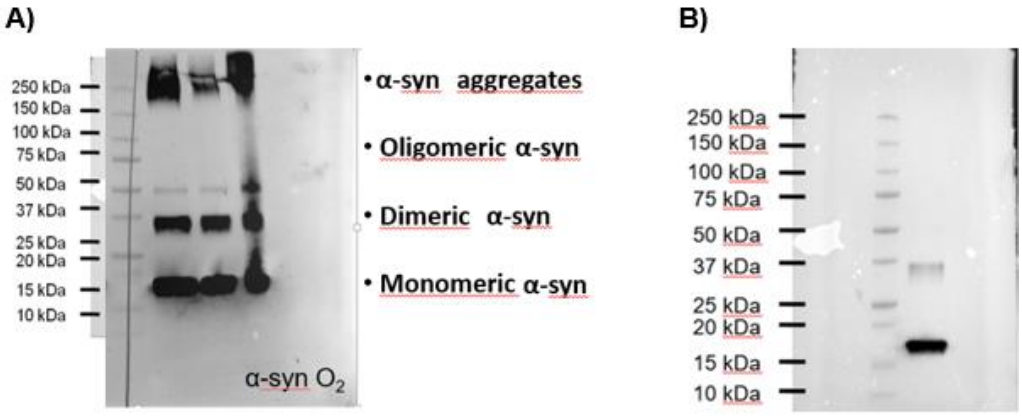

Fig. 27: Sample quality check. A) detection by anti-α-synuclein antibody with specifically binds aggregated forms of alpha-synuclein. B) monomeric alpha-synuclein detected by the same antibody.

2.5: Cerebrospinal fluid pH monitoring

A relevant aspect to consider when biological fluids are manipulated is their biochemistry.

In particular, when ex vivo pooled cerebrospinal fluid of patients not affected by synucleinopathies is handled, the pH can increase with respect to the original physiological value (pH= 7.4). In Figure 28 and in Figure 29 are reported CSF pH variations monitored as a function of time in the presence and in absence of Phosphate-buffered saline (PBS) buffer. To exclude any pH variation due to bacterial contamination, 0.08% of NaN_3 was added to 200 µL of pooled CSF.

After vortexing and air-exposing cyclically the fluid for several times at RT, a dramatic increase of the pH up to alkaline values was observed (highest pH=9.2).

When the biological fluid is stored in Eppendorf tube with closed hermetic seal at 4°C, the pH remained constant.

This pH-lability suggests the relevance of biological fluids processing and storage.

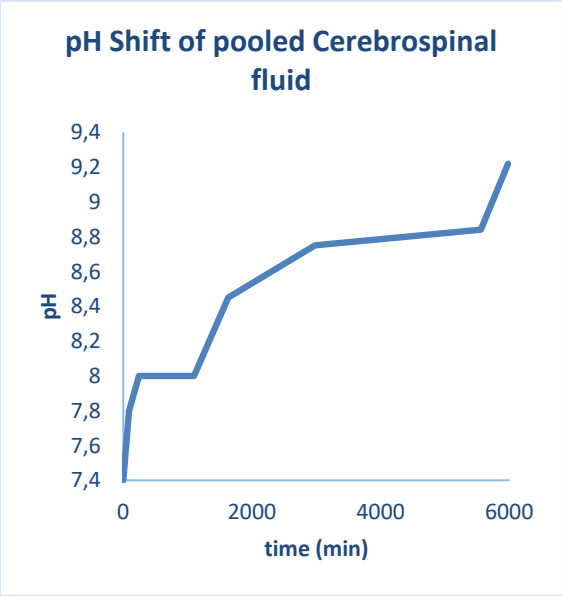

time (min)	pH
0	7,4
90	7,8
246	8
1100	8
1630	8,45
2980	8,75
5560	8,84
5980	9,22

Fig. 28: Pooled Cerebrospinal fluid pH shifts (no buffer added).

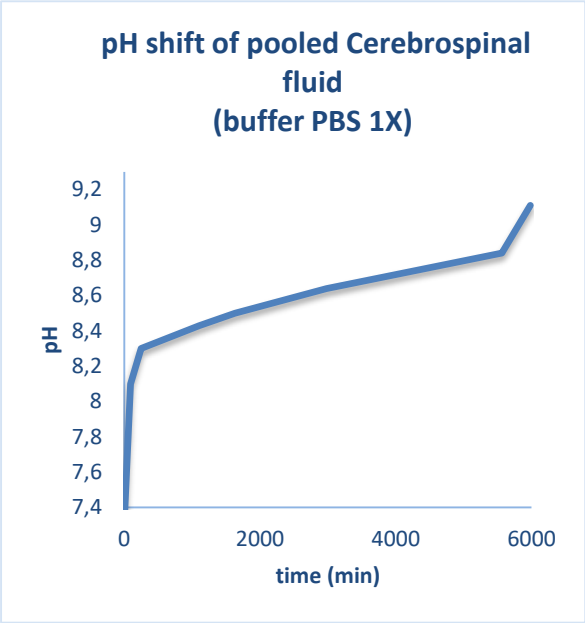

time (min)	pH
0	7,3
90	8,1
246	8,3
1100	8,43
1630	8,5
2980	8,64
5560	8,84
5980	9,11

Fig. 29: Pooled Cerebrospinal fluid pH shifts (PBS buffer added).

These results are in accordance with data coming from the literature (ex vivo pH changes resulting from loss of CO_2).[50],[51]

2.6 References

1. Stanbury, P. F., Whitaker, A. & Hall, S. J. Chapter 12 - The production of heterologous proteins. Principles of Fermentation Technology (Third Edition)

2. Bimboim, H. C. & Doly, J. A rapid alkaline extraction procedure for screening recombinant plasmid DNA. Nucleic Acids Res **7**, 1513–1523 (1979).

3. Mülhardt, C. & Beese, E. W. 2 - Fundamental Methods. in Molecular Biology and Genomics (eds. Mülhardt, C. & Beese, E. W.) 11–36 (Academic Press, 2007).

4.http://www.merckmillipore.com/IT/it/product/BL21DE3pLysS-Competent-Cells-Novagen,EMD_BIO-69451

5. Hasegawa, H., Suzuki, E. & Maeda, S. Horizontal Plasmid Transfer by Transformation in Escherichia coli: Environmental Factors and Possible Mechanisms. Front Microbiol **9**, (2018).

6. Mitchell, S. F. & Lorsch, J. R. Chapter Eight - Protein Affinity Purification using Intein/Chitin Binding Protein Tags. in Methods in Enzymology (ed. Lorsch, J. R.) **559**, 111–125 (Academic Press, 2015).

7. Marley, J., Lu, M. & Bracken, C. A method for efficient isotopic labeling of recombinant proteins. *J Biomol NMR* **20**, 71–75 (2001).

8. Sambrook, Joseph. Molecular Cloning : a Laboratory Manual. Cold Spring Harbor, N.Y. (Cold Spring Harbor Laboratory Press, 2001).

9. Elbing, K. & Brent, R. Media Preparation and Bacteriological Tools. *Current Protocols in Molecular Biology* **59**, 1.1.1-1.1.7 (2002).

10. Singh, A., Upadhyay, V., Upadhyay, A. K., Singh, S. M. & Panda, A. K. Protein recovery from inclusion bodies of Escherichia coli using mild solubilization process. *Microbial Cell Factories* **14**, 41 (2015).

11.García-Fruitós, E. *et al.* Bacterial inclusion bodies: making gold from waste. *Trends Biotechnol.* **30**, 65–70 (2012).

12. Slouka, C., Kopp, J., Spadiut, O. & Herwig, C. Perspectives of inclusion bodies for bio-based products:
curse or blessing? *Appl Microbiol Biotechnol* **103**, 1143–1153 (2019).

13. Berlec, A. & Štrukelj, B. Current state and recent advances in biopharmaceutical production in Escherichia coli, yeasts and mammalian cells. *J Ind Microbiol Biotechnol* **40**, 257–274 (2013).

14. Govers, S. K., Dutré, P. & Aertsen, A. In Vivo Disassembly and Reassembly of Protein Aggregates in Escherichia coli. *Journal of Bacteriology* **196**, 2325–2332 (2014).

15. Rudolph, R. & Lilie, H. In vitro folding of inclusion body proteins. *FASEB J.* **10**, 49–56 (1996).

16. Castellanos-Mendoza, A. *et al.* Influence of pH control in the formation of inclusion bodies during production of recombinant sphingomyelinase-D in Escherichia coli. *Microb. Cell Fact.* **13**, 137 (2014).

17.Walsh, D. M. *et al.* A facile method for expression and purification of the Alzheimer's disease-associated amyloid β-peptide. *The Febs Journal* **276**, 1266–1281 (2009).

18. Stellwagen, E. Chapter 23 Gel-filtration1. in *Methods in Enzymology* (eds. Burgess, R. R. & Deutscher, M. P.) **463**, 373–385 (Academic Press, 2009).

19. Hagel, L. & Haneskog, L. Size-exclusion Chromatography. in *eLS* (American Cancer Society, 2010).

20. Fekete, S., Beck, A., Veuthey, J.-L. & Guillarme, D. Theory and practice of size-exclusion chromatography for the analysis of protein aggregates. *J Pharm Biomed Anal* **101**, 161–173 (2014).

21. Hellstrand, E., Boland, B., Walsh, D. M. & Linse, S. Amyloid β-Protein Aggregation Produces Highly Reproducible Kinetic Data and Occurs by a Two-Phase Process. *ACS Chem. Neurosci.* **1**, 13–18 (2010).

22. Johnson, R. D., Schauerte, J. A., Wisser, K. C., Gafni, A. & Steel, D. G. Direct observation of single amyloid-β(1-40) oligomers on live cells: binding and growth at physiological concentrations. *PLoS ONE* **6**, e23970 (2011).

23. Schmid, F.-X. Biological Macromolecules: UV-VISible Spectrophotometry. in *eLS* (American Cancer Society, 2001)

24. Schägger, H. Tricine–SDS-PAGE. *Nature Protocols* **1**, 16–22 (2006).

25. Matejtschuk, P. 24. Lyophilization of Proteins. in *Cryopreservation and Freeze-Drying Protocols* (eds. Day, J. G. & Stacey, G. N.) 59–72 (Humana Press, 2007).

26. Salvi, G., De Los Rios, P. & Vendruscolo, M. Effective interactions between chaotropic agents and proteins. *Proteins* **61**, 492–499 (2005).

27. Povarova, O. I., Kuznetsova, I. M. & Turoverov, K. K. Differences in the Pathways of Proteins Unfolding Induced by Urea and Guanidine Hydrochloride: Molten Globule State and Aggregates. *PLOS ONE* **5**, e15035 (2010).

28. Rashid, F., Sharma, S. & Bano, B. Comparison of guanidine hydrochloride (GdnHCl) and Urea denaturation on inactivation and unfolding of human placental cystatin (HPC). *Protein J.* **24**, 283–292 (2005).

29. Monera, O. D., Kay, C. M. & Hodges, R. S. Protein denaturation with guanidine hydrochloride or Urea provides a different estimate of stability depending on the contributions of electrostatic interactions. *Protein Sci.* **3**, 1984–1991 (1994).

30. Lee, J., Culyba, E. K., Powers, E. T. & Kelly, J. W. Amyloid-β forms fibrils by nucleated conformational conversion of oligomers. *Nat. Chem. Biol.* **7**, 602–609 (2011).

31. Ryan, T. M. *et al.* Ammonium hydroxide treatment of Aβ produces an aggregate free solution suitable for biophysical and cell culture characterization. *PeerJ* **1**, e73 (2013).

32. Bertini, I. *et al.* Formation kinetics and structural features of Beta-amyloid aggregates by sedimented solute NMR. *Chembiochem* **14**, 1891–1897 (2013).

33. Saido, T. & Leissring, M. A. Proteolytic degradation of amyloid β-protein. *Cold Spring Harb Perspect Med* **2**, a006379 (2012).

34. Leissring, M. A. Aβ degradation—the inside story. *Front Aging Neurosci* **6**, (2014).

35. Lichstein, H. C. & Soule, M. H. Studies of the Effect of Sodium Azide on Microbic Growth and Respiration. *J. Bacteriol.* **47,** 221–230 (1944).

36. NMR Sample Preparation. in *Structural Biology: Practical NMR Applications* (ed. Teng, Q.) 89–100 (Springer US, 2005).

37. Diermayr, P., Kroll, S. & Klostermeyer, H. Influence of EDTA and metal ions on a metalloproteinase from pseudomonas fluorescens biotype I. *Biol. Chem. Hoppe-Seyler* **368**, 57–61 (1987).

38. Hazra, S. *et al.* Modulation of matrix metalloproteinase activity by EDTA prevents posterior capsular opacification. *Mol Vis* **18**, 1701–1711 (2012).

39. Bellomo, G. *et al.* Aggregation kinetics of the Aβ1-40 peptide monitored by NMR. *Chem. Commun. (Camb.)* **54**, 7601–7604 (2018).

40. Shevchik, V. E., Condemine, G. & Robert-Baudouy, J. Characterization of DsbC, a periplasmic protein of Erwinia chrysanthemi and Escherichia coli with disulfide isomerase activity. *EMBO J* **13**, 2007–2012 (1994).

41. Huang, C., Ren, G., Zhou, H. & Wang, C. A new method for purification of recombinant human alpha-synuclein in Escherichia coli. *Protein Expr. Purif.* **42**, 173–177 (2005).

42. Ren, G., Wang, X., Hao, S., Hu, H. & Wang, C. Translocation of α-synuclein Expressed in Escherichia coli. *J Bacteriol* **189**, 2777–2786 (2007).

43. McNulty, B. C., Young, G. B. & Pielak, G. J. Macromolecular crowding in the Escherichia coli periplasm maintains alpha-synuclein disorder. *J. Mol. Biol.* **355**, 893–897 (2006).

44. Konno, M. *et al.* Suppression of dynamin GTPase decreases α-synuclein uptake by neuronal and oligodendroglial cells: a potent therapeutic target for synucleinopathy. *Mol Neurodegener* **7**, 38 (2012).

45. Giasson, B. I., Uryu, K., Trojanowski, J. Q. & Lee, V. M.-Y. Mutant and Wild Type Human α-synucleins Assemble into Elongated Filaments with Distinct Morphologies in Vitro. *J. Biol. Chem.* **274**, 7619–7622 (1999).

46. Hoyer, W. *et al.* Dependence of alpha-synuclein aggregate morphology on solution conditions. *J. Mol. Biol.* **322**, 383–393 (2002).

47. Ren, G., Wang, X., Hao, S., Hu, H. & Wang, C. Translocation of α-synuclein Expressed in Escherichia coli. *J Bacteriol* **189**, 2777–2786 (2007).

48. Baba, M. *et al.* Aggregation of alpha-synuclein in Lewy bodies of sporadic Parkinson's disease and dementia with Lewy bodies. *Am J Pathol* **152**, 879–884 (1998).

49. Schmid, F.-X. Biological Macromolecules: UV-VISible Spectrophotometry. in *eLS* (American Cancer Society, 2001).

50. Cunniffe, J. G., Whitby-Strevens, S. & Wilcox, M. H. Effect of pH changes in cerebrospinal fluid specimens on bacterial survival and antigen test results. *J. Clin. Pathol.* **49**, 249–253 (1996).

51. Fura, A., Harper, T. W., Zhang, H., Fung, L. & Shyu, W. C. Shift in pH of biological fluids during storage and processing: effect on bioanalysis. *Journal of Pharmaceutical and Biomedical Analysis* **32**, 513–522 (2003).

Chapter 3

Results

3.1 Aggregation kinetics of Aβ1-40 monitored by NMR

In this work, the aggregation of Aβ1–40 was monitored by solution NMR. My specific contribution to this project was the Aβ1–40 expression and purification and the preparation of samples for the kinetic experiments.

In order to obtain quantitative information about the aggregation kinetics of Aβ1–40, series of 1D ^{1}H NMR spectra were acquired under quiescent conditions. The NMR investigation was performed using a 700 MHz (16.4 T) spectrometer on recombinant monomeric samples of Aβ1–40 at pH 8.5, with concentrations varying between 30 and 100 μM, at the temperature of 310 K. The NMR signals used for kinetic analysis were those originating from methyl protons; 1D spectra were preferred to 2D spectra because they provide a higher signal-to-noise ratio for the same amount of time.

To deeply investigate the complementarity between solution NMR and fluorescence, the experiments were repeated by monitoring a 50 μM Aβ1–40 sample simultaneously through NMR and ThT fluorescence in a Cary Eclipse spectrophotometer (Agilent).

The decay of the monomer methyl signals from 1D ^{1}H NMR experiments showed a behaviour complementary with respect to the growing of ThT fluorescence intensity.

In our conversion kinetics model, secondary nucleation was not included and a direct conformational conversion from oligomers to fibrils was hypothesized in our conditions of concentration and pH.

In the Supporting Information were included all the experimental details that can affect the aggregation kinetics (i.e. monomer degradation, methionine-35 oxidation, presence of preformed aggregates and electrostatic surfaces), which highlight how complex is the problem of reproducibility on Aβ samples.

Showcasing research from the Magnetic Resonance Center (CERM) and Chemistry Department of the University of Florence, Sesto Fiorentino, Italy.

Aggregation kinetics of the Aβ1–40 peptide monitored by NMR

The aggregation of Aβ1–40 was studied by solution NMR. The data support a kinetic model where monomers initially aggregate with the reversible formation of oligomers, which then irreversibly convert into fibrils. This, not only sheds new light on the aggregation process, but helps in designing new potential drugs.

As featured in:

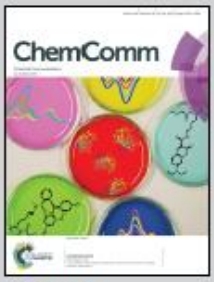

See Moreno Lelli, Claudio Luchinat *et al.*, *Chem. Commun.*, 2018, **54**, 7601.

ROYAL SOCIETY OF CHEMISTRY

rsc.li/chemcomm

Registered charity number: 207890

ChemComm

COMMUNICATION

View Article Online
View Journal | View Issue

Cite this: *Chem. Commun.*, 2018, 54, 7601

Received 20th March 2018,
Accepted 3rd May 2018

DOI: 10.1039/c8cc01710g

rsc.li/chemcomm

Aggregation kinetics of the Aβ1–40 peptide monitored by NMR†

Giovanni Bellomo,[a] Sara Bologna,[a] Leonardo Gonnelli,[a] Enrico Ravera,[ab] Marco Fragai,[ab] Moreno Lelli *[ab] and Claudio Luchinat *[abc]

The aggregation of Aβ1–40 was monitored by solution NMR, which showed a trend complementary to the one observed by ThT-fluorescence. The NMR data support a kinetic model where Aβ1–40 initially aggregates with the reversible formation of oligomeric species, which then irreversibly convert into fibrils.

Aβ1–40, Aβ1–42 and τ-protein are involved in the onset and progression of Alzheimer's disease (AD).[1] In particular, the Aβ peptides are the major constituents of the amyloid plaques found in biopsies of AD patients. Although Aβ1–40 is the most common isoform of Aβ, Aβ1–42 seems to be more toxic and more prone to aggregation.[2] Moreover, the structure of the final fibrillary aggregates of Aβ1–40[3,4] is found to be different from the one of Aβ1–42[5–7] and not univocal.[8] There is also evidence that the structure of the transient oligomeric species might be different for the two isoforms, with Aβ1–42 forming more fibril-like oligomers, rich in β-sheets, and Aβ1–40 forming more globular and amorphous aggregates.[9–11] The soluble oligomers and especially the low molecular weight (LMW) oligomers were shown to be the most toxic species among all the Aβ aggregates.[12,13] These findings suggest that the aggregation kinetics may be different for the two isoforms of Aβ as proposed in some of the kinetic models developed over the years.[14–18] The development of kinetic models and the understanding of the aggregation mechanisms of amyloidogenic proteins would be dramatically important in designing new therapies and drugs. In 2011, Knowles and co-workers[17] developed a two-species (monomers and fibrils) model describing the aggregation of Aβ1–42. They also introduced the idea of surface-catalysed secondary nucleation[19] and tested the model against ThT fluorescence data at different monomer concentrations.[20] The model was then adapted[18] to Aβ1–40, observing strong differences in nucleation behaviour and suggesting that secondary nucleation saturates above 6 μM of Aβ1–40 monomer concentration. However, Kelly and co-workers[21] brought up evidence of conversion of soluble globular oligomers of Aβ1–40 into fibrils; this evidence was also supported by other works.[22–24] These findings suggest that considering only two species for the kinetic modelling of amyloid aggregation, at least for Aβ1–40, could be reductive. For this reason, we investigated the aggregation kinetics of Aβ1–40 by solution NMR, focusing our attention on the early stage of the aggregation. The peculiarity of NMR is that it monitors directly the free monomer concentration, which is affected from the beginning of the aggregation process, thus providing complementary information with respect to ThT-fluorescence. With modern high-field instruments the NMR experiments can be performed under near physiological conditions, at a micromolar concentration range and without the need to add fluorescent or chromophoric probes that may alter the aggregation.[25] Solution NMR was already applied to study the aggregation of the Aβ peptides: Fawzi *et al.*[26,27] obtained information about oligomeric species of Aβ1–40/42 using the dark-state exchange saturation transfer (DEST), probing the exchange processes between monomers and protofibril-bound states. Pauwels *et al.*[28] and Bax and coworkers[29] monitored the Aβ1–40/42 aggregation with NMR and ThT-fluorescence but they did not propose kinetic models for the amyloidogenic process. Ramamoorthy and coworkers obtained a high resolution structure of a partially folded Aβ1–40 monomer with solution NMR[30] and observed directly the formation of at least five different oligomeric species by using ^{19}F-NMR on a ^{19}F labelled Aβ1–40 peptide.[31] They also further characterized some oligomeric aggregates with solid-state NMR in a subsequent work.[32] Oligomerization kinetics was monitored also by Bertini and co-workers with sedimentation NMR,[9,33] trapping oligomeric species of about 70–80 kDa by MAS induced sedimentation. In order to obtain information about the aggregation kinetics of Aβ1–40 we acquired a series

[a] *Magnetic Resonance Center (CERM), University of Florence, Via L. Sacconi 6, 50019 Sesto Fiorentino, Italy. E-mail: lelli@cerm.unifi.it, luchinat@cerm.unifi.it*
[b] *Department of Chemistry "Ugo Schiff", University of Florence, Via della Lastruccia 3, 50019 Sesto Fiorentino, Italy*
[c] *Giotto Biotech S.R.L., Via Madonna del Piano 6, 50019 Sesto Fiorentino, Florence, Italy*

† Electronic supplementary information (ESI) available: Supporting figures, mathematical description of kinetic models, and experimental details. See DOI: 10.1039/c8cc01710g

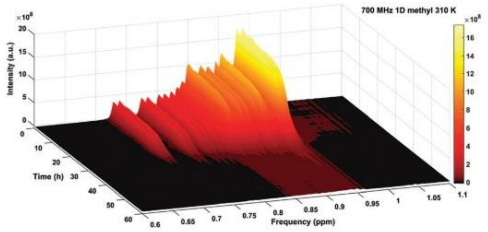

Fig. 1 Series of 1D ^{1}H NMR spectra of the methyl region of a 50 μM sample of Aβ1–40 plotted with MATLAB. Spectra were acquired using a 700 MHz (16.4 T) spectrometer, using an ammonium acetate buffer at pH 8.5 (see details in the ESI†). Spectra were binned with AMIX software (bin width = 0.005 ppm) prior to image formation.

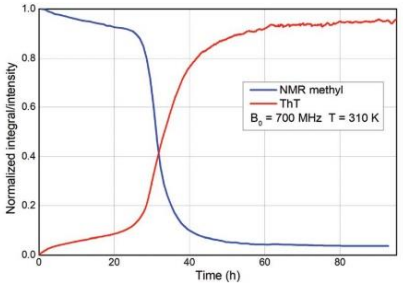

Fig. 2 Aggregation kinetics of 50 μM of Aβ1–40 at 310 K and pH 8.5. The decrease in the methyl proton integral showed a behaviour complementary to the ThT fluorescence intensity. NMR integrals were normalized by dividing them by the highest value. ThT fluorescence data were normalized setting the point at 92.8 h to 1 – (the NMR normalised integral) in that point.

of 1D ^{1}H NMR spectra under quiescent conditions. The NMR investigation was performed on recombinant Aβ1–40 samples at pH 8.5 and with concentrations between 30 and 100 μM, for details see the ESI.† This higher than physiological pH was chosen because it corresponds to the pH where Aβ1–40 easily forms fibrils with high reproducibility.[3] The temperature was set to the physiological value of 310 K in order to avoid a too long lag-time, considering that the elongation rate of amyloids strongly increases with temperature,[34] while lower temperatures can promote a partially folded state of the monomer.[30] In Fig. 1, we report the trend of the methyl region of the 1D ^{1}H spectrum as a function of time up to the almost complete disappearance of the monomer resonances. The intensities of the methyl peaks decreased with an almost sigmoidal behaviour with a slow decrease in monomer concentration of about 10% during the first 20 hours; then a sharp concentration decrease is observed, with the consumption of most of the monomer, followed by a final plateau where the monomer concentration remained almost stationary at less than 2% of the initial amount. Similar trends were observed also for the aromatic resonances (see the ESI,† Fig. S3), but we analysed the methyl region because of the higher signal to noise ratio.

To get insight into this process, we repeated the aggregation experiment by monitoring another 50 μM Aβ1–40 sample simultaneously through NMR and ThT fluorescence. Fig. 2 reports the NMR integral of the methyl region as a function of time compared with the increase in the fluorescence signal. The presence of ThT can affect the kinetics of the fibril formation, especially with ThT concentration comparable to the one of Aβ1–40.[25] Thus we kept the ThT concentration at 5 μM (1/10 of the Aβ1–40 concentration) and we added it in both the NMR tube and the quartz cuvette. Notably, the drop of the monomer concentration happens in concomitance with the growth of the fluorescence (due to fibril formation), with an almost complementary trend. The NMR experiments were repeated at different initial monomer concentrations (30, 50 and 100 μM) in order to understand the impact of the concentration on the aggregation kinetics. The decrease in the integrals of the methyl spectrum as a function of time is reported in Fig. 3 and is almost entirely associated to the monomer consumption (see the ESI† and Fig. S1). We fitted these experimental data using three different kinetic models. In Fig. 3A, the NMR integrals are fitted with the model developed by Knowles and coworkers.[18] This model was created also considering the previous works of Oosawa,[35] Ferrone,[16] Murphy[17] and Pöschel.[36] In this two-species model, the monomeric Aβ is expected to nucleate directly to fibrils, which in turn can elongate, dissociate or fragment into shorter fibrils.

Secondary nucleation catalysed by the fibril surface is also included, as it was demonstrated to have a key role for Aβ1–42. This model was adapted[19] to fit the aggregation trend of Aβ1–40 at pH 7.4, introducing a saturation limit for the secondary nucleation for Aβ1–40 monomer concentration: the results of the fitting to this model are shown in Fig. 3B. In Fig. 3A and B the simulated curves reproduce the sigmoidal-like decrease at the main inflection point, but the agreement is rather poor for the initial part of the trend. We thus decided to modify the model of Knowles considering also the formation of oligomeric species. In our model (depicted in Fig. S4 and eqn (S1), (S2) in the ESI†), monomers can nucleate into oligomers, the nucleation kinetics considered is fundamentally equal to the one used by Knowles,[18] Ferrone,[16] Pöschel[36] and to the one originally developed by Oosawa.[35] In our case, however, monomers do not nucleate directly into fibrils but into transient oligomeric aggregates. Oligomers can grow and decrease by addition or dissociation of monomers, as well as fibrils, but with different kinetic rates with respect to the latter. For the depolymerization kinetics we used slightly different terms in the kinetic equations resulting in a total probability of monomer detachment proportional to the oligomer size (see the ESI†). The crucial part of the model is the introduction of a conversion kinetics step from oligomers to fibrils: when the oligomers reach a given critical size n_c (*e.g.* 20 monomers in the present case) they are allowed to irreversibly convert into fibrils. Fibrils can then grow and decrease through polymerization and depolymerization by the addition or release of monomers with a kinetics identical to the one of the previously cited models.[15,16,20,35,36] Likewise, fibrils can also fragment producing smaller fibrils (not oligomers or monomers)

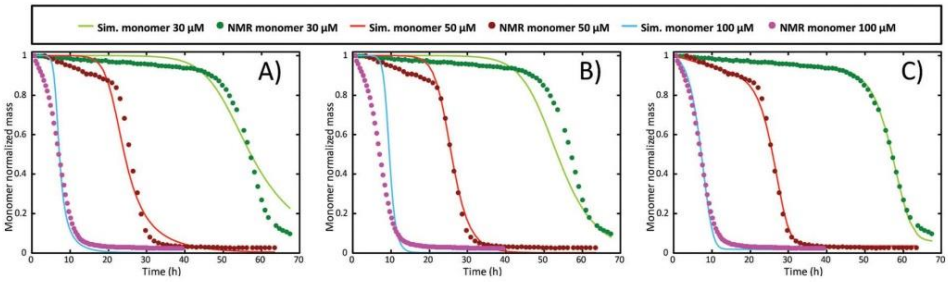

Fig. 3 Simulated monomer populations were fitted in parallel to the experimental NMR data: integrals of the methyl region of 1D solution NMR spectra at 30, 50 and 100 μM Aβ1–40 initial monomer concentration (pH 8.5, T = 310 K). Three different kinetic models were tested on these data: in (A) the two-species model for Aβ1–42, in (B) the two-species model for Aβ1–40, while in (C) the "conversion" model developed in this work.

that can then act as new seeds for polymerization. In this model fibrils are not allowed to fragment in species smaller than the critical size n_c. In this way, fragmentation of fibrils only produces fibrils above the critical size and this is why we named this process "fibril closed fragmentation". With this kinetic model we fitted the experimental data in Fig. 3C. The addition of the irreversible conversion from oligomers into fibrils allowed for a significantly better agreement between the simulated and the experimental data with respect to the previous models, especially for the initial part of the aggregation. Notably, this model fits well the evolution during the lag-time when oligomers are supposed to be formed; by NMR we can monitor this evolution through the monomer consumption while the fluorescence remains quite low. The fitted kinetic constants of the three tested models are shown in Table S1 in the ESI.† In our "conversion model" the kinetic constant for the fibril growth (k_+) is an order of magnitude higher than the one for the monomer addition to oligomeric species (k_{+ol}). This difference explains why, once a sufficient amount of large oligomers is converted to fibrils, monomers start to be rapidly consumed while the mass of fibrils rapidly increases producing a sigmoidal-like behaviour for the monomer consumption kinetics. In the third part of the trend, in the tail of the sigmoidal decrease, where most of the peptides are aggregated into fibrils, the process of monomer dissociation remains the only relevant, and is responsible for the residual amount of monomer still present in solution. In the previously published models for Aβ1–40[19] and Aβ1–42[18] there is no distinction between "oligomers" and "fibrils" and a single polymerization constant is fitted for all the aggregation steps. With these models the rapid monomer consumption of the sigmoidal trend is the result of a strong secondary nucleation that becomes explosively strong as soon as there is a small amount of long-fibrils formed. On the basis of the fitted kinetic constants we back-calculated the relative fibril size distribution for the three models (Fig. S7–S9, ESI†). As shown in Fig. S7 (ESI†) (50 μM sample) for the Aβ1–42 and Aβ1–40 models, it can be observed that, at the end of the aggregation process ($t \sim 60$ h), the majority of the fibrils should have a size smaller than 20 monomers, and for the Aβ1–42 model even smaller than 10 monomers (40 kDa). In the trials we made, only the model based on the oligomer-to-fibril conversion predicts the formation of fibrils larger than 433 kDa (>100 mers). Indeed, the strong secondary nucleation process of the first two models results in a rapid formation of dimers during the sigmoidal step that are not able to elongate much because of the depleted monomer concentration in solution. In our conversion model, we have not included secondary nucleation and the "limited" number of converted fibrils favours their elongation towards high molecular weights. We do not exclude that the secondary nucleation process exists for Aβ1–40, since it has been well demonstrated for Aβ1–42,[21] but for Aβ1–40 in our conditions of concentration and pH (8.5), the secondary nucleation seems not to be determinant. Indeed, if secondary nucleation is included in the conversion model (Fig. S5 and Table S2, ESI†), its impact on the fit quality is minimal and the relative kinetic constant remains quite small. Solution NMR is a profitable technique to follow these aggregation processes, because it gives an overview of the sample status. In several cases, the presence of impurities or the concomitant occurrence of degradation processes (for example due to undetectable amounts of proteases[37]) can be determined by 1D ^{1}H NMR spectra. In the ESI† we report the case of degradation (Fig S10), which usually manifests itself with the formation of sharp resonances near the ones of the monomer. Another aspect which needs attention is the presence of preformed aggregates and/or electrostatic surfaces that can drastically promote fibrillation *in vitro*.[38] As an example, in Fig. 4 we show a sample where presumably the presence of a solid impurity promoted the formation of a macroscopic fibrillary aggregate into the NMR tube. The presence of this impurity had a dramatic effect on the aggregation kinetics. Some fibrillary nuclei were formed on its surface at the bottom of the NMR tube. From these quickly formed nuclei the aggregation proceeded mainly through polymerization. This hypothesis is also in line with the observation of an exponential decay of the monomer signal (Fig. 4B). Indeed, with reference to eqn (S6) (ESI†), a pure polymerization kinetics from a preformed concentration of fibrils implies an exponential decay of the monomer.

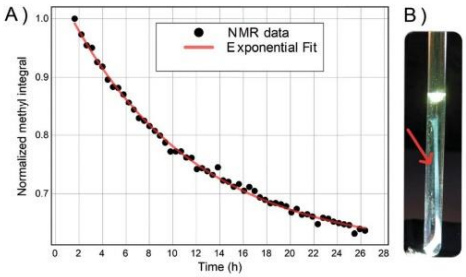

Fig. 4 (A) The kinetic profile of the NMR signal (B_0 = 700 MHz T = 310 K) was fitted with an exponential decay that is typical of a polymerization kinetics. (B) A curious image of an agglomerate of fibrils presumably grown over the surface of an impurity present in the bottom of the NMR tube, the pale blue color resulted from the addition of 5 μM of ThT.

In conclusion, solution NMR is a valuable technique for the investigation of the aggregation kinetics of the Aβ1–40 peptide, giving a complementary point of view compared to ThT fluorescence. We developed a computational model that well fits the trend of the monomer consumption and supports the existence of at least two categories of aggregates: oligomers and fibrils, with different rates of growth. Despite the existence of oligomeric and fibrillar species in Aβ1–40 aggregation is a well-established concept, the quantification of the aggregation rates involving these species and the development of a reliable computational model is an important step forward for the comprehension of Aβ aggregation processes. Furthermore, it makes it possible to quantify the actual impact of drug candidates in contrasting aggregation and protein misfolding.

This work was supported by ERA-NET NEURON ABETA ID, MIUR PRIN 2012SK7ASN, Fondazione Cassa di Risparmio di Firenze, the University of Florence CERM-TT and Instruct-ERIC, an ESFRI Landmark, supported by national member subscriptions. Specifically, we thank the Instruct-ERIC Core Centre CERM, Italy.

Conflicts of interest

There are no conflicts to declare.

Notes and references

1 J. Wang, B. J. Gu, C. L. Masters and Y.-J. Wang, *Nat. Rev. Neurol.*, 2017, **13**, 612–623.
2 K. Parameshwaran, C. Sims, P. Kanju, T. Vaithianathan, B. C. Shonesy, M. Dhanasekaran, B. A. Bahr and V. Suppiramaniam, *Synapse*, 2007, **61**, 367–374.
3 I. Bertini, L. Gonnelli, C. Luchinat, J. Mao and A. Nesi, *J. Am. Chem. Soc.*, 2011, **133**, 16013–16022.
4 J.-X. Lu, W. Qiang, W.-M. Yau, C. D. Schwieters, S. C. Meredith and R. Tycko, *Cell*, 2013, **154**, 1257–1268.
5 Y. Xiao, B. Ma, D. McElheny, S. Parthasarathy, F. Long, M. Hoshi, R. Nussinov and Y. Ishii, *Nat. Struct. Mol. Biol.*, 2015, **22**, 499–505.
6 M. A. Wälti, F. Ravotti, H. Arai, C. G. Glabe, J. S. Wall, A. Böckmann, P. Güntert, B. H. Meier and R. Riek, *Proc. Natl. Acad. Sci. U. S. A.*, 2016, **113**, E4976–E4984.
7 M. T. Colvin, R. Silvers, Q. Z. Ni, T. V. Can, I. Sergeyev, M. Rosay, K. J. Donovan, B. Michael, J. Wall, S. Linse and R. G. Griffin, *J. Am. Chem. Soc.*, 2016, **138**, 9663–9674.
8 R. Tycko, *Protein Sci.*, 2014, **23**, 1528–1539.
9 I. Bertini, G. Gallo, M. Korsak, C. Luchinat, J. Mao and E. Ravera, *ChemBioChem*, 2013, **14**, 1891–1897.
10 C. G. Glabe, *J. Biol. Chem.*, 2008, **283**, 29639–29643.
11 N. J. Economou, M. J. Giammona, T. D. Do, X. Zheng, D. B. Teplow, S. K. Buratto and M. T. Bowers, *J. Am. Chem. Soc.*, 2016, **138**, 1772–1775.
12 D. M. Walsh, I. Klyubin, J. V. Fadeeva, W. K. Cullen, R. Anwyl, M. S. Wolfe, M. J. Rowan and D. J. Selkoe, *Nature*, 2002, **416**, 535–539.
13 S. Lesné, M. T. Koh, L. Kotilinek, R. Kayed, C. G. Glabe, A. Yang, M. Gallagher and K. H. Ashe, *Nature*, 2006, **440**, 352.
14 J. P. Bernacki and R. M. Murphy, *Biophys. J.*, 2009, **96**, 2871–2887.
15 F. Ferrone, *Methods Enzymol.*, 1999, **309**, 256–274.
16 M. M. Pallitto and R. M. Murphy, *Biophys. J.*, 2001, **81**, 1805–1822.
17 S. I. A. Cohen, M. Vendruscolo, M. E. Welland, C. M. Dobson, E. M. Terentjev and T. P. J. Knowles, *J. Chem. Phys.*, 2011, **135**, 065105.
18 G. Meisl, X. Yang, E. Hellstrand, B. Frohm, J. B. Kirkegaard, S. I. A. Cohen, C. M. Dobson, S. Linse and T. P. J. Knowles, *Proc. Natl. Acad. Sci. U. S. A.*, 2014, **111**, 9384–9389.
19 S. Linse, *Biophys. Rev.*, 2017, **9**, 329–338.
20 S. I. A. Cohen, S. Linse, L. M. Luheshi, E. Hellstrand, D. A. White, L. Rajah, D. E. Otzen, M. Vendruscolo, C. M. Dobson and T. P. J. Knowles, *Proc. Natl. Acad. Sci. U. S. A.*, 2013, **110**, 9758–9763.
21 J. Lee, E. K. Culyba, E. T. Powers and J. W. Kelly, *Nat. Chem. Biol.*, 2011, **7**, 602–609.
22 Z. Fu, D. Aucoin, J. Davis, W. E. Van Nostrand and S. O. Smith, *Biochemistry*, 2015, **54**, 4197–4207.
23 M. Cheon, C. K. Hall and I. Chang, *PLoS Comput. Biol.*, 2015, **11**, e1004258.
24 N. Benseny-Cases, M. Cócera and J. Cladera, *Biochem. Biophys. Res. Commun.*, 2007, **361**, 916–921.
25 M. D'Amico, M. G. Di Carlo, M. Groenning, V. Militello, V. Vetri and M. Leone, *J. Phys. Chem. Lett.*, 2012, **3**, 1596–1601.
26 N. L. Fawzi, J. Ying, R. Ghirlando, D. A. Torchia and G. M. Clore, *Nature*, 2011, **480**, 268–272.
27 N. L. Fawzi, J. Ying, D. A. Torchia and G. M. Clore, *Nat. Protoc.*, 2012, **7**, 1523–1533.
28 K. Pauwels, T. L. Williams, K. L. Morris, W. Jonckheere, A. Vandersteen, G. Kelly, J. Schymkowitz, F. Rousseau, A. Pastore, L. C. Serpell and K. Broersen, *J. Biol. Chem.*, 2012, **287**, 5650–5660.
29 J. Roche, Y. Shen, J. H. Lee, J. Ying and A. Bax, *Biochemistry*, 2016, **55**, 762–775.
30 S. Vivekanandan, J. R. Brender, S. Y. Lee and A. Ramamoorthy, *Biochem. Biophys. Res. Commun.*, 2011, **411**, 312–316.
31 Y. Suzuki, J. R. Brender, M. T. Soper, J. Krishnamoorthy, Y. Zhou, B. T. Ruotolo, N. A. Kotov, A. Ramamoorthy and E. N. G. Marsh, *Biochemistry*, 2013, **52**, 1903–1912.
32 S. A. Kotler, J. R. Brender, S. Vivekanandan, Y. Suzuki, K. Yamamoto, M. Monette, J. Krishnamoorthy, P. Walsh, M. Cauble, M. M. B. Holl, E. N. G. Marsh and A. Ramamoorthy, *Sci. Rep.*, 2015, **5**, 11811.
33 I. Bertini, C. Luchinat, G. Parigi and E. Ravera, *Acc. Chem. Res.*, 2013, **46**, 2059–2069.
34 Y. Kusumoto, A. Lomakin, D. B. Teplow and G. B. Benedek, *Proc. Natl. Acad. Sci. U. S. A.*, 1998, **95**, 12277–12282.
35 F. Oosawa and M. Kasai, *J. Mol. Biol.*, 1962, **4**, 10–21.
36 T. Pöschel, N. V. Brilliantov and C. Frömmel, *Biophys. J.*, 2003, **85**, 3460–3474.
37 T. Saido and M. A. Leissring, *Cold Spring Harbor Perspect. Med.*, 2012, **2**, a006379.
38 B. Moores, E. Drolle, S. J. Attwood, J. Simons and Z. Leonenko, *PLoS One*, 2011, **6**, e25954.

Electronic Supplementary Material (ESI) for Chemical Communications.

Supporting Information

Aggregation kinetics of the Aβ1-40 peptide monitored by NMR

Giovanni Bellomo,[a] Sara Bologna,[a] Leonardo Gonnelli,[a] Enrico Ravera,[a,b] Marco Fragai, [a,b] Moreno Lelli,[a,b,*] and Claudio Luchinat [a,b,*]

[a] Magnetic Resonance Center (CERM), University of Florence, Via L. Sacconi 6, 50019 Sesto Fiorentino, Italy.
[b] Department of Chemistry "Ugo Schiff", University of Florence, Via della Lastruccia 3, 50019 Sesto Fiorentino, Italy.
[c] Giotto Biotech S.R.L., Via Madonna del Piano 6, 50019 Sesto Fiorentino, Florence, Italy
*To whom correspondence should be addressed

Contents

1. 1D ^{1}H NMR experiments to monitor kinetics

The NMR investigation was performed on Aβ1-40 samples at pH 8.5 and with concentrations between 30 and 100 μM. This higher than physiological pH was chosen because it corresponds to the pH where Aβ1-40 easily form fibrils with high reproducibility.[1] Most of the analyses were performed on 1D ^{1}H NMR spectra. 1D spectra were preferred compared to 2D because they provide a higher signal-to-noise ratio for the same amount of time. Figure S1 shows the methyl region of the 1D ^{1}H NMR spectrum of Aβ1-40 acquired at 50 μM, at 310 K and at different times (t). It can be seen that during aggregation the protein signals decay without the growth of any new visible peak or change in the pattern profile: in Figure S1B it is possible to appreciate that the spectrum after 33.2 h maintains the same profile of the monomeric spectrum acquired at 0.66 h with some small differences around 0.95 ppm (that accounts less than 2% of methyl protons starting integral), due to the rescaled signals of protease inhibitors added to prevent protein degradation (see details below, in the Experimental session). We decided to compare our NMR integrals with the simulated monomer concentration (estimated by kinetic models) because we had no hints (no new growing peaks in the 1D NMR spectra) about any contribution from other species in the integration regions we considered, up to 80 h of aggregation.

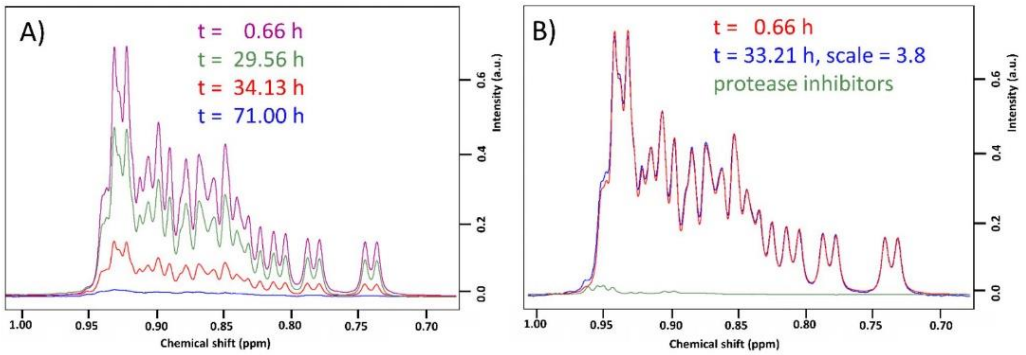

Figure S1: A) Decay of the monomer methyl signals from 1D ^{1}H NMR experiments acquired in a 700 MHz spectrometer. Line broadening was set to 1.0 Hz. The Aβ1-40 monomer starting concentration was 50 μM in ammonium acetate buffer, pH 8.5 and T = 310 K. B) Superposition of the methyl signal at 0.66h (red) with those at 33.21h rescaled (x3.8, blue). The methyl signals retain their shape during aggregation, indicating that species with a spectrum different from monomer are almost not visible by 1D ^{1}H NMR in this spectra region and in our experimental conditions. The only differences between the monomer and the rescaled spectrum, at t = 33 h, can be found at 0.95 ppm where small signals from protease inhibitors are present.

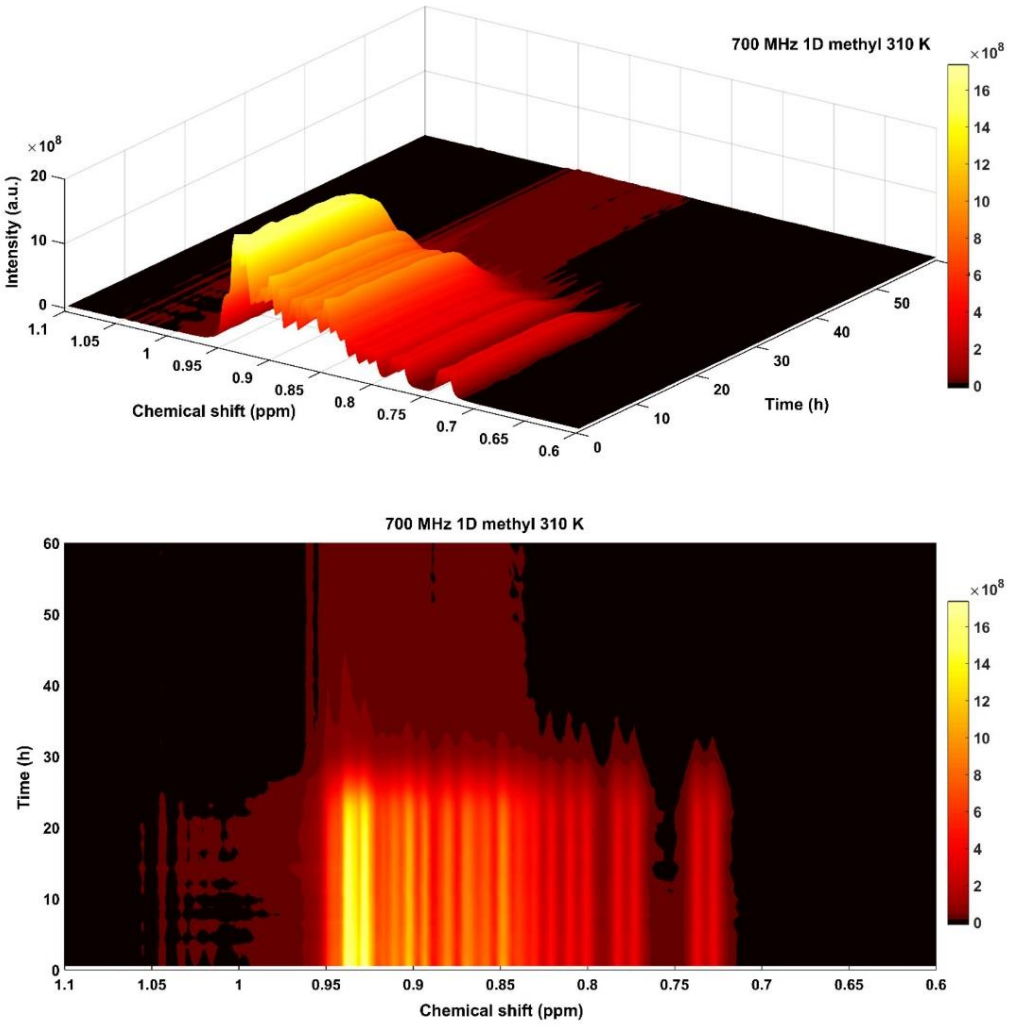

Figure S2: Series of 1D ^{1}H NMR spectra of the methyl region of a 50 µM sample of Aβ1-40 plotted in two different projections (graphical image produced with MATLAB R2017a). Spectra were acquired in a 700 MHz (16.4 T) spectrometer, using an ammonium acetate buffer with 0.2% of sodium azide, 1.0 mM EDTA and protease inhibitors at low concentrations (the ABSF was 10 µM, see Experimental for details). Spectra were binned (bin width = 0.005 ppm) with AMIX (Analysis of MIXtures software, Bruker Biospin) prior to image formation.

In addition to the methyl spectral region, also the aromatic resonances were analysed with very little interference from the background. On these signals, the 1D-NOESY spectra performed better than the 1D ^{1}H excitation sculpting experiments, because the water pre-saturation steps strongly attenuated the buffer resonances in exchange with water (i.e. ammonium and ammonia).

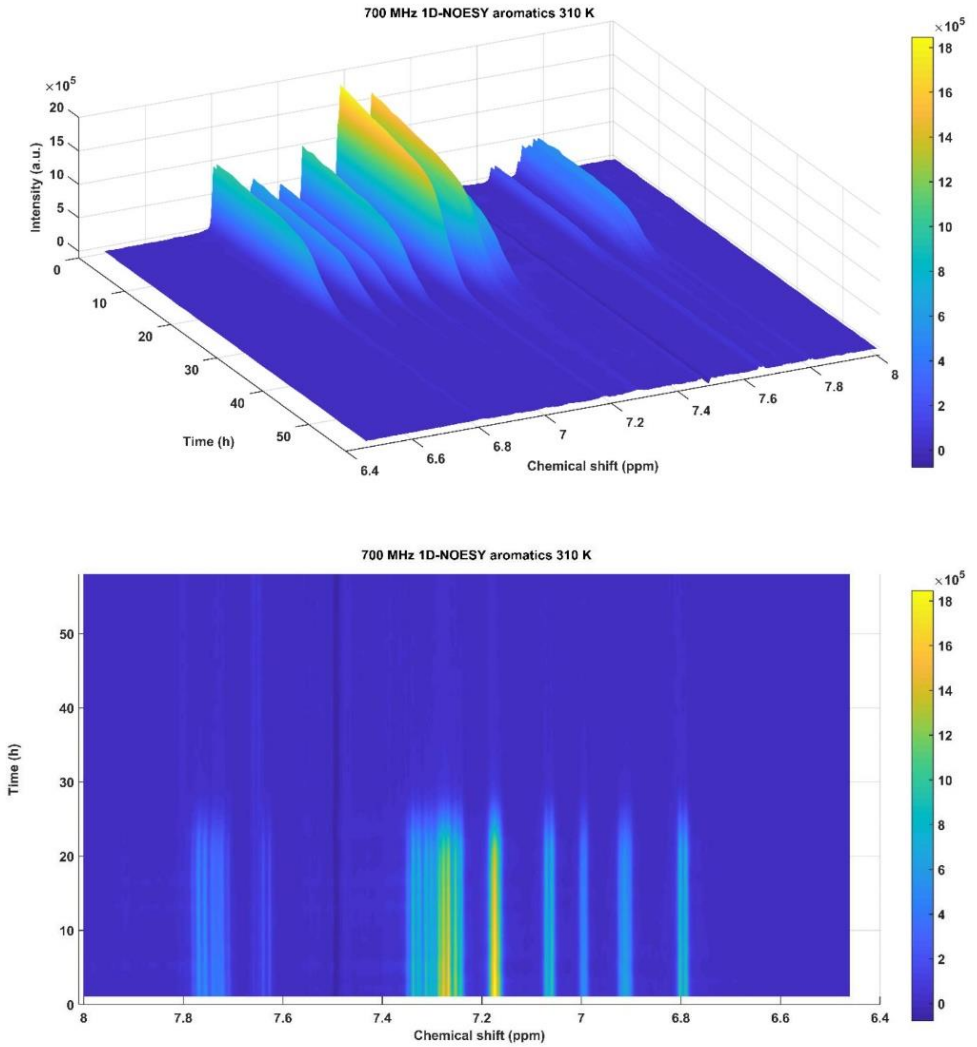

Figure S3: Series of 1D ^{1}H-NOESY spectra of the aromatic region of a 50 µM sample of Aβ1-40 plotted in two different projections, from one side (upper panel) and from the top(lower panel) (graphical image produced with MATLAB R2017a). Spectra were acquired in a 700 MHz (16.4 T) spectrometer, using an ammonium acetate buffer with 0.2% of sodium azide, 1.0 mM EDTA and protease inhibitors at low concentrations (the ABSF was 10 µM, see Experimental Session for details). Spectra were binned (bin width = 0.005 ppm) with AMIX (Analysis of MIXtures software, Bruker Biospin) prior to image formation.

2. Kinetic models

In the model we tested in this work (depicted graphically in Fig. S4 and mathematically in Eq. S1 and S2), monomers can nucleate into oligomers, the nucleation kinetics we considered is fundamentally equal to the one used by Knowles,[2] Ferrone,[3] Pöschel[4] and to the one originally developed by Oosawa.[5] In our case, however, monomers do not nucleate directly into fibrils but into a transient, on pathway oligomeric aggregates. Oligomers can grow and decrease by addition or dissociation of monomers, as well as fibrils, but with different

kinetic rates with respect to the latter. For the growth kinetics of oligomers we applied the same mathematical description of Knowles,[2] Ferrone,[3] Pöschel[4] and Oosawa,[5] while for the depolymerization kinetics we used slightly different terms in the kinetic equations: since oligomers are generally species less stable than fibrils, the overall dissociation rate of a single peptide is likely not the same for any oligomer and we scaled it for the larger monomer content in the aggregate, resulting in a total probability of detachment proportional to the oligomer size. The crucial part of the model is the introduction of a conversion kinetics step from oligomers to fibrils: when the oligomers reach a given critical size n_c (e.g. 20 monomers in the present case) they are allowed to irreversibly convert into fibrils. Fibrils can then grow and decrease through polymerization and depolymerization by addition or release of Aβ1-40 monomers. The mathematical description of the polymerization and depolymerization of fibrils is identical to the one of the cited models.[3–7] Fibrils can then also fragment producing smaller fibrils that can then act as new seeds for polymerization. In this model fibrils are not allowed to fragment in species smaller than the critical size n_c, in this way fragmentation of fibrils only produces fibrils above the critical size and this is why we dubbed this process "fibril closed fragmentation". With this constraint we wanted to force the fibrillary "nuclei" converted from oligomers to be stable and to be only subjected to depolymerization. The mathematical description of the model is reported in Eq. S1 and Eq. S2 in the master equation formalism. We report as fi and Oi the fibrils and oligomers populations made by i monomers, respectively. θ is the Heaviside theta function, δ is the Dirac delta function, n0 is the minimum nucleus size, nc is the critical size for oligomer conversion into fibrils, m is the Aβ1-40 monomer population. The values of the k constants reflect the importance of the corresponding process (the colour code in Eq. S1 and S2 matches the one in Fig. S4).

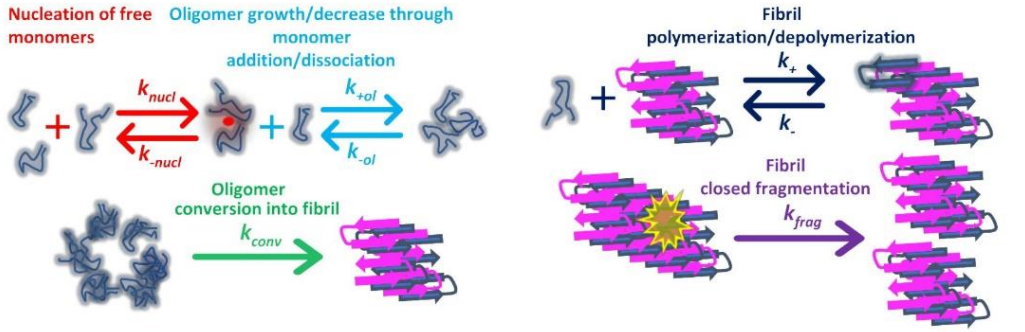

Figure S4: Schematic description of the developed kinetic model for the aggregation of Aβ1-40. The colors of the processes names correspond to the colors of the terms descriptive of the model in Eq. S1 and Eq. S2.

$$\frac{df_i}{dt} = +k_{conv}O_i\theta(i-n_c) - k_+f_im + k_+f_{i-1}m - k_-f_i + k_-f_{i+1} - k_{frag}(i-2n_c+1)f_i\theta(i-2n_c) + 2k_{frag}\sum_{j=i+n_c}^{\infty} f_j \quad \text{(S1)}$$

$$\frac{dO_i}{dt} = +k_{nucl}\delta(i-n_0)m^{n_0} - k_{-nucl}\delta(i-n_0)n_0O_{n_0} - k_{+ol}O_im + k_{+ol}O_{i-1}m - k_{-ol}iO_i\theta(i-n_0) +$$
$$+k_{-ol}(i+1)O_{i+1}\theta(i-n_0+1) - k_{conv}O_i\theta(i-n_c) \quad \text{(S2)}$$

As depicted in the equations below, oligomer total population and mass are calculated by summing up all the O_i terms (Eq. S3), while the differential equations for fibril total population and mass are calculated by using the condensed expressions for the summations (Eq. S3). These condensed expressions were obtained from Eq. S1 with calculations similar to the ones performed by Pöschel et al..[4] comparing the experimental time points of monomer depletion with the simulated monomer m(t), calculated by Eq. S5 through the numerical integration of Eq. S3 and Eq. S4. In the equations below, the terms O_{Max} represent the maximum allowed size of oligomers for the numerical solving of the differential equations, theoretically this term can go up to ∞ but in our simulations oligomer population were almost empty after $i = 30$, see Fig. S8B.

$$\frac{dO}{dt} = \sum_{i=n_0}^{O_{Max}} \frac{dO_i}{dt}; \qquad \frac{dO_{crit}}{dt} = \sum_{i=n_c}^{O_{Max}} \frac{dO_i}{dt}; \qquad \frac{dM_O}{dt} = \sum_{i=n_0}^{O_{Max}} i\frac{dO_i}{dt}; \qquad \frac{dM_{O\,crit}}{dt} = \sum_{i=n_c}^{O_{Max}} i\frac{dO_i}{dt} \tag{S3}$$

$$\frac{dF}{dt} = \sum_{i=n_c}^{\infty} \frac{df_i}{dt} = k_{conv}O_{crit} + k_{frag}\left(M_f - F(2n_c+1)\right); \qquad \frac{dM_f}{dt} = \sum_{i=n_c}^{\infty} i\frac{df_i}{dt} = k_{conv}M_{O\,crit} + k_+ mF - k_- F \tag{S4}$$

$$m = m_0 - \sum_{i=n_c}^{\infty} if_i - \sum_{i=n_0}^{\infty} iO_i = m_0 - M_f - M_O \tag{S5}$$

The cumulative masses of aggregated species are defined as M_f, M_O, M_{Ocrit}, for the total mass of fibrils, oligomers and oligomers above the critical size (n_c), respectively. This new proposed model contains oligomeric intermediates with different aggregation properties and kinetic constants with respect to fibrils. We put $n_0 = 2$, we considered the smallest oligomer as the dimer and the best fit was achieved using $n_c = 20$ as critical size. In Table S1 we reported the fitted kinetic constants for this model and for the other two model considered in the main text, that one developed for the aggregation of Aβ1-42[2] and that one for Aβ1-40[8] at pH 7.4. The agreement between calculated and experimental values is now optimal also during the lag-time where the monomer concentration is decreasing due to the progressive formation of oligomeric species. In our model, the kinetic constant for the monomer addition to fibrils species (k_+) is an order of magnitude higher than the one for the monomer addition to oligomeric species (k_{+ol}). This difference explains why, once a sufficient amount of large oligomers is converted to fibrils, monomers start to be rapidly consumed while the mass of fibrils rapidly increases producing a sigmoidal behaviour for the monomer consumption kinetics. In the third part of the trend, where most of the peptides are aggregated into fibrils, the process of monomer dissociation becomes relevant and is responsible for the residual amount of monomer still present in solution in the tail of the sigmoidal decrease. The critical size of the oligomer-to-fibril conversion was found to be $n_c = 20$; this number is anyway just an estimate, since reasonably good values were found also for $15<n_c<40$, and we cannot exclude that conversion may begin at even larger sizes.

Parameters	Conversion model	Model Aβ1-40	Model Aβ1-42
k_{nucl} $[M^{-1}s^{-1}]$	$1.25\cdot10^{-6}$	$2.64\cdot10^{-10}$	$1.28\cdot10^{-9}$
k_{-nucl} $[s^{-1}]$	$6.96\cdot10^{-9}$	-	-
k_+ $[M^{-1}s^{-1}]$	$2.83\cdot10^{-1}$	$7.09\cdot10^{-3}$	$6.19\cdot10^{-4}$
k_- $[s^{-1}]$	$5.22\cdot10^{-7}$	$6.11\cdot10^{-21}$	$2.57\cdot10^{-12}$
k_{frag} $[s^{-1}]$	$8.68\cdot10^{-11}$	-	$2.52\cdot10^{-12}$
k_{nucl2} $[M^{-2}s^{-1}]$	-	1.92	6.54
k_{+ol} $[M^{-1}s^{-1}]$	$2.11E\cdot10^{-2}$	-	-
k_{-ol} $[s^{-1}]$	$1.30\cdot10^{-7}$	-	-
k_{conv} $[s^{-1}]$	$1.35\cdot10^{-8}$	-	-
K_{sat} $[M^2]$	-	$9.73\cdot10^{-5}$	-

Table S1: Fitted parameters for the conversion model developed in this work, for the Aβ1-40 model from the work of Meisl, Knowles and co-workers[8] and for the Aβ1-42 model from the works of Knowles, Dobson and co-workers.[2]

3. Test with secondary nucleation active

We repeated the fitting procedure by adding the secondary nucleation term (depicted in the line below) in Eq. S1.

$$+\delta(i-n_2)m^{n_2}\sum_{j=2}^{\infty} jf_j$$

In this term we considered the fibrillary nucleus size $n_2 = 2$, with the meaning that fibril-like dimers are allowed to form on the fibril surface of all the other fibrils. The fitting results are shown in Fig. S5 and the fitted kinetic constants are in Table S2.

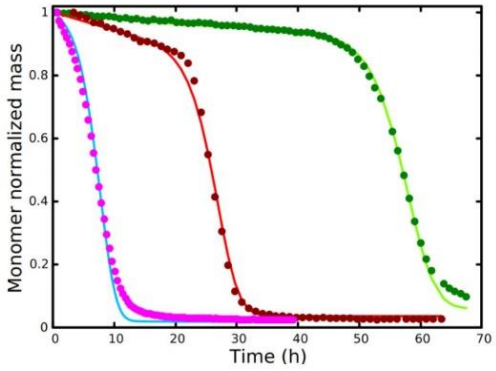

Figure S5: Simulated monomer populations coming from the "conversion" model with secondary nucleation were fitted to the experimental data coming from the integration of the methyl region of 1D solution NMR spectra at different starting monomer concentrations (30, 50 and 100 μM).

Parameters	Conversion Model with secondary nucleation
k_{nucl} $[M^{-1}s^{-1}]$	$1.23 \cdot 10^{-6}$
k_{-nucl} $[s^{-1}]$	$7.87 \cdot 10^{-9}$
k_{+} $[M^{-1}s^{-1}]$	$3.18 \cdot 10^{-1}$
k_{-} $[s^{-1}]$	$5.49 \cdot 10^{-7}$
k_{frag} $[s^{-1}]$	$7.41 \cdot 10^{-11}$
k_{nucl2} $[M^{-2}s^{-1}]$	$5.89 \cdot 10^{-6}$
k_{+ol} $[M^{-1}s^{-1}]$	$2.30 \cdot 10^{-2}$
k_{-ol} $[s^{-1}]$	$1.39 \cdot 10^{-7}$
k_{conv} $[s^{-1}]$	$1.04 \cdot 10^{-8}$

Table S2: Fitted kinetic constants for the conversion model developed in this work with secondary nucleation added. The kinetic constant relative to the secondary surface catalyzed nucleation remains quite smal (see the fitted values for the two-species models in Table 1) in order to fit the NMR data.

4. Including low molecular weight (LMW) oligomers in the fitting

In the first chapter of these Supporting Information we showed how the observed species in the 1D spectrum is essentially the monomeric peptide. Nevertheless, oligomers even up to about 10 units have a molecular weight <50 kDa and should be visible in the NMR spectrum. Thus, we cannot exclude that integrating the methyl region we can include resonances of small oligomeric species. To demonstrate the robustness of the analysis, we repeated the simulation of the oligomer-to-fibril conversion model considering as visible in the integral also LMW oligomeric species until hexamers (species until hexamers should be clearly visible by 1D NMR). We examined two cases: first we repeated the fit using the same constants of Table 1, but including in the simulated curve the LMW oligomers (Figure S6A). Second, we repeated the fit allowing the constant to be adapted (Figure S6B & Table S3). Since these small-size oligomeric species are transient and present in low concentration (at least in our simulations) taking them into account while fitting the NMR data caused only minimal differences in the trend of the calculated curves.

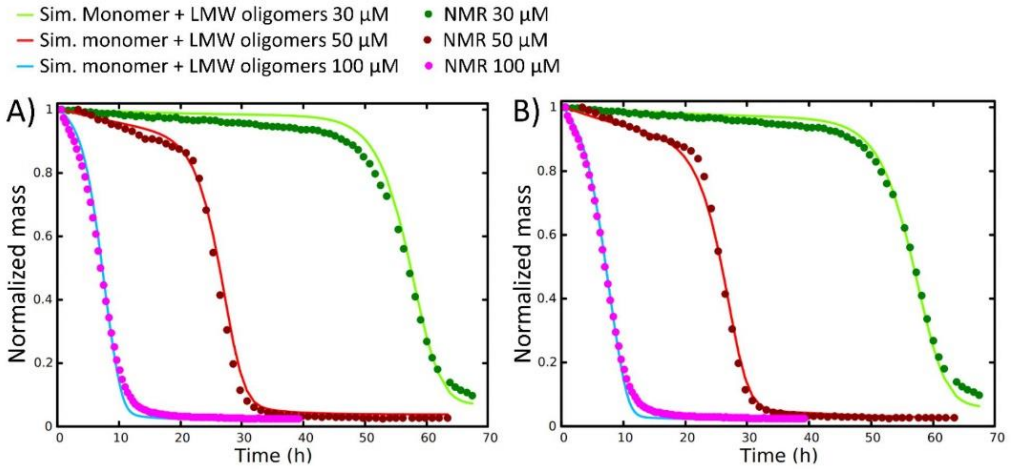

Figure S6: A) Simulated monomer and small oligomer populations (oligomers of size ≤6 and monomers were included) coming from the "conversion" model were fitted to the experimental data coming from the integration of the methyl region of 1D solution NMR spectra at different starting monomer concentrations (30, 50 and 100 µM), the kinetic constants used were the ones of Table 1. B) kinetic constants were optimized to fit monomers and species until hexamers (fitted parameters are present in Table S3).

Parameters	Conversion model with LMW oligomeric species
k_{nucl} $[M^{-1}s^{-1}]$	$1.51 \cdot 10^{-6}$
k_{-nucl} $[s^{-1}]$	$1.53 \cdot 10^{-9}$
k_{+} $[M^{-1}s^{-1}]$	$2.67 \cdot 10^{-1}$
k_{-} $[s^{-1}]$	$1.93 \cdot 10^{-7}$
k_{frag} $[s^{-1}]$	$8.50 \cdot 10^{-11}$
k_{nucl2} $[M^{-2}s^{-1}]$	-
k_{+ol} $[M^{-1}s^{-1}]$	$2.87 \cdot 10^{-2}$
k_{-ol} $[s^{-1}]$	$1.64 \cdot 10^{-7}$
k_{conv} $[s^{-1}]$	$7.32 \cdot 10^{-9}$

Table S3: kinetic constants relative to the fitted data in Figure S6 (right).

5. Populations of the aggregates

On the basis of the fitted constants of Table S1, we back-calculated the relative size of the fibril distribution for the three models (Fig. S8 and Fig. S9). With reference to Figure S7, it results that, for the Aβ1-42 and Aβ1-40 models at the end of the aggregation process of the 50 µM sample (t ~60h), the majority of the fibrils should have a size smaller than 20 monomers, and for the Aβ1-42 model even smaller than 10 monomers (40 kDa). In the trials we made, only the model based on the oligomer-to-fibril conversion predicts the formation of fibrils larger than 433 kDa (>100mers). Indeed, the strong secondary nucleation process of the first two models results in a rapid formation of nucleation seeds during the sigmoidal step that are not able to elongate much because of the depleted monomers in solution. In our conversion model we have not included the secondary nucleation process and the "limited" number of converted fibrils favors their elongation towards higher molecular weights.

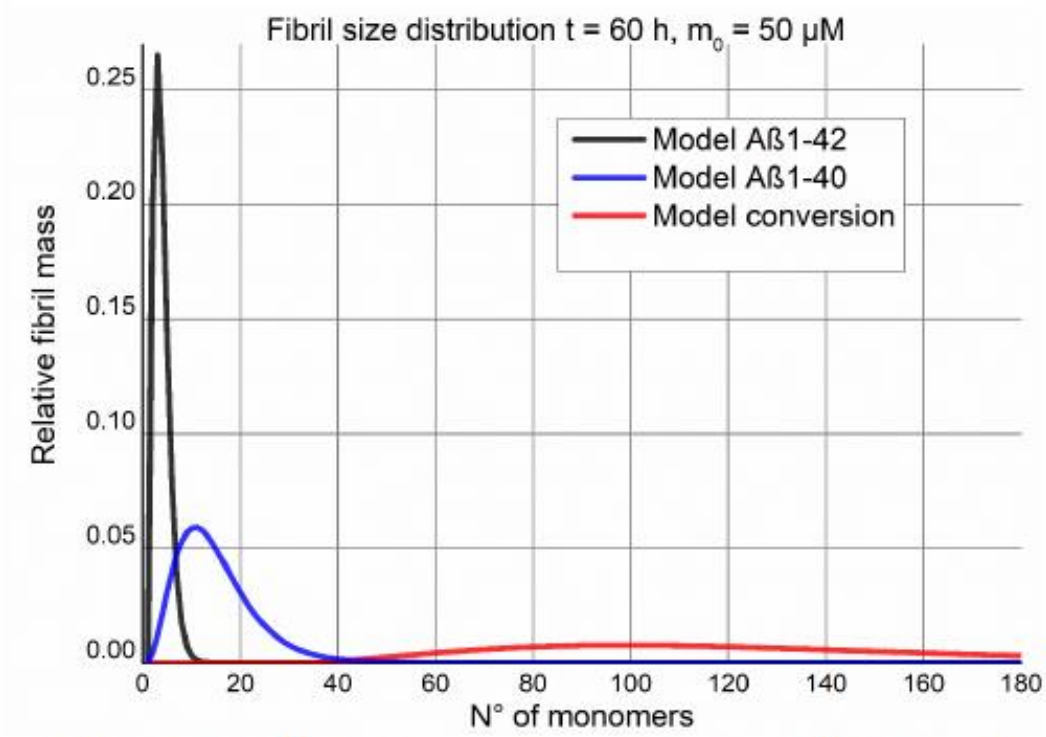

Figure S7: The distributions of the fibril size at t = 60 for the three models tested are plotted together. The model for Aβ1-42 produced a large amount of dimers through secondary nucleation in order to fit the experimental data.

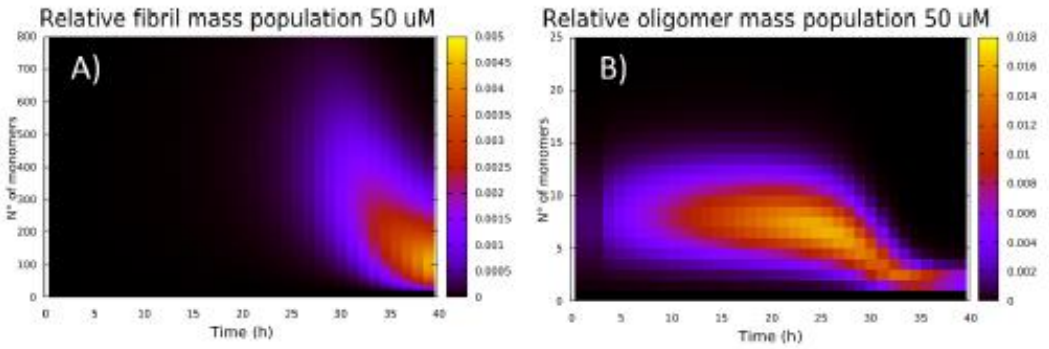

Figure S8: Size distribution of fibrillary (A) and oligomeric (B) species during the simulation of the aggregation kinetics of the 50 µM sample of Aβ1-40. The simulations are relative to the conversion model. The decay of the average size of fibrils (from ~500 peptide units to ~100) over time is caused by the fragmentation kinetics[4,9] which is not countered by any agglomeration of aggregates in this simplified model.

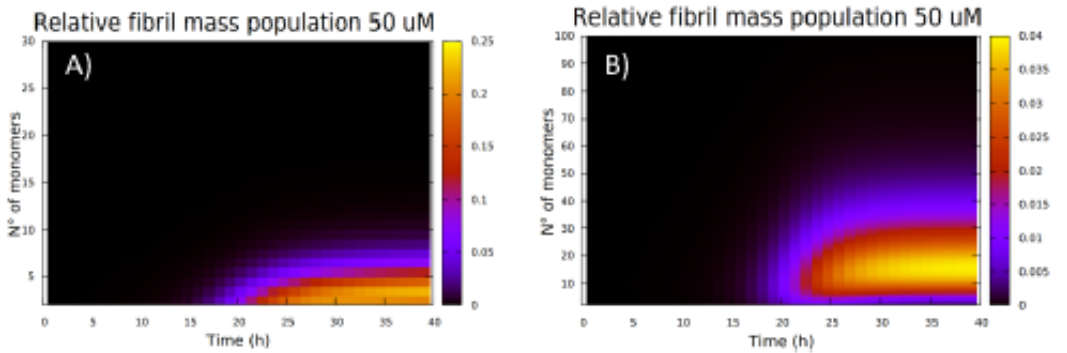

Figure S9: Size distribution of fibrillary species during the simulation of the aggregation kinetics of the 50 µM sample of Aβ1-40. In A) the simulations are relative to the model for Aβ1-42[7] while in B) are relative to the model for Aβ1-40.[8]

6. Experimental details that can affect the aggregation kinetics

The experimental investigation of the aggregation kinetics with Aβ peptides is quite challenging, since there are many factors that can influence the behavior of these short peptides. The aggregation kinetics of Aβ depends on the presence of metal ions,[10] lipids,[11] methionine-35 oxidation,[12] shaking,[13] salt concentration, temperature and pH.[14] Moreover, the presence of preformed aggregates and electrostatic surfaces can drastically promote fibrillation *in vitro*[15] As an example of the extreme variability of these assays, in Fig. 4 of the main text we showed a sample where the presence of a single piece of dust promoted the formation of a long macroscopic fibrillary aggregate into the NMR tube.

The presence of this impurity had a dramatic effect on the aggregation kinetics. Some fibril nuclei were formed on the surface of the dust particle in the bottom of the tube, where the macroscopic fibrillary aggregate started to grow. From these quickly formed aggregates the aggregation proceeded mainly through polymerization. This hypothesis is also in line with the observation of an exponential decay of the monomer signal (Fig.4A). Indeed, with reference to Eq. S6, a pure polymerization kinetics from a preformed concentration of fibrils (F_0) implies an exponential decay of the monomer ($m(t)$), considering a fixed monomer initial concentration (m_0)

$$\frac{dm(t)}{dt} \sim m_0 - k_+ F_0 m \rightarrow m(t) \sim Ae^{-k_+ F_0 t} + B \qquad (S6)$$

This curious example just highlights how complex is the problem of reproducibility on these samples, which requires working on extremely clean and freshly monomerized Aβ1-40. Despite all these attentions, the kinetics can sometimes follow slightly different trends depending on difficulties in carefully controlling all these variables. For example, the trends of the experimental monomer consumption measured for the Aβ1-40 50 µM in Fig. 2 and Fig. 3 are very similar but not superimposable. This could be due to the presence of ThT, but also to the difficulties to control the very small concentrations of impurities. For the above reasons, solution NMR is a profitable technique to follow these aggregation processes, because it gives an overview of the whole sample. In several cases, the presence of impurities in the sample or the concomitant occurrence of degradation processes (for example due to undetectable amounts of proteases)[16] can be determined by 1D ^{1}H NMR spectra (Fig. S10), NMR allows one to recognize a biased aggregation kinetics from a relevant one. Protein degradation can be prevented, at first instance, by obtaining an ultra-pure sample from the purification step. Then, we found that using EDTA (1.0 mM), protease inhibitors (Roche cOmplete™, EDTA-free Protease Inhibitor Cocktail, diluted 1:200) and sodium azide (0.2%) it is possible to block any form of bacterial contamination and residual proteases activity.

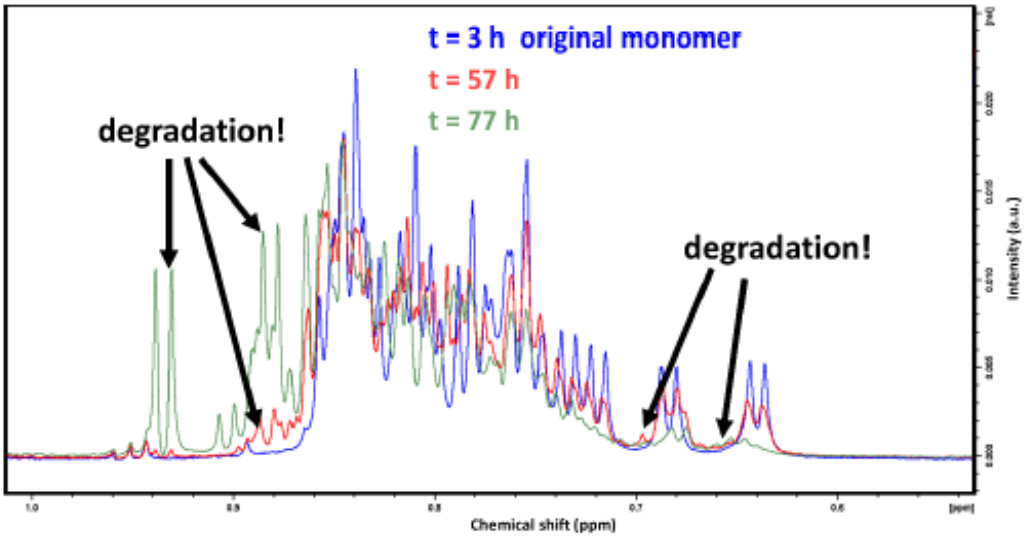

Figure S10: Spectra at different time points of a 40 µM Aβ1-40 sample at 298 K, pH 8.5 in ammonium acetate buffer in absence of EDTA, NaN_3 and protease inhibitors. The growth of sharp peaks near the monomer signals in the methyl region is a hallmark of degradation.

7. Experimental

7.1 AβM1-40 expression and purification

Escherichia Coli BL21(DE3) pLysS cells were transformed with pET-3a(+) vector containing the gene encoding the AβM1-40 peptide gene. The expression was performed using the Marley method.[17] Transformed cells were grown in LB medium until OD600 value reached 0.6-0.8 and, after a centrifugation at 3500 rpm (JA-10, Beckman Coulter), the pellet was exchanged into the M9 minimal medium containing $(^{15}NH_4)_2SO_4$ 1.0 g/L as sole nitrogen source. The same method was used to obtain unlabelled samples. The expression was induced with 1.2 mM Isopropyl-β-D-thiogalactoside and, after 4 hours incubation at 39 °C, cells were harvested at 4000 rpm (JA-10, Beckman Coulter). The pellet was suspended in TRIS 10mM, EDTA 1.0 mM, pH 8.0 buffer and sonicated for 40 minutes (cycle ON 2 seconds, cycle OFF 15 seconds). The suspension was utracentrifuged at 40000 rpm (Type 70 Ti rotor, Beckman Coulter) for 25 min and the pellet was collected, washed with TRIS 10 mM, EDTA 1.0 mM, pH 8.0 buffer and utracentrifuged a second time. Surnatant was discarded and, since Aβ peptides are expressed into inclusion bodies (IBs), a homogenization step with a buffer TRIS 10mM, EDTA 1.0 mM, pH 8.0 containing Urea 8.0 M, until the IBs were fully solubilized, was needed. Purification was performed through anion exchange chromatography in batch with TRIS 10 mM, EDTA 1.0 mM, NaCl 20 mM, 50 mM, 125 mM, 150 mM, 300 mM, 1.0 M at pH 8.0 as elution buffer[18] using DEAE 52 cellulose (DE52) resin. Fractions containing the protein were collected and added to Guanidine hydrochloride 6.0 M. A size-exclusion chromatography step was carried out exploiting the preparative column HiLoad 26/600 Superdex 75 pg with 50 mM $(NH_4)OAc$ pH 8.5 as final buffer [19]. The typical NMR sample conditions counted 30 µM to 100 µM AβM1-40 in 50 mM $(NH_4)OAc$, EDTA 1.0 mM, NaN3 0.2%, Thioflavin-T 5.0 µM (only for samples which were used in parallel with fluorescence), SigmaFast Protease Inhibitor Cocktail (the most abundant component was ABSF 10 µM), 10% D_2O at pH 8.5.

7.2 NMR experiments

Solution NMR experiment were acquired on an Avance III 950 MHz Bruker spectrometer and 700 MHz spectrometer both equipped with a $^1H/^{13}C/^{15}N$ triple resonance cryoprobe. 1D ^1H NMR spectra were acquired with standard direct excitation sequence with excitation sculpting water suppression[20] and a standard 1D NOESY sequence with water presaturation.[21] ^1H π/2 pulse was calibrated at 12.51 µs, 24576 complex points were acquired with an overall acquisition time of 1.95 s, each experiment was acquired accumulating 512 scans with a recycle delay of 1.0 s. Experiments were processed with 65536 complex points and an exponential window function of 0.3 Hz. All the 1D NMR experiments were run at 310 K while the 2D ones at 298 K using new and clean 5 mm glass tubes.

7.3 ThT fluorescence

Fluorescence experiments were performed in a Cary Eclipse fluorescence spectrophotometer (Agilent). The excitation wavelength was set to 450 nm, the emission wavelength to 485 nm and the temperature was kept at 310 K, with emission and excitation slits of 5 nm. ThT final concentration was 5 μM. Fluorescence intensity was recorded every 5 minutes in quiescent conditions. A quartz cuvette with a sample volume 550 μL was used. We preferred the use of a quartz cuvette instead of the more frequently used well plates because it is known that the water/air interface can promote aggregation.[22] In a NMR tube, the ratio between the exposed interface and the sample volume is, in general, smaller than the one of well plate (0.036 mm^{-1} for a typical 5 mm NMR-tube with 550 μL of sample and 0.15-0.14 mm^{-1} for a common flat bottom well with 250 μL of sample). In a quartz cuvette (10 mm x 2 mm) with a sample volume of 550 μL, the exposed interface/sample volume ratio is 0.036 mm^{-1}, equal to the value obtained for the NMR tube.

7.4 Kinetic analysis

Monomer simulated concentrations were compared with the integral values of methyl signals of the 1D spectra (0.67-1.0 ppm) or with the integrals of the signals of QD2 protons of H6, H13 and H14 and QE protons of Y10 of the aromatic regions of 1D-NOESY spectra (6.7-7.1 ppm). While NMR integrals were normalized by simply dividing by the highest value in the 1D series, the ThT fluorescence data were normalized to 1 minus the final plateau value (normalized integral) of the replicate sample in the NMR spectrometer. The kinetic simulations were performed by integrating with Euler method (total points 150000, discrete time interval = 2 s) the kinetic differential equations (Eq. 2 and Eq. 3) describing oligomer and fibril population. The squared differences between the normalized integrals of the methyl signals and the simulated monomer populations were minimized in parallel for different monomer concentrations by optimizing the kinetic constants using a Nelder-Mead minimization algorithm.[23]

7.5 HPLC-Mass Spectrometry

One aliquot of freshly purified and monomerized AβM1-40 (that is the peptide used in manuscript, which corresponds to the Aβ1-40 peptide with an additional methionine in the position 0, and is commonly named AβM1-40 in the text) was frozen (–80 °C) and successively checked by HPLC-MS in a HPLC Dionex Thermo instrument, model Ultimate 3000, coupled to a Thermo LTQ-Orbitrap mass spectrometer via ESI interface. The HPLC column was an Agilent Zorbax 300SB C8 2.1 x 100 mm, 3.5 μm. A gradient elution was performed with two solvents: solvent A H2O with 0.1% formic acid, and solvent B acetonitrile with 0.1% formic acid. The gradient started at time 0.00 minutes with 97% A and 3% of solvent B, reaching at 11.75 min 50% of B, and at time 14.75 min 20% of A and 80% of B. The flow rate was 0.40 mL/min and the injected sample volume was 5 μL. The Mass spectra of the eluted sample were continuously acquired with an Orbitrap system at resolution 30000 (at m/z = 400) in the range of m/z 300–2000. The ESI interface parameters were: Spray voltage 5 kV; Capillary voltage 10 V; Tube lens 60 V; Capillary temperature 280°C. Gas: Sheath gas 10 (arbitrary units), Auxiliary gas 5, Sweep gas 5.

Figure S11 reports the elution profile acquired for m/z comprised between 1000 and 1500. The main peak is composed by the monomeric AβM1-40 with high degree of purity. The figure S12 reports the mass distribution in the central region of the elution peak at times comprised between 8.15 min and 8.48 min. The main patterns, with charges z=4, 5, 6, 7, correspond to the multicharged AβM1-40 peptide. Figure S13 reports the enlarged region around m/z = 893 where is possible to see, together with the isotopic profile of the positive pentacharged AβM1-40 peptide, also the pentacharged isotopic pattern of a small amount of oxidized peptide ($MW_{A\beta M1-40} + {}^{16}O$), probably related to the oxidation of one of the two methionine residues, (either M0 or M35). Figure S14 reports the enlargement of the tetracharged peptide (m/z= 1116.06) where is possible to recognize also here a small amount of the oxidized peptide (m/z=1120.06) and of the peptide without the initial methionine (–131 uma) (m/z=1083.30). The relative amount of these impurities is estimated on the bases of the integrals of the multi charged patterns: the amount of oxidized peptide is of the order of 5.82% of the not oxidized AβM1-40, while the Aβ1-40 (missing the first methionine) is about 2.82% of the entire peptide.

While the presence, or the missing of the first methionine is expected to have almost no-influence in the aggregation kinetics,[18] the Aβ1-40 peptide fully oxidized at the methionine-35 shows large differences in the aggregation behaviour.[24,25] Nevertheless, since we are in presence of only a very small amount of oxidized species (that could be either M0 or M35) we expect this impurity has no influence in the observed aggregation kinetics.

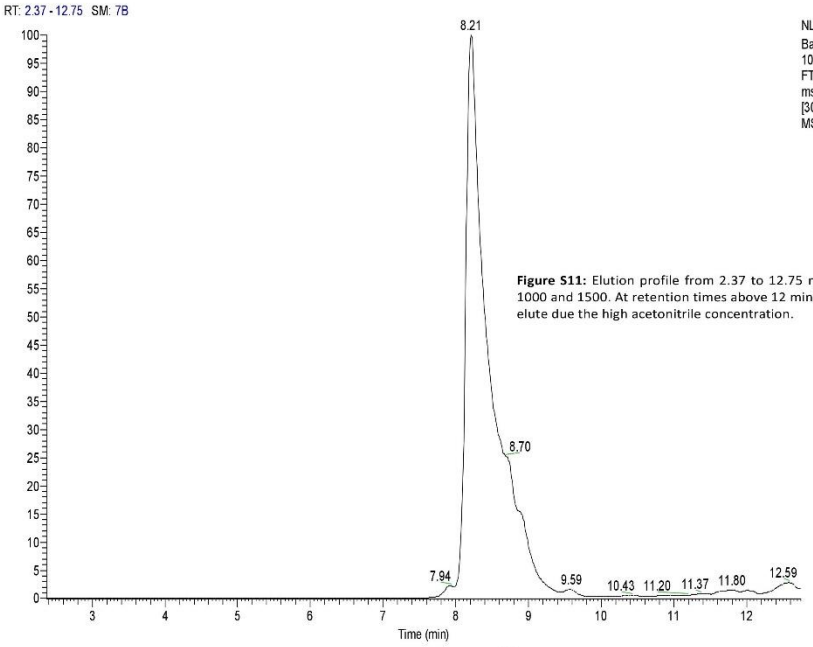

13

Figure S11: Elution profile from 2.37 to 12.75 min acquired at m/z between 1000 and 1500. At retention times above 12 min column impurities start to be elute due the high acetonitrile concentration.

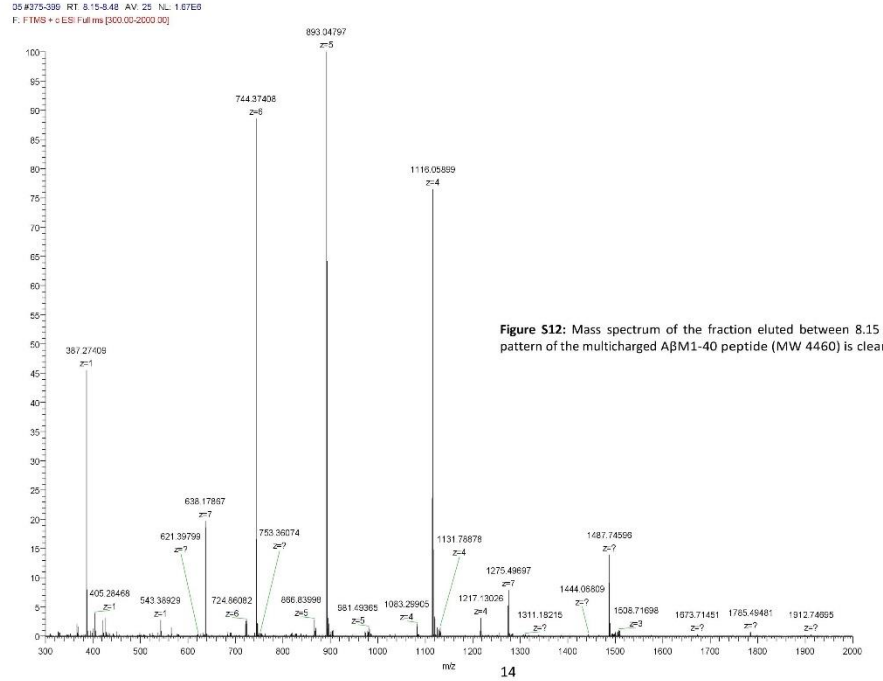

14

Figure S12: Mass spectrum of the fraction eluted between 8.15 and 8.48 min. The pattern of the multicharged AβM1-40 peptide (MW 4460) is clearly visible.

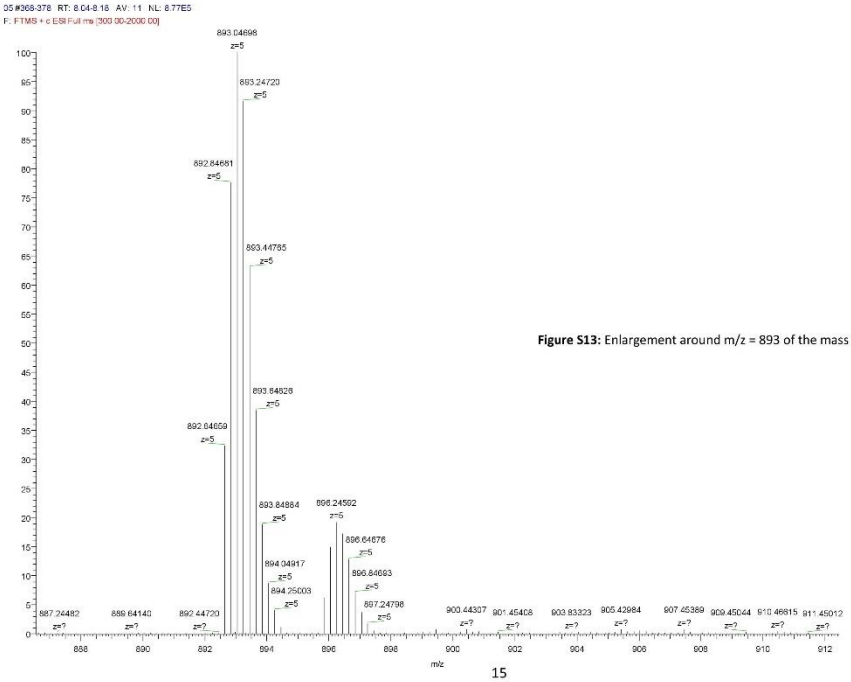

Figure S13: Enlargement around m/z = 893 of the mass spectrum of Figure S12.

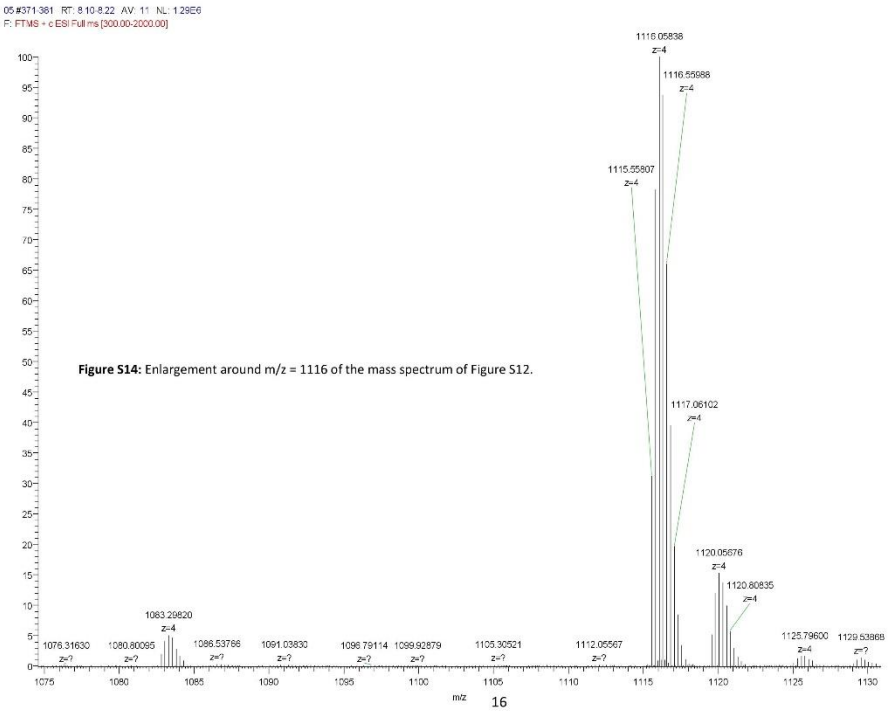

Figure S14: Enlargement around m/z = 1116 of the mass spectrum of Figure S12.

References

1 I. Bertini, G. Gallo, M. Korsak, C. Luchinat, J. Mao and E. Ravera, *Chembiochem Eur. J. Chem. Biol.*, 2013, **14**, 1891–1897.
2 S. I. A. Cohen, M. Vendruscolo, M. E. Welland, C. M. Dobson, E. M. Terentjev and T. P. J. Knowles, *J. Chem. Phys.*, 2011, **135**, 065105.
3 F. Ferrone, *Methods Enzymol.*, 1999, **309**, 256–274.
4 T. Pöschel, N. V. Brilliantov and C. Frömmel, *Biophys. J.*, 2003, **85**, 3460–3474.
5 F. Oosawa and M. Kasai, *J. Mol. Biol.*, 1962, **4**, 10–21.
6 S. I. A. Cohen, S. Linse, L. M. Luheshi, E. Hellstrand, D. A. White, L. Rajah, D. E. Otzen, M. Vendruscolo, C. M. Dobson and T. P. J. Knowles, *Proc. Natl. Acad. Sci.*, 2013, **110**, 9758–9763.
7 M. M. Pallitto and R. M. Murphy, *Biophys. J.*, 2001, **81**, 1805–1822.
8 G. Meisl, X. Yang, E. Hellstrand, B. Frohm, J. B. Kirkegaard, S. I. A. Cohen, C. M. Dobson, S. Linse and T. P. J. Knowles, *Proc. Natl. Acad. Sci. U. S. A.*, 2014, **111**, 9384–9389.
9 J. K. Davis and S. S. Sindi, *Appl. Math. Lett.*, 2015, **40**, 97–101.
10 F. Hane and Z. Leonenko, *Biomolecules*, 2014, **4**, 101–116.
11 M. Vestergaard, T. Hamada, M. Morita and M. Takagi, *Curr. Alzheimer Res.*, 2010, **7**, 262–270.
12 L. Hou, I. Kang, R. E. Marchant and M. G. Zagorski, *J. Biol. Chem.*, 2002, **277**, 40173–40176.
13 C. F. Lee, S. Bird, M. Shaw, L. Jean and D. J. Vaux, *J. Biol. Chem.*, 2012, **287**, 38006–38019.
14 B. Morel, L. Varela, A. I. Azuaga and F. Conejero-Lara, *Biophys. J.*, 2010, **99**, 3801–3810.
15 B. Moores, E. Drolle, S. J. Attwood, J. Simons and Z. Leonenko, *PLoS ONE*, , DOI:10.1371/journal.pone.0025954.
16 T. Saido and M. A. Leissring, *Cold Spring Harb. Perspect. Med.*, , DOI:10.1101/cshperspect.a006379.
17 J. Marley, M. Lu and C. Bracken, *J. Biomol. NMR*, 2001, **20**, 71–75.
18 D. M. Walsh, E. Thulin, A. M. Minogue, N. Gustavsson, E. Pang, D. B. Teplow and S. Linse, *FEBS J.*, 2009, **276**, 1266–1281.
19 I. Bertini, L. Gonnelli, C. Luchinat, J. Mao and A. Nesi, *J. Am. Chem. Soc.*, 2011, **133**, 16013–16022.
20 T. L. Hwang and A. J. Shaka, *J. Magn. Reson. A*, 1995, **112**, 275–279.
21 S. Bouatra, F. Aziat, R. Mandal, A. C. Guo, M. R. Wilson, C. Knox, T. C. Bjorndahl, R. Krishnamurthy, F. Saleem, P. Liu, Z. T. Dame, J. Poelzer, J. Huynh, F. S. Yallou, N. Psychogios, E. Dong, R. Bogumil, C. Roehring and D. S. Wishart, *PloS One*, 2013, **8**, e73076.
22 C. Schladitz, E. P. Vieira, H. Hermel and H. Möhwald, *Biophys. J.*, 1999, **77**, 3305–3310.
23 R. O'Neill, *J. R. Stat. Soc. Ser. C Appl. Stat.*, 1971, **20**, 338–345.
24 L. Hou, H. Shao, Y. Zhang, H. Li, N. K. Menon, E. B. Neuhaus, J. M. Brewer, I.-J. L. Byeon, D. G. Ray, M. P. Vitek, T. Iwashita, R. A. Makula, A. B. Przybyla and M. G. Zagorski, *J. Am. Chem. Soc.*, 2004, **126**, 1992–2005.
25 M. Friedemann, E. Helk, A. Tiiman, K. Zovo, P. Palumaa and V. Tõugu, *Biochem. Biophys. Rep.*, 2015, **3**, 94–99.

3.2 Mixing Aβ1-40 and Aβ1-42 peptides generates unique amyloid fibrils (manuscript in preparation)

This project is in the frame of an integrative study, aimed to characterize the structure of the mixed fibrils (containing Aβ1-42 and Aβ1-40 peptides) at atomic detail. My contribution to this project was to express and purify Aβ1-42 and Aβ1-40 monomers and to generate fibrils by mixing an equimolar ratio of isotopically enriched samples.

Aβ peptides have been expressed through different labeling schemes to confirm the observations previously hypothesized in our lab during the past years. In our experimental conditions, under vigorous agitation (aimed at favoring the establishment of a thermodynamic equilibrium of Aβ1-40 and Aβ1-42), a very stable and homogeneous interlaced 1:1 assembly was formed.

The characterization of mixed Aβ fibrils has been carried out by acquiring High-Resolution SS-NMR Spectra in combination with microscopy (AFM and TEM).

Mixing Aβ(1-40) and Aβ(1-42) peptides generates unique amyloid fibrils

Mixing Aβ(1-40) and Aβ(1-42) peptides generates unique amyloid fibrils

Linda Cerofolini[1], Enrico Ravera[1], Thomas Wiglenda[2], Annett Böddrich[2], Bettina Purfuerst[6], Iryna Benilova[3,§], Magdalena Korsak[4], Gianluca Gallo[1], Sara Bologna[1], Domenico Rizzo[1], Leonardo Gonnelli[1], Marco Fragai[1], Bart De Strooper[3,5], Erich E. Wanker*[,2], Claudio Luchinat*[,1,4]

1. Magnetic Resonance Center (CERM), University of Florence, Via L. Sacconi 6, and Department of Chemistry "Ugo Schiff", University of Florence, Via della Lastruccia 3, 50019 Sesto Fiorentino (FI), Italy

2. Neuroproteomics, Max Delbrueck Center for Molecular Medicine, Robert-Roessle-Strasse 10, 13125 Berlin, Germany

3. VIB Center for the Biology of Disease, Herestraat 49, 3000 Leuven

4. Giotto Biotech S.R.L., Via Madonna del Piano 6, 50019 Sesto Fiorentino (FI), Italy.

5. KULeuven, Center for Human Genetics, Herestraat 49, 3000 Leuven.

6. Core facility electron microscopy, Max-Delbrück Center for Molecular Medicine, Robert-Roessle-Strasse 10, 13125 Berlin, Germany

[§]Present address: MRC Prion Unit, UCL Institute of Neurology, Department of Neurodegenerative Disease, Queen Square, London WC1N 3BG, UK.

* To whom correspondence may be addressed. Email: claudioluchinat@cerm.unifi.it, ewanker@mdc-berlin.de.

[§]Present address: MRC Prion Unit, UCL Institute of Neurology, Department of Neurodegenerative Disease, Queen Square, , London WC1N 3BG, UK.

* To whom correspondence may be addressed.
Email: claudioluchinat@cerm.unifi.it, ewanker@mdc-berlin.de.

Authors contributions

BDS, CL, EEW designed the research; SB, DR, MK, GG, LG expressed and purified the peptide; LC, MF, ER recorded the NMR experiments; LC, MF analyzed the data; AB, TW performed the AFM and in-vitro characterization of the fibrils; IB performed the cell tests; LC, BDS, MF, CL, ER, EEW, TW wrote the manuscript.

Abstract. Formation and propagation of oligomeric aggregates of Aβ(1-42) and Aβ(1-40) play a critical role in the pathogenesis of Alzheimer's disease. It is however unclear what constitutes exactly a toxic species and whether pure or mixed oligomeric species contribute to toxicity. It is commonly believed that Aβ(1-40) and Aβ(1-42) segregate in their mixtures, and recent structural studies suggest that Aβ(1-40) and Aβ(1-42) generate mature amyloid fibrils of very distinct morphologies. Surprisingly, we describe here fibrils obtained from mixed solutions of Aβ(1-42) and Aβ(1-40) peptides that contain a never previously reported, structurally-uniform 1:1 species. This mixed species differs structurally from pure Aβ(1-40) fibrils obtained under the same conditions as well as from the recently reported structures of Aβ(1-42) fibrils. The mixed species forms preferentially even when a non-stoichiometric ratio of Aβ(1-42):Aβ(1-40) is used. This species appears to be toxic for neurons in culture.

Significance statement. The precise nature of the structures responsible for amyloid toxicity is a major question in Alzheimer's Research. Several Alzheimer-related amyloid-β peptides of different lengths occur together *in vivo*, and their relative amounts change during the disease. We demonstrate here that the two main alloforms of the amyloid peptide (Aβ(1-42) and Aβ(1-40)) are able to form interlaced mixed fibrils whose structure is quite different from the structures recently published of fibrils made from either species alone. Our findings clearly demonstrate an interaction between the two major Alzheimer-related peptides, and provide new insights into how changes in the relative ratio of these peptides can determine structure and function.

Amyloid-β (Aβ) peptides are widely considered responsible for the onset and progression of neurodegeneration in Alzheimer's disease (AD) (1, 2). One of the principal hallmarks of AD are, indeed, amyloid plaques, constituted by largely fibrillar amyloid aggregates formed by aggregation-prone peptides (3, 4), which are present in brain parenchyma and vessels (5, 6). Aβ peptides are cleaved from the amyloid precursor protein (APP) by the combined action of β- and γ-secretases, which yields a heterogeneous mixture of peptides varying in length at their carboxy-termini (from 37 to 43 amino acids) (7–10). The two major Aβ alloforms are 40 and 42 amino acids long, respectively. Aβ(1-42) shows a much higher propensity to aggregate *in vitro* than the Aβ(1-40) peptide (11). Evidence has been provided for the ratio between the two alloforms to have a pathological significance (12, 13). In the plaques found post-mortem in AD afflicted people, the Aβ(1-42):Aβ(1-40) peptide ratio was found to range from 1:1 to 9:1 (5, 6), whereas the physiological ratio of the two soluble peptides is 1:9. Indeed, the ratio of Aβ(1-42) and Aβ(1-40) was found to be shifted to higher values (2:8/3:7) in familial AD patients caused by presenilin mutations (13–17), and the aggregation rate and toxicity both already increase with a shift in ratios from 1:9 to 3:7 (13, 18).

The imbalance of the Aβ(1-42):Aβ(1-40) ratios determines a variation in the patterns of detectable oligomeric species (12, 13, 18–20), i.e. in the size and composition of aggregated species, and has been the subject of several studies. In case of excess of monomeric Aβ(1-40) (as expected under normal physiological conditions), the aggregation of Aβ(1-42) monomer is inhibited by Aβ(1-40), as indicated by *in vivo* studies, which show that a high percentage of Aβ(1-40) peptides in the brain might have a protective effect (21, 22). Monomeric Aβ(1:40) has also been reported to alter the stability of Aβ(1:42) aggregates, and prevent their conversion into mature fibrils approximately at - or above - an equimolar ratio (12). Kuperstein et al. (13) found that through shifting of the Aβ(1:42):Aβ(1:40) ratio from 1:9 to 3:7 the nucleation time of the mixture was reduced, but without a significant alteration of the fibril elongation time. For Aβ(1:42):Aβ(1:40) ratios higher than ~3:7, instead, a plateau was reached and no significant variation neither in the nucleation time nor in the fibril elongation time were observed (13). Conversely, in the presence of the two alloforms (Aβ(1:42):Aβ(1:40)) in a 1:9 ratio, once nucleation is induced, fast aggregation into non-toxic mature fibrils occurs

without the formation of toxic intermediates, while in the presence of a 3:7 Aβ(1:42):Aβ(1:40) ratio synaptotoxic intermediates were readily formed (13).

Using a combination of solution nuclear magnetic resonance spectroscopy, high molecular weight mass spectrometry and cross-seeding experiments Pauwels et al. (18) found that Aβ(1-40) and Aβ(1-42) peptides mutually influence their aggregation kinetics, with the general trend that Aβ(1-42) makes the aggregation of Aβ(1-40) faster and Aβ(1-40) makes the aggregation of Aβ(1-42) slower. Surprisingly, results based on the analysis of kinetic data from ThT fluorescence-based aggregation assays, mass spectrometry and solution NMR on more diluted solutions suggested the formation of heteromolecular nuclei that subsequently evolve into homomolecular fibrils (23). The preference for homomolecular mature fibrils seems corroborated by the evidence that either pure fibrillary species cannot cross-seed the other (24, 25), and this may have implications in the propagation of fibrillar seeds in brain, whether the two alloforms interplay or act separately instead (26). The Aβ(1-40) alloform was extensively characterized by SS-NMR in the past several years (27–32) and was found to yield different - although similar - fibrils under different conditions (33–35), in all cases featuring pairs of U-shaped protofilaments. Conversely, the characterization of the Aβ(1-42) alloform was delayed because of faster aggregation and more difficult purification (25, 36), leading to the formation of heterogeneous species (24, 37, 38). More recently, three reports of an S-shaped fibrillar species have appeared (24, 25, 36). These fibrils are unable to seed a solution of Aβ(1-40) monomers (24).

Fibrils obtained by mixing Aβ(1-42) and Aβ(1-40) peptides in the 3:7 and 1:1 molar ratios were analyzed here using solid state NMR (SS-NMR), transmission electron microscopy (TEM) and atomic force microscopy (AFM). We show that fibrils obtained from mixtures of Aβ(1-42) and Aβ(1-40) peptides (with one exogenous N-terminal methionine residue, Met0) in different molar ratios do co-aggregate. In our experimental conditions, and in particular under vigorous agitation aimed at favoring the establishment of a thermodynamic equilibrium of Aβ(1-40) and Aβ(1-42), a very stable interlaced 1:1 assembly that adopts a very homogeneous conformation is observed.

Results

Characterization of Aβ fibrils and High-Resolution SS-NMR Spectra.

Samples of mixed Aβ(1-42):Aβ(1-40) fibrils were analyzed by transmission electron microscopy (TEM) (Figure 1). Under the fibrillization conditions used in the present work the resulting fibrils appear short (around 100 nm) and highly associated in flat bundles, which do not disassemble to isolated fibrils upon sonication. From the STEM images (Figure S1) a rough estimate of the fibril breadth is around 3 -5 nm as previously observed for the fibrils of pure Aβ(1-40) obtained under the same conditions(29). The fibrillary preparations obtained by mixing Aβ(1-42) and Aβ(1-40) polypeptides in different ratios (respectively 3:7 and 1:1), were then analyzed by NMR.

Previous results on the toxicity of the aggregates obtained from Aβ(1-42):Aβ(1-40) solution mixtures with a ratio of 3:7, prompted at first the investigation of this specific stoichiometry (13). Mature fibril samples obtained from the 3:7 mixture, where only the Aβ(1-40) polypeptide was isotopically enriched, were analyzed through 2D ^{13}C-^{13}C and ^{15}N-^{13}C correlation spectra. The spectra of 3:7 mixed fibrils clearly show the presence of two subsets of peaks, belonging to different fibrillary species. A subset of peaks is almost superimposable with those of the fibrils formed by the pure Aβ(1-40) alloform previously characterized under the same experimental conditions (29) (Figure S2). The other subset thus indicates the presence of a second species, with a different conformation and/or contacts. Importantly, no cross-peaks are observed between the two species. The ratio between the two species was estimated from the intensity of the signals in the 2D ^{13}C-^{13}C correlation spectra to be approximately 4:3. This ratio is not consistent with the presence of an asymmetric dimer as basic subunit (34), which would instead display a 1:1 ratio. We thus postulated that the first species corresponds to the already described fibrils of pure Aβ(1-40) (29) (4 equivalents) while, at the same time, the residual Aβ(1-40) (3 equivalents) may form mixed fibrils with the 3 equivalents of Aβ(1-42) originally present in solution, i.e. in a 1:1 ratio. These fibrils exhibit distinct structural features with respect to those constituted by pure Aβ(1-40).

A new sample of fibrils was thus prepared starting from an equimolar solution (i.e. 1:1) of unlabeled Aβ(1-42) and ^{13}C-^{15}N isotopically enriched Aβ(1-40), and characterized by SS-NMR. The spectra of the fibrils obtained from the 1:1

mixture were extremely well resolved and showed a single set of resonances, identical to the new species observed in the 3:7 mixture and not to the pure Aβ(1-40) fibrils, consistent with our hypothesis (Figure 2).

Spectra of a sample containing a 1:1 mixture of ^{13}C-^{15}N isotopically enriched Aβ(1-42) and non-enriched Aβ(1-40) polypeptides were also acquired to reveal the Aβ(1-42) component. The spectra of Aβ(1-42) in this 1:1 mixture appear almost completely superimposable to those of Aβ(1-40) in the 1:1 mixture, indicating that the conformations of the two peptides in the mixed fibrils are virtually the same (Figure S3). The few slight differences can be all attributed to the presence, in Aβ(1-42), of the two extra residues Ile41 and Ala42, as discussed below.

A sample of pure Aβ(1-42) fibrils was also prepared under the same fibrillization conditions. The 2D ^{13}C-^{13}C and ^{15}N-^{13}C correlation spectra of the fibrillary material obtained from pure Aβ(1-42) are characterized by high signal overlap, indicating high heterogeneity of the fibrils with several different species present in the assembly (Figure S4).

Structural features of the Aβ(1-40) monomer in the Aβ(1-42):Aβ(1-40) fibrils

Full assignment of the resonances of Aβ(1-40) in the newly formed 1:1 species was achieved through SS-NMR experiments acquired on the sample of mixed Aβ(1-42):Aβ(1-40) fibrils (1:1 ratio) in which only Aβ(1-40) was ^{13}C-^{15}N isotopically enriched (Figure S5, BMRB ID: 30166).

The secondary structures of the Aβ(1-40) polypeptide in the mixed fibrils, predicted by TALOS+, contain a β-strand-turn-β-strand motif as found in other Aβ(1-40) fibrils (27, 29, 40–42), with the N-terminal region also showing a β-strand conformation (Figure S6).

The organization of the β-strand-turn-β-strand motif was investigated in detail. Signals correlating the side chains of Leu17 with Leu34/Val36, Phe19 with Gly33/Leu34, Ala21 with Ile32, and His13 with Val40 were detected and assigned unambiguously on the ^{13}C-^{13}C SHANGHAI spectra at different mixing times (see Table S1). These signals are only consistent with a U-shaped conformation of the monomer. The folding of the monomer, called also β–arch, was calculated with the same protocol reported in (29) (see Materials and methods). When the observed unambiguous contacts are reported on topology models of the monomer in the fibril, it is clear that in the current conformation of the β–arch the contacts indicate

a reciprocal packing of the two β-strands (β_1 and β_2) (Figure 3A), which is different from that previously calculated for the fibrils of pure Aβ(1-40) (29) (Figure 3B). Instead, the conformation adopted by Aβ(1-40) in the presence of Aβ(1-42) resembles that reported for fibrils of pure Aβ(1-40) by Tycko and coworkers (40, 41) (Scheme 1).

The analysis of the cross-peaks in the ^{13}C-^{13}C correlation spectra supports the presence of a parallel arrangement of the protein molecules along the β-spine. In particular, no cross peaks correlating the N-terminus and C-terminus of β_1 or β_2 strands have been observed in the spectra. This indicates that the β-strand-turn-β-strand motif is organized in parallel cross-β sheets as reported in the literature for mature fibrils of Aβ(1-40) (27, 29, 40–43). This model is further supported by the presence of a single pattern of signals for each residue in the SS-NMR spectra. For symmetry considerations, this is consistent only with the presence of a parallel in-registry β-spine (44). Each of the β-spines constituting the sides of the cross-β sheet arrangement is called “protofilament” for simplicity.

The spectra observed on fibrils where the Aβ(1-42) component is isotopically enriched are virtually identical to those where the Aβ(1-40) is isotopically enriched, and provide the same intrafilament contacts. Therefore, both Aβ(1-40) and Aβ(1-42) in the mixed fibrils adopt the same U-shaped conformation.

It is worth noting that, while this conformation belongs to the same broad class of U-shaped conformations observed for several Aβ(1-40) fibrils obtained under different conditions, it is strikingly different from the S-shaped arrangement of the recently reported fibrils obtained from pure Aβ(1-42) solutions (24, 25, 36). Interestingly, the U-shaped conformation adopted by Aβ(1-42) in the present mixed fibrils was proposed earlier for Aβ(1-42) by Smith et al. (42), although the data upon which that model was based are also fully compatible with the S-shaped conformation currently accepted Aβ(1-42) (24).

Inter-protofilament interactions in mature Aβ(1-42):Aβ(1-40) mixed fibrils.

Contacts between the C-terminus and the N-terminus of the β_2-strand have been identified from the analysis of the spectra, indicating the presence of a head-to-tail antiparallel association of two β_2-strands of different monomers. In particular, contacts of the side chains of Ile31 with Gly38/Val39/Val40, and of Met35 with Gly38/Val39, have been assigned from ^{13}C-^{13}C spectra (see Table S2). These

experimental restraints are in agreement with a two-fold rotational symmetry (also reported for the co-aligned homo-zipper model (44)) and with the parallel registry of the protofilament. The lateral association among different proto-filaments in the fibrils has been calculated implementing long-range distance restraints in HADDOCK (45). The contacts and the generated model are similar, but not identical, to those reported for fibrils of the pure Aβ(1-40) polypeptide (29) (Figure 4A and B, and Scheme 1).

As anticipated, the spectrum of the 1:1 mixture in which Aβ(1-42) instead of Aβ(1-40) was ^{13}C ^{15}N isotopically enriched was practically identical to that where Aβ(1-40) was enriched. The small difference between the two differently isotopically enriched but otherwise identical 1:1 samples is completely ascribable to the presence of the two additional C-terminal residues of Aβ(1-42). In the Aβ(1-42) stretch, the chemical shifts of the Cα of Val39 and Val40 (that are the last two residues in the Aβ(1-40) polypeptide) undergo an upfield shift of -1 ± 0.1 ppm. This variation of the chemical shift is usually observed on passing from random coil to β-strand secondary structure. At the same time, the presence of the two additional residues at the C-terminus induces a chemical shift variation of about -10 ppm of the carbonyl of Val40 that is here involved in a peptide bond. Some new contacts involving Val39 and Val40 with Ile31 in the N-terminal part of the β_2 stretch were also assigned. This data further indicate that these residues are structured in the Aβ(1-42) polypeptide. Some contacts between Ile31 and Ile41/Ala42 were also assigned (Scheme 1). Overall, apart from these differences at the C-terminus of the longer peptide, the structural arrangements of the two peptides in the 1:1 mixed fibrils appear to be identical.

Aβ(1-42):Aβ(1-40) reciprocal association in the mixed fibrils

In the light of the results discussed above, and particularly of the precise 1:1 stoichiometry of the observed fibrils, we could already conclude that we are in the presence of *a mixed fibrillary species*. Three possible reciprocal packing modes of Aβ(1-40) and Aβ(1-42) peptides along the fibril axis were generated (Figure 5) and scored by HADDOCK 2.2 (45). The generated models were: homogeneous protofilaments (all composed of Aβ(1-40) or Aβ(1-42) peptides) that form a mixed cross-β structure (model A); or interlaced protofilaments that form a paired (B), or staggered (C) cross-β structure (for comparison, panel D reports the structural model of pure Aβ(1-40) fibrils (29)). Model A is readily excluded by the presence

in the spectra of cross-peaks between N-terminus and C-terminus of the β_2 strand, which would not be present if all the labelled peptide molecules were in the same protofibril. We are thus left with the other two models (B and C), both requiring an interlaced arrangement. Arrangements B and C are equally possible, since the observed cross-peaks between N-terminus and C-terminus of the β_2 strand are equally consistent with both of them (see Table S2).

Although only interlaced models (B or C) are consistent with the present NMR data, having a further and more direct proof of an interlaced arrangement is crucial as, on the contrary, most of the recent literature favors segregation of Aβ(1-42) and Aβ(1-40), and consequently the mechanistic models for the onset of AD rarely include intimate interrelationships between Aβ(1-42) and Aβ(1-40). The most direct way to prove/disprove an interlaced arrangement at atomic level is to prepare fibrils by mixing e.g. ^{15}N-enriched Aβ(1-42) and ^{13}C-enriched Aβ(1-40) (or viceversa). Fibrils from 1:1 mixtures of ^{15}N-enriched Aβ(1-42) and ^{13}C-enriched Aβ(1-40) were thus prepared, and examined by SS-NMR experiments. The experiments were designed in such a way as to give rise to signals only when ^{15}N and ^{13}C nuclei are in close proximity. Obviously, this can only occur in intimately mixed fibrils. The two-dimensional nitrogen-carbon correlation experiment 2D ^{15}N-^{13}C hNhhC was acquired on this sample (Figure 6A), showing good signal intensity in several parts of the spectrum and particularly in the NH-carbonyl region. To rule out the possibility that the observed signals are arising from transfer to ^{13}C in natural abundance, the experiment was repeated, under the same conditions, on a sample where only Aβ(1-42) is ^{15}N-enriched while Aβ(1-40) is in natural isotopic abundance (Figure 6B). The absence of signals in the latter experiment clearly confirms that the transfer is occurring between the two alloforms.

This finding was further confirmed by acquiring a zTEDOR nitrogen-carbon correlation experiment (^{13}C(^{15}N)-zTEDOR) in one dimension, where the mixing time has been optimized to minimize the ^{H}N-C' transfer across a single bond (see below) and, instead, favor the correlation across different filaments, i.e. across the N-H…O=C hydrogen bonds. In this case, the signal of the backbone carbonyls appears only in the sample of ^{15}N-enriched Aβ(1-42) and ^{13}C-enriched Aβ(1-40), whereas it is absent in the spectrum of the ^{15}N-enriched Aβ(1-42) with Aβ(1-40) in natural abundance. For comparison, Figure 7c shows the ^{13}C(^{15}N)-zTEDOR spectrum acquired on the sample of ^{15}N- ^{13}C-enriched Aβ(1-40). The spectrum

shows very intense resonances, but relatively lower intensity in the carbonyl region because the coupling across the hydrogen bond is masked by many other intra-filament couplings. The above experiments provide the final proof that the fibrils obtained under the present conditions are indeed *interlaced mixed fibrils*.

To attempt to discriminate between models B and C their structures were generated in silico with the program HADDOCK 2.2 starting from combinations of two different protofilaments, each constituted of eight interlaced Aβ(1-40)/Aβ(1-42) or Aβ(1-42)/Aβ(1-40) monomers. An experimental restraint-driven calculation between two identical interlaced Aβ(1-40)/Aβ(1-42) protofilaments provided a family of four structures corresponding to model B (Figure S7A). Conversely, a set of calculations performed starting from two different interlaced protofilaments, Aβ(1-40)/Aβ(1-42) and Aβ(1-42)/Aβ(1-40), respectively, provided the family of four structures corresponding to model C (Figure S7B). The HADDOCK-scores for the models of the two families are not very different, although somewhat more favorable for model B (Table S3), so that firm conclusions for one or the other model cannot be drawn.

The pdb structures obtained for the mixed Aβ(1-42) and Aβ(1-40) fibrils have been deposited in the protein data bank (model B, PDB ID: 5T5R and model C, PDB ID: 5TD0), together with the pdb structure of the pure Aβ(1-40) fibrils previously reported by Bertini and co-workers (model D, PDB ID: 5TD1, BMRB ID: 30183) (29).

Biochemical analysis of Aβ fibrils

First, the generated fibrillar preparations (pure Aβ(1-40), pure Aβ(1-42), and mixed Aβ(1-42):Aβ(1-40) fibrils) were characterized in terms of their stability and size in native SDS gels (Figure S8A). We observed that the prepared amyloid fibrils are detectable in the gel pockets, while monomers or smaller protofibrillar Aβ(1-42) oligomers, which were used as controls, can enter the separating gel. This indicates that all three aggregate preparations contain large, relatively stable structures that cannot be dissociated with native polyacrylamide gels.

Mixed Aβ(1-42):Aβ(1-40) fibrils show toxicity in cell-based assays

To investigate the potential disease relevance of the mixed Aβ(1-42):Aβ(1-40) fibrils we tested the toxicity of all fibrils preparations in a Cell-Titer blue assay on primary hippocampal mouse neurons (Figure 6) (13). In this assay only the 1:1 Aβ(1-42):Aβ(1-40) fibrils exhibit a significant reduction of cell viability of about 30 %. All other end stage aggregation products did not significantly reduce cell viability, indicating that they are less toxic than the 1:1 Aβ(1-42):Aβ(1-40) fibrils.

Discussion

One of the major unknowns in AD research are the mechanisms by which different Aβ(1-42) and/or Aβ(1-40) aggregate species cause toxicity in mammalian cells.

Most biophysical studies on Aβ peptides reported in literature only deal with the behavior of a single alloform of the peptide, and do not consider the many Aβ peptides that coexist *in vivo* (24, 25, 29, 33, 36, 41). However, it has been widely demonstrated that increasing amounts of Aβ(1-42) relative to Aβ(1-40) speed up the aggregation kinetics and also alter the pattern of spontaneously formed oligomeric species (12, 13, 18–20). The present observation that a single fibrillary species is obtained from mixtures of Aβ(1-42) and Aβ(1-40) indicates that the interplay between the two alloforms may contribute to extend the number of possible polymorphs formed by these peptides, increasing the complexity of the structural landscape of the amyloid aggregates, which may correspond to phenotypic differences (47).

Kuperstein et al. have previously reported that all mixtures of Aβ(1-42) and Aβ(1-40) peptides with ratios higher than 3:7 are equally prone to aggregation, and show a similar lag-phase (13). Based on this observation, it was concluded that toxicity results from unbalance in their natural ratio (13).

The matching of the chemical shifts between Aβ(1-40) and Aβ(1-42) observed in the present mixed fibrils (obtained by labeling either Aβ(1-40) or Aβ(1-42)), containing the two peptides in the 1:1 ratio, univocally indicates that Aβ(1-40) and Aβ(1-42) adopt one and the same conformation in the mixed species. The analysis of the fibrils formed by mixing Aβ(1-42) and Aβ(1-40) in a 3:7 ratio reveals

a further interesting feature: the presence in the spectra of the mixed 1:1 species, while only the excess Aβ(1-40) adopts the pure Aβ(1-40) fibril form. This indicates that Aβ(1-40) and Aβ(1-42) interplay in a preferential manner to provide mixed fibrils with an equimolar distribution of Aβ(1-40) and Aβ(1-42). In this respect, the Aβ(1-40) seems to impede the formation of aggregates of pure Aβ(1-42), while the latter imparts a different folding and assembly of the fibers.

To analyze the structural features of the 1:1 Aβ(1-42):Aβ(1-40) mixed fibrils, the contacts observed in the correlation spectra have been compared with the data obtained for fibrils of pure Aβ(1-40) (29) (Scheme 1). These contacts point to a different conformation of the β-arch motif and to a different packing of the hydrophobic side-chains in the core of the protofilament with respect to those observed in fibrils of pure Aβ(1-40). As previously observed in fibrils of pure Aβ(1-40) (29), also in mixed fibrils of Aβ(1-42) and Aβ(1-40), Lys28 is exposed to the solvent and is not involved in the formation of salt-bridges (24, 25, 30, 48).

Concerning the distribution of the Aβ(1-40) and Aβ(1-42) within the protofilament and the assembly of the two protofilaments to form the fiber, the structural models obtained by taking into account the experimental restraints provide information on the arrangement of this mixed fibril. A fibril constituted by the assembly of a protofilament of Aβ(1-40) with one of the Aβ(1-42) is inconsistent with the presence of contacts between the isotopically labelled N-termini and C-termini of the β_2 strand. Moreover, the contacts between the two β_2 strands in the cross-section formed by two β-strand-turn-β-strand units in the mixed fibril and in the fibril of pure Aβ(1-40) are almost the same (see Scheme 1, panel G and H). In this respect it is hard to imagine how Aβ(1-40) and Aβ(1-42) can interplay to provide a new folding of the β-arch. *Therefore, only an assembly of two identical protofilaments, each constituted by an interlaced arrangement of the Aβ(1-40) and Aβ(1-42) monomers, is consistent with the presence of the contacts between the N-terminus and the C-terminus of the β_2-strand and with the well-defined 1:1 molar ratio of Aβ(1-40) and Aβ(1-42) monomers.* The intimate relationship between Aβ(1-40) and Aβ(1-42) monomers in the present fibrils is definitely proved by the ^{15}N-^{13}C close proximity observed when one monomer is ^{15}N-enriched and the other is ^{13}C-enriched. It is interesting to notice that the presence of an interlaced arrangement, although without atomic structural details, had been proposed by EPR spectroscopy for mixed fibrils of Aβ(1-40) and Aβ(1-42) peptides obtained in

different experimental conditions, but in a 1:1 stoichiometric ratio (49). To summarize, the “mixed” fibrils obtained with 1:1 stoichiometry can be definitely and more correctly referred to as “interlaced”.

It is more difficult to discriminate between the “paired” and the “staggered” assembly of the two protofilaments, corresponding to model B and model C in Figure 5, even if the Haddock-score seems to suggest that model B is slightly preferred over model C (Table S3), and model B has a lower score also with respect to the fibrils of pure Aβ(1-40) refined under the same conditions (Table S4). Moreover, the presence of a heterogeneous mixture of “paired” and “staggered” fibrils cannot be excluded by the experimental and computational data. Actually, the different symmetry of the “paired” and “staggered” assembly should result in non-identical spectra, and therefore in the splitting of signals especially in the loop region facing residues Ile41 and Ala42. In this respect, only residue G25 shows a splitting in the NCA spectrum, with two signals of comparable intensity. Therefore, the whole of the present data is probably not enough to demonstrate or exclude the presence of a mixture of “paired” and “staggered” – but anyway interlaced - fibrils in the sample.

Concerning the mechanism that drives the formation of the interlaced distribution of Aβ(1-40) and Aβ(1-42) peptides, the analysis of the models may provide an indication on the driving force that leads to this very specific and apparently favorable structural arrangement, and at the same time on the less favorable formation of pure Aβ(1-42) fibrils under our experimental conditions. In a not interlaced protofilament of Aβ(1-42), Ile41 and Ala42 could form two hydrogen bonds that would provide a valuable contribution to the stabilization of the structure. However, visual inspection of the model (model A) suggests the presence of possible steric clashes among the side-chains of the two terminal residues. Conversely, the analysis of models B and C shows a good packing of the Ile41 and Ala42 residues in the interlaced conformation. The presence of a steric hindrance involving the side chains of residues Ile41 and Ala42 could thus also explain both the heterogeneity and the lower overall stability of the fibrils of pure Aβ(1-42) in model A with respect to the 1:1 interlaced conformation. In fact, in Aβ(1-42):Aβ(1-40) mixed fibrils the C-terminus of Ala42 is not involved in a stabilizing salt bridge with Lys28 as observed in the S-shaped fibrils of pure Aβ(1-42) (24, 25, 36), that exhibit a larger contact buried surface area between the two protofilaments, as

revealed by the HADDOCK refinement of a recently released structure (Table S4) (25). We can conclude that Aβ(1-42), due to the presence of Ile41 and Ala42, is less stable than Aβ(1-40) in its U-shaped form (29). Instead, a shift in register of the C-terminal contacts, as observed in another U-shaped form of Aβ(1-40) (40) and as also proposed for Aβ(1-42) (42), could be preferentially adopted by Aβ(1-42) under many circumstances.

Summarizing, the present results demonstrate that, under our experimental conditions, a well-defined 1:1 Aβ(1-42):Aβ(1-40) species is preferentially obtained. This behavior is favored when vigorous agitation is applied. Solutions containing mixtures of the two alloforms are more toxic than either solutions of the pure peptides (Figure 6). It is therefore tempting to speculate that mixed oligomeric species preferentially form from mixtures of the two alloforms. Even in experiments that report on segregation of the two forms, mixed oligomeric species have been proposed to exist at the early stages of the process (23). The mixed mature fibrils observed by us under the present conditions are obviously in good agreement with this picture. The heterogeneity observed in the SS-NMR spectra of pure Aβ(1-42) under the present conditions may reflect the endpoint of a fast aggregation reaction, which is instead prevented by the formation of the more stable 1:1 product when Aβ(1-40) and Aβ(1-42) are present simultaneously in solution. Along with these species, in the presence of a molar excess of Aβ(1-40) the pure Aβ(1-40) species previously characterized in (29) is also formed. Structures formed by a molar excess of Aβ(1-42) were not analyzed, but Aβ(1-42) by itself yields a strongly heterogeneous mixture under the present conditions, with the heterogeneity possibly arising from steric hindrance by the two additional terminal residues and from the known tendency of Aβ(1-42) to fibrillate fast. In the present interlaced fibrils, the observed U-shape register ideally accommodates the requirements of both filaments, and also provides an extra stabilization by preventing the steric clashes potentially caused by Ile41 and Ala42 because these two residues are alternatively present and absent in the interlaced fibrils.

Materials and Methods

Expression, purification, and sample preparation of Aβ(1-42):Aβ(1-40) mixed fibrils

Both Aβ(1-42) and Aβ(1-40) bear the exogenous N-terminal Met0 due to the introduction of a translation start codon that has been shown previously to not significantly influence aggregation or toxicity of Aβ aggregates (50, 51). Both peptides were expressed using the Marley method (52), and purified as reported in literature (29, 50, 53–55) but using a combination of anion-exchange and size exclusion chromatography (29). These two-steps of purification allowed us to obtain highly pure products with the yield in the range of 10 mg for Aβ(1-40) and 5-10 mg for Aβ(1-42) per liter of culture.

The fibrils for SS-NMR studies were produced as described in (29). Some samples were obtained by mixing ^{13}C, ^{15}N-uniformly enriched Aβ(1-40) polypeptide with Aβ(1-42) in natural isotopic abundance. Solutions containing Aβ(1-42) and Aβ(1-40) (total concentration of 100 μM) in 50 mM ammonium acetate (pH 8.5) were incubated at 310 K under agitation (950 rpm) for 5 weeks. The 3:7 mixture sample was prepared using 30 μM and 70 μM of Aβ(1-42) and Aβ(1-40) respectively, while the 1:1 sample was produced using the same concentration (50 μM) of both proteins. Fibrils were collected by ultracentrifugation at 60,000 rpm and 277 K for 24 h. The pellet was washed with fresh and cold ultrapure water (Millipore) for three times (1 mL per time). About 14 mg of wet material were packed into a 3.2 mm ZrO_2 magic angle spinning (MAS) rotor at 277 K using an ultracentrifugal device (GiottoBiotech) (56, 57). The fibril samples were kept fully hydrated during all steps.

An equimolar mixture of ^{13}C, ^{15}N-uniformly enriched Aβ(1-42) polypeptide (50 μM) and Aβ(1:40) polypeptide (50 μM) in natural isotopic abundance was prepared using the same protocol.

^{13}C, ^{15}N-uniformly enriched Aβ(1:42) fibrils were also grown, incubating the Aβ(1:42) polypeptide at the concentration of 20 μM to slow down the oligomerization process.

Equimolar mixtures of Aβ(1-42) and Aβ(1-40) polypeptides with different labeling schemes [^{15}N-uniformly enriched Aβ(1-42)/^{13}C-uniformly enriched Aβ(1-40) and ^{15}N-uniformly enriched Aβ(1-42)/natural isotopic abundance Aβ(1-40)] were also prepared following the same protocol.

Microscopic characterization

NMR samples of mixed fibrils of Aβ(1-42):Aβ(1-40) and fibrils formed by the Aβ(1-42) polypeptide alone, were removed from the NMR rotors and used for AFM measurements. For Aβ(1-40) fibrils, freshly prepared samples not subjected to MAS were used for AFM analysis. For the AFM measurements, sheet mica (Nanoworld) was glued to a microscope slide and samples (20 μL, 10 μM) were adsorbed for 10 min onto the freshly cleaved mica, washed with freshly filtered deionized water (4×30 μl) and dried overnight. Dry AFM images were recorded on a Nanowizard II/Zeiss Axiovert setup (JPK, Germany) using intermittent contact mode and FEBS cantilevers (Veeco, USA).

Preparation of Aβ(1-42) monomer solutions and Aβ(1-42) protofibrillar aggregates

Synthetic Aβ(1-42) peptide produced by Bachem (Bubendorf, Schwitzerland) was dissolved in 1,1,1,3,3,3-Hexafluoro-2-propanol (HFIP) for three days, aliquoted and then lyophilized. Monomeric Aβ(1-42) solutions were prepared by dissolving peptides in 10 mM NaOH, sonication for 5 min and dilution to the final concentration in low salt buffer (LSB, 1.9 mM KH_2PO_4, 8.1 mM K_2HPO_4, 10 mM NaCl, pH 7.4). Synthetic Aβ(1-42) peptide produced by the laboratory of Dr. Volkmar-Engert (Institute for Medical Immunology, Charité, Berlin, Germany) was dissolved in HFIP overnight, sonicated for 30 min, aliquoted and then lyophilized. HFIP-treated peptide was dissolved in 100 mM NaOH, sonicated for 5 min and diluted in LSB to a final concentration of 200 μM. The solution was incubated for 6 h in an Eppendorf Thermomixer (Wesseling-Berzdorf, Germany) at 310 K and 300 rpm. The protofibrillar aggregate species was aliquoted and stored at 193 K.

Separation of Aβ(1-42) aggregates by native gels.

Aβ aggregates or monomers (4.5 µL, 10 µM) were diluted with NativePAGE 4x sample buffer (2.5 µL, Invitogen/Thermo Scientific, Dreieich, Germany) and LSB. Samples were loaded onto a Novex Bis-Tris 4-16% gel (Invitogen/Thermo Scientific, Dreieich, Germany) and separated. Aggregates were transferred to a nitrocellulose membrane (GE Healthcare, Freiburg, Germany) and visualized using the 6E10 antibody (BioLegend, San Diego, US) and a mouse anti-POD detection antibody (Sigma, Taufkirchen, Germany). Secondary antibody binding was detected by chemiluminescence using ChemiGlow West Substrate (Alpha Innotech, Kasendorf, Germany); luminescence was measured using a FujiFilm LAS-3000 imager (Fuji, Kleve, Germany).

Thioflavin T assays.

Samples of 25 µM Aβ fibrils or monomers were incubated with Thioflavin T (25 µM final) at 298 K for 10 min. Thioflavin T fluorescence was recorded using a plate reader (Infinite M200, Tecan, Austria) using an excitation wavelength of 420 ± 9 nm and an emission wavelength of 485 ± 20 nm. Data points represent mean ± SD, n = 4.

Cell viability assay

Primary hippocampal neurons were prepared from trypsinized brains of 17-days old mouse embryos, grown in B27-supplemented Neurobasal medium (Invitrogen) for 1 week, and then were treated with 10 µM of pre-aggregated Aβ(1-40), Aβ(1-42) and a mixture thereof. After 72 h treatment, 10 µl Cell-Titer-Blue dye (Promega) was added to 200 µl of the culture medium on the cells. After 3 h, the fluorescence intensity of the samples was measured at an excitation wavelength of 560 nm and an emission wavelength of 590 nm. Statistical significance is indicated by ***, $p<0.001$, unpaired t-test, n=3-4.

NMR measurements

^{15}N ^{13}C NCA and NCO (2D), NCACX, NCOCX, NCACB, N(CO)CACB and CANCO (3D) experiments were performed either on a Bruker Avance III 850 MHz wide-bore spectrometer (20.0 T, 213.7 MHz ^{13}C Larmor frequency), or on a Bruker Avance II 700 MHz wide-bore spectrometer (16.4 T, 176.1 MHz ^{13}C Larmor

frequency) using 3.2 mm DVT MAS probeheads in triple-resonance mode. MAS frequency ($\omega_r/2\pi$) was set to 17.0, 14.0 or 12.0 kHz (± 2 Hz) depending on the experiment. The NCA, NCO, NCACX, NCOCX, NCACB, N(CO)CACB and CANCO experiments were carried out using the pulse sequences reported in the literature (58). At 700 MHz NC transfers were achieved by optimal-control derived pulses (59, 60). Backwards CN transfer was achieved with a time-reversal of the same optimal-control pulses.

2D ^{13}C-^{13}C proton-driven spin diffusion (PDSD) (61), dipolar-assisted rotational resonance (DARR) (61, 62) and Second-order Hamiltonian among Analogous Nuclei Generated by Hetero-nuclear Assistance Irradiation (SHANGHAI) (63) correlation spectra with different mixing times (15 to 800 ms) were recorded on the 700 MHz instrument. For these experiments, the MAS frequency was stabilized at 12 kHz (± 2 Hz).

Bidimensional (2D ^{15}N-^{13}C hNhhC, 500 µs HH mixing time) and monodimensional (zTEDOR, 10 ms mixing time) nitrogen and carbon correlation spectra were recorded on a Bruker AvanceIII spectrometer operating at 800 MHz (19 T, 201.2 MHz ^{13}C Larmor frequency) equipped with Bruker 3.2 mm Efree NCH probe-head. The spectra were recorded at 16 kHz (± 2 Hz) MAS frequency; the number of scans was 2048 for the bidimensional and 10240 or 40960 (according to the fibril amount) for the monodimensional experiments, respectively.

In all cases, ^{1}H decoupling was applied at 80-100 kHz (optimized on the basis of the $^{13}C'$ echo lifetime (64)) using sw_fTPPM (65–67). During the experiments, the sample was cooled by a dry, cold air flow (> 935 L/h), and the effective sample temperature was estimated to be ~283 K (57).

Spectra were analyzed by the program CARA (Computer Aided Resonance Assignment, ETH Zurich) (68).

SS-NMR data analysis and structural modeling.

Sequential assignment of the new species present in the Aβ(1-42):Aβ(1-40) mixed fibrils, where either Aβ(1-40) or Aβ(1-42) was ^{13}C, ^{15}N-uniformly enriched, was performed using the same procedure for both samples, starting from the identification of the residues 31Ile-32Ile. These two consecutive residues can be identified following the signals of the two sidechains, which can be easily

distinguished in the 2D ^{13}C-^{13}C correlation spectra. Starting from these residues, the sequential assignment was obtained by analyzing the 3D ^{15}N ^{13}C spectra according to the procedure reported in (29). The secondary structure was predicted by TALOS+ (69) using the chemical shifts of the N, C, Cα and Cβ.

For model building, the length of the β_1 and β_2 strands was based on the secondary structure predicted by TALOS+. The β_1- and β_2-strands were then docked to one another by HADDOCK (45) using all the experimental long-range β_1-β_2 restraints. HADDOCK calculations were performed on the WeNMR GRID (http://www.wenmr.eu/, Guru interface, see supporting information for details).

The β-sheets were then generated by duplicating the β_1 and β_2 strands along the direction of the backbone N-H and C=O bonds with PYMOL, using the inter-strand distance of 4.8 Å (70), typical of the parallel register (see Results section). Eight β-strands for each β_1 and β_2 sheets were generated, considering for the β_2-sheet an interlaced arrangement of the Aβ(1-40) and Aβ(1-42) monomers.

The turn regions were randomly generated using MODELLER (71) and the final one was selected from the resulting pool of 50 structures.

The inter-protofilament structural models were generated by docking calculations starting from two β_2-sheets belonging to two different protofilaments, and imposing non-crystallographic symmetry restraints between the two β_2-sheets (see supporting information for details).

ACKNOWLEDGEMENTS

This research activity has been supported by EC funding initiative ERA-NET NEURON ABETA ID (“Novel Methods and Approaches towards the Understanding of Brain Diseases”), funded by the German Federal Ministry for Education and Research (BMBF), grant no. 01W1301, by the Fonds voor Wetenschappelijk Onderzoek (FWO) and the italian Ministero della Salute.

Support has been provided also by: Ente Cassa di Risparmio di Firenze, MIUR PRIN 2012SK7ASN, the University of Florence CERM-TT Regione Toscana PAR FAS 2007-2013, and Instruct, part of the European Strategy Forum on Research Infrastructures (ESFRI) and supported by national member

subscriptions. Specifically, we thank the EU ESFRI Instruct Core Centre CERM, Italy.

BDS is supported by the Fonds voor Wetenschappelijk Onderzoek (FWO), the KU Leuven and VIB, a Methusalem grant of the KU Leuven/Flemish Government. BDS is supported by the Bax-Vanluffelen Chair for Alzheimer's Disease and "Opening the Future" of the Leuven Universiteit Fonds (LUF).

The research leading to these results has received funding from the Helmholtz Validation Fund grant no. HVF-0013 "Enabling Technologies for Drug Discovery against Protein Misfolding Diseases" by the Helmholtz Association, Germany and the Berlin Institute of Health Collaborative Research Grant no. 1.1.2.a.3 "Elucidating the proteostasis network to control Alzheimer's disease", funded by the BMBF.

1. Annaert W, De Strooper B (2002) A cell biological perspective on Alzheimer's disease. *Annu Rev Cell Dev Biol* 18:25–51.
2. Chiti F, Dobson CM (2006) Protein Misfolding, Functional Amyloid, and Human Disease. *Annu Rev Biochem* 75(1):333–366.

3. Sipe JD, Cohen AS (2000) Review: History of the Amyloid Fibril. *J Struct Biol* 130(2–3):88–98.

4. Querfurth HW, LaFerla FM (2010) Alzheimer's Disease. *N Engl J Med* 362(4):329–344.

5. Roher AE, et al. (1993) beta-Amyloid-(1-42) is a major component of cerebrovascular amyloid deposits: implications for the pathology of Alzheimer disease. *Proc Natl Acad Sci U S A* 90(22):10836–10840.

6. Roher AE, et al. (1993) Structural alterations in the peptide backbone of beta-amyloid core protein may account for its deposition and stability in Alzheimer's disease. *J Biol Chem* 268(5):3072–3083.

7. Qi-Takahara Y, et al. (2005) Longer forms of amyloid beta protein: implications for the mechanism of intramembrane cleavage by gamma-secretase. *J Neurosci Off J Soc Neurosci* 25(2):436–445.

8. Bolduc DM, Wolfe MS (2014) Structure of nicastrin unveils secrets of γ-secretase. *Proc Natl Acad Sci* 111(41):14643–14644.

9. Bolduc DM, Montagna DR, Seghers MC, Wolfe MS, Selkoe DJ (2016) The amyloid-beta forming tripeptide cleavage mechanism of γ-secretase. *eLife* 5:e17578.

10. Colletier J-P, et al. (2011) Molecular basis for amyloid-beta polymorphism. *Proc Natl Acad Sci U S A* 108(41):16938–16943.

11. Brorsson A-C, et al. (2010) Intrinsic Determinants of Neurotoxic Aggregate Formation by the Amyloid β Peptide. *Biophys J* 98(8):1677–1684.

12. Jan A, Gokce O, Luthi-Carter R, Lashuel HA (2008) The Ratio of Monomeric to Aggregated Forms of Aβ40 and Aβ42 Is an Important Determinant of Amyloid-β Aggregation, Fibrillogenesis, and Toxicity. *J Biol Chem* 283(42):28176–28189.

13. Kuperstein I, et al. (2010) Neurotoxicity of Alzheimer's disease Aβ peptides is induced by small changes in the Aβ42 to Aβ40 ratio. *EMBO J* 29(19):3408–3420.

14. Duff K, et al. (1996) Increased amyloid-beta42(43) in brains of mice expressing mutant presenilin 1. *Nature* 383(6602):710–713.

15. Scheuner D, et al. (1996) Secreted amyloid β–protein similar to that in the senile plaques of Alzheimer's disease is increased in vivo by the presenilin 1 and 2 and APP mutations linked to familial Alzheimer's disease. *Nat Med* 2(8):864–870.

16. Szaruga M, et al. (2015) Qualitative changes in human γ-secretase underlie familial Alzheimer's disease. *J Exp Med* 212(12):2003–2013.

17. Chávez-Gutiérrez L, et al. (2012) The mechanism of γ-Secretase dysfunction in familial Alzheimer disease. *EMBO J* 31(10):2261–2274.

18. Pauwels K, et al. (2012) Structural basis for increased toxicity of pathological aβ42:aβ40 ratios in Alzheimer disease. *J Biol Chem* 287(8):5650–5660.

19. Yoshiike Y, Chui D-H, Akagi T, Tanaka N, Takashima A (2003) Specific compositions of amyloid-beta peptides as the determinant of toxic beta-aggregation. *J Biol Chem* 278(26):23648–23655.

20. Jan A, Hartley DM, Lashuel HA (2010) Preparation and characterization of toxic Aβ aggregates for structural and functional studies in Alzheimer's disease research. *Nat Protoc* 5(6):1186–1209.

21. Wang R, Wang B, He W, Zheng H (2006) Wild-type Presenilin 1 Protects against Alzheimer Disease Mutation-induced Amyloid Pathology. *J Biol Chem* 281(22):15330–15336.

22. Kim J, et al. (2007) Abeta40 inhibits amyloid deposition in vivo. *J Neurosci Off J Soc Neurosci* 27(3):627–633.

23. Cukalevski R, et al. (2015) The Aβ40 and Aβ42 peptides self-assemble into separate homomolecular fibrils in binary mixtures but cross-react during primary nucleation. *Chem Sci* 6(7):4215–4233.

24. Xiao Y, et al. (2015) Aβ(1-42) fibril structure illuminates self-recognition and replication of amyloid in Alzheimer's disease. *Nat Struct Mol Biol* advance online publication. doi:10.1038/nsmb.2991.

25. Colvin MT, et al. (2016) Atomic Resolution Structure of Monomorphic Aβ42 Amyloid Fibrils. *J Am Chem Soc*. doi:10.1021/jacs.6b05129.

26. Tycko R (2016) Alzheimer's disease: Structure of aggregates revealed. *Nature* advance online publication. doi:10.1038/nature19470.

27. Petkova AT, et al. (2002) A structural model for Alzheimer's β-amyloid fibrils based on experimental constraints from solid state NMR. *Proc Natl Acad Sci* 99(26):16742–16747.

28. Parthasarathy S, et al. (2011) Molecular-Level Examination of Cu2+ Binding Structure for Amyloid Fibrils of 40-Residue Alzheimer's ? by Solid-State NMR Spectroscopy. *J Am Chem Soc* 133(10):3390–3400.

29. Bertini I, Gonnelli L, Luchinat C, Mao J, Nesi A (2011) A new structural model of Aβ40 fibrils. *J Am Chem Soc* 133(40):16013–16022.

30. Lu J-X, et al. (2013) Molecular Structure of β-Amyloid Fibrils in Alzheimer's Disease Brain Tissue. *Cell* 154(6):1257–1268.

31. Bertini I, et al. (2013) Formation kinetics and structural features of Beta-amyloid aggregates by sedimented solute NMR. *Chembiochem Eur J Chem Biol* 14(14):1891–1897.

32. Bieschke J, et al. (2012) Small-molecule conversion of toxic oligomers to nontoxic β-sheet-rich amyloid fibrils. *Nat Chem Biol* 8(1):93–101.

33. Tycko R (2014) Physical and structural basis for polymorphism in amyloid fibrils. *Protein Sci Publ Protein Soc* 23(11):1528–1539.

34. Lopez del Amo JM, et al. (2012) An Asymmetric Dimer as the Basic Subunit in Alzheimer's Disease Amyloid β Fibrils. *Angew Chem Int Ed* 51(25):6136–6139.

35. Bera S, et al. (2016) Biophysical insights into the membrane interaction of the core amyloid-forming Aβ40 fragment K16-K28 and its role in the pathogenesis of Alzheimer's disease. *Phys Chem Chem Phys PCCP* 18(25):16890–16901.

36. Wälti MA, et al. (2016) Atomic-resolution structure of a disease-relevant Aβ(1–42) amyloid fibril. *Proc Natl Acad Sci*:201600749.

37. Colvin MT, et al. (2015) High Resolution Structural Characterization of Aβ42 Amyloid Fibrils by MAS NMR. *J Am Chem Soc*. doi:10.1021/jacs.5b03997.

38. Ravotti F, et al. (2016) Solid-state NMR sequential assignment of an Amyloid-β(1–42) fibril polymorph. *Biomol NMR Assign*:1–8.

39. Schreck JS, Yuan J-M (2013) A Kinetic Study of Amyloid Formation: Fibril Growth and Length Distributions. *J Phys Chem B* 117(21):6574–6583.

40. Petkova AT, Yau W-M, Tycko R (2006) Experimental Constraints on Quaternary Structure in Alzheimer's β-Amyloid Fibrils†. *Biochemistry (Mosc)* 45(2):498–512.

41. Paravastu AK, Leapman RD, Yau W-M, Tycko R (2008) Molecular structural basis for polymorphism in Alzheimer's β-amyloid fibrils. *Proc Natl Acad Sci* 105(47):18349–18354.

42. Ahmed M, et al. (2010) Structural conversion of neurotoxic amyloid-beta(1-42) oligomers to fibrils. *Nat Struct Mol Biol* 17(5):561–567.

43. Qiang W, Yau W-M, Luo Y, Mattson MP, Tycko R (2012) Antiparallel β-sheet architecture in Iowa-mutant β-amyloid fibrils. *Proc Natl Acad Sci U S A* 109(12):4443–4448.

44. Nielsen JT, et al. (2009) Unique identification of supramolecular structures in amyloid fibrils by solid-state NMR spectroscopy. *Angew Chem Int Ed Engl* 48(12):2118–2121.

45. de Vries SJ, van Dijk M, Bonvin AMJJ (2010) The HADDOCK web server for data-driven biomolecular docking. *Nat Protoc* 5(5):883–897.

46. LeVine H (1993) Thioflavine T interaction with synthetic Alzheimer's disease beta-amyloid peptides: detection of amyloid aggregation in solution. *Protein Sci Publ Protein Soc* 2(3):404–410.

47. Stöhr J, et al. (2014) Distinct synthetic Aβ prion strains producing different amyloid deposits in bigenic mice. *Proc Natl Acad Sci U S A* 111(28):10329–10334.

48. Petkova AT, et al. (2005) Self-Propagating, Molecular-Level Polymorphism in Alzheimer's ß-Amyloid Fibrils. *Science* 307(5707):262–265.

49. Gu L, Guo Z (2013) Alzheimer's Aβ42 and Aβ40 peptides form interlaced amyloid fibrils. *J Neurochem* 126(3):305–311.

50. Walsh DM, et al. (2009) A facile method for expression and purification of the Alzheimer's disease-associated amyloid beta-peptide. *FEBS J* 276(5):1266–1281.

51. Szczepankiewicz O, et al. (2015) N-terminal extensions retard Aβ42 fibril formation but allow cross-seeding and co-aggregation with Aβ42. *J Am Chem Soc*. doi:10.1021/jacs.5b07849.

52. Marley J, Lu M, Bracken C (2001) A method for efficient isotopic labeling of recombinant proteins. *J Biomol NMR* 20(1):71–75.

53. Hellstrand E, Boland B, Walsh DM, Linse S (2009) Amyloid ?-Protein Aggregation Produces Highly Reproducible Kinetic Data and Occurs by a Two-Phase Process. *ACS Chem Neurosci* 1(1):13–18.

54. Jan A, Gokce O, Luthi-Carter R, Lashuel HA (2008) The Ratio of Monomeric to Aggregated Forms of Aβ40 and Aβ42 Is an Important Determinant of Amyloid-β Aggregation, Fibrillogenesis, and Toxicity. *J Biol Chem* 283(42):28176–28189.

55. Walsh DM, et al. (1999) Amyloid β-Protein Fibrillogenesis STRUCTURE AND BIOLOGICAL ACTIVITY OF PROTOFIBRILLAR INTERMEDIATES. *J Biol Chem* 274(36):25945–25952.

56. Bertini I, et al. (2012) On the use of ultracentrifugal devices for sedimented solute NMR. *J Biomol NMR* 54(2):123–127.

57. Böckmann A, et al. (2009) Characterization of different water pools in solid-state NMR protein samples. *J Biomol NMR* 45(3):319–327.

58. Schuetz A, et al. (2010) Protocols for the Sequential Solid-State NMR Spectroscopic Assignment of a Uniformly Labeled 25 kDa Protein: HET-s(1-227). *ChemBioChem* 11(11):1543–1551.

59. Loening NM, Bjerring M, Nielsen NC, Oschkinat H (2012) A comparison of NCO and NCA transfer methods for biological solid-state NMR spectroscopy. *J Magn Reson* 214:81–90.

60. Loening NM, Bjerring M, Nielsen NC, Oschkinat H (2012) A comparison of NCO and NCA transfer methods for biological solid-state NMR spectroscopy. *J Magn Reson San Diego Calif 1997* 214(1):81–90.

61. Takegoshi K, Nakamura S, Terao T (2003) 13C–1H dipolar-driven 13C–13C recoupling without 13C rf irradiation in nuclear magnetic resonance of rotating solids. *J Chem Phys* 118(5):2325–2341.

62. Takegoshi K, Nakamura S, Terao T (2001) 13C–1H dipolar-assisted rotational resonance in magic-angle spinning NMR. *Chem Phys Lett* 344(5–6):631–637.

63. Hu B, Lafon O, Trébosc J, Chen Q, Amoureux J-P (2011) Broad-band homo-nuclear correlations assisted by 1H irradiation for bio-molecules in very high magnetic field at fast and ultra-fast MAS frequencies. *J Magn Reson* 212(2):320–329.

64. Rothwell WP, Waugh JS (1981) Transverse relaxation of dipolar coupled spin systems under rf irradiation: Detecting motions in solids. *J Chem Phys* 74(5):2721–2732.

65. Thakur RS, Kurur ND, Madhu PK (2006) Swept-frequency two-pulse phase modulation for heteronuclear dipolar decoupling in solid-state NMR. *Chem Phys Lett* 426(4–6):459–463.

66. Thakur RS, Kurur ND, Madhu PK (2008) An experimental study of decoupling sequences for multiple-quantum and high-resolution MAS experiments in solid-state NMR. *Magn Reson Chem MRC* 46(2):166–169.

67. Thakur RS, Kurur ND, Madhu PK (2008) An analysis of phase-modulated heteronuclear dipolar decoupling sequences in solid-state nuclear magnetic resonance. *J Magn Reson San Diego Calif 1997* 193(1):77–88.

68. Keller R (2004) *The Computer Aided Resonance Assignment Tutorial (CARA)* (CANTINA Verlag).

69. Shen Y, Delaglio F, Cornilescu G, Bax A (2009) TALOS+: a hybrid method for predicting protein backbone torsion angles from NMR chemical shifts. *J Biomol NMR* 44(4):213–223.

70. Kirschner DA, Abraham C, Selkoe DJ (1986) X-ray diffraction from intraneuronal paired helical filaments and extraneuronal amyloid fibers in Alzheimer disease indicates cross-beta conformation. *Proc Natl Acad Sci U S A* 83(2):503–507.

71. Fiser A, Šali A (2003) Modeller: Generation and Refinement of Homology-Based Protein Structure Models. *Methods in Enzymology*, Macromolecular Crystallography, Part D., ed Charles W. Carter J and RMS (Academic Press), pp 461–491.

Figures:

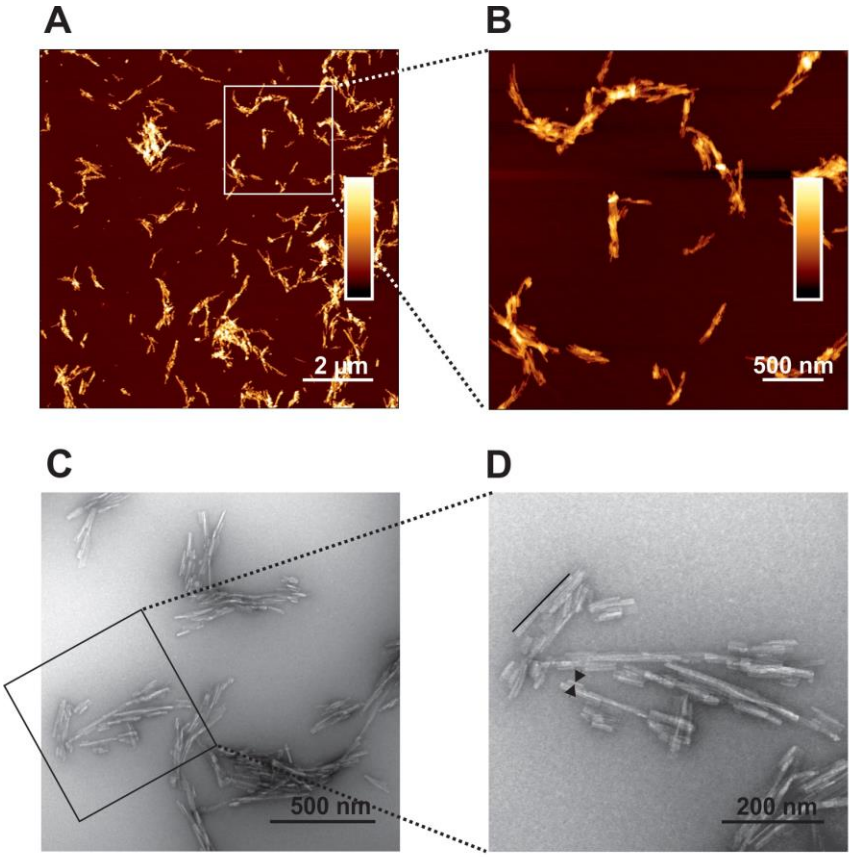

Figure 1. Analysis of 1:1 Aβ(1-42):Aβ(1-40) mixed fibrils by AFM (A, B) and TEM (C, D). B) and D) show a detail from A and C in higher magnification (see frames). A) and B) color gradient: 0-40 nm height. D) The line and the arrow heads illustrate how the length and breadth of fibrils were determined. For length determination 592 fibrils have been measured which show an average length of 106,61 nm (SD = 54,75). For breadth determination 244 fibrils have been analysed which show an average breadth of 3.25 nm (SD = 0,67).

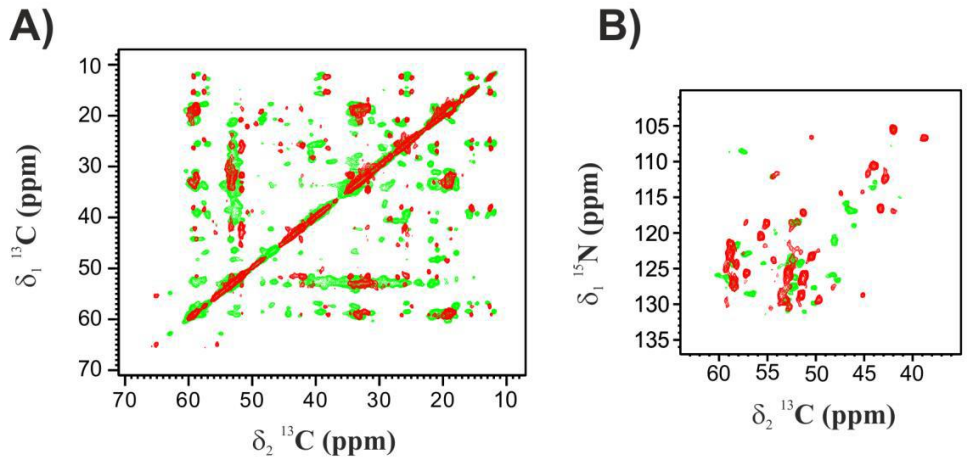

Figure 2. A) 2D ^{13}C-^{13}C-SHANGHAI spectrum of the Aβ1-42:Aβ1-40 mixed fibrils in the 1:1 molar ratio (green) overlaid with the 2D ^{13}C-^{13}C-DARR spectrum of fibrils of pure Aβ1-40 (red). Magnetic field: 700 MHz (16.4 T), dimension of rotor: 3.2 mm (~14 mg of fibrils), 12 kHz spinning, 100 kHz ^{1}H decoupling, B) 2D ^{15}N-^{13}C NCA spectrum of the Aβ1-42:Aβ1-40 mixed fibrils in the 1:1 molar ratio (green) overlaid with the 2D ^{15}N-^{13}C NCA spectrum of fibrils of pure Aβ1-40 (red). Magnetic field: 700 MHz (16.4 T), dimension of rotor: 3.2 mm (~14 mg of fibrils), 14 kHz spinning, 100 kHz ^{1}H decoupling.

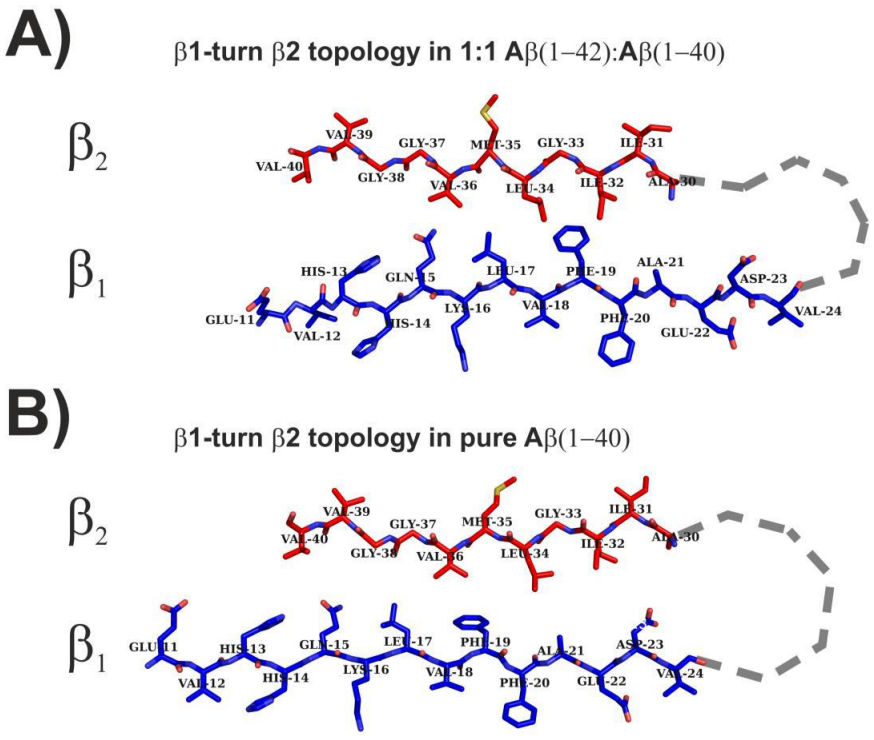

Figure 3. Folding of the monomeric Aβ1-40 peptide in the model of 1:1 Aβ1-42:Aβ1-40 mixed fibrils (A) and in the model obtained for the fibrils of pure Aβ1-40 (29) (B).

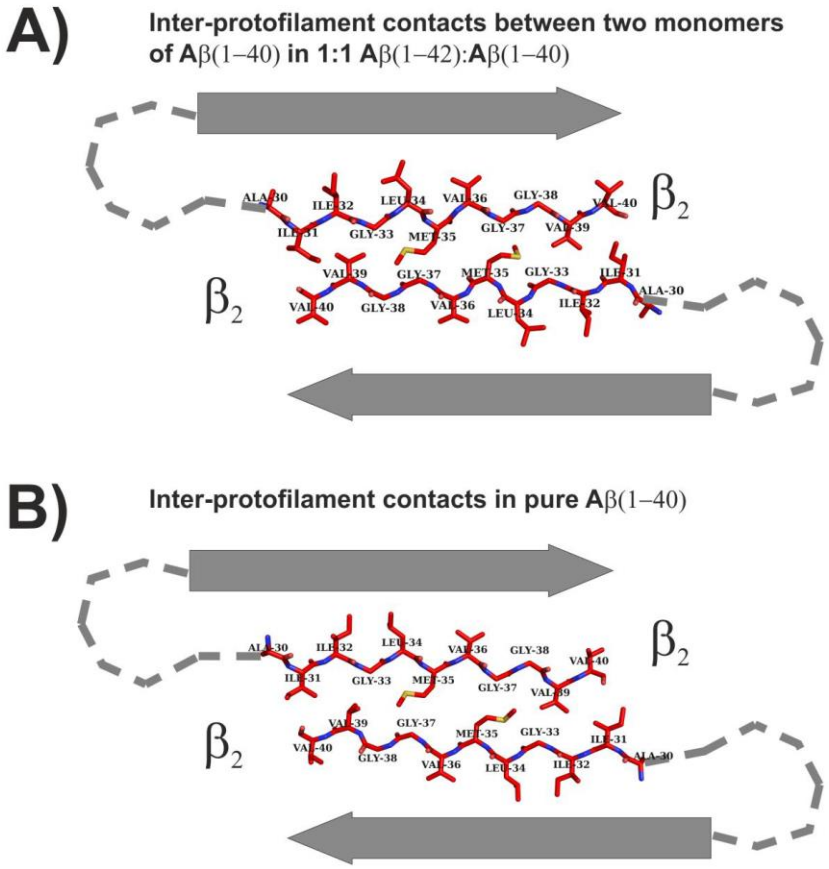

Figure 4. Lateral packing of two different protofilaments in the model of 1:1 Aβ1-42:Aβ1-40 mixed fibrils (A) and in the model of the fibrils of pure Aβ1-40 (29) (B).

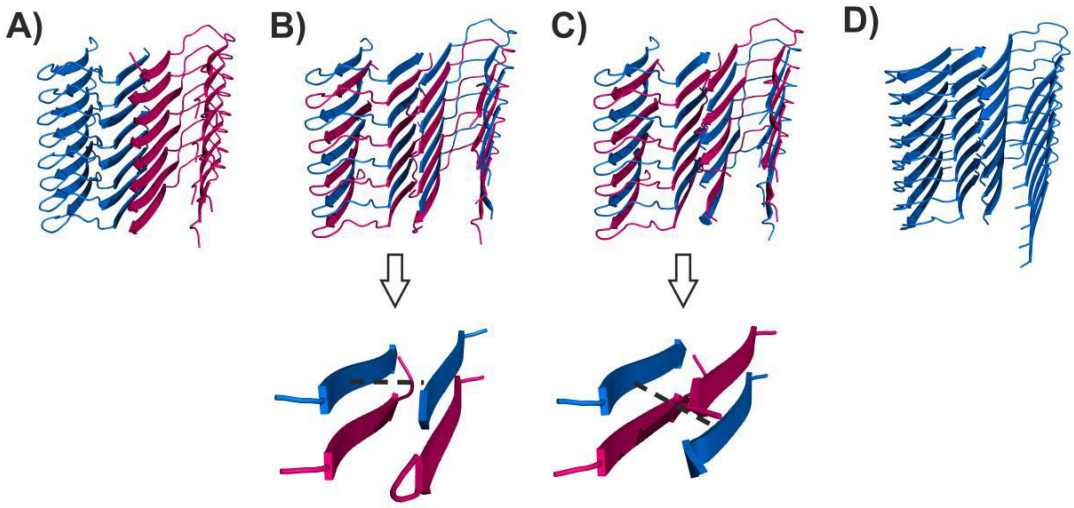

Figure 5. Structural models of the three possible reciprocal packing modes of Aβ1-40 and Aβ1-42 polypeptides in the mixed fibrils (panel A, B, C). The Aβ1-42 polypeptide is colored magenta and the Aβ1-40 polypeptide in blue. The model of pure Aβ1-40 fibrils is also displayed (panel D).

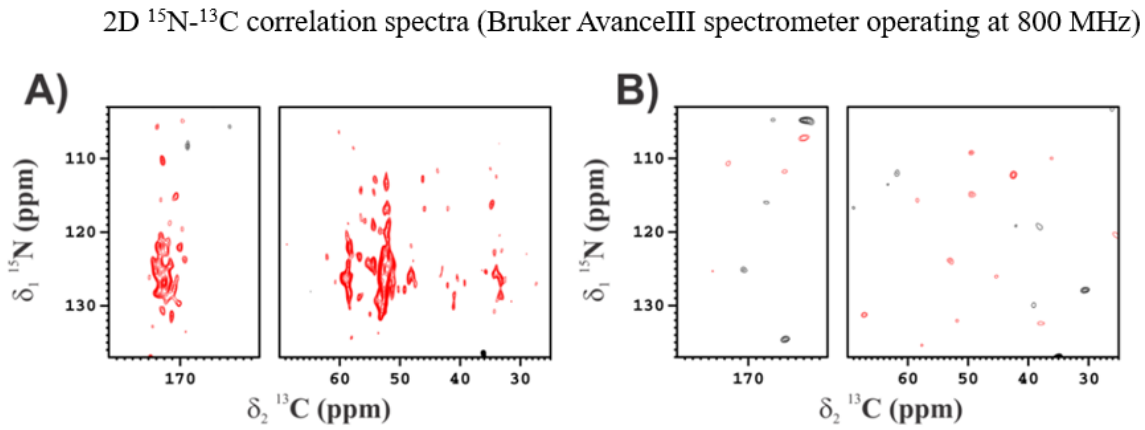

Figure 6. 2D ^{15}N-^{13}C hNhhC spectra of the Aβ1-42:Aβ1-40 mixed fibrils in the 1:1 molar ratio, where A) Aβ1-42 is ^{15}N-enriched and Aβ1-40 is ^{13}C- enriched, B) Aβ1-42 is ^{15}N-enriched and Aβ1-40 is in natural abundance. Magnetic field: 800 MHz (19 T, 201.2 MHz ^{13}C Larmor frequency), dimension of rotor: 3.2 mm, 16 kHz spinning, 80 kHz ^{1}H decoupling; number of scans: 2048.

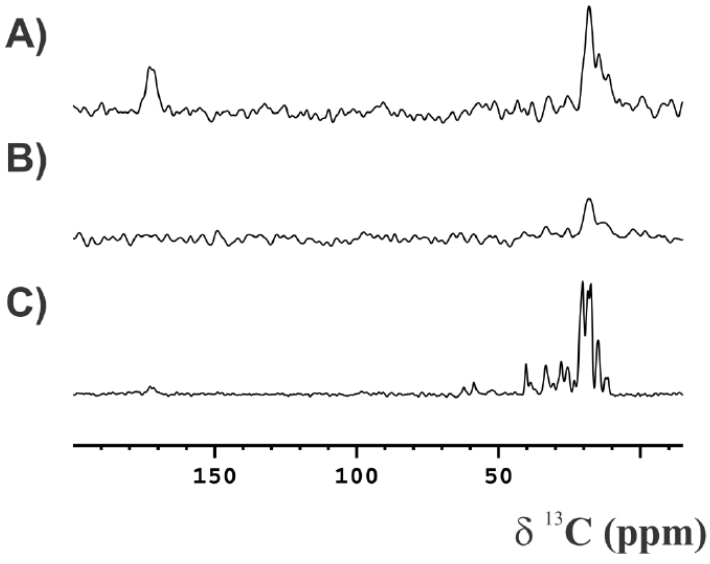

Figure 7. 1D zTEDOR spectra of the Aβ1-42:Aβ1-40 mixed fibrils in the 1:1 molar ratio, where A) Aβ1-42 is ^{15}N-enriched and Aβ1-40 is ^{13}C-enriched and B) Aβ1-42 is ^{15}N-enriched and Aβ1-40 is in natural abundance, and C) Aβ1-42 is in natural abundance and Aβ1-40 is ^{15}N-^{13}C-enriched. Magnetic field: 800 MHz (19 T, 201.2 MHz ^{13}C Larmor frequency), dimension of rotor: 3.2 mm, 16 kHz spinning, 80 kHz ^{1}H decoupling. The number of scans was tuned according to the sample amount (10240, for sample A and C, and 40960 for sample B).

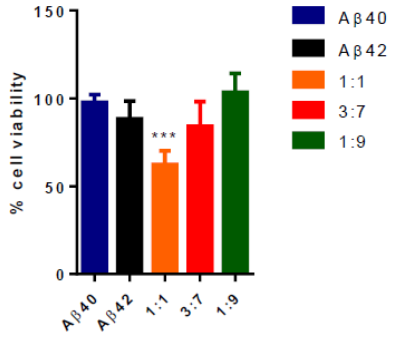

Figure 8

Figure 8. Viability of primary hippocampal neurons after treatment with 10 µM of pre-aggregated pure Aβ1-40, Aβ1-42, and mixture of Aβ1-42:Aβ1-40 peptides in different ratios.

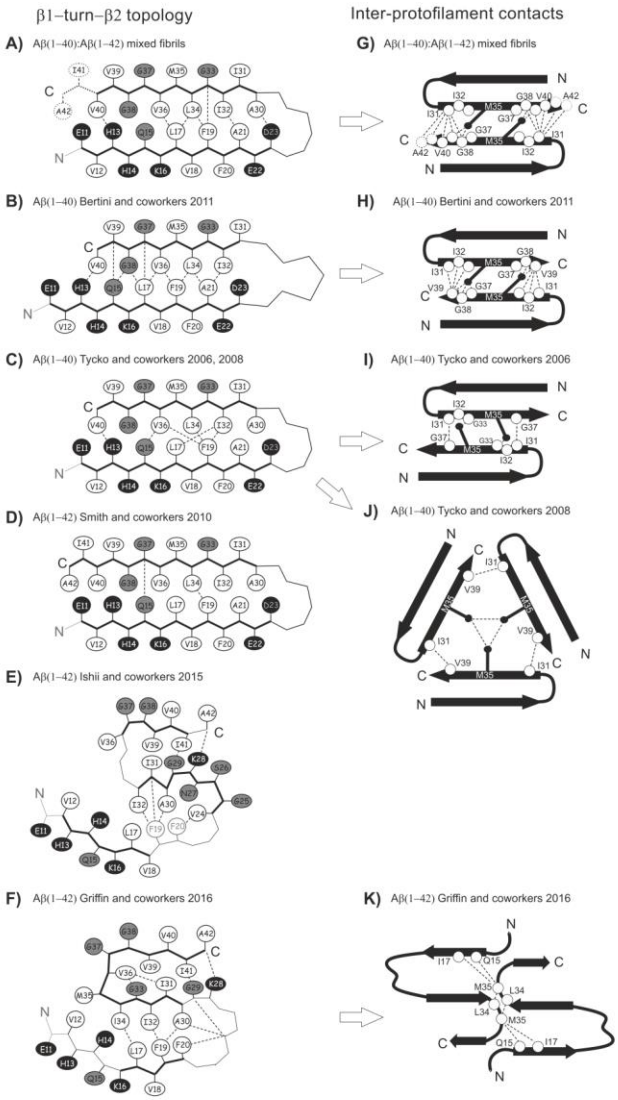

Scheme 1. Different β-strand zippers in various SS-NMR-derived structural models of Aβ fibrils. The topologies of the β_1-turn-β_2 motif identified in the present work (A) and in other previously studied Aβ1-40 fibrils (B, C) (29, 40, 41) and Aβ1-42 fibrils (D, E, F) (24, 25, 42) are shown in the left column. The dashed/dotted lines represent unambiguous experimental restraints used to derive the corresponding topology. In the schematic description of distinct structures of the U-shaped motif, the hydrophobic, acidic/basic, and other types of residues are shown in white, black, and gray, respectively. The topologies of the interprotofilament interface (β_2-β_2 zippers) in the fibrils determined in the present work (G) and proposed in previous studies (H, I, J, K) (25, 29, 40, 41) are shown in the right column. The dashed lines represent unambiguous experimental restraints used to derive the corresponding topology. The filled black circles represent the Cε of the Met35 residue. Other residues included in SS-NMR-observed structural restraints for linking the two β_2-strands are shown as hollow circles. Residues Ile41 and Ala42, in the present model of the mixed fibrils, are indicated with dashed circles to stress that both Aβ1-40 and Aβ1-42 share the same arrangement.

References

1. Annaert W, De Strooper B (2002) A cell biological perspective on Alzheimer's disease. *Annu Rev Cell Dev Biol* 18:25–51.
2. Chiti F, Dobson CM (2006) Protein Misfolding, Functional Amyloid, and Human Disease. *Annu Rev Biochem* 75(1):333–366.
3. Sipe JD, Cohen AS (2000) Review: History of the Amyloid Fibril. *J Struct Biol* 130(2–3):88–98.
4. Querfurth HW, LaFerla FM (2010) Alzheimer's Disease. *N Engl J Med* 362(4):329–344.
5. Roher AE, et al. (1993) beta-Amyloid-(1-42) is a major component of cerebrovascular amyloid deposits: implications for the pathology of Alzheimer disease. *Proc Natl Acad Sci U S A* 90(22):10836–10840.
6. Roher AE, et al. (1993) Structural alterations in the peptide backbone of beta-amyloid core protein may account for its deposition and stability in Alzheimer's disease. *J Biol Chem* 268(5):3072–3083.
7. Qi-Takahara Y, et al. (2005) Longer forms of amyloid beta protein: implications for the mechanism of intramembrane cleavage by gamma-secretase. *J Neurosci Off J Soc Neurosci* 25(2):436–445.
8. Bolduc DM, Wolfe MS (2014) Structure of nicastrin unveils secrets of γ-secretase. *Proc Natl Acad Sci* 111(41):14643–14644.
9. Bolduc DM, Montagna DR, Seghers MC, Wolfe MS, Selkoe DJ (2016) The amyloid-beta forming tripeptide cleavage mechanism of γ-secretase. *eLife* 5:e17578.
10. Colletier J-P, et al. (2011) Molecular basis for amyloid-beta polymorphism. *Proc Natl Acad Sci U S A* 108(41):16938–16943.
11. Brorsson A-C, et al. (2010) Intrinsic Determinants of Neurotoxic Aggregate Formation by the Amyloid β Peptide. *Biophys J* 98(8):1677–1684.
12. Jan A, Gokce O, Luthi-Carter R, Lashuel HA (2008) The Ratio of Monomeric to Aggregated Forms of Aβ40 and Aβ42 Is an Important Determinant of Amyloid-β Aggregation, Fibrillogenesis, and Toxicity. *J Biol Chem* 283(42):28176–28189.
13. Kuperstein I, et al. (2010) Neurotoxicity of Alzheimer's disease Aβ peptides is induced by small changes in the Aβ42 to Aβ40 ratio. *EMBO J* 29(19):3408–3420.
14. Duff K, et al. (1996) Increased amyloid-beta42(43) in brains of mice expressing mutant presenilin 1. *Nature* 383(6602):710–713.
15. Scheuner D, et al. (1996) Secreted amyloid β–protein similar to that in the senile plaques of Alzheimer's disease is increased in vivo by the presenilin 1 and 2 and APP mutations linked to familial Alzheimer's disease. *Nat Med* 2(8):864–870.
16. Szaruga M, et al. (2015) Qualitative changes in human γ-secretase underlie familial Alzheimer's disease. *J Exp Med* 212(12):2003–2013.
17. Chávez-Gutiérrez L, et al. (2012) The mechanism of γ-Secretase dysfunction in familial Alzheimer disease. *EMBO J* 31(10):2261–2274.
18. Pauwels K, et al. (2012) Structural basis for increased toxicity of pathological aβ42:aβ40 ratios in Alzheimer disease. *J Biol Chem* 287(8):5650–5660.
19. Yoshiike Y, Chui D-H, Akagi T, Tanaka N, Takashima A (2003) Specific compositions of amyloid-beta peptides as the determinant of toxic beta-aggregation. *J Biol Chem* 278(26):23648–23655.
20. Jan A, Hartley DM, Lashuel HA (2010) Preparation and characterization of toxic Aβ aggregates for structural and functional studies in Alzheimer's disease research. *Nat Protoc* 5(6):1186–1209.
21. Wang R, Wang B, He W, Zheng H (2006) Wild-type Presenilin 1 Protects against Alzheimer Disease Mutation-induced Amyloid Pathology. *J Biol Chem* 281(22):15330–15336.
22. Kim J, et al. (2007) Abeta40 inhibits amyloid deposition in vivo. *J Neurosci Off J Soc Neurosci* 27(3):627–633.
23. Cukalevski R, et al. (2015) The Aβ40 and Aβ42 peptides self-assemble into separate homomolecular fibrils in binary mixtures but cross-react during primary nucleation. *Chem Sci* 6(7):4215–4233.
24. Xiao Y, et al. (2015) Aβ1-42 fibril structure illuminates self-recognition and replication of amyloid in Alzheimer's disease. *Nat Struct Mol Biol* advance online publication. doi:10.1038/nsmb.2991.
25. Colvin MT, et al. (2016) Atomic Resolution Structure of Monomorphic Aβ42 Amyloid Fibrils. *J Am Chem Soc*. doi:10.1021/jacs.6b05129.

26. Tycko R (2016) Alzheimer's disease: Structure of aggregates revealed. *Nature* advance online publication. doi:10.1038/nature19470.
27. Petkova AT, et al. (2002) A structural model for Alzheimer's β-amyloid fibrils based on experimental constraints from solid state NMR. *Proc Natl Acad Sci* 99(26):16742–16747.
28. Parthasarathy S, et al. (2011) Molecular-Level Examination of Cu2+ Binding Structure for Amyloid Fibrils of 40-Residue Alzheimer's ? by Solid-State NMR Spectroscopy. *J Am Chem Soc* 133(10):3390–3400.
29. Bertini I, Gonnelli L, Luchinat C, Mao J, Nesi A (2011) A new structural model of Aβ40 fibrils. *J Am Chem Soc* 133(40):16013–16022.
30. Lu J-X, et al. (2013) Molecular Structure of β-Amyloid Fibrils in Alzheimer's Disease Brain Tissue. *Cell* 154(6):1257–1268.
31. Bertini I, et al. (2013) Formation kinetics and structural features of Beta-amyloid aggregates by sedimented solute NMR. *Chembiochem Eur J Chem Biol* 14(14):1891–1897.
32. Bieschke J, et al. (2012) Small-molecule conversion of toxic oligomers to nontoxic β-sheet-rich amyloid fibrils. *Nat Chem Biol* 8(1):93–101.
33. Tycko R (2014) Physical and structural basis for polymorphism in amyloid fibrils. *Protein Sci Publ Protein Soc* 23(11):1528–1539.
34. Lopez del Amo JM, et al. (2012) An Asymmetric Dimer as the Basic Subunit in Alzheimer's Disease Amyloid β Fibrils. *Angew Chem Int Ed* 51(25):6136–6139.
35. Bera S, et al. (2016) Biophysical insights into the membrane interaction of the core amyloid-forming Aβ40 fragment K16-K28 and its role in the pathogenesis of Alzheimer's disease. *Phys Chem Chem Phys PCCP* 18(25):16890–16901.
36. Wälti MA, et al. (2016) Atomic-resolution structure of a disease-relevant Aβ(1–42) amyloid fibril. *Proc Natl Acad Sci*:201600749.
37. Colvin MT, et al. (2015) High Resolution Structural Characterization of Aβ42 Amyloid Fibrils by MAS NMR. *J Am Chem Soc*. doi:10.1021/jacs.5b03997.
38. Ravotti F, et al. (2016) Solid-state NMR sequential assignment of an Amyloid-β(1–42) fibril polymorph. *Biomol NMR Assign*:1–8.
39. Schreck JS, Yuan J-M (2013) A Kinetic Study of Amyloid Formation: Fibril Growth and Length Distributions. *J Phys Chem B* 117(21):6574–6583.
40. Petkova AT, Yau W-M, Tycko R (2006) Experimental Constraints on Quaternary Structure in Alzheimer's β-Amyloid Fibrils†. *Biochemistry (Mosc)* 45(2):498–512.
41. Paravastu AK, Leapman RD, Yau W-M, Tycko R (2008) Molecular structural basis for polymorphism in Alzheimer's β-amyloid fibrils. *Proc Natl Acad Sci* 105(47):18349–18354.
42. Ahmed M, et al. (2010) Structural conversion of neurotoxic amyloid-beta(1-42) oligomers to fibrils. *Nat Struct Mol Biol* 17(5):561–567.
43. Qiang W, Yau W-M, Luo Y, Mattson MP, Tycko R (2012) Antiparallel β-sheet architecture in Iowa-mutant β-amyloid fibrils. *Proc Natl Acad Sci U S A* 109(12):4443–4448.
44. Nielsen JT, et al. (2009) Unique identification of supramolecular structures in amyloid fibrils by solid-state NMR spectroscopy. *Angew Chem Int Ed Engl* 48(12):2118–2121.
45. de Vries SJ, van Dijk M, Bonvin AMJJ (2010) The HADDOCK web server for data-driven biomolecular docking. *Nat Protoc* 5(5):883–897.
46. LeVine H (1993) Thioflavine T interaction with synthetic Alzheimer's disease beta-amyloid peptides: detection of amyloid aggregation in solution. *Protein Sci Publ Protein Soc* 2(3):404–410.
47. Stöhr J, et al. (2014) Distinct synthetic Aβ prion strains producing different amyloid deposits in bigenic mice. *Proc Natl Acad Sci U S A* 111(28):10329–10334.
48. Petkova AT, et al. (2005) Self-Propagating, Molecular-Level Polymorphism in Alzheimer's ß-Amyloid Fibrils. *Science* 307(5707):262–265.
49. Gu L, Guo Z (2013) Alzheimer's Aβ42 and Aβ40 peptides form interlaced amyloid fibrils. *J Neurochem* 126(3):305–311.
50. Walsh DM, et al. (2009) A facile method for expression and purification of the Alzheimer's disease-associated amyloid beta-peptide. *FEBS J* 276(5):1266–1281.
51. Szczepankiewicz O, et al. (2015) N-terminal extensions retard Aβ42 fibril formation but allow cross-seeding and co-aggregation with Aβ42. *J Am Chem Soc*. doi:10.1021/jacs.5b07849.
52. Marley J, Lu M, Bracken C (2001) A method for efficient isotopic labeling of recombinant proteins. *J Biomol NMR* 20(1):71–75.
53. Hellstrand E, Boland B, Walsh DM, Linse S (2009) Amyloid ?-Protein Aggregation Produces Highly Reproducible Kinetic Data and Occurs by a Two-Phase Process. *ACS Chem Neurosci* 1(1):13–18.

54. Jan A, Gokce O, Luthi-Carter R, Lashuel HA (2008) The Ratio of Monomeric to Aggregated Forms of Aβ40 and Aβ42 Is an Important Determinant of Amyloid-β Aggregation, Fibrillogenesis, and Toxicity. *J Biol Chem* 283(42):28176–28189.
55. Walsh DM, et al. (1999) Amyloid β-Protein Fibrillogenesis STRUCTURE AND BIOLOGICAL ACTIVITY OF PROTOFIBRILLAR INTERMEDIATES. *J Biol Chem* 274(36):25945–25952.
56. Bertini I, et al. (2012) On the use of ultracentrifugal devices for sedimented solute NMR. *J Biomol NMR* 54(2):123–127.
57. Böckmann A, et al. (2009) Characterization of different water pools in solid-state NMR protein samples. *J Biomol NMR* 45(3):319–327.
58. Schuetz A, et al. (2010) Protocols for the Sequential Solid-State NMR Spectroscopic Assignment of a Uniformly Labeled 25 kDa Protein: HET-s(1-227). *ChemBioChem* 11(11):1543–1551.
59. Loening NM, Bjerring M, Nielsen NC, Oschkinat H (2012) A comparison of NCO and NCA transfer methods for biological solid-state NMR spectroscopy. *J Magn Reson* 214:81–90.
60. Loening NM, Bjerring M, Nielsen NC, Oschkinat H (2012) A comparison of NCO and NCA transfer methods for biological solid-state NMR spectroscopy. *J Magn Reson San Diego Calif 1997* 214(1):81–90.
61. Takegoshi K, Nakamura S, Terao T (2003) 13C–1H dipolar-driven 13C–13C recoupling without 13C rf irradiation in nuclear magnetic resonance of rotating solids. *J Chem Phys* 118(5):2325–2341.
62. Takegoshi K, Nakamura S, Terao T (2001) 13C–1H dipolar-assisted rotational resonance in magic-angle spinning NMR. *Chem Phys Lett* 344(5–6):631–637.
63. Hu B, Lafon O, Trébosc J, Chen Q, Amoureux J-P (2011) Broad-band homo-nuclear correlations assisted by 1H irradiation for bio-molecules in very high magnetic field at fast and ultra-fast MAS frequencies. *J Magn Reson* 212(2):320–329.
64. Rothwell WP, Waugh JS (1981) Transverse relaxation of dipolar coupled spin systems under rf irradiation: Detecting motions in solids. *J Chem Phys* 74(5):2721–2732.
65. Thakur RS, Kurur ND, Madhu PK (2006) Swept-frequency two-pulse phase modulation for heteronuclear dipolar decoupling in solid-state NMR. *Chem Phys Lett* 426(4–6):459–463.
66. Thakur RS, Kurur ND, Madhu PK (2008) An experimental study of decoupling sequences for multiple-quantum and high-resolution MAS experiments in solid-state NMR. *Magn Reson Chem MRC* 46(2):166–169.
67. Thakur RS, Kurur ND, Madhu PK (2008) An analysis of phase-modulated heteronuclear dipolar decoupling sequences in solid-state nuclear magnetic resonance. *J Magn Reson San Diego Calif 1997* 193(1):77–88.
68. Keller R (2004) *The Computer Aided Resonance Assignment Tutorial (CARA)* (CANTINA Verlag).
69. Shen Y, Delaglio F, Cornilescu G, Bax A (2009) TALOS+: a hybrid method for predicting protein backbone torsion angles from NMR chemical shifts. *J Biomol NMR* 44(4):213–223.
70. Kirschner DA, Abraham C, Selkoe DJ (1986) X-ray diffraction from intraneuronal paired helical filaments and extraneuronal amyloid fibers in Alzheimer disease indicates cross-beta conformation. *Proc Natl Acad Sci U S A* 83(2):503–507.
71. Fiser A, Šali A (2003) Modeller: Generation and Refinement of Homology-Based Protein Structure Models. *Methods in Enzymology*, Macromolecular Crystallography, Part D., ed Charles W. Carter J and RMS (Academic Press), pp 461–491.

SUPPORTING INFORMATION

Mixing Aβ(1-40) and Aβ(1-42) peptides generates unique amyloid fibrils

Linda Cerofolini[1], Enrico Ravera[1], Thomas Wiglenda[2], Annett Böddrich[2], Bettina Purfuerst[6], Iryna Benilova[3,§], Magdalena Korsak[4], Gianluca Gallo[1], Sara Bologna[1], Domenico Rizzo[1], Leonardo Gonnelli[1], Marco Fragai[1], Bart De Strooper[3,5], Erich E. Wanker*[,2], Claudio Luchinat*[,1,4]

1. Magnetic Resonance Center (CERM), University of Florence, Via L. Sacconi 6, and Department of Chemistry "Ugo Schiff", University of Florence, Via della Lastruccia 3, 50019 Sesto Fiorentino (FI), Italy

2. Neuroproteomics, Max Delbrueck Center for Molecular Medicine, Robert-Roessle-Strasse 10, 13125 Berlin, Germany

3. VIB Center for the Biology of Disease, Herestraat 49, 3000 Leuven

4. Giotto Biotech S.R.L., Via Madonna del Piano 6, 50019 Sesto Fiorentino (FI), Italy.

5. KULeuven, Center for Human Genetics, Herestraat 49, 3000 Leuven.

6. Core facility electron microscopy, Max-Delbrück Center for Molecular Medicine, Robert-Roessle-Strasse 10, 13125 Berlin, Germany

[§]Present address: MRC Prion Unit, UCL Institute of Neurology, Department of Neurodegenerative Disease, Queen Square, London WC1N 3BG, UK.

* To whom correspondence may be addressed. Email: claudioluchinat@cerm.unifi.it, ewanker@mdc-berlin.de.

[§]Present address: MRC Prion Unit, UCL Institute of Neurology, Department of Neurodegenerative Disease, Queen Square, , London WC1N 3BG, UK.

* To whom correspondence may be addressed.

Email: claudioluchinat@cerm.unifi.it, ewanker@mdc-berlin.de.

Expression and purification of Aβ1-42 and Aβ1-40 polypeptides.

The cDNAs encoding the Aβ1-40 and Aβ1-42 polypeptides were cloned in the pET3a vector using the NdeI and BamHI restriction enzymes. The peptides were expressed in the BL21 (DE3)pLys *E. coli* strain.
The peptides were purified as reported in the literature (1–5) with the modification of using a combination of anion-exchange and size-exclusion chromatography. All the manipulations were performed at slightly alkaline pH in order to avoid the formation of structural contaminants produced by isoelectric precipitation. The inclusion bodies were first solubilized with 8 M Urea and then purified by ion exchange chromatography performed in batch. All the obtained fractions of the diluted proteins were concentrated to a final volume using an Amicon device. The next step of purification was gel-filtration, which was performed using the preparative column Sephadex 75 HiLoad 26/60 with 50 mM (NH_4)OAc pH 8.5 as a buffer. The obtained fractions were collected together and concentrated. During all the purification steps, the protein purity was analysed by SDS-PAGE, whereas the protein concentration was estimated spectrophotometrically.

Structural modeling using HADDOCK

During HADDOCK calculations, first the β_1- and β_2-strands were docked to one another, using all the experimental long-range β_1-β_2 restraints of β_1- and β_2-strands. The lower distance cutoff was set to 3.0 Å, and the upper to 6.0 Å for the shorter mixing times (100 and 200 ms) and to 7.5-8.0 Å for longer mixing (300 and 400 ms). The charges on the N- and C-termini of the β_1-strands and on the N-termini of the β_2-strands were not included in the calculations in order to prevent electrostatic interactions, which do not exist when the two β-strands are linked by a turn region. The histidine protonation states were automatically determined by the Molprobity module embedded in the HADDOCK server. During the rigid docking calculations, 1000 structures were generated, then the best 200 structures were selected for the semi-rigid simulated annealing in torsion angle space, and finally refined in Cartesian space with explicit solvent.

The structural models were then generated by implementing in the calculations all the observed intermolecular β_2-β_2 long-range contacts and inter-strand distance restraints. All the restraints were duplicated symmetrically between the two β_2-sheets using the same protocol used for structural calculations of symmetric protein dimers. Since these long range distance restraints could be identified only using long mixing times, the upper distance cutoffs in the HADDOCK calculation was set to 8.0 Å. Semi-flexible refinement was enabled on both β_2-sheets.

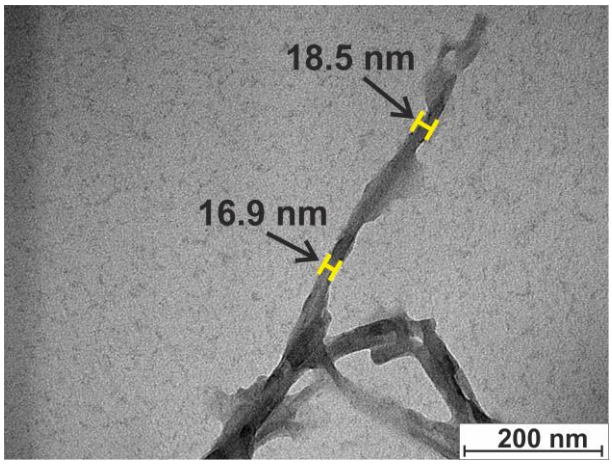

Figure S1. Transmission electron microscopy (TEM) micrographs of the mixed fibrils of Aβ1-42 polypeptide in natural isotopic abundance and ^{13}C-^{15}N isotopically enriched Aβ1-40 polypeptide in the 3:7 molar ratio.

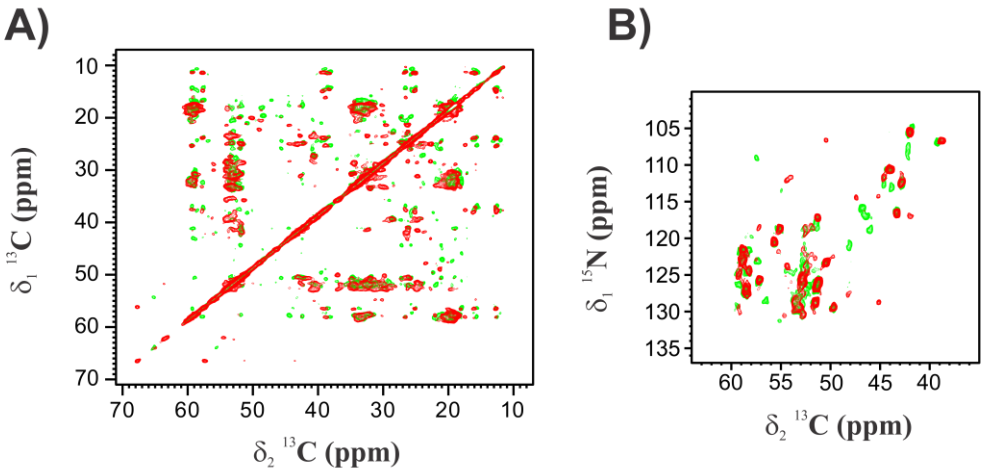

Figure S2. A) 2D ^{13}C-^{13}C-SHANGHAI spectrum of the Aβ1-42:Aβ1-40 mixed fibrils in the 3:7 molar ratio (green) overlaid with the 2D ^{13}C-^{13}C-DARR spectra of fibrils of pure Aβ1-40 (red). Magnetic field: 700 MHz (16.4 T), dimension of rotor: 3.2 mm (~14 mg of fibrils), 12 kHz spinning, 100 kHz ^{1}H decoupling; B) 2D ^{15}N-^{13}C NCA spectrum of the Aβ1-42:Aβ1-40 mixed fibrils in the 3:7 molar ratio (green) overlaid with the 2D ^{15}N-^{13}C NCA spectra of fibrils of pure Aβ1-40 (red). Magnetic field: 700 MHz (16.4 T), dimension of rotor: 3.2 mm (~14 mg of fibrils), 14 kHz spinning, 100 kHz ^{1}H decoupling.

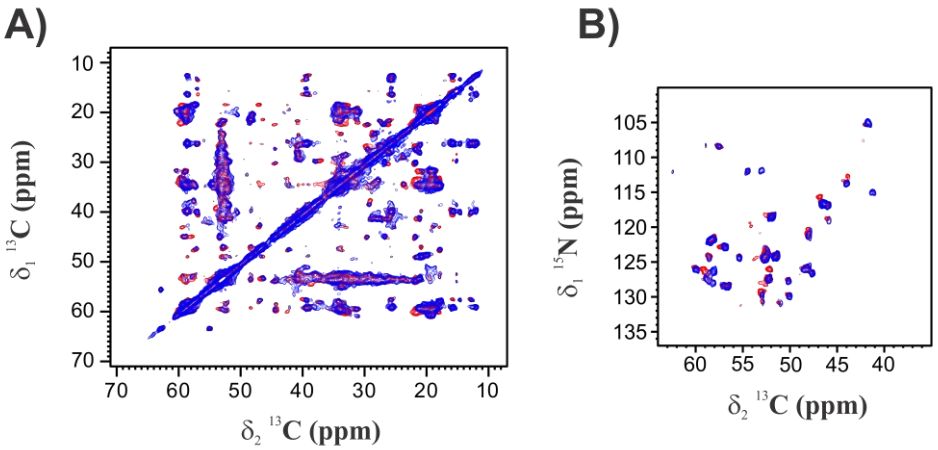

Figure S3. A) 2D ^{15}N-^{13}C NCA spectrum of Aβ1-40 (red) overlaid with the 2D ^{15}N-^{13}C NCA spectrum of Aβ1-42 (blue) in the 1:1 Aβ1-42:Aβ1-40 mixed fibrils. Magnetic field: 700 MHz (16.4 T), dimension of rotor: 3.2 mm (~14 mg of fibrils), 12 kHz spinning, 100 kHz ^{1}H decoupling, T = 283 K; B) 2D ^{13}C-^{13}C- SHANGHAI spectrum of Aβ1-40 (red) overlaid with the 2D ^{13}C-^{13}C- SHANGHAI spectrum of Aβ1-42 (blue) in the 1:1 Aβ1-42:Aβ1-40 mixed fibrils. Mixing time = 100 ms. Magnetic field: 700 MHz (16.4 T), dimension of rotor: 3.2 mm (~14 mg of fibrils), 12 kHz spinning, 100 kHz ^{1}H decoupling, T = 283 K.

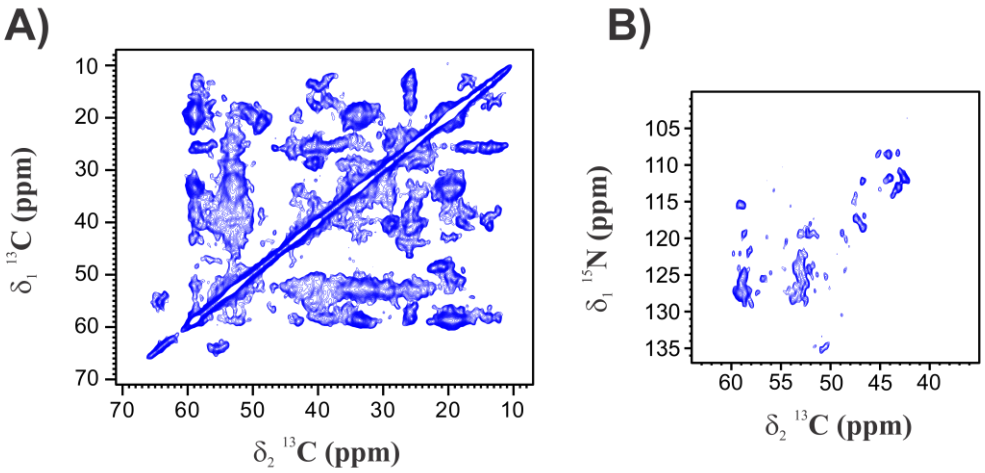

Figure S4. A) 2D ^{13}C-^{13}C-SHANGHAI spectrum of the Aβ1-42 fibrils. Magnetic field: 700 MHz (16.4 T), dimension of rotor: 3.2 mm (~14 mg of fibrils), 12 kHz spinning, 100 kHz ^{1}H decoupling; B) 2D ^{15}N-^{13}C NCA spectrum of the Aβ1-42. Magnetic field: 700 MHz (16.4 T), dimension of rotor: 3.2 mm (~14 mg of fibrils), 14 kHz spinning, 100 kHz ^{1}H decoupling.

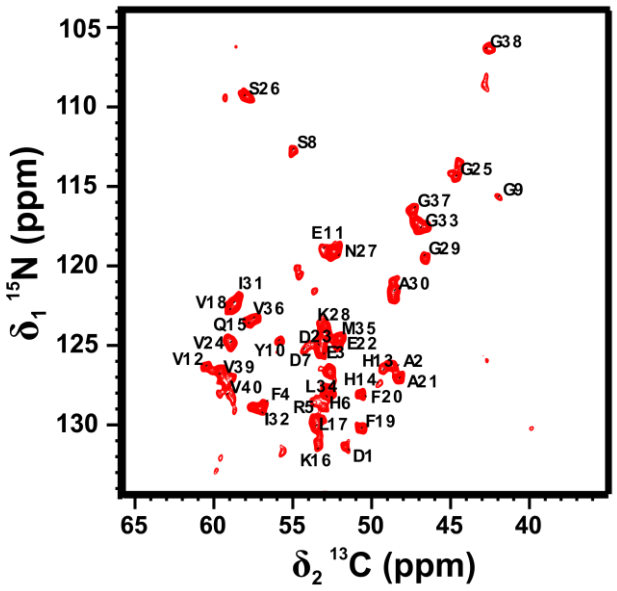

Figure S5. 2D ^{15}N-^{13}C NCA spectrum of the mixed fibrils in 1:1 molar ratio; the full assignment of the spectrum is shown.

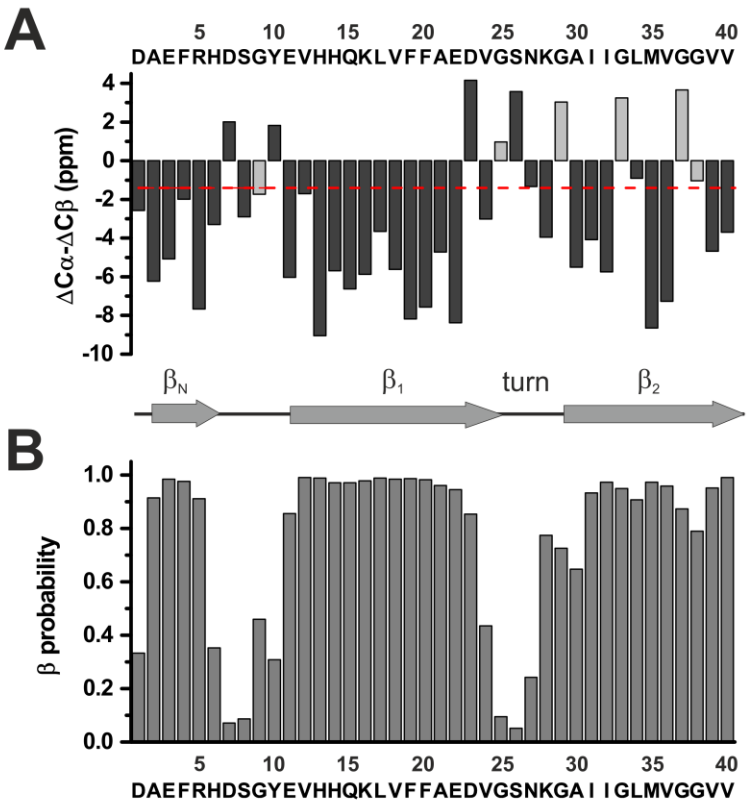

Figure S6. Secondary structural analysis of Aβ1-42:Aβ1-40 mixed fibrils (1:1 ratio). Chemical shift differences in respect to the corresponding random coil values (panel A) and residue specific β-probabilities predicted by TALOS+ (panel B) are displayed. In panel A the red line indicates the cutoff of -1.4 ppm and the ΔδCα shifts for the glycines are displayed in light-grey.

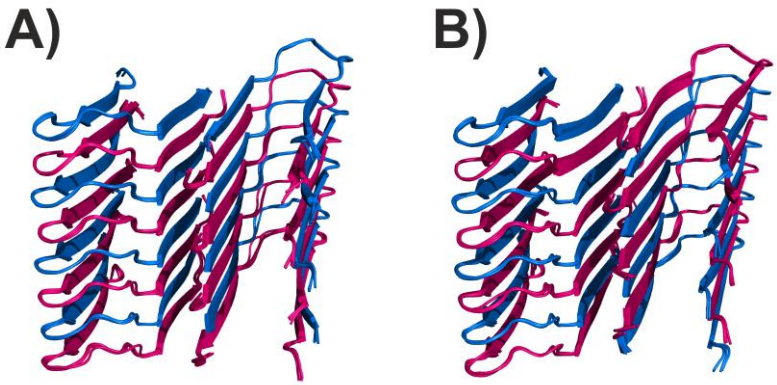

Figure S7. Family of the best four structures corresponding to model B (A) and model C (B), obtained with an experimental restraint-driven calculation with HADDOCK 2.2. Two identical interlaced Aβ1-40/Aβ1-42 protofilaments (A) and two different interlaced protofilaments, Aβ1-40/Aβ1-42 and Aβ1-42/Aβ1-40 (B) have been considered, respectively, in the calculations.

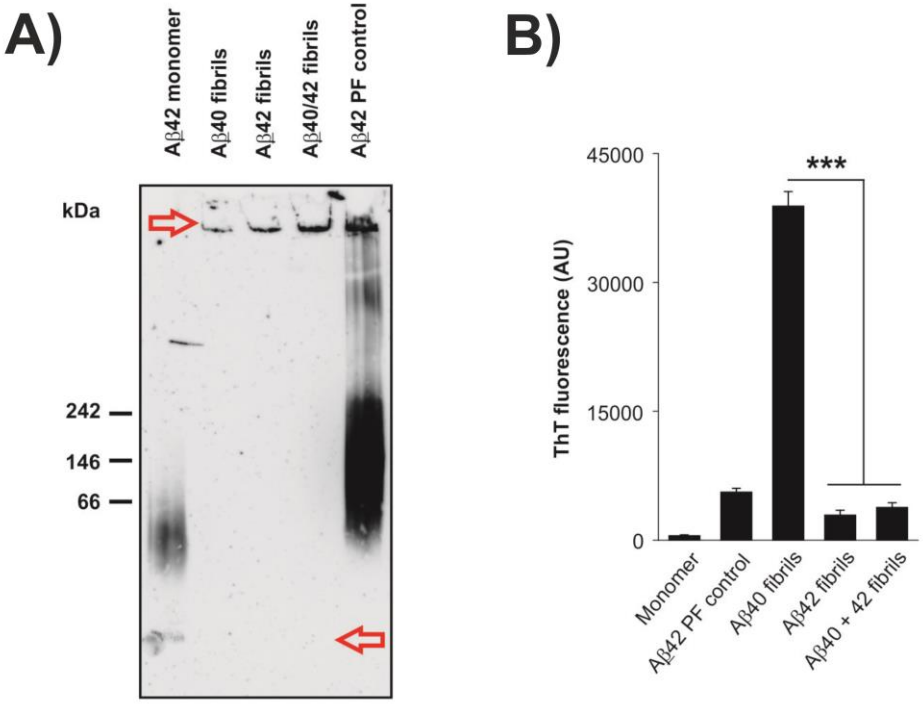

Figure S8. A) Native gel electrophoresis of mature fibrils showing no sign of smaller aggregates; B) ThT fluorescence of the same fibrillar preparations.

Table S1. Long-range intramolecular contacts between β_1- and β_2-strands observed and used for deriving the structural models of Aβ1-42:Aβ1-40 mixed fibrils in present work.

Number	Contacts	Source spectra
1	H13 $C\varepsilon_1$ - V40 $C\beta$	DARR (300 ms)
2	H13 $C\gamma$ - V40 $C\gamma_2$	DARR (300 ms)
3	H13 $C\gamma$ - V40 $C\beta$	DARR (300 ms)
4	L17 $C\beta$ - L34 $C\delta_2$	DARR (100 ms)
5	L17 $C\beta$ - L34 $C\delta_1$	DARR (100 ms)
6	L17 $C\beta$ - L34 $C\beta$	DARR (100 ms)
7	L17 $C\delta_1$ - V36 $C\gamma_1$	DARR (100 ms)
8	L17 N - L34 $C\delta_2$	PAIN(10ms)
9	L17 N - L34 $C\delta_1$	PAIN(10 ms)
10	F19 $C\delta_1$ - L34 $C\delta_2$	DARR (200 ms)
11	F19 $C\beta$ - G33 $C\alpha$	DARR (100 ms)
12	A21 $C\alpha$ - I32 $C\gamma_2$	DARR (300 ms)
13	A21 $C\beta$ - I32 $C\gamma_1$	DARR (100 ms)
14	A21 $C\beta$ - I32 $C\beta$	DARR (300 ms)
15	D23 $C\beta$ - A30 $C\beta$	DARR (100 ms)

Table S2. Long-range intermolecular contacts between two β_2-strands observed and used for deriving the structural models of Aβ1-42:Aβ1-40 mixed fibrils in present work.

Number	Contacts	Source spectra
1	M35 Cε - V39 Cβ	DARR (200 ms)
2	M35 Cβ - G38 Cα	DARR (400 ms)
3	I31 $C\delta_1$ - G38 Cα	DARR (400 ms)
4	I31 $C\gamma_2$ - G38 Cα	DARR (400 ms)
5	I31 Cβ - V39 $C\gamma_1$	DARR (200 ms)
6	I31 $C\delta_1$ - V39 $C\gamma_2$	DARR (200 ms)
7	I31 $C\gamma_2$ - V39 C	DARR (100 ms)
8	I31 $C\gamma_2$ - V39 Cβ	DARR (200 ms)
9	I31 $C\gamma_2$ - V39 $C\gamma_2$	DARR (100 ms)
10	I31 $C\gamma_2$ - V40 $C\gamma_1$	DARR (200 ms)

Table S3. HADDOCK statistics evaluated on the 200 water refined models. The reported data are related to the best four structures of the clusters with the lowest HADDOCK-scores. The packing density and number of cavities have been evaluated using the Voronoia plugin in Pymol (6).

	Model B	**Model C**
HADDOCK-Score	-353 ± 5	-267 ± 2
HADDOCK-Score (without E_{AIR})	-394 ± 5	-299 ± 2
N° of structures of the cluster	199	200
RMSD	0.3 ± 0.2	0.3 ± 0.2
Desolvation Energy	-185 ± 4	-150 ± 5
Buried surface area (BSA)	4862 ± 33	4686 ± 21

Ambiguous interaction restraint energy (E_{AIR})	418 ± 23	321 ± 8
Average packing density	0.81 ± 0.01	0.82 ± 0.01
Number of cavities	22 ± 4	29 ± 5

Table S4. HADDOCK statistics evaluated on the water refined models of model B, fibrils of pure Aβ1-40 and fibrils of pure Aβ1-42 in the S-shaped conformation after HADDOCK minimization. The reported data are related to the best four structures of the clusters with the lowest HADDOCK-scores.

	Model B	**Aβ1-40** (1)	**Aβ1-42** (7) **S-shaped conformation**
HADDOCK-Score	-353 ± 5	-322 ± 3	-407 ± 0.4
HADDOCK-Score (without E_{AIR})	-394 ± 5	-326 ± 3	-408 ± 0.4
RMSD	0.3 ± 0.2	0.2 ± 0.1	0.2 ± 0.1
Desolvation Energy	-185 ± 4	-135 ± 4	-104 ± 5
Buried surface area (BSA)	4862 ± 33	4073 ± 30	5617 ± 71
Ambiguous interaction restraint energy (E_{AIR})	418 ± 23	38 ± 4	15 ± 2

1. Bertini I, Gonnelli L, Luchinat C, Mao J, Nesi A (2011) A new structural model of Aβ40 fibrils. *J Am Chem Soc* 133(40):16013–16022.

2. Hellstrand E, Boland B, Walsh DM, Linse S (2009) Amyloid β-Protein Aggregation Produces Highly Reproducible Kinetic Data and Occurs by a Two-Phase Process. *ACS Chem Neurosci* 1(1):13–18.

3. Jan A, Gokce O, Luthi-Carter R, Lashuel HA (2008) The Ratio of Monomeric to Aggregated Forms of Aβ40 and Aβ42 Is an Important Determinant of Amyloid-β Aggregation, Fibrillogenesis, and Toxicity. *J Biol Chem* 283(42):28176–28189.

4. Walsh DM, et al. (1999) Amyloid β-Protein Fibrillogenesis Structure and Biological Activity of Protofibrillar Intermediates. *J Biol Chem* 274(36):25945–25952.

5. Walsh DM, et al. (2009) A facile method for expression and purification of the Alzheimer's disease-associated amyloid beta-peptide. *FEBS J* 276(5):1266–1281.

6. Rother K, Hildebrand PW, Goede A, Gruening B, Preissner R (2009) Voronoia: analyzing packing in protein structures. *Nucleic Acids Res* 37(Database issue):D393-395.

7. Colvin MT, et al. (2016) Atomic Resolution Structure of Monomorphic Aβ42 Amyloid Fibrils. *J Am Chem Soc*. doi:10.1021/jacs.6b05129.

3.3 Impact of experimental factors on α-synuclein PMCA and RT-QuIC assays (manuscript in preparation)

This work is part of a project entitled “Protein aggregation assays for the diagnosis of synucleinopathies” and was born from a collaboration between CERM (Centro Risonanze Magnetiche) of the University of Florence and the Laboratory of Clinical Neurochemistry of the University of Perugia. Several scientists with different academic background have been involved in this research to achieve the objective of developing SAA (seeding aggregation assays) for the pre-symptomatic diagnosis of PD and other synucleinopathies.

My personal contribution to the realization of this project was to express and purify human recombinant α-synuclein used in SAA with synthetic seeds (preformed aggregates). My goal have been the obtaining monomeric and ultrapure α-synuclein without preformed aggregates that could affect the seeding reaction.

Introduction

Protein-Misfolding Cyclic Amplification (PMCA) and Real-Time Quaking-Induced Conversion (RT-QuIC) consist of two ultrasensitive protein amplification methods for detecting pathological protein aggregates in patients affected by protein misfolding disorders[1-3]. The first PMCA protocol was born by Soto's group in 2001 to detect the misfolded prion protein (PrPSc).[4] The multiplication of the template units was realized by sonication followed by an incubation phase to let the aggregates grow. The PMCA technique was then tested in the years on biological samples coming from animals and patients affected by transmissible spongiform encephalopathy.[5],[6] On the other hand, the QuIC assay was developed by introducing some variants in the PMCA protocol[7],[8]: the PrPC substrate coming from hamsters BH was replaced by recombinant PrPC and sonication was replaced with a vigorous intermittent shaking which promoted seeded aggregation of the monomeric substrate. Starting from the successful application in the diagnosis of human prion diseases, these techniques were recently tested for the detection of misfolded α-synuclein in brain homogenates and cerebrospinal fluid samples of patients affected by synucleinopathies.

The positive results obtained from different studies, confirm that α-synuclein PMCA and RT-QuIC are suitable assays for detecting a-syn aggregates in CSF samples.[9-11] The high sensitivity and specificity of these tests in detecting synucleinopathies, even at the pre-clinical stage, suggest their possible use as diagnostic tools.

Several physical (temperature and sonication/shaking), chemical (ionic strength, pH, monomer concentration, detergents) and exogenous factors, affect α-synuclein aggregation kinetics[12],[13]. During the development of this project, different screening tests were performed in order to find the most reliable and repeatable results to make PMCA and RT-QuIC trials as reproducible as possible.

Materials and Methods

α-synuclein expression and purification

Escherichia Coli BL21(DE3) Gold were transformed with pT7-7 vector cloned with the gene encoding α-synuclein. The overnight preculture of transformed cells was diluted 100-fold in LB medium and induced at an OD_{600} value of 0.6-0.8 with 1 mM Isopropyl-β-D-thiogalactoside and, after 5 hours incubation at 37 °C, the cells were harvested at 4000 rpm (JA-10, Beckman Coulter). The extraction was carried out through osmotic shock using 100 ml of buffer TRIS 30 mM, EDTA 2 mM and sucrose 40%, at pH 7.2 according to Shevchik et al.[14] and Huang et al.[15] . The suspension was then ultracentrifuged at 20000 rpm (Type 70 Ti rotor, Beckman Coulter) for 25 min and pellet was collected and resuspended with 90 ml precooled ultrapure water additioned with 38µL of $MgCl_2$ 1 M and then ultracentrifuged a second time. Supernatants derived from these two centrifugation steps, were joined and dialyzed against 4 liters of buffer 20 mM TRIS/HCl at pH 8.0. The protein then was loaded in the FPLC system and an anion exchange chromatography was carried out with 0-50% linear gradient NaCl 1 M (GE Healthcare HiPrep™ Q HP 16/10 Column). The collected fractions were lyophilized and resuspended in 10 mM TRIS/HCl, 1 mM EDTA and Urea 8 M at pH 8.0 for the chemical denaturation. To eliminate all the protein formed aggregates, two size-exclusion chromatographies (HiLoad™ 16/600 Superdex™ 75 pg Column) were performed with 20 mM phosphate and 0.5 mM EDTA at pH 8.0 as elution buffer. Purified α-synuclein (α-synuclein) was dialyzed against Milli-Q water and lyophilized in batches for long-term storage. Roche cOmplete™ protease inhibitor cocktail was added only during the extraction step in the quantity suggested by the producer.

Setup of the RT-QuIC experiments

The lyophilized aliquots α-synuclein were resuspended in NaOH 3.5 mM (pH 11.54) right before the experiments to avoid the instantaneous formation of aggregates. At high pH, the negatively charged monomers (the isoelectric point of α-synuclein is 4.67) experience an electrostatic repulsion that impedes the

aggregation and favors the dissociation of small aggregates.[16],[17] The solution of α-synuclein and NaOH was brought to the desired pH by adding concentrated buffer. Thioflavin-T (ThT) was also added in a final concentration of 10 μM. To avoid the possible growth of bacteria during the experiment, a 0.08% of NaN_3 was present in the reaction buffer. Each sample was then split in 3 replicates that were then put in a *TECAN* clear-bottom 96-well plate. We added acid-washed glass beads in each well, of different size and number depending on the experiment, to enhance the aggregation speed and increase homogeneity among replicates.[18] The plates were always sealed with a sealing tape to minimize evaporation during the experiments. Successively, plates were inserted in a BMG LABTECH ClarioStar fluorimeter and subjected to the incubation/shaking protocol of Shahnawaz et al.[19] (T = 310 K, 29 min. incubation, 1 min. shaking at 500 rpm) or to the one of Groveman *et al*..[20] Once every 30 minutes, the fluorescence was read from the bottom using an excitation and emission wavelength of 450 nm and 480 nm, respectively.

Preformed seeds preparation

Monomeric α-synuclein at the concentration of 2 mg/ml was incubated in PIPES buffer with 500 mM NaCl at 310 K in two wells (250 μl per well) under constant agitation at 500 rpm. One of the two wells contained 10 μM ThT in order to monitor the aggregation. Once the plateau of the aggregation ThT profiles was abundantly passed (usually after seven days), the sample without ThT was subjected to cycles of sonication, using an immersion sonicator, in order to obtain smaller aggregates. Usually 5 repetitions of cycles of 15 sec sonication (12 μM amplitude) and 15 seconds rest were enough for the purpose. The solution containing the preformed aggregates was then split in aliquots, diluted to the desired concentrations and stored at -80°C for later use.

Results and Discussion

Ab initio simulations

We started our analysis by making simulations to understand what kind of models could rely under the RT-QuIC/PMCA techniques. Before working on experimental data, we wanted to reproduce the linear relation observed by Shahnawaz et al.[19] and by Arosio et al.,[21] between the $t_{1/2}$ (time to the half of the maximum value) and the logarithm of the seed (preformed aggregates) mass concentration (mass of the preformed aggregates present in solution). A nucleated polymerization model (Eq. 3.3.1) with variable fragmentation (Fig.3.3.1) was enough to reproduce an approximate linear relation (see Fig. 3.3.2). This result is in accord with the fact that, for α-synuclein, secondary nucleation can be neglected with respect to elongation and fragmentation at pH above 6.0.[22]

$$f_i(t) = +k_n m(t)^{n_0}\delta_{i,n_0} - k_{on}m(t)f_i(t) + k_{on}m(t)f_{i-1}(t) - k_{off}f_i(t) + k_{off}f_{i+1}(t) - k_{frag}(t)(i-1)f_i(t) + 2k_{frag}(t)\sum_{j=i+1}^{\infty} f_j(t)$$

$$P_f(t) = \sum_{i=n_0}^{\infty} f_i(t) \;\; ; \;\; M_f(t) = \sum_{i=n_0}^{\infty} i f_i(t)$$

$$\begin{cases} \frac{dP_f(t)}{dt} = k_{frag}(t)\left[M_f(t) - (2n_0 - 1)P_f(t)\right] + k_n m(t)^{n_0} \\ \frac{dM_f(t)}{dt} = \left(m(t)k_{on} - k_{off} - k_{frag}(t)n_0(n_0-1)\right)P_f(t) + +n_0 k_n m(t)^{n_c} \end{cases}$$

(Eq. 3.3.1)

$f_i(t) = population\ of\ fibrils\ made\ by\ i\ monomers;\ k_n = primary\ nucleation\ rate\ constant;$

$m(t) = monomer\ population; n_0 = size\ of\ smallest\ nucleus\ (2);\ \delta_{ij} = Kronecker's\ delta\ function;$

$k_{on} = fibril\ polymerisation\ rate\ constant;\ k_{off} = depolymerisation\ rate\ constant;$

$$k_{frag}(t) = variable\ fragmentation\ rate;\ P_f(t) = fibril\ total\ population;\ M_f(t) = fibril\ total\ mass$$

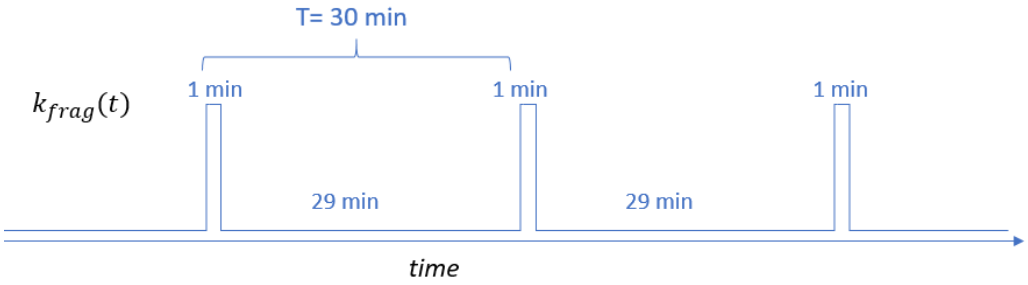

Fig. 3.3.1 The variable fragmentation constant, in the model of differential equations used for the simulations, varies according to the incubation/shaking cycles of a PMCA protocol.

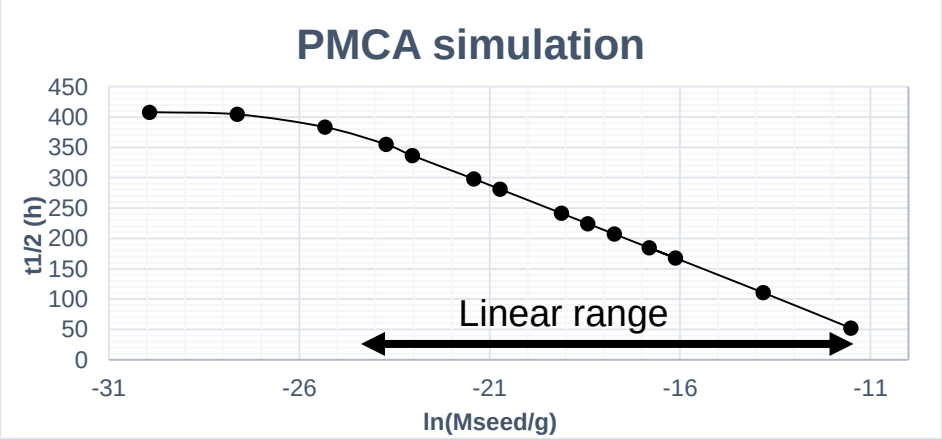

Fig. 3.3.2 By numerically integrating the differential equation system in Eq. 4.3.1 with a Runge-Kutta[23] routine, it was possible to extract the $t_{1/2}$. In this way, it was possible to demonstrate the existence of a range of preformed aggregates (seeds) concentrations (starting from arbitrary kinetic constants) in which the relation between the logarithm of the initial mass of the seeds and the $t_{1/2}$ of the "sigmoidal" growth of the fibrillary species is linear.

Obviously, the simulated linear range of seed masses in Fig. 3.3.2 is arbitrary and not related to experimental values. The range of seed masses, for which it is possible to obtain this linear relation depends on the kinetic constants of the processes, which themselves depend on the nature of the protein-protein interaction and on experimental variables like temperature, pH, shaking cycles, protein concentrations and ionic strength. Optimizing the experimental variables, in order to maximize the differentiation between seed masses, is nowadays the crucial part of the development of PMCA and RT-QuIC techniques for the diagnosis of synucleinopathies.

Variables influencing α-synuclein RT-QuIC

We evaluated the impact on α-synuclein aggregation of some experimental variables like the addition of glass beads, size and number of glass beads and the addition of human CSF. The addition of glass beads to wells containing ThT and monomeric α-synuclein is reported in literature to be beneficial for reducing the fibrillization time and for increasing the homogeneity among replicates.[18] Actually, by making tests on equivalent samples with and without glass beads, we found that is actually the case. In Fig. 3.3.3 are shown the ThT fluorescence profiles of α-synuclein samples with seeds, subjected to a PMCA protocol, with and without glass beads. The replicates in Fig. 3.3.3 A produced very different fluorescence lineshapes and, at 160 h, they still did not reach the final plateau of the aggregation profiles. The replicates in Fig. 3.3.3 B instead produced very similar fluorescence lineshapes and reached the final plateau of the aggregation profiles in about 100 h.

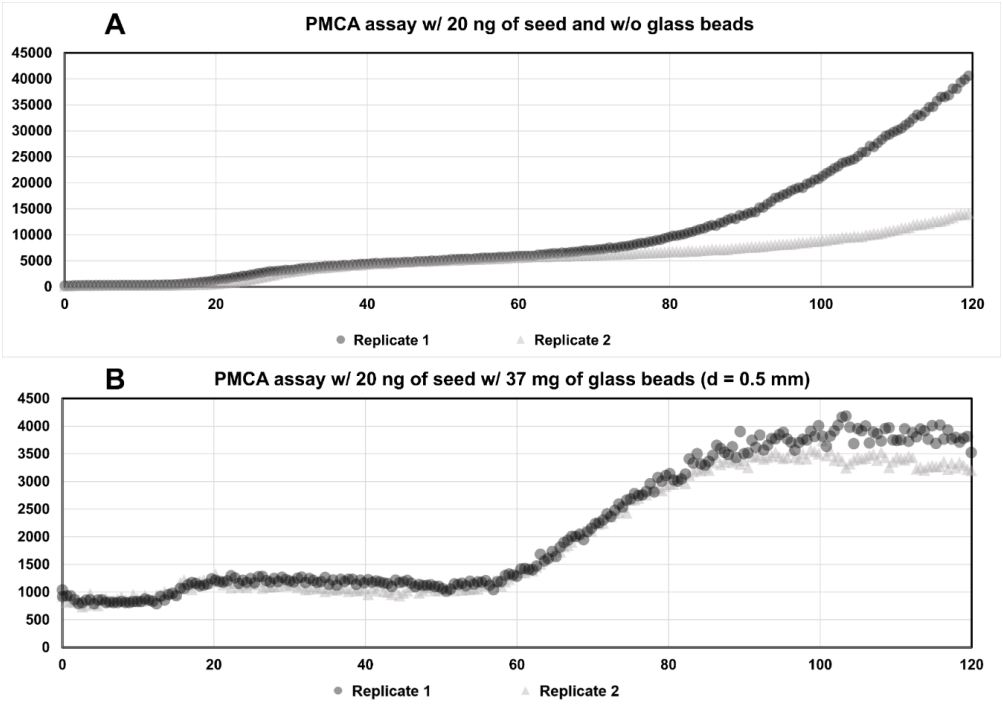

*Fig. 3.3.3 Monomeric α-synuclein 0.125 mg/ml (8.7 μM) was left aggregating in the presence of ThT 10 μM and 0.2 ng of preformed seeds. The experiments were performed in duplicate in a 96-wells plate in PIPES buffer pH 6.5 (with 500 mM NaCl). The plate was subjected to cycles of shaking (1 min. shaking 500 rpm, 29 min. rest) at 310 K, inside a BMG Labtech ClarioStar fluorimeter. In **A)** no glass beads were added while, in **B),** 37 mg of 0.5 mm diameter glass beads were added to the samples.*

A second experiment was performed to evaluate the impact of different size and number of glass beads in three different buffers, the results are shown in Fig. 4.3.4. From this image, it is possible to appreciate that a single bead of 3 mm of diameter produced a faster aggregation with respect to 17 beads with a diameter of 0.5 mm. moreover for any beads size and number, the buffers with higher pH produced a slower aggregation.

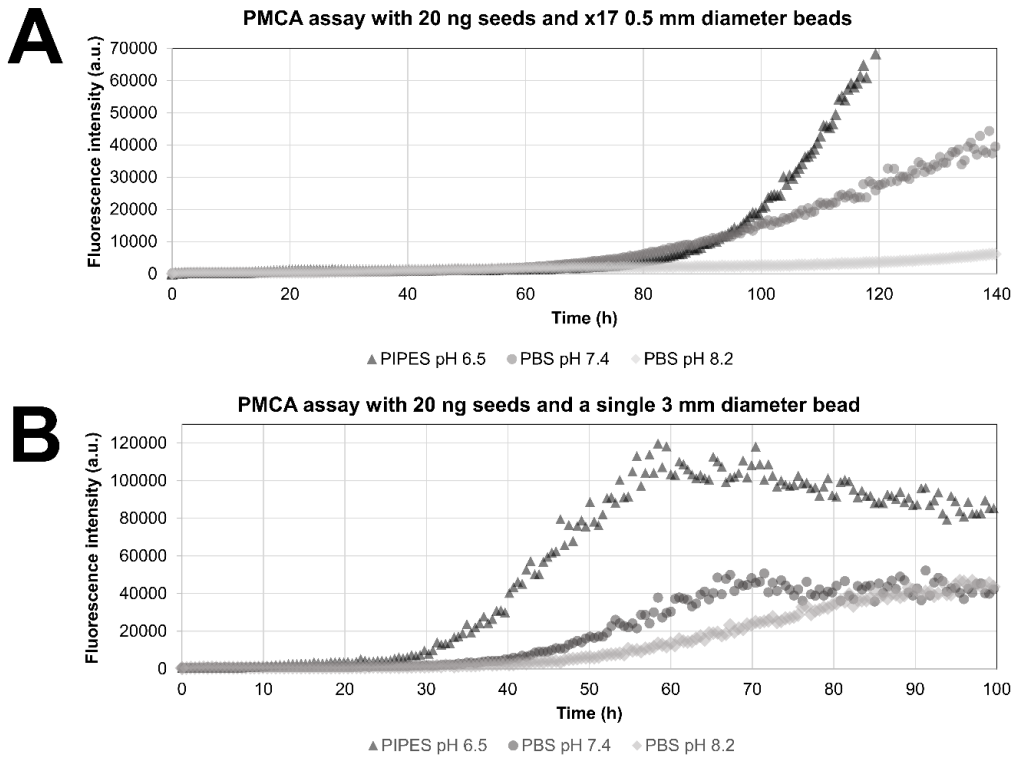

*Fig. 3.3.4 Monomeric α-synuclein 0.08 mg/ml (6.9 μM) was left aggregating in the presence of ThT 10 μM and 20 ng of preformed seeds. The experiments were performed in duplicate in a 96-wells plate in three different buffers: PIPES buffer pH 6.5 (with 500 mM NaCl), PBS buffer pH 7.4 and PBS buffer pH 8.2. The plate was subjected to cycles of shaking (1 min. shaking 500 rpm, 29 min. rest) at 310 K, inside a BMG Labtech ClarioStar fluorimeter. The displayed data is the result of average of the two replicates for each sample. In **A)** 17 glass beads with a diameter of 0.5 mm were added, in **B),** a single bead with a diameter of 3 mm was added to the samples.*

Among the tested experimental variables, one of the major effects on α-synuclein aggregation was due to the addition of human CSF. From α-synuclein aggregation experiments we observed that CSF is able to slow down reproducibly and significantly the aggregation process, probably due to the interaction of α-synuclein with some compounds present in the human biofluid. We tested the antiaggregatory effect of CSF on α-synuclein by RT-QuIC ThT fluorescence assays by adding aliquots of CSF of neurological controls (Fig. 3.3.5 A). Results similar to the one shown in Fig. 3.3.5 A were obtained also using PBS buffer and CSF from other controls subjects, PD patients and DLB patients.

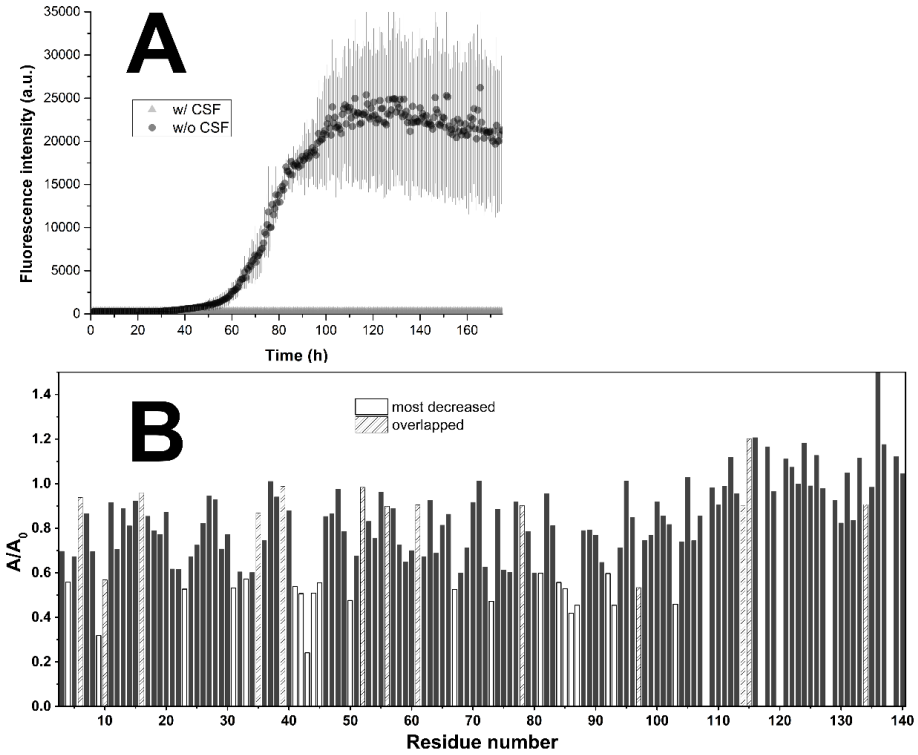

Fig. 3.3.5 ***A)*** *RT-QuIC assay performed using 0.8 mg/mL of recombinant α-synuclein in PIPES pH 6.5 (500 mM NaCl) with (light grey) and without (dark grey) 40 µl of hydrocephalus CSF (final volume of 200 µl). 21 glass beads with a diameter of 0.5 mm were added in each well. The data shown are the averages of three replicates on a 96-wells plate. The experiment was repeated in PBS buffer with 137 mM NaCl at pH 7.4 and at pH 8.0 with similar results.* ***B)*** *Amplitude ratios (corrected for dilution) of peaks coming from 2D ^{15}N-^{1}H HSQC NMR experiments performed at T = 283 K, using a Bruker 950 MHz NMR spectrometer. 100 µl of CSF were added to PBS buffer containing 50 µM of ^{15}N labelled α-synuclein. The smaller amplitude ratios at the N-terminus and at the NAC region of α-synuclein are a sign of interaction with unknown CSF constituents. The ratios highlighted as "most decreased" are the ones which are smaller by one or more standard deviation with respect to the average value. The ones highlighted as "overlapped" come from intensity measurements of partially overlapped peaks in the 2D ^{15}N-^{1}H HSQC spectrum and are less reliable.*

We also investigated the possible interaction of ^{15}N labelled α-synuclein monomers with human CSF with solution NMR (Fig. 3.3.5 B) and we found that the resonances relative to peaks in the N-terminus and NAC region of α-synuclein had decreased intensity in the presence of human CSF. The resonances relative to the amide protons of the C-terminus increased their intensities suggesting an increased mobility in the presence of CSF. No relevant changes in chemical shifts were observed, suggesting that the interacting compounds might be of high molecular weight. The inhibitory effect of CSF on α-synuclein aggregation was previously reported by Shahnawaz, Soto and coworkers[24] but was not further investigated. In 2016 Linse and coworkers[25] observed a similar effect produced by human CSF on the Aβ aggregation kinetics, they found that possible candidates for that inhibition could be high-density lipoproteins (HDL). However, as can be

seen from the Chapter 3.5, we found that the addition of human HDL (from human plasma), although it significantly reduced the quantity of both oligomeric and fibrillary aggregates, could not produce the intensity decrease observed by NMR experiments resulting from the addition of human CSF. However, there is the possibility that the effect on monomeric α-synuclein and the effect on the aggregation can be two distinct phenomena, since it is known that aggregation inhibitors can interact with oligomeric and prefibrillar species and not with the monomer.[26] In this respect, we cannot exclude that lipoproteins may be responsible for the antiaggregatory effect of human CSF.

RT-QuIC tests with preformed seeds

PMCA and RT-QuIC protocols were tested by using CSF coming from a hydrocephalus subjects not suffering from neurodegenerative diseases. This choice was made because we had abundant aliquots from these types of patients and because CSF samples of healthy subjects and PD patients are very rare and must be used only for validation tests, once the protocols have been already optimized. The sensitivity and the differentiation capability of the assays were tested by adding in-lab made preformed aggregates (seeds) in different quantity in each well, the protocol used to produce α-synuclein seeds is reported in the Materials and Methods section. The incubation/agitation protocol and the reaction buffer (PIPES buffer pH 6.5 with NaCl 500 mM) of Shahnawaz, Soto and coworkers (29 minutes agitation, 1 minute shaking at 500 rpm) were used for all the experiments described in Fig. 3.3.4, 4.3.5, 3.3.6 and Fig. 3.3.7. In Fig 3.3.4 A are reported the kinetic traces, averaged on three replicates for each seed quantity, relative to an RT-QuIC experiment performed with 37 mg of glass beads (diameter of 0.5 mm) per well. From the figure it can be appreciated the fact that for samples containing seeds the fluorescence profiles have two inflection points: a first inflection point, situated between 0 h and 25 h and a second one, situated between 60 h and 70 h. The unseeded samples instead showed only one inflection point, at ~30 h for the sample without CSF and at ~70 h for the sample with CSF. The fact that the second inflection point of the seeded samples precedes of few hours the one of the unseeded sample without CSF made us hypothesize that the increase in fluorescence in correspondence of the first inflection point is due to the growth

of the oligomeric/fibrillary seeds while the second increase of fluorescence happens because of the spontaneous nucleation (and consequent fibrillization) of the free monomer in solution. The decrease of the fluorescence after having reached the maximum value is probably produced by the formation of macroscopic insoluble aggregates, which are able to entrap the molecules of ThT. To accurately measure the position of the first inflection point (t_0), the first parts of the aggregation profiles were fitted with a Boltzmann's sigmoidal function (Eq. 4.3.2), using *OriginPro 9.0*. In the non-linear curve fitting procedure used, the parameters A_1, A_2, t_0 and *dt* of Eq. 3.3.2 were let free.

$$y(t) = A_2 + \frac{A_1 - A_2}{1 + \exp\left(\frac{t - t_0}{dt}\right)} \qquad (3.3.2)$$

The results of the fitting are shown in Fig. 4.3.4 B. The measured t_0 parameters were then plotted against the natural logarithm of the mass (in ng) of the added seed. From the linear regression shown in Fig. 2.3.4 C we can see that there is a good linearity between the t_0 parameters (R^2~1) and the logarithm of the seed mass, as was expected from simulations and literature.[21],[24] The linear response was maintained up to 0.02 pg (0.1 pg/ml) of seed, which coincides with upper detection limit for this protocol.

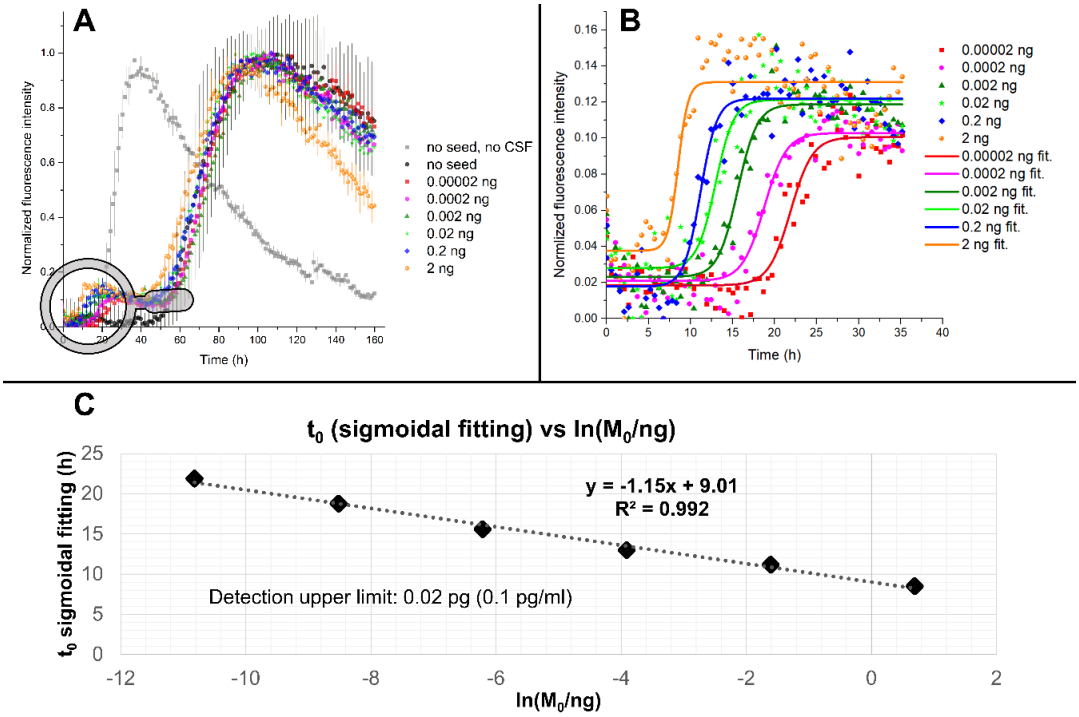

Fig. 3.3.4 ***A)*** *RT-QuIC assay performed using 0.125 mg/mL of recombinant α-synuclein in PIPES pH 6.5 (500 mM NaCl) with 40 µl of CSF (final volume of 250 µl) in the presence of different quantities of preformed aggregates and 37 mg of glass beads with a diameter of 0.5 mm. The data shown are the averages of three replicates on a 96-wells plate while the error bars were calculated as the standard deviations of the averages.* ***B)*** *The first part of the aggregation curves was fitted with a Boltzmann's sigmoidal function, using OriginPro 9.0, to extract the position t_0 of the inflection point.* ***C)*** *The measured t_0 values were plotted against the logarithm of the added quantity of seed and fitted with a line with the linear regression tool of Microsoft Excel.*

What we learnt from this experiment is that, to optimize the assay, it is necessary to promote the "seeded" aggregation and limit the spontaneous aggregation of the free monomer in order to obtain the maximum possible differentiation of the masses of the added seeds. From the linear regression of Fig. 3.3.4 B, it is possible to notice that, although the R^2 coefficient is almost 1, the slope of the line is pretty low, which represent the fact that the first inflection point of the aggregation profiles lays in in a short range of time (5 h - 20 h) for all the curves. In the second trial we lowered the monomer concentration from 1.25 mg/ml to 0.8 mg/ml. This choice was made to discourage the primary nucleation kinetics, which is thought to depend on the square of the monomer concentration while the polymerization kinetics of the fibrils is thought to depend linearly from that. We also decreased the amount of glass beads per well from 37 mg to a fixed number of 15, this was made because we noticed that with the previous quantity, the beads arranged in a way that limited their motion during the shaking, thus probably diminishing the impact of the fragmentation kinetics produced by agitation. As before, we analyzed the

first part of the aggregation curves extracting the t_0 parameters with the sigmoidal fitting (Fig. 3.3.5 A) but we tried also to estimate the so-called *lag-time* to quantify the time at which the fluorescence starts to deviate significantly from its initial value. We defined it, in a way similar to the one used by Groveman et al.,[9] as the time at which the fluorescence (F) of each well becomes higher than the average fluorescence of the first 10 h ($\overline{F(t)}_{t<10\,h}$) of the sample without seeds plus 5 standard deviations (5σ) for 5 consecutive measurements:

$$F\left(t_{lag}+i\Delta t\right) \geq \overline{F(t)}_{t<10\,h} + 5\sigma\left(F(t)\right)_{t<10\,h};\ \forall\, i \in (0,1,2,3,4) \qquad (3.3.3)$$

Where Δt is the time between two consecutive measurements (30 minutes in this case). The inverse of the lag-time, the lag-rate, is usually used in the RT-QuIC literature to visualize the data since it provides a faster and easier way to examine together the outcome of multiple experiments with respect of plotting the fluorescence profiles for all the samples in the same graph (an example of this representation is provided in Fig. 3.3.5 C). The averages of the lag-times (estimated with the threshold method of Eq. 3.3.3) on the three replicates were plotted against the natural logarithm of the seed masses, the result of the linear regression procedure is shown in Fig. 3.3.5 D.

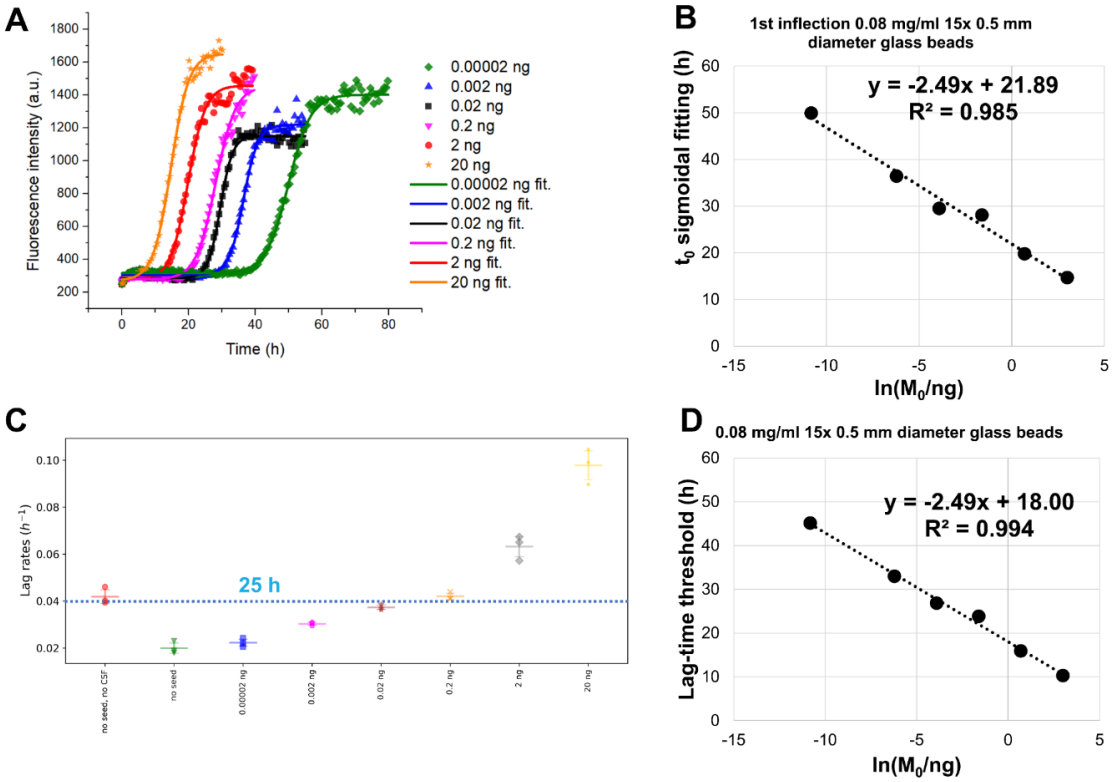

Fig. 3.3.5 RT-QuIC assay performed using 0.08 mg/mL of recombinant α-synuclein in PIPES pH 6.5 (500 mM NaCl) with 40 µl of CSF (final volume of 250 µl) in the presence of different quantities of preformed aggregates and 15 glass beads with a diameter of 0.5 mm. ***A)*** *The first part of the aggregation curves, averaged on the three replicates, was fitted with a Boltzmann's sigmoidal function, using OriginPro 9.0, to extract the position t_0 of the inflection point.* ***B)*** *The measured t_0 values were plotted against the logarithm of the added quantity of seed and fitted with a line with the linear regression tool of Microsoft Excel.* ***C)*** *The lag-rates are calculated as the inverse of the lag-times for each sample.* ***D)*** *The measured lag-times, averaged on the three replicates, were plotted against the logarithm of the added quantity of seed and fitted with a line with the linear regression tool of Microsoft Excel.*

The R^2 values and the slopes of the linear regressions for the t_0 values and the lag-times were similar, as expected, with the slope being more than twice the one calculated in Fig. 4.3.4 C. The tested protocol was still able to differentiate seed masses with an upper detection limit of 0.02 pg. In Fig. 4.3.6 is reported a summary of the measured t_0 value for different bead size and initial monomer concentrations. The t_0 parameter was calculated both on the first and on the second inflection point in the same conditions in Fig. 3.3.6 A and in Fig.3.3.6 B.

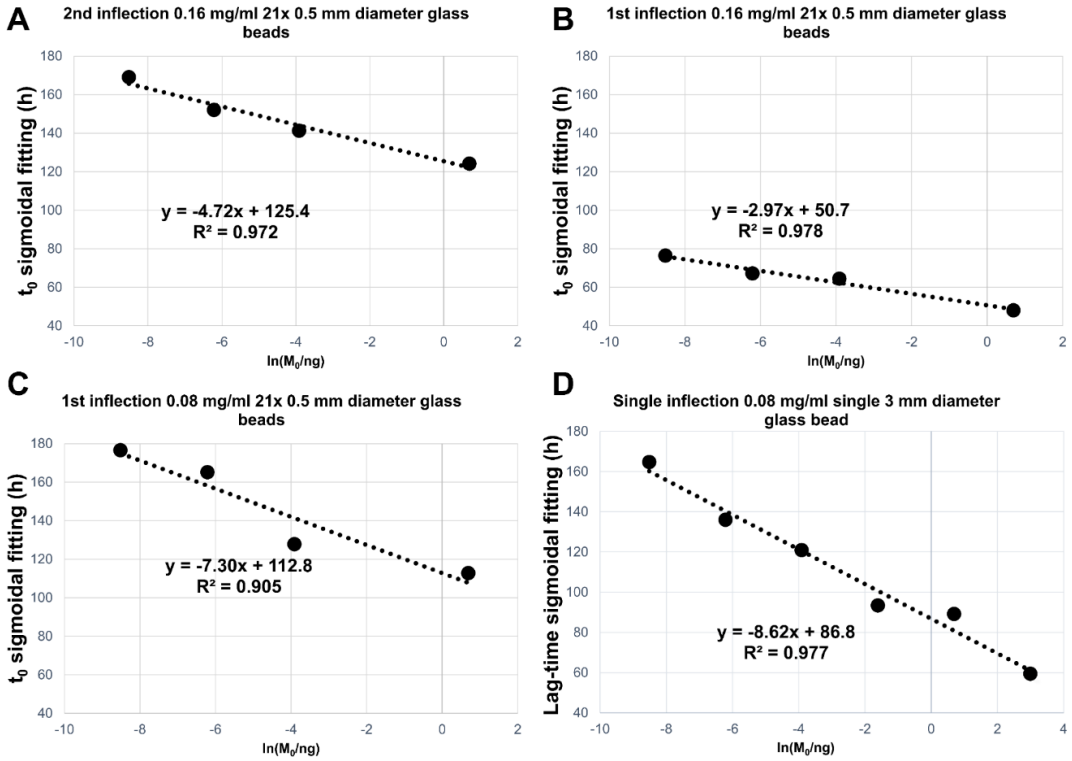

Fig. 3.3.6 Linear regression analyses, performed with the linear regression tool of Microsoft Excel, of the t_0 relative to RT-QuIC assays performed in in PIPES pH 6.5 (500 mM NaCl) with 40 µL of CSF (final volume of 250 µl) in the presence of different quantities of preformed aggregates. The t_0 parameters were obtained by fitting the first or the second part of the normalized and averaged fluorescence profiles with Boltzmann's sigmoidal functions in OriginPro 9.0. In ***A)*** *a starting concentration of 0.16 mg/mL monomeric α-synuclein was used together with 21 glass beads with a diameter of 0.5 mm. The t_0 parameters were obtained by fitting the second part of the normalized and averaged fluorescence profiles. In* ***B)*** *a starting concentration of 0.16 mg/mL monomeric α-synuclein was used together with 21 glass beads with a diameter of 0.5 mm. The t_0 parameters were obtained by fitting the first part of the normalized and averaged fluorescence profiles. In* ***C)*** *a starting concentration of 0.08 mg/mL monomeric α-synuclein was used together with 21 glass beads with a diameter of 0.5 mm. The t_0 parameters were obtained by fitting the first part of the normalized and averaged fluorescence profiles. In* ***D)*** *a starting concentration of 0.08 mg/mL monomeric α-synuclein was used together with 1 glass bead with a diameter of 3 mm. The t_0 parameters were obtained by fitting the normalized and averaged fluorescence profiles.*

All the tested conditions produced satisfactory differentiations between seed masses with a good linear correlation between the measured t_0 parameters and the logarithm of the added seed masses. By looking at Fig. 3.3.6 B and Fig. 3.3.6 C it is possible to notice that, as expected from the considerations on the nucleation and polymerization kinetics, the samples with a monomer starting concentration of 0.08 mg/ml produced an increased slope compared to the ones with 0.16 mg/ml; although the overall experiment duration was also longer. The second inflection point showed also to be discriminative for the 0.16 mg/ml monomer concentration, as can be seen from Fig. 3.3.6 A, while for the 0.08 mg/ml monomer concentration it was still not reached after 250 h. The increased number of beads, with respect to Fig. 3.3.5 C, did not produce neither a significative increase in the aggregation speed nor seed mass discrimination, nor any effect on the presence of the two

inflection points. However, by substituting the 21 beads with a diameter of 0.5 mm with a single bead with a diameter of 3 mm (the total bead mass is ~ 10 times greater) we observed the disappearance of the first inflection point (Fig.3.3.7 A). The t_0 values and the lag-times measured for this kinetics produced good results in terms of R^2 and slope of the linear regression, as can be seen from Fig. 4.3.6 D and from Fig. 3.3.7 B.

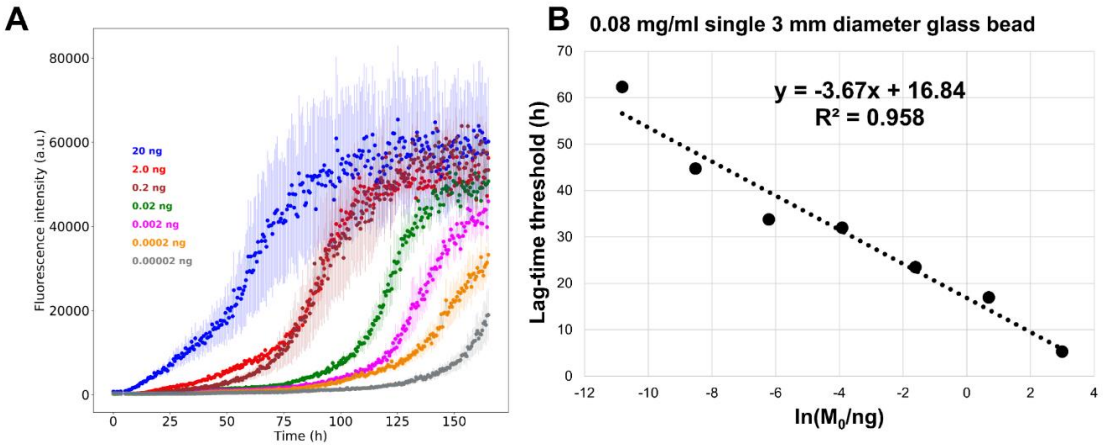

Fig. 3.3.7 RT-QuIC assay performed using 0.08 mg/mL of recombinant α-synuclein in PIPES pH 6.5 (500 mM NaCl) with 40 µl of CSF (final volume of 250 µl) in the presence of different quantities of preformed aggregates and 1 single glass bead with a diameter of 3 mm. The data shown are the averages of three replicates on a 96-wells plate while the error bars were calculated as the standard deviations of the averages.

Another variable that emerged in some protocols present in literature[53,54] is the presence of detergents, such as *Sodium Dodecyl Sulphate* (SDS), which is commonly used in the RT-QuIC protocols for the detection of PrP^{Sc}. The SDS-induced fibrillization of α-synuclein was extensively and accurately characterized by Otzen and coworkers[(12)] and it is currently used to increase the speed and reproducibility of screening assays to measure the effects of antiaggregatory compounds on α-synuclein fibrillization.[(13)]

SDS (%)	seed (pg)	lag-time (h)
0.00	0.00	> 120
0.05	0.00	> 120
0.25	0.00	18 ± 7
0.50	0.00	17 ± 5
0.00	0.01	> 120
0.05	0.01	39.0 ± 0.7
0.25	0.01	10 ± 3
0.50	0.01	7 ± 1

Table 3.3.1: Effect of the addition of different quantities of SDS to the reaction buffer. The lag times were evaluated for each well using the formula in Eq. 2.3.3 by considering the average fluorescence of the first 5 h instead of 10 h due to the high aggregation propensity of samples containing seeds and 0.5% SDS.

We tested the addition of SDS using α-synuclein 0.8 mg/ml in PBS pH 7.4, 6 x 1 mm diameter glass beads and 15 µl of pooled CSF from control subjects for a final volume of 100 µL per well. As can be evinced from Table 4.3.1, the addition of SDS dramatically accelerated the aggregation kinetics of α-synuclein both in seeded and unseeded experiments. The SDS-induced α-synuclein fibrils are known for containing a mixture of α-helix and β-sheet and their morphology differs from that of only agitation-induced α-synuclein fibrils. Anyway, the two morphologies can interconvert and, thanks to temperature and strong agitation, converge into ThT responsive structures rich in β-sheet motifs.[12]

Conclusions

The results of the experiments performed for this work showed the impact on RT-QuIC experiments of some experimental variables like monomer concentration, addition of glass beads, size and number of glass beads, buffer pH and composition and the effect of human CSF on seeded and unseeded experiments. For most of the seeded experiments we usually observed the presence of two inflection points. We associated the first one to the seeded aggregation (growth of preformed aggregates) and the second to the spontaneous nucleation of new aggregates from the monomer present in solution. The monomer starting concentration affects the speed of both the seeded and unseeded aggregation. Decreasing the starting monomer concentration increased the experiment duration but produced a greater slope in seeded aggregation experiments, thus increasing the differentiation between the masses of the added seeds. By taking into account

nucleated-polymerization kinetic models for protein aggregation,[28] like the one described in Eq. 3.3.1, the monomer concentration dependence of the nucleation kinetics is of a higher order with respect of the growth of preformed aggregates. Consequently, the decrease of the monomer concentration affects more the unseeded aggregation than the seeded one.

The addition of glass beads increased both the aggregation speed and the homogeneity among replicates of seeded experiments, a result that is in accord with the results previously published by Giehm and Otzen.[18] The size and the number of the beads showed to play a major role also in the differentiation of added seeds. Increasing the number and size of the beads, in a way that they were able to move and did not scatter the light too much, we found that the assay was able to better differentiate among seeds with greater slopes in linear regression analyses. These findings can be motivated by considering the fragmentation kinetics[29],[30] of prion-like proteins: preformed aggregates, when fragmented, produce more template units, which can then act as new seeds for the fibrillization process. This result implies that RT-QuIC and PMCA experiments with α-synuclein may benefit from the use of beads inside samples to increase the reproducibility of the assay, decrease the experiment duration and increase the differentiation among CSF containing different quantities of preformed aggregates.

The addition of SDS in the reaction buffer significantly accelerated the aggregation of α-synuclein for the tested condition, this result is perfectly in accord with previous studies of Otzen and co-workers,[29],[31] who accurately characterized the SDS-induced aggregation of α-synuclein.

Three reaction buffers were also tested: PIPES buffer 100 mM pH 6.5 with NaCl 500 mM, PBS buffer pH 7.4 and PBS buffer pH 8.2. we observed a decrease in the aggregation speed by moving to higher pH in seeded conditions. This is in accord to the fact that, at high pH, the negatively charged monomers of α-synuclein (isoelectric point: 4.67) experience an electrostatic repulsion that makes nucleation and the growth of aggregates energetically less favorable.[32],[33]

Among the tested experimental variables, the addition of CSF showed to have one of the major impacts. The addition of CSF, also in small quantities (15% of the total volume), is sufficient to slow down the aggregation process of dozens of hours. This slowdown was observed for different buffers and the interaction between α-synuclein and CSF was confirmed by solution NMR with ^{1}H ^{15}N HSQC

experiments. This finding implies that the presence of aggregates may not be the only variable influencing the outcome of PMCA and RT-QuIC assays for the diagnosis of synucleinopathies and that there are unknown compounds present in CSF that physiologically interacts with monomeric or oligomeric α-synuclein and slow down its aggregation.

Tests with CSF coming from patients and controls (preliminary results)

The good results obtained while testing RT-QuIC assays allowed us to start performing tests on patients with the knowledge of some of the experimental variables influencing these assays. To perform tests on CSF coming from patients we scaled the total sample volume from 250 µL to 200 µL to decrease the amount of protein needed for the experiments but maintaining the CSF added volume of 40 µl. The increased CSF/buffer ratio brought us to increase also the monomer concentration in order to obtain a reasonable experimental time for this diagnostic assay. We continued to use the buffer and incubation/shaking protocol of Shahnawaz, Soto and co-worker[19] with the addition of glass beads, a combination which showed to be able to detect seed masses below $2 \cdot 10^{-14}$ g. In Fig. 4.3.8 A are present the results, in terms of lag-rates, of a preliminary test performed in quadruplicate on CSF of 2 PD patients, 2 normal-pressure hydrocephalic (NPH) patients and 2 patients with other neurological disease (OND). In this test, 21 glass beads were used in each sample and a monomer concentration of 0.5 mg/ml was used. In Fig. 3.4.1 B are present the results of another preliminary test performed in triplicate on CSF of 2 PD patients, 1 DLB patient, 1 NPH patient and 1 OND patient. In this test, 21 glass beads were used in each sample while the monomer concentration was risen to 0.67 mg/ml.

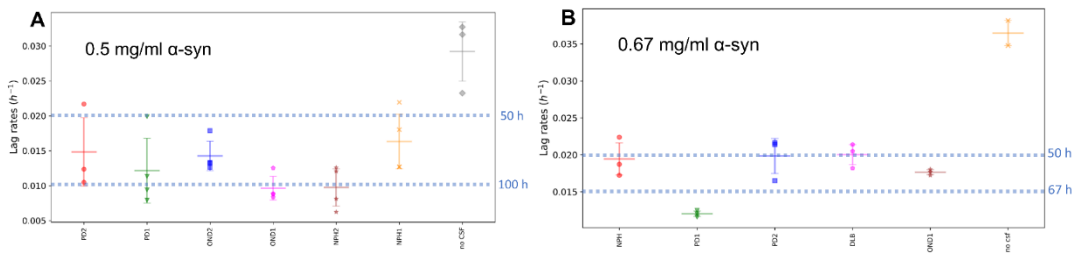

*Fig.3.3.8 RT-QuIC assay performed using 0.5 mg/mL **(A)** and 0.67 mg/mL **(B)** of recombinant α-synuclein in PIPES pH 6.5 (500 mM NaCl) with 40 µl of CSF (final volume of 200 µl) coming from PD, DLB, OND and NPH patients in the presence of 21 glass beads with a diameter of 0.5 mm.*

The differentiation between CSF of PD and DLB from the CSF of OND and NPH, appear very poor and the only sample which is showing a significantly higher lag-rate with respect to OND and NPH samples (considering the internal variability among replicates) is the sample without CSF, Thus confirming that CSF constituents different from preformed α-synuclein aggregates plays a major role in these kind of assays. To diminish the spontaneous nucleation of α-synuclein

aggregates with respect to the growth of preformed ones we brought the monomer concentration to 0.2 mg/ml and used 6 glass beads with a diameter of 1 mm in each well to further promote the fragmentation kinetics (we increased the total volume of glass beads of more than 2 times). For this last test, the CSF of 9 OND, 5 PD and 4 DLB patients was used. The measured lag-rates for this experiment are shown in Fig. 4.3.9 A.

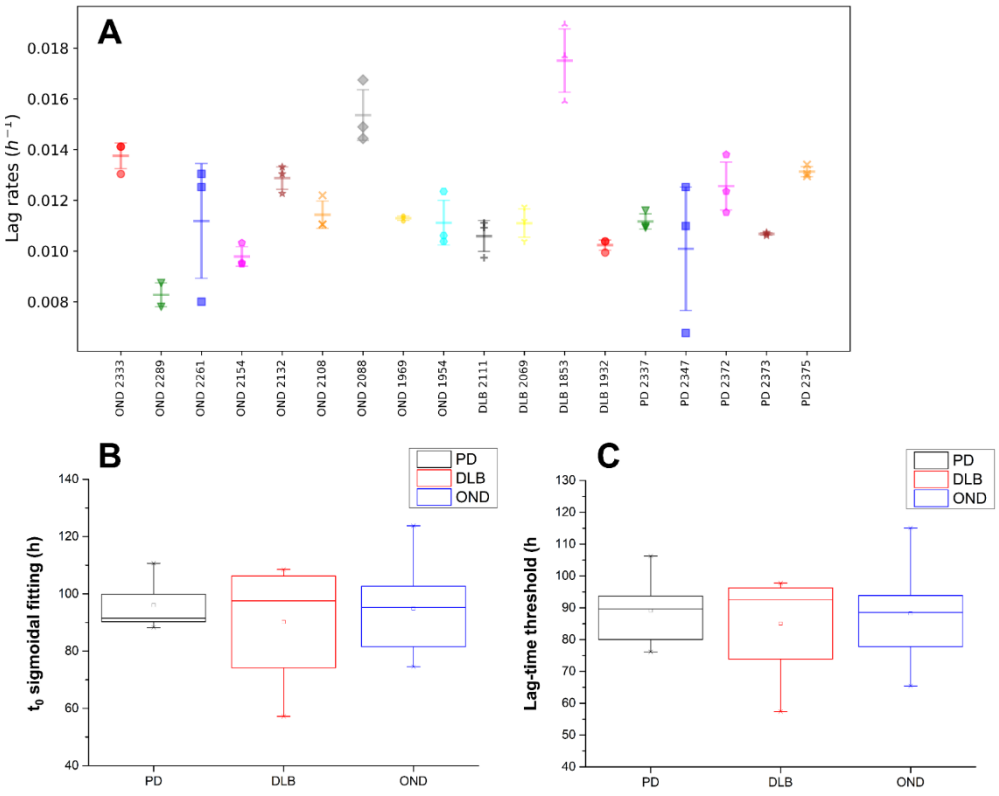

*Fig. 3.3.9 RT-QuIC assay performed using 0.16 mg/mL of recombinant α-synuclein in PIPES pH 6.5 (500 mM NaCl) with 40 µl of CSF (final volume of 200 µl) coming from PD, DLB, OND and NPH patients in the presence of 6 glass beads with a diameter of 1.0 mm. In **A)** the lag-rates relative to all the samples are shown, while in **B)** and **C)** the summary box plots relative to the t_0 parameters and lag-times are shown. The t_0 parameters were obtained by fitting the first part of the normalized and averaged fluorescence profiles.*

As can be noticed from the box charts of Fig. 4.3.9 B and C, the RT-QuIC protocol used for this test did not provide a good performance in differentiating patients affected by synucleinopathies (PD and DLB) from OND. In fact, none of the three groups showed a significative difference for all the parameters analyzed. Considering these results, we switched to the incubation/shaking protocol and buffer of Groveman et al.[20] These changes consisted in decreasing the reaction volume to 100 µl, with 85 µl of reaction buffer and 15 µl of CSF. The final solution

consisted in 40 mM phosphate buffer (pH 8.0), 170 mM NaCl with 0.1 mg/ml monomeric α-synuclein and 10 μM ThT. The only differences with the published protocol were the absence of SDS, the use of wild-type α-synuclein instead of the mutated form K23Q which the scientists used in their work and the monomerization procedure with NaOH that is described in paragraph 2.3. In each well we also put 6 glass beads with a diameter of 1 mm each. The incubation/shaking protocol of Groveman et al.[20] consists of cycles of 1 minute shaking at 400 rpm and 1 minute rest at the temperature of 42°C. In our experiments we did not observe any increase of fluorescence in any sample containing CSF within 140 h. We performed again this test by substituting the reaction buffer with PBS at pH 7.4 (with the same concentrations of ThT and α-synuclein), this time some of the wells produced fluorescence and the results are shown in Fig. 3.3.10. Although some of the wells produced fluorescence, not all CSF from PD patients reacted to the added α-synuclein monomer while other samples, in which the CSF of OND subjects was inserted, reacted earlier. At this pH, still we detected poor aggregation and the samples which produced relevant amounts of fibrils were the ones without CSF and the ones with a preformed quantity of synthetic seeds.

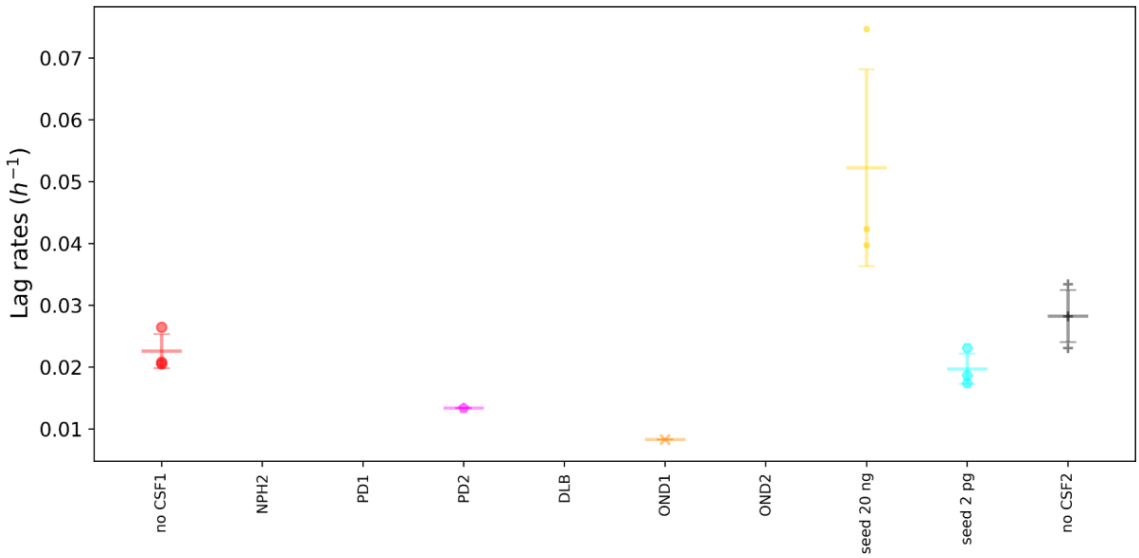

Fig. 3.3.10 RT-QuIC assay performed using 0.08 mg/mL of recombinant α-synuclein in PBS pH 7.4 with 15 μl of CSF (final volume of 100 μl) coming from PD, DLB, OND and NPH patients in the presence of 6 glass beads with a diameter of 1.0 mm. The lag-rates relative to all the samples are shown.

The experiment was successively repeated on four patients and four controls (OND) by adding with respect to this last case 0.015% SDS and bringing the final

NaCl concentration to 500 mM. The protein concentration was also raised from 0.08 to 0.3 mg/ml. A box-plot relative to this last set of experiments is shown below in Fig. 3.3.11.

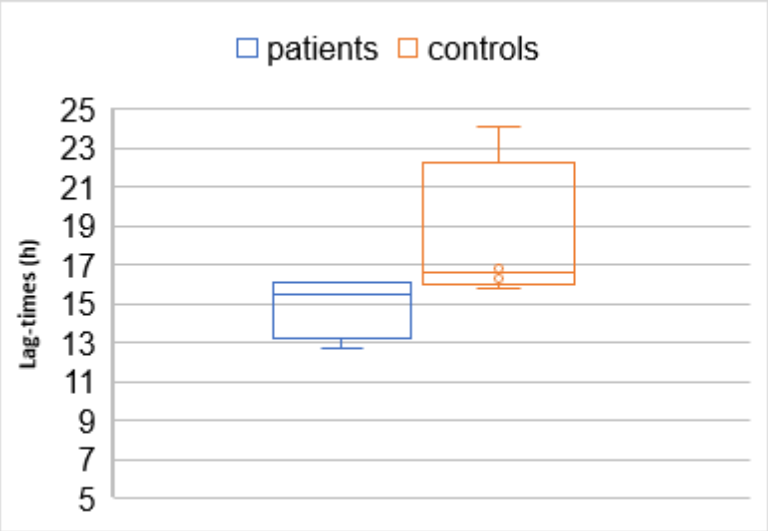

Fig. 3.3.11. The lag-times relative to patients and controls, averaged on replicates were calculated by the formula in Eq. 2.3.3 by using the average fluorescence on the first 5 h instead of 10 h. the RT-QuIC assay was performed using 0.1 mg/mL of recombinant α-synuclein in PBS pH 7.4 with 15 µl of CSF (final volume of 100 µl) coming from 2 PD and 2 DLB patients and 4 OND controls in the presence of 6 glass beads with a diameter of 1.0 mm. The lag-times relative to all the samples are shown. The samples were subjected to incubation/shaking protocol of cycles of 1-minute shaking at 400 rpm and 1-minute rest at the temperature of 42°C.

Although the changes on the experimental condition accelerated too much the aggregation of α-synuclein, this last trial produced a better discrimination between samples containing CSF coming from patients affected by synucleinopathies and OND controls.

Discussion and perspectives

Although in the last set of experiments we obtained a better differentiation in a small number of CSFs coming from patients and controls (Fig. 2.4.4), still we cannot explain why other tests we performed did not provide such differentiation. Among all the groups working on these techniques in Italy (Bologna, Milan, Perugia, Padova, Verona and Rome) no one is nowadays able to reproduce the results obtained by the three major groups working on PMCA[19] and RT-QuIC[24],[34] for the diagnosis of synucleinopathies. In our experiments, we determined the antiaggregatory effect of CSF as one of the main variables affecting α-synuclein aggregation, this effect was previously observed by the group of

Soto[19] but not investigated. The unknown compounds present in CSF that can modulate α-synuclein aggregation may be responsible to the high variability between the lag-times measured for different CSFs, the fact that some authors obtained good results also considering this effect may imply that certain experimental strategies (e.g. the addition of SDS, sample handling and storage) may be useful to compensate or normalize the antiaggregatory effect of human CSF. Apart from increasing the number of CSFs in our tests and optimizing the experimental setup, due to the clinical importance of the development of this assay, for the future we hope to get more in contact with other groups working on RT-QuIC and PMCA to figure out the best strategies to optimize the sensitivity and specificity of the technique. The multiple variables influencing α-synuclein aggregation in the presence of biofluids imply that a global effort should be performed in order to test as many conditions as possible and standardize the experimental procedures. Although the antiaggregatory effect of CSF is dramatically important for the development of protein aggregation assays for the diagnosis of synucleinopathies, the isolation of the endogenous macromolecules able to interfere with the aggregation of α-synuclein, will provide information about the physiological proteostasis of α-synuclein in CSF and on novel possible targets for PD treatment or prevention strategies. The CSF plays a key role in the brain glymphatic system[34],[35] and the deficiency of one of these components, with a consequent decreased waste-clearing ability of CSF,[37] may be implicated in the pathogenesis of PD and other synucleinopathies.[38]

References

1. Soto, C. Unfolding the role of protein misfolding in neurodegenerative diseases. *Nature Reviews Neuroscience* **4**, 49–60 (2003).

2. Atarashi, R., Sano, K., Satoh, K. & Nishida, N. Real-time quaking-induced conversion. *Prion* **5**, 150–153 (2011).

3. Properzi, F. & Pocchiari, M. Identification of Misfolded Proteins in Body Fluids for the Diagnosis of Prion Diseases. *International Journal of Cell Biology* (2013).

4. Soto, C., Saborio, G. P. & Anderes, L. Cyclic amplification of protein misfolding: application to prion-related disorders and beyond. *Trends Neurosci.* **25**, 390–394 (2002).

5. Soto, C. *et al.* Pre-symptomatic detection of prions by cyclic amplification of protein misfolding. *FEBS Letters* **579**, 638–642 (2005).

6. Haley, N. J., Seelig, D. M., Zabel, M. D., Telling, G. C. & Hoover, E. A. Detection of CWD Prions in Urine and Saliva of Deer by Transgenic Mouse Bioassay. *PLOS ONE* **4**, e4848 (2009).

7. Atarashi, R. *et al.* Simplified ultrasensitive prion detection by recombinant PrP conversion with shaking. *Nature Methods* **5**, 211–212 (2008).

8. Atarashi, R. *et al.* Ultrasensitive human prion detection in cerebrospinal fluid by real-time quaking-induced conversion. *Nature Medicine* **17**, 175–178 (2011).

9. Groveman, B. R. *et al.* Rapid and ultra-sensitive quantitation of disease-associated α-synuclein seeds in brain and cerebrospinal fluid by αSyn RT-QuIC. *Acta Neuropathol Commun* **6**, (2018)

10. Yoshinaga, S., Yamanaka, T., Furukawa, Y. & Nukina, N. The detection of seeds alpha-synuclein using protein misfolding cyclic amplification(PMCA). *Journal of the Neurological Sciences* **381**, 972–973 (2017).

11. Jung, B. C. *et al.* Amplification of distinct α-synuclein fibril conformers through protein misfolding cyclic amplification. *Exp Mol Med* **49**, e314 (2017).

12. Giehm, L. & Otzen, D. E. Strategies to increase the reproducibility of protein fibrillization in plate reader assays. *Analytical Biochemistry* **400**, 270–281 (2010).

13. Narkiewicz, J., Giachin, G. & Legname, G. In vitro aggregation assays for the characterization of α-synuclein prion-like properties. *Prion* **8**, 19–32 (2014).

(2019).

14. Shevchik, V. E., Condemine, G. & Robert-Baudouy, J. Characterization of DsbC, a periplasmic protein of Erwinia chrysanthemi and Escherichia coli with disulfide isomerase activity. *EMBO J.* **13,** 2007–2012 (1994).

15. Huang, C., Ren, G., Zhou, H. & Wang, C. A new method for purification of recombinant human alpha-synuclein in Escherichia coli. *Protein Expr. Purif.* **42,** 173–177 (2005).

16. Shammas, S. L., Knowles, T. P. J., Baldwin, A. J., MacPhee, C. E., Welland, M. E., Dobson, C. M. & Devlin, G. L. Perturbation of the Stability of Amyloid Fibrils through Alteration of Electrostatic Interactions. *Biophys. J.* **100,** 2783–2791 (2011).

17. Cohlberg, J. A., Li, J., Uversky, V. N. & Fink, A. L. Heparin and other glycosaminoglycans stimulate the formation of amyloid fibrils from alpha-synuclein in vitro. *Biochemistry* **41,** 1502–1511 (2002).

18. Giehm, L. & Otzen, D. E. Strategies to increase the reproducibility of protein fibrillization in plate reader assays. *Anal. Biochem.* **400,** 270–281 (2010).

19. Shahnawaz, M. *et al.* Development of a Biochemical Diagnosis of Parkinson Disease by Detection of α-synuclein Misfolded Aggregates in Cerebrospinal Fluid. *JAMA Neurol* **74**, 163–172 (2017).

20. Groveman, B. R. *et al.* Rapid and ultra-sensitive quantitation of disease-associated α-synuclein seeds in brain and cerebrospinal fluid by αSyn RT-QuIC. *Acta Neuropathol Commun* **6**, (2018)

21. Arosio, P., Cukalevski, R., Frohm, B., Knowles, T. P. J. & Linse, S. Quantification of the Concentration of Aβ42 Propagons during the Lag Phase by an Amyloid Chain Reaction Assay. *J. Am. Chem. Soc.* **136,** 219–225 (2014).

22. Linse, S. Mechanism of amyloid protein aggregation and the role of inhibitors. *Pure Appl. Chem.* **91,** 211–229 (2019).

23. Runge, C. Ueber die numerische Auflösung von Differentialgleichungen. *Math. Ann.* **46,** 167–178 (1895).

24. Shahnawaz, M., Tokuda, T., Waragai, M., Mendez, N., Ishii, R., Trenkwalder, C., Mollenhauer, B. & Soto, C. Development of a Biochemical Diagnosis of Parkinson Disease by Detection of α-synuclein Misfolded Aggregates in Cerebrospinal Fluid. *JAMA Neurol.* **74,** 163–172 (2017).

25. Padayachee, E. R., Zetterberg, H., Portelius, E., Borén, J., Molinuevo, J. L., Andreasen, N., Cukalevski, R., Linse, S., Blennow, K. & Andreasson, U. Cerebrospinal fluid-induced retardation of amyloid β aggregation correlates with Alzheimer's disease and the APOE ε4 allele. *Brain Res.* **1651,** 11–16 (2016).

26. Pujols, J., Peña-Díaz, S., Lázaro, D. F., Peccati, F., Pinheiro, F., González, D., Carija, A., Navarro, S., Conde-Giménez, M., García, J., Guardiola, S., Giralt, E., Salvatella, X., Sancho, J., Sodupe, M., Outeiro, T. F., Dalfó, E. & Ventura, S. Small molecule inhibits α-synuclein aggregation, disrupts amyloid fibrils, and prevents degeneration of dopaminergic neurons. *Proc. Natl. Acad. Sci.* **115,** 10481–10486 (2018).

27. Giehm, L., Oliveira, C. L. P., Christiansen, G., Pedersen, J. S. & Otzen, D. E. SDS-induced fibrillation of alpha-synuclein: an alternative fibrillation pathway. *J. Mol. Biol.* **401,** 115–133 (2010).
28. Cohen, S. I. A., Vendruscolo, M., Welland, M. E., Dobson, C. M., Terentjev, E. M. & Knowles, T. P. J. Nucleated polymerization with secondary pathways. I. Time evolution of the principal moments. *J. Chem. Phys.* **135,** 065105 (2011).

29. Ferrone, F. Analysis of protein aggregation kinetics. *Methods Enzymol.* **309,** 256–274 (1999).

30. Pöschel, T., Brilliantov, N. V. & Frömmel, C. Kinetics of Prion Growth. *Biophys. J.* **85,** 3460–3474 (2003).

31. Kurnik, M., Sahin, C., Andersen, C. B., Lorenzen, N., Giehm, L., Mohammad-Beigi, H., Jessen, C. M., Pedersen, J. S., Christiansen, G., Petersen, S. V., Staal, R., Krishnamurthy, G., Pitts, K., Reinhart, P. H., Mulder, F. A. A., Mente, S., Hirst, W. D. & Otzen, D. E. Potent α-synuclein Aggregation Inhibitors, Identified by High-Throughput Screening, Mainly Target the Monomeric State. *Cell Chem. Biol.* **25,** 1389-1402.e9 (2018).

32. Shammas, S. L., Knowles, T. P. J., Baldwin, A. J., MacPhee, C. E., Welland, M. E., Dobson, C. M. & Devlin, G. L. Perturbation of the Stability of Amyloid Fibrils through Alteration of Electrostatic Interactions. *Biophys. J.* **100,** 2783–2791 (2011).

33. Cohlberg, J. A., Li, J., Uversky, V. N. & Fink, A. L. Heparin and other glycosaminoglycans stimulate the formation of amyloid fibrils from alpha-synuclein in vitro. *Biochemistry* **41,** 1502–1511 (2002).

34. Fairfoul, G., McGuire, L. I., Pal, S., Ironside, J. W., Neumann, J., Christie, S., Joachim, C., Esiri, M., Evetts, S. G., Rolinski, M., Baig, F., Ruffmann, C., Wade-Martins, R., Hu, M. T. M., Parkkinen, L. & Green, A. J. E. Alpha-synuclein RT-QuIC in the CSF of patients with alpha-synucleinopathies. *Ann. Clin. Transl. Neurol.* **3,** 812–818 (2016).

35. Jessen, N. A., Munk, A. S. F., Lundgaard, I. & Nedergaard, M. The Glymphatic System: A Beginner's Guide. *Neurochem. Res.* **40,** 2583–2599 (2015).

36. Sweeney, M. D. & Zlokovic, B. V. A lymphatic waste-disposal system implicated in Alzheimer's disease. *Nature* (2018). doi:10.1038/d41586-018-05763-0

37. Iliff, J. J., Wang, M., Liao, Y., Plogg, B. A., Peng, W., Gundersen, G. A., Benveniste, H., Vates, G. E., Deane, R., Goldman, S. A., Nagelhus, E. A. & Nedergaard, M. A Paravascular Pathway Facilitates CSF Flow Through the Brain Parenchyma and the Clearance of Interstitial Solutes, Including Amyloid β. *Sci. Transl. Med.* **4,** 147ra111-147ra111 (2012).

38. Valdinocci, D., Radford, R. A. W., Siow, S. M., Chung, R. S. & Pountney, D. L. Potential Modes of Intercellular α-synuclein Transmission. *Int. J. Mol. Sci.* **18,** (2017).

3.4 Dissecting the Interactions between Human Serum Albumin and α-Synuclein: New insights on the Factors Influencing α-Synuclein Aggregation in Biological Fluids

In this study, was investigated the inhibitory effect of Human serum albumin (HSA) on α-synuclein aggregation.

This work was born starting from some unexpected observations arising from SAA and NMR experiments involving the aggregation of α-synuclein in the presence of small aliquots of Cerebrospinal fluid (project: "Protein aggregation assays for the diagnosis of sinucleinophaties"). A slowing-down of the aggregation process in the presence of this biofluid was observed: for this reason a screening of the CSF components had begun, starting from HSA, the most abundant protein in CSF and other biological fluids .

The effect of HSA on α-synuclein aggregation was characterized by ThT fluorescence both in low ionic strength and physiological conditions at the albumin concentration found in serum and CSF. Moreover, by high-field solution Nuclear Magnetic Resonance (NMR) spectroscopy, was determined the binding region of HSA on α-synuclein that is driven by hydrophobic interactions at the N-terminus in physiological experimental conditions, and by electrostatic interactions at the C-terminus at low ionic strength.

The NMR spectra (2D ^{15}N ^{1}H HSQC) were acquired at 283 K with a Bruker Avance III HD NMR spectrometer operating at 950 MHz ^{1}H Larmor frequency while the aggregation of α-synuclein in the presence of increasing concentrations of HSA were monitored using a BMG Labtech ClarioStar fluorimeter. I contributed to this project by expressing α-synuclein and by optimizing its purification protocol to obtain samples with high degree of purity. The presence of preformed aggregates could have affected our interaction/aggregation experiments.

THE JOURNAL OF PHYSICAL CHEMISTRY B

Article

Cite This: J. Phys. Chem. B 2019, 123, 4380−4386

pubs.acs.org/JPCB

Dissecting the Interactions between Human Serum Albumin and α-Synuclein: New Insights on the Factors Influencing α-Synuclein Aggregation in Biological Fluids

Giovanni Bellomo,[†] Sara Bologna,[†] Linda Cerofolini,[†] Silvia Paciotti,[§] Leonardo Gatticchi,[§] Enrico Ravera,[†,‡] Lucilla Parnetti,[*,∥] Marco Fragai,[*,†,‡] and Claudio Luchinat[*,†,‡]

[†]Magnetic Resonance Center (CERM), University of Florence, Via L. Sacconi 6, 50019 Sesto Fiorentino, Italy

[‡]Department of Chemistry "Ugo Schiff", University of Florence, Via della Lastruccia 3, 50019 Sesto Fiorentino, Italy

[§]Department of Experimental Medicine, University of Perugia, Piazzale Gambuli 1, 06132 Perugia, Italy

[∥]Clinica Neurologica, Università degli Studi di Perugia, Piazzale Gambuli 1, 06132 Perugia, Italy

Supporting Information

ABSTRACT: α-Synuclein (α-syn) is found to be naturally present in biofluids such as cerebrospinal fluid (CSF) and serum. Human serum albumin (HSA) is the most abundant protein found in these biofluids, which, beyond transporting hormones and drugs, also exerts a chaperone-like activity binding other proteins in blood and inhibiting their aggregation. Contrasting results are reported in the literature about the effects of albumin on α-syn aggregation. We characterized the binding region of HSA on α-syn by high-field solution NMR spectroscopy and the effect of HSA on α-syn aggregation by thioflavin-T (ThT) fluorescence under both low-ionic-strength and physiological conditions at the albumin concentration in serum and CSF. We found that HSA, at the concentration found in human serum, slows the aggregation of α-syn significantly. α-Syn interacts with HSA in an ionic strength- and pH-dependent manner. The binding is driven by hydrophobic interactions at the N-terminus under physiological experimental conditions and by electrostatic interactions at the C-terminus at low ionic strength. This work provides novel information about the proteostasis of α-syn in biofluids and supports the hypothesis of a chaperone-like behavior of HSA.

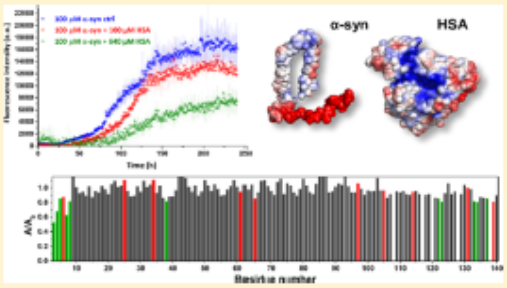

INTRODUCTION

The misfolding and uncontrolled aggregation of α-synuclein (α-syn) is linked to the onset and progression of a branch of neurological disorders named synucleinopathies, which include Parkinson's disease (PD).[1] Monomeric and oligomeric α-syn have been found to be present in biological fluids[2] such as saliva,[3] cerebrospinal fluid (CSF),[4] serum, and plasma.[5] Because α-syn is highly expressed in blood cells,[6] levels of α-synuclein in plasma are about 30-fold higher than those in CSF,[7] and α-syn was shown to be able to cross the brain−blood barrier bidirectionally,[8] also involving exosomal pathways.[7] These findings suggest that both free and exosomal α-syn found in CSF may be originated from blood and vice versa. The implications of extracellular spreading of α-syn through biological fluids in the development of neurological disorders[9] raised doubts about the proteostasis of α-syn in biofluids, such as whether the misfolding could start in these environments and whether extracellular α-synuclein species could work as a biomarker for disease onset and progression. The interest in detecting exosomal, oligomeric, and total α-syn in biological fluids (especially in CSF and serum) is increasing due to the need for identifying new biomarkers for an accurate and timely diagnosis.[10,11] However, modest results have been obtained so far by using enzyme-linked immunosorbent assay-detected α-syn species,[10] and, nowadays, the diagnosis of PD and other synucleinopathies still relies mainly on clinical symptoms. In this respect, the recent developments of real-time quaking-induced conversion (RT-QuIC) and α-syn protein misfolding cyclic amplification (PMCA)[12−15] have provided new perspectives for the early-stage diagnosis of synucleinopathies. These assays work by amplifying a small amount of preformed aggregates by measuring the aggregation rate of recombinant α-syn monomers added to a solution containing an aliquot of a biological fluid. Thus, also for the optimization of these promising techniques, it is necessary to obtain information about α-syn proteostasis and its interaction with the most abundant compounds or macromolecules present in biofluids, which can influence its aggregation. Human serum albumin

Received: March 13, 2019
Revised: April 29, 2019
Published: April 29, 2019

DOI: 10.1021/acs.jpcb.9b02981
J. Phys. Chem. B 2019, 123, 4380−4386

(HSA) is the most abundant protein found in serum[16] (HSA average concentration ~640 μM) and CSF[16] (HSA average concentration ~4.5 μM). HSA is a 66.5 kDa transport protein that has multiple functions in human biofluids, among which it helps in maintaining the oncotic pressure and transports thyroid hormones, fatty acids, and drugs.[17] More recently, HSA was also found to exert a chaperone-like activity.[18] HSA binds Aβ peptides in blood plasma[19] and has been reported to inhibit Aβ fibrillization.[20] The mechanism of an inhibitory effect of HSA on α-syn aggregation and membrane damage, produced by α-syn aggregates, has also been characterized in 2018 by thioflavin T (ThT) kinetic assay, transmission electron microscopy, and with a hemolysis assay.[21] However, in this study, experiments were performed in pure water, under ionic strength conditions far from the physiological ones. Moreover, these results appear in contrast to two previously published studies in 2002[22] and 2004,[23] which showed that bovine serum albumin (BSA), which presents 76% sequence identity with HSA,[24] promotes the fibrillization of α-syn, due to excluded volume effects, in phosphate buffer with nearly physiological concentrations, pH, and ionic strength. To shed light on these contradictions and to clarify the partnership between α-syn and the most common protein in serum and CSF, here we characterize the binding region of HSA on α-syn by high-field solution NMR and the inhibitory effect of HSA on α-syn aggregation kinetics by ThT fluorescence assays both in a low ionic strength environment and under physiological conditions.

MATERIALS AND METHODS

α-Synuclein Expression and Purification. *Escherichia coli* BL21(DE3)Gold were transformed with a pT7-7 vector cloned with the gene encoding α-synuclein. The overnight preculture of transformed cells was diluted 100-fold in LB medium and induced at an OD_{600} value of 0.6−0.8 with 1 mM isopropyl-β-D-thiogalactoside; after 5 h of incubation at 37 °C, the cells were harvested at 4000 rpm (JA-10, Beckman Coulter). The extraction was carried out through osmotic shock using 100 mL of the buffer Tris 30 mM, ethylenediaminetetraacetic acid (EDTA) 2 mM, and sucrose 40%, at pH 7.2, according to Shevchik et al.[25] and Huang et al.[26] The suspension was then ultracentrifuged at 20 000 rpm (Type 70 Ti rotor, Beckman Coulter) for 25 min, and the pellet was collected and resuspended with 90 mL precooled ultrapure water containing 38 μL of 1 M $MgCl_2$ and then ultracentrifuged a second time. Supernatants derived from these two centrifugation steps were combined and dialyzed against 4 L of 20 mM Tris/HCl buffer at pH 8.0. The protein was then loaded in the fast protein liquid chromatography system, and anion-exchange chromatography was carried out with 0−50% linear gradient 1 M NaCl (GE Healthcare HiPrep Q HP 16/10 Column). The collected fractions were lyophilized and resuspended in 10 mM Tris/HCl, 1 mM EDTA, and 8 M urea at pH 8.0 for chemical denaturation. To eliminate all of the protein that formed aggregates, two size-exclusion chromatographies (HiLoad 16/600 Superdex 75 pg Column) were performed with 20 mM phosphate and 0.5 mM EDTA at pH 8.0 as the elution buffer. Purified α-synuclein (α-syn) was dialyzed against Milli-Q water and lyophilized in batches for long-term storage. The Roche complete protease inhibitor cocktail was added only during the extraction step in the quantity suggested by the producer.

ThT Aggregation Experiments. The lyophilized aliquots of α-syn were resuspended in 3.5 mM NaOH (pH 11.54) right before the experiments to avoid the instantaneous formation of aggregates. At high pH, the negatively charged monomers (the isoelectric point of α-syn is 4.67) experience an electrostatic repulsion that impedes the aggregation and favors the dissociation of small aggregates.[27,28]

Setup of ThT Aggregation Experiments in KPi. The solution of α-syn and NaOH was brought to pH 6.0 and to the desired α-syn concentration by diluting it with potassium phosphate buffer. The final samples, of 600 μL each, contained 20 mM KPi, 50 mM NaCl, 50 μM α-syn, 0.1% NaN_3, 10 μM ThT, and 0, 50, and 640 μM HSA. Each sample was then split into three replicates of 200 μL that were then put in a TECAN clear-bottom 96-well plate. We added glass beads in each well (21 × 0.5 mm^2 diameter glass beads) to enhance the aggregation speed and increase homogeneity among replicates.[29] Successively, the plate was inserted in a BMG LABTECH ClarioStar fluorimeter and subjected to an incubation/shaking protocol similar to the one used by Shahnawaz et al.[30] (T = 310 K, 29 min incubation, 1 min shaking at 500 rpm). At every cycle of 30 min. the fluorescence was read from the bottom using excitation and emission wavelengths of 450 and 480 nm, respectively.

Setup of ThT Aggregation Experiments in Phosphate-Buffered Saline (PBS). The solution containing α-syn and NaOH was brought to pH 7.4 and to the desired α-syn concentration with concentrated PBS buffer. The final samples, of 600 μL each, contained standard PBS, 100 μM α-syn, 0.1% NaN_3, 10 μM ThT, and 0, 4.5, 100, and 640 μM HSA. Each sample was then split into three replicates of 200 μL that were then put in a TECAN clear-bottom 96-well plate. Analogous samples containing 4.5, 100, and 640 μM HSA without α-syn were also prepared to monitor the background fluorescence of ThT bound to HSA. We added glass beads in each well (6 × 1 mm^2 diameter glass beads) to enhance the aggregation speed and increase homogeneity among replicates.[29] The plate was then inserted in a BMG LABTECH ClarioStar fluorimeter and subjected to an incubation/shaking protocol similar to the one used by Shahnawaz et al.[30] (T = 310 K, 29 min incubation, 1 min shaking at 500 rpm). At every cycle of 30 min the fluorescence was read from the bottom using excitation and emission wavelengths of 450 and 480 nm, respectively. In this sample, we observed a progressive decrease of the background fluorescence produced by ThT bound to HSA, which was not evident in KPi at pH 6.0 (see Figure S1). The decrease of the offset fluorescence may be due to the change of oligomeric populations of HSA, which have a higher binding affinity for ThT compared with the monomer,[31] and a partial dissociation of these multimers, due to the higher pH compared with the previous experiments in KPi, may be the cause for this slow decrease.

Definition of the t_0 and t_{lag} Parameters. To quantitatively estimate the lag phase from ThT fluorescence profiles, we fit the data obtained from each well (without removing the offset and without normalizing) with a Boltzmann's sigmoidal function (eq 1), using OriginPro 9. In the nonlinear curve-fitting procedure used, the parameters A_1, A_2, t_0, and dt of eq 1 were let free.

$$y(t) = A_2 + \frac{A_1 - A_2}{1 + \exp\left(\frac{t - t_0}{dt}\right)} \quad (1)$$

DOI: 10.1021/acs.jpcb.9b02381
J. Phys. Chem. B 2019, 123, 4380−4386

The parameter t_0 corresponds to the inflection point of the sigmoidal curves used to fit the data and can be used to quantify the time necessary to produce a consistent quantity of fibrillary aggregates.

Conversely, the t_{lag} parameter quantifies the time at which fibrils start to form. We defined it, in a way similar to that used by Groveman et al.,[14] as the time at which the fluorescence (F) of a well becomes higher than its average fluorescence in the first 5 h ($\overline{F(t)}_{t<5\,h}$) plus 2 standard deviations (2σ), for five consecutive measurements.

$$F(t_{lag} + i\Delta t) \geq \overline{F(t)}_{t<5\,h} + 2\sigma(F(t))_{t<5\,h}, \quad \forall\, i \in (0, 1, 2, 3, 4) \tag{2}$$

where Δt is the time between two consecutive measurements.

NMR Experiments. All of the NMR spectra were acquired at 283 K with a Bruker Avance III HD NMR spectrometer operating at 950 MHz ^{1}H Larmor frequency, equipped with a cryogenically cooled probe. The spectra were processed with the Bruker TOPSPIN 4.0 software tools and analyzed by the program Computer Aided Resonance Assignment.[32] During the NMR titration of the protein with HSA, three aliquots of a concentrated 8 mM solution of HSA (same buffer conditions as the final samples) were added to the buffered solution containing ^{15}N isotopically enriched α-syn at the concentration of 100 μM. The tested buffered solutions were [20 mM KPi, pH 6.0, with 50, 100, and 150 mM NaCl] and PBS (pH 7.4). For samples in PBS buffer, we also added 0.5 mM of EDTA to block residual traces of metalloproteases. For the NMR experiments, standard 3 mm glass tubes were used with a final sample volume of 200 μL. The added volumes of the HSA solution (8 mM) were 2.5, 17.5, and 25.5 μL for the 100, 640, and 900 μM samples, respectively, in all of the buffer used. While testing the electrostatic nature of the interaction between α-syn and HSA, also 2 and 4 μL of a solution of 20 mM KPi, pH 6.0, with 5 M NaCl were added in the NMR tube containing α-syn 100 μM and HSA 900 μM, respectively, to reach the final concentrations of 100 and 150 mM NaCl, respectively.

RESULTS AND DISCUSSION

At first, to test the possible inhibitory effect of HSA on α-syn fibrillization, monomeric recombinant α-syn (at the concentration of 50 μM) was incubated alone or in the presence of different amounts of HSA (50 and 640 μM) in a potassium phosphate buffer (KPi, 20 mM potassium phosphate, 50 mM NaCl, pH 6.0). The protocols used for the expression, purification, and resuspension of α-syn are presented in Materials and Methods. We applied a PMCA protocol[13] and added glass beads (21 × 0.5 mm^2 diameter glass beads) inside the wells to increase the homogeneity among replicates[29] and to speed up the aggregation of α-syn. The outcome of the ThT fluorescence experiment performed in KPi is summarized in Figure 1A. To better visualize the difference in the lag phases in the figure, for each well, we removed the background fluorescence produced by ThT bound to HSA and averaged the results of the three replicates prepared for each HSA concentration. Both monomeric and multimeric HSA bind ThT, with K_D's of ~140 and ~20 μM, respectively,[31] thus producing a background fluorescence. To remove this offset in fluorescence intensity, we subtracted the average fluorescence value of the first 10 h, where the fluorescence was constant and produced mostly by ThT bound to HSA (Figure 1A).

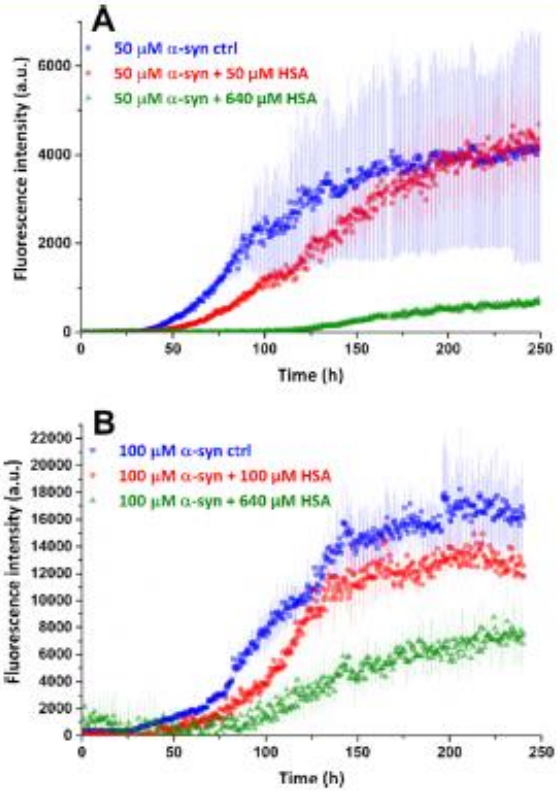

Figure 1. (A) Monomeric α-syn (50 μM) was left to aggregate in the presence of ThT (10 μM) and different HSA concentrations. The experiments were performed in triplicate in a 96-well plate in KPi buffer (20 mM KPi, 50 mM NaCl, pH 6.0, T = 310 K). Glass beads (21 × 0.5 mm^2 diameter) were added to the samples. (B) Monomeric α-syn (100 μM) was left to aggregate in the presence of ThT (10 μM) and increasing HSA concentrations. The experiments were performed in triplicate in a 96-well plate in PBS, pH 7.4, T = 310 K. Glass beads (6 × 1 mm^2 diameter) were added to the samples. In both experiments, samples were subjected to cycles of shaking (1 min shaking at 500 rpm, 29 min rest) inside a BMG Labtech ClarioStar fluorimeter. The shown kinetic profiles result from the averages and standard deviation of the averages of the three replicates with offset removed.

The measured t_0 parameters (defined in Materials and Methods), averaged on the three replicates, are reported in Table 1. As evinced by the table, the estimated t_0 values are longer for samples containing HSA in KPi, both at its physiological concentration in serum (640 μM) and in a 1:1 ratio with α-syn (50 μM). Successively, the experiments were repeated in a different buffer under more physiological experimental conditions: phosphate-buffered saline (PBS: 137 mM NaCl, 10 mM Na_2HPO_4, 2 mM KH_2HPO_4, 2.7 mM KCl, pH 7.4). In this second set of experiments, the concentration of α-syn was raised to 100 μM and the number and size of the glass beads were changed from 21 × 0.5 mm^2 diameter beads to 6 × 1 mm^2 diameter beads. The change in the experimental setup was made to further encourage the fibrillization of α-syn. Indeed, the higher pH value slowed down the whole aggregation process because of the electro-

DOI: 10.1021/acs.jpcb.9b02381
J. Phys. Chem. B 2019, 123, 4380−4386

Table 1. t_0 and t_{lag} Parameters for the Experiments Performed with 50 μM α-syn in 20 mM KPi, 50 mM NaCl, pH 6.0, T = 310 K, and 100 μM α-syn in PBS, pH 7.4, T = 310 K[a]

experiment	HSA (μM)	t_0 (h)	t_{lag} (h)
50 μM α-syn 20 mM KPi, 50 mM NaCl, pH 6	0	86 ± 6	27 ± 1
	50	135 ± 9	29 ± 2
	640	167 ± 4	119 ± 4
100 μM α-syn PBS, pH 7.4	0	105 ± 2	28.3 ± 0.4
	4.5	116 ± 3	30 ± 1
	100	114 ± 2	61 ± 1
	640	141 ± 6	130 ± 10

[a]Values presented in the table result from the average of three replicates, whereas their uncertainty corresponds to the standard deviation of the average value.

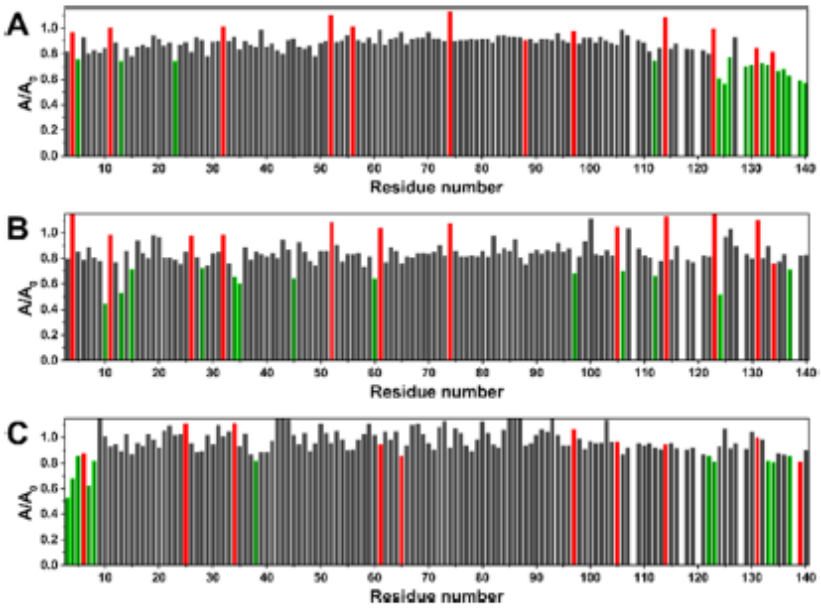

Figure 2. Intensity decreases of the signals of two-dimensional (2D) $^{15}N-^{1}H$ HSQC experiments acquired at 950 MHz on α-syn (100 μM) after the addition of HSA (900 μM) at T = 283 K under different buffer conditions: (A) 20 mM KPi, 50 mM NaCl, pH 6.0; (B) 20 mM KPi, 150 mM NaCl, pH 6.0; (C) PBS (137 mM NaCl), pH 7.4. The residues experiencing the largest decreases in signal intensity (smaller by one or more standard deviations with respect to the average value) are highlighted in green. The intensity ratios corresponding to overlapping peaks are highlighted in red (their values were not considered in the calculation of the average decreases and standard deviations).

static repulsion between α-syn monomers that become more negatively charged while increasing the pH.[33] For the PBS experiments, α-syn was incubated alone and with increasing quantities of HSA: 4.5 μM (shown in the Supporting Information (SI), physiological concentration in CSF), 100, and 640 μM. At high HSA concentrations (100 and 640 μM), we observed a progressive decrease of the background fluorescence of HSA over time (Figure S1 in the SI). We hypothesize that this was due to a slight change in the oligomeric populations of HSA, which have different binding affinities for ThT.[31] To overcome this problem, the average fluorescence of three replicates in wells containing HSA alone was subtracted from the fluorescence of the wells containing both HSA and α-syn. We measured the t_0 values of each well by fitting the data with the background removed. The averaged t_0 values are shown in Table 1, whereas the averaged ThT profiles with offset removed are shown in Figure 1B. Also, in the last set of ThT aggregation experiments, we observed an increased t_0 for samples containing HSA. A strong decrease in the amplitudes of the fitted sigmoids ($A_1 - A_2$) was also observed for samples with 640 μM HSA (see Figure 2 and Table S1 in the SI), but although ThT is a good probe for fibril formation, caution should be used in interpreting this result since HSA competes with α-syn fibrils in binding ThT. Another parameter that can be useful to characterize the speed of aggregation is the time at which the fluorescence starts to deviate significantly from its initial value (t_{lag}), as defined in Materials and Methods. The measured t_{lag} values are presented in Table 1.

Although the physiological concentration of HSA in serum produced the most marked effects both on the t_0 and t_{lag} of the kinetic profiles, in our experiments, the physiological HSA concentration in CSF still was able to generate a slight delay in the aggregation of 100 μM α-syn in PBS (Figure S2 in the SI). It produced a t_{lag} of 30 h and a t_0 of 116 h on the aggregation of 100 μM α-syn, with the t_{lag} and t_0 of the control sample being 28 and 105 h, respectively. This t_0 is comparable to that

DOI: 10.1021/acs.jpcb.9b02381
J. Phys. Chem. B 2019, 123, 4380−4386

produced by 100 μM HSA, although this sample produced a longer t_{lag} (61 h).

To clarify the molecular basis of the inhibition of α-syn aggregation by HSA, the interaction between the two proteins was investigated through solution NMR. We added different aliquots of HSA (100, 640, and 900 μM) to solutions of ^{15}N isotopically enriched α-syn (100 μM) and evaluated the changes in intensity of the resonances in 2D ^{1}H−^{15}N HSQC solution NMR spectra. We also tested lower amounts of HSA under the same conditions, but negligible variations were observed up to 100 μM HSA (Figure S6 in the SI). The experiments were performed on a Bruker Avance III HD 950 MHz NMR spectrometer at 283 K in the same two buffers that were previously used for the fluorimetric assays. The data relative to the experiments performed at 100 and 640 μM HSA and the experimental details of the measurements are presented in the SI. In the presence of HSA, several signals in the 2D ^{1}H−^{15}N HSQC of α-syn experienced large decreases in intensity, because of a line-broadening effect on these cross-peaks, arising after the interaction with HSA. In a low-ionic-strength environment (Figure 2A), the residues located on the C-terminus of α-syn are mainly affected by this decrease, indicating an interaction with HSA occurring at this level.

We hypothesize that this interaction is mainly electrostatic: by calculating the charge of HSA with the APBS[34] plugin of PyMOL, we found a positively charged pocket (see Figure 3) that may be an eligible site for the interaction with the negatively charged C-terminus of α-syn.

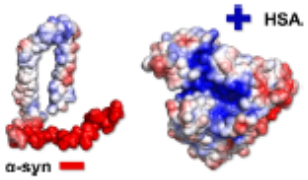

Figure 3. Surface charge representation of α-syn (PDB code: 2KKW, conformer no. 2) and HSA (PDB code: 4K2C), with blue and red representing regions of positive and negative electrostatic potentials, respectively. All of the electrostatic surfaces were generated with the APBS plugin of PyMOL. Different scales of dimensions of the two proteins are used in the figure.

As a support for the electrostatic interaction hypothesis, we also found that the effect on these resonances can be decreased by increasing the ionic strength of the solution (Figure 2B). Nevertheless, at a higher ionic strength also, α-syn interacts with HSA, but mostly by residues located on its amphipathic N-terminus, as shown by the intensity decrease of the amide cross-peaks of residues Lys10, Glu13, and Val15 (Figure 2B). Another different behavior was observed in PBS, at a more physiological salt concentration and pH value. In this environment, α-syn is still able to slightly interact with HSA by its C-terminus, but the interaction is mainly located at the N-terminus (Figure 2C), with a pattern similar to that previously reported in the literature,[35] where the interaction of BSA with α-syn was evaluated in PBS buffer. The region Val3−Lys8 (there is no information available for residues 1, 2) seems to be particularly involved in this interaction. The residues highlighted in Figure 2C are different with respect to those highlighted in Figure 2B, probably due to the pH change (from pH 6.0 to 7.4) and the slight difference in ionic strength.

CONCLUSIONS

In conclusion, HSA, at the concentration found in human serum, slows the aggregation of α-syn significantly, supporting the hypothesis of the chaperone-like behavior of HSA. α-Syn is found to interact with HSA in an ionic strength- and pH-dependent manner.

In KPi buffer, pH 6.0, at low ionic strength (50 mM NaCl), α-syn binds HSA with its negatively charged C-terminus (Figure 4A), especially involving the region from Glu123 to

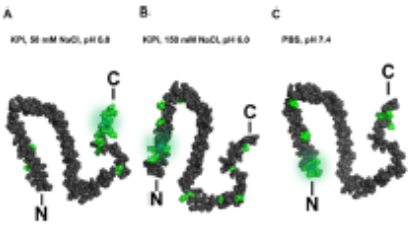

Figure 4. Residues experiencing the largest effects are highlighted in green on the α-syn structure (PDB code: 2KKW, conformer no. 13). (A) KPi buffer (50 mM NaCl, pH 6.0), (B) KPi buffer (150 mM NaCl, pH 6.0), and (C) PBS buffer (137 mM NaCl, pH 7.4).

Ala140. Conversely, with the addition of 100 mM NaCl to the solution, the intensity of many signals belonging to the C-terminus is restored and the dominant effect involves residues located in the N-terminus (Figure 4B), with Lys10, Glu13, and Val15 being the residues with the most decreased signal intensities in the 2D ^{1}H−^{15}N HSQC spectrum. Under physiological conditions (Figure 4C), the interaction is mainly located at the amphipathic N-terminus of α-syn, in the region Val3−Lys8 with a weak residual interaction at the C-terminus involving Asn122−Glu123 and Tyr133−Glu137. The absence of relevant chemical shift variations or appearance of new peaks in ^{15}N−^{1}H HSQC experiments, both in low and physiological ionic strength environments, suggests that the interaction between HSA and monomeric α-syn occurs in the intermediate exchange regime, thus with a dissociation constant in the low micromolar range, assuming a diffusion-controlled association regime.[36] However, the interactions involving intrinsically disordered proteins like α-syn are generally heterogeneous, difficult to characterize, and only upper limits can be usually provided for affinity and dissociation constants.[37] We thus hypothesize that HSA, due to its high concentration, could bind monomeric α-syn in serum on its N-terminus and impede its aggregation, in a manner similar to that observed for Aβ.[18,20,37] The extended t_0 and t_{lag} of the ThT aggregation profiles and the direct interaction with the α-syn monomer observed by NMR imply a possible stabilization of α-syn monomers[38] that interferes with the primary nucleation and elongation of the aggregates.[39−41] However, the observed direct interaction between HSA and monomeric α-syn does not exclude the possibility that other mechanisms involving oligomeric and prefibrillar intermediates may contribute to the observed antiaggregatory effect of HSA on α-syn fibrillization. The data reported in Figure 1 and Table S1 show that apart from the strong effect on t_0 and t_{lag}, the addition of HSA also produced a general decrease in the fitted $A_1 - A_2$ parameter of eq 1, which may be a consequence of both the interaction of HSA with α-syn monomers and the interaction with oligomeric or

DOI: 10.1021/acs.jpcb.9b02381
J. Phys. Chem. B 2019, 123, 4380−4386

prefibrillar intermediates. Generally, the presence of negatively charged proteins at high concentration may also lead to an overall increased repulsion in solution and increased solution stability, which may also contribute to α-syn aggregation inhibition, particularly in low-ionic-strength environments.[42] The characterization of the partnership between α-syn and HSA is not only a first step in the comprehension of the proteostasis of α-syn in biological fluids, but should be also considered in the development of α-syn PMCA and RT-QuIC assays. The albumin content in CSF varies among patients, because of the different blood−brain barrier permeabilities and/or blood contamination of samples.[43] Altered HSA levels in CSF may modulate α-syn aggregation differently, increasing false-negative and positive results in the clinical trials of these assays. Excluding blood-contaminated samples or normalizing the protein content of CSF samples prior to the analysis (by diluting samples with a higher protein content of or by adding HSA in samples with a lower protein content) may compensate for this effect.

■ ASSOCIATED CONTENT

Supporting Information

The Supporting Information is available free of charge on the ACS Publications website at DOI: 10.1021/acs.jpcb.9b02381.

ThT f profiles of α-syn in PBS in the presence of HSA and HSA alone, normalized on the unbound ThT fluorescence; ThT aggregation profile of α-syn in PBS in the presence of 4.5 μM HSA; t_0, t_{lag}, and $A_2 - A_1$ parameters measured for the experiments performed; portions of 2D $^{15}N-^{1}H$ HSQC spectra performed in KPi and PBS; intensity ratios of peaks coming from 2D $^{15}N-^{1}H$ HSQC experiments performed in KPi at different concentrations of NaCl, in KPi at 100 μM HSA, in KPi and PBS at 640 μM HSA, and in KPi with native and fatty-acid-free HSA (PDF)

■ AUTHOR INFORMATION

Corresponding Authors

*E-mail: lucilla.parnetti@unipg.it. Phone: +39 0755783545 (L.C.).

*E-mail: fragai@cerm.unifi.it. Phone: +39 055 4574261 (M.F.).

*E-mail: claudioluchinat@cerm.unifi.it. Phone: +39 055 4574296 (C.L.).

ORCID

Giovanni Bellomo: 0000-0003-0456-5650

Enrico Ravera: 0000-0001-7708-9208

Marco Fragai: 0000-0002-8440-1690

Claudio Luchinat: 0000-0003-2271-8921

Notes

The authors declare no competing financial interest.

■ ACKNOWLEDGMENTS

This work was supported by ERA-NET NEURON ABETA ID, MIUR PRIN 2012SK7ASN, Fondazione Cassa di Risparmio di Firenze, MEDINTECH (CTN01_001177_962865), the University of Florence CERM-TT, Recombinant Proteins JOY-NLAB and Instruct-ERIC, an ESFRI Landmark, supported by national member subscriptions. Specifically, we thank the Instruct-ERIC Core Centre CERM, Italy.

■ REFERENCES

(1) Spillantini, M. G.; Schmidt, M. L.; Lee, V. M.; Trojanowski, J. Q.; Jakes, R.; Goedert, M. Alpha-Synuclein in Lewy Bodies. *Nature* **1997**, *388*, 839−840.

(2) Malek, N.; Swallow, D.; Grosset, K. A.; Anichtchik, O.; Spillantini, M.; Grosset, D. G. Alpha-Synuclein in Peripheral Tissues and Body Fluids as a Biomarker for Parkinson's Disease − a Systematic Review. *Acta Neurol. Scand.* **2014**, *130*, 59−72.

(3) Kang, W.; Chen, W.; Yang, Q.; Zhang, L.; Zhang, L.; Wang, X.; Dong, F.; Zhao, Y.; Chen, S.; Quinn, T. J.; et al. Salivary Total α-Synuclein, Oligomeric α-Synuclein and SNCA Variants in Parkinson's Disease Patients. *Sci. Rep.* **2016**, *6*, DOI: 10.1038/srep28143.

(4) Farotti, L.; Paciotti, S.; Tasegian, A.; Eusebi, P.; Parnetti, L. Discovery, Validation and Optimization of Cerebrospinal Fluid Biomarkers for Use in Parkinson's Disease. *Expert Rev. Mol. Diagn.* **2017**, *17*, 771−780.

(5) El-Agnaf, O. M. A.; Salem, S. A.; Paleologou, K. E.; Curran, M. D.; Gibson, M. J.; Court, J. A.; Schlossmacher, M. G.; Allsop, D. Detection of Oligomeric Forms of Alpha-Synuclein Protein in Human Plasma as a Potential Biomarker for Parkinson's Disease. *FASEB J.* **2006**, *20*, 419−425.

(6) Barbour, R.; Kling, K.; Anderson, J. P.; Banducci, K.; Cole, T.; Diep, L.; Fox, M.; Goldstein, J. M.; Soriano, F.; Seubert, P.; et al. Red Blood Cells Are the Major Source of Alpha-Synuclein in Blood. *Neurodegener. Dis.* **2008**, *5*, 55−59.

(7) Shi, M.; Liu, C.; Cook, T. J.; Bullock, K. M.; Zhao, Y.; Ginghina, C.; Li, Y.; Aro, P.; Dator, R.; He, C.; et al. Plasma Exosomal α-Synuclein Is Likely CNS-Derived and Increased in Parkinson's Disease. *Acta Neuropathol.* **2014**, *128*, 639−650.

(8) Sui, Y.-T.; Bullock, K. M.; Erickson, M. A.; Zhang, J.; Banks, W. A. Alpha Synuclein Is Transported into and out of the Brain by the Blood−Brain Barrier. *Peptides* **2014**, *62*, 197−202.

(9) Lee, H.-J.; Bae, E.-J.; Lee, S.-J. Extracellular α-Synuclein—a Novel and Crucial Factor in Lewy Body Diseases. *Nat. Rev. Neurol.* **2014**, *10*, 92−98.

(10) Eusebi, P.; Giannandrea, D.; Biscetti, L.; Abraha, I.; Chiasserini, D.; Orso, M.; Calabresi, P.; Parnetti, L. Diagnostic Utility of Cerebrospinal Fluid α-Synuclein in Parkinson's Disease: A Systematic Review and Meta-Analysis. *Mov. Disord.* **2017**, *32*, 1389−1400.

(11) Cerri, S.; Ghezzi, C.; Sampieri, M.; Siani, F.; Avenali, M.; Dornini, G.; Zangaglia, R.; Minafra, B.; Blandini, F. The Exosomal/Total α-Synuclein Ratio in Plasma Is Associated With Glucocerebrosidase Activity and Correlates With Measures of Disease Severity in PD Patients. *Front. Cell. Neurosci.* **2018**, *12*, No. 125.

(12) Paciotti, S.; Bellomo, G.; Gatticchi, L.; Parnetti, L. Are We Ready for Detecting α-Synuclein Prone to Aggregation in Patients? The Case of "Protein-Misfolding Cyclic Amplification" and "Real-Time Quaking-Induced Conversion" as Diagnostic Tools. *Front. Neurol.* **2018**, *9*, No. 415.

(13) Shahnawaz, M.; Tokuda, T.; Waragai, M.; Mendez, N.; Ishii, R.; Trenkwalder, C.; Mollenhauer, B.; Soto, C. Development of a Biochemical Diagnosis of Parkinson Disease by Detection of α-Synuclein Misfolded Aggregates in Cerebrospinal Fluid. *JAMA Neurol.* **2017**, *74*, 163−172.

(14) Groveman, B. R.; Orrù, C. D.; Hughson, A. G.; Raymond, L. D.; Zanusso, G.; Ghetti, B.; Campbell, K. J.; Safar, J.; Galasko, D.; Caughey, B. Rapid and Ultra-Sensitive Quantitation of Disease-Associated α-Synuclein Seeds in Brain and Cerebrospinal Fluid by ASyn RT-QuIC. *Acta Neuropathol. Commun.* **2018**, *6*, 7.

(15) Fairfoul, G.; McGuire, L. I.; Pal, S.; Ironside, J. W.; Neumann, J.; Christie, S.; Joachim, C.; Esiri, M.; Evetts, S. G.; Rolinski, M.; et al. Alpha-Synuclein RT-QuIC in the CSF of Patients with Alpha-Synucleinopathies. *Ann. Clin. Transl. Neurol.* **2016**, *3*, 812−818.

(16) Tibbling, G.; Link, H.; Öhman, S. Principles of Albumin and IgG Analyses in Neurological Disorders. I. Establishment of Reference Values. *Scand. J. Clin. Lab. Invest.* **1977**, *37*, 385−390.

(17) Fanali, G.; di Masi, A.; Trezza, V.; Marino, M.; Fasano, M.; Ascenzi, P. Human Serum Albumin: From Bench to Bedside. *Mol. Aspects Med.* **2012**, *33*, 209−290.

Supplementary Information

Dissecting the interactions between human serum albumin and α-synuclein: new insights on the factors influencing α-synuclein aggregation in biological fluids

Giovanni Bellomo,[†] Sara Bologna,[†] Linda Cerofolini,[†] Silvia Paciotti,[§] Leonardo Gatticchi,[§] Enrico Ravera,[†,‡] Lucilla Parnetti,[∥] Marco Fragai[†,‡] and Claudio Luchinat[†,‡**]*

[†] *Magnetic Resonance Center (CERM), University of Florence, Via L. Sacconi 6, 50019 Sesto Fiorentino, Italy*

[‡] *Department of Chemistry "Ugo Schiff", University of Florence, Via della Lastruccia 3, 50019 Sesto Fiorentino, Italy*

[§] Department of Experimental Medicine, University of Perugia, Piazzale Gambuli 1, 06132 Perugia, Italy

[∥] *Clinica Neurologica, Università degli Studi di Perugia, Piazzale Gambuli 1, 06132 Perugia, Italy*

*E-mail: lucilla.parnetti@unipg.it. Phone: +39 0755783545.

**E-mail: fragai@cerm.unifi.it. Phone: +39 055 4574261.

***E-mail: claudioluchinat@cerm.unifi.it. Phone: +39 055 4574296.

Contents

Details relative to ThT aggregation experiments

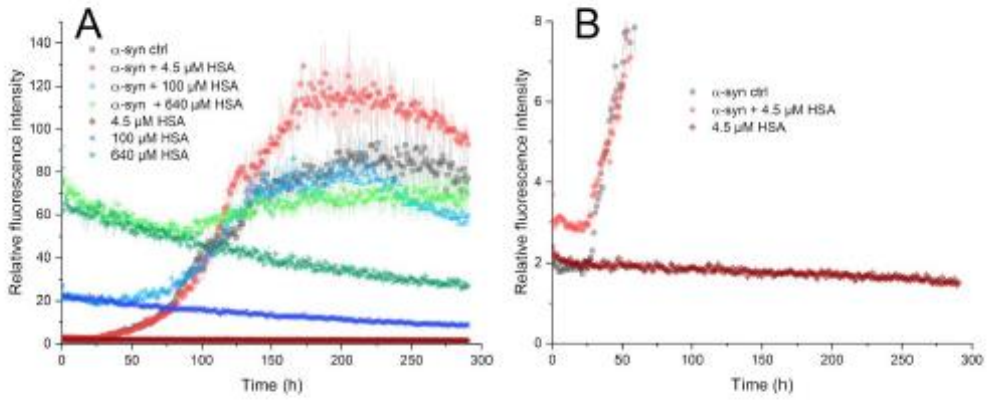

*Fig. S1 (A) Monomeric α-syn (100 μM) was left aggregating in the presence of ThT (10 μM) and varying quantities of HSA. Wells containing only HSA and ThT were also prepared to measure the baseline fluorescence produced by ThT bound to HSA. The experiments were performed in triplicate in a 96-wells plate in PBS pH 7.4, T = 310 K. 6*1mm diameter glass beads were added in each well. The plate was subjected to cycles of shaking (1 min. shaking 500 rpm, 29 min. rest) inside a BMG Labtech ClarioStar fluorimeter. In this experiment, we observed a progressive decay of fluorescence in the samples containing 100 μM and 640 μM HSA. The average fluorescence among replicates of samples with and without α-syn is shown in the image normalized on the average fluorescence value of the wells containing 10 μM of unbound ThT in PBS (195 a.u ± 8 a.u. constant for the whole duration of the experiment) to better appreciate the fluorescence enhancement. (B) Zoom on the low fluorescence intensity to better visualize the behaviour of the 4.5 μM HSA samples.*

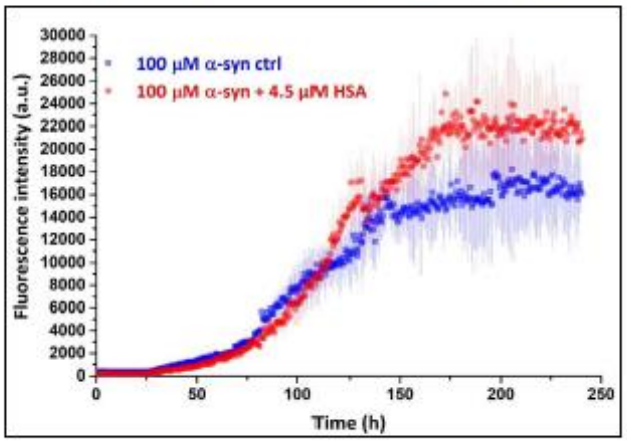

*Fig. S2 Monomeric α-syn (100 μM) was left aggregating in the presence of ThT (10 μM) and HSA (4.5 μM). The experiments were performed in triplicate in a 96-wells plate in PBS pH 7.4, T = 310 K. 6*1mm diameter glass beads were added to the samples. The plate was subjected to cycles of shaking (1 min. shaking 500 rpm, 29 min. rest) inside a BMG Labtech ClarioStar fluorimeter.*

The measured t_{lag}, t_0 and A_1-A_2 parameters are shown in Table S1. The values in this table were measured on not averaged and not normalized curves with the methods described in the main text, in particular the t_0 and A_1-A_2 parameters were measured by fitting the data with a sigmoidal function (Eq. 1 in the main text) and the t_{lag} values by applying a threshold on the experimental intensities. Apart from the increase in t_0 and t_{lag} values, also the levels of fluorescence, quantified by the A_1-A_2 parameter, appear lower in samples containing 640 μM HSA with respect to samples containing only α-syn (Fig. S3 and Table S1). Although ThT fluorescence is a good probe for fibril formation, caution should be use in interpreting this result, since HSA competes with α-syn fibrils in binding ThT.

Experiment	HSA (μM)	t_0 (h)	t_{lag} (h)	A_2-A_1 (a.u.)
50 μM α-syn KPi, pH 6.0	0	86 ± 6	27 ± 1	$(4.2 \pm 1.4) \cdot 10^3$
	50	135 ± 9	29 ± 2	$(5 \pm 1) \cdot 10^3$
	640	167 ± 4	119 ± 4	$(7.2 \pm 0.7) \cdot 10^2$
100 μM α-syn PBS, pH 7.4	0	105 ± 2	28.3 ± 0.4	$(1.7 \pm 0.2) \cdot 10^4$
	4.5	116 ± 3	30 ± 1	$(2.2 \pm 0.2) \cdot 10^4$
	100	114 ± 2	61 ± 1	$(1.33 \pm 0.07) \cdot 10^4$
	640	141 ± 6	130 ± 10	$(8 \pm 2) \cdot 10^3$

Table S1 t_0, t_{lag} and A_2-A_1 parameters for the experiments performed with 50 μM α-syn in 20 mM KPi, 50 mM NaCl, pH 6.0, T = 310 K and 100 μM α-syn in PBS, pH 7.4, T = 310 K. The values present in the table result from the average on three replicates while their uncertainty corresponds to the standard deviation of the average value.

NMR experiments

All the NMR spectra were acquired at 283 K with a Bruker Avance III HD NMR spectrometer operating at 950 MHz ^{1}H Larmor frequency, equipped with a cryogenically cooled probe. The spectra were processed with the Bruker TOPSPIN 4.0 software packages and analysed by the program Computer Aided Resonance Assignment [8]. During the NMR titration of the protein with HSA, 3 aliquots of a concentrated 8 mM solution of HSA (same buffer conditions of the final samples) were added to the buffered solution containing ^{15}N isotopically enriched α-syn at the concentration of 100 μM. The tested buffered solutions were: [20 mM KPi, pH 6.0 with 50, 100 and 150 mM NaCl] and PBS (pH 7.4). For the NMR experiments, standard 3 mm glass tubes were used with a final sample volume of of 200 μL. The added volumes of the HSA solution were 2.5, 16 and 22.5 μL for the 100, 640 and 900 μM samples, respectively, in all the buffer used. While testing the electrostatic nature of the interaction between α-syn and HSA, also 2 μL and 4 μL of a solution of 20 mM KPi, pH 6.0 with 5 M NaCl were added in the NMR tube containing 100 μM α-syn and 900 μM HSA, to reach the final concentration of 100 and 150 mM NaCl, respectively. The data relative to the 100 mM NaCl sample are shown in Fig. S5B. At this ionic strength, the intensity reduction observed at the C-terminus of α-syn was less evident compared to the 50 mM NaCl sample but not completely disappeared as in the 150 mM sample.

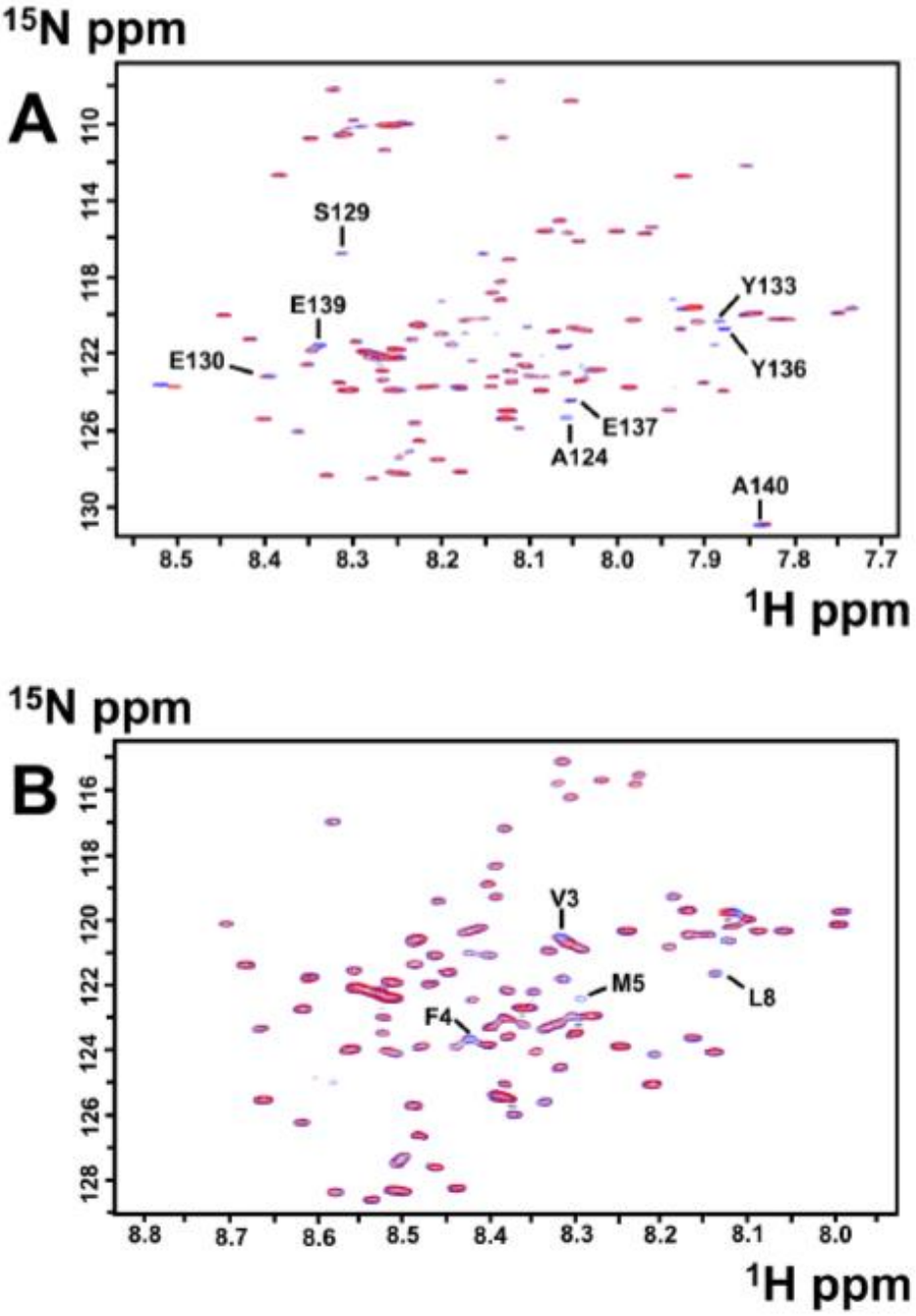

Fig. S3 Portion of 2D ^{15}N ^{1}H HSQC experiments performed at T = 283 K using a Bruker Avance III HD 950 MHz NMR spectrometer in different buffer conditions. The spectra coloured in red correspond to samples containing α-syn (100 μM) and HSA (900 μM) while the ones in blue correspond to the reference samples containing α-syn (100 μM) alone. (A) Experiment performed in 20 mM KPi, 50 mM NaCl pH 6.0 with α-syn (100 μM) and HSA (900 μM). (B) Experiment performed PBS pH 7.4 with α-syn (100 μM) and HSA (900 μM). The residues which showed an evident decrease in intensity are displayed on the image.

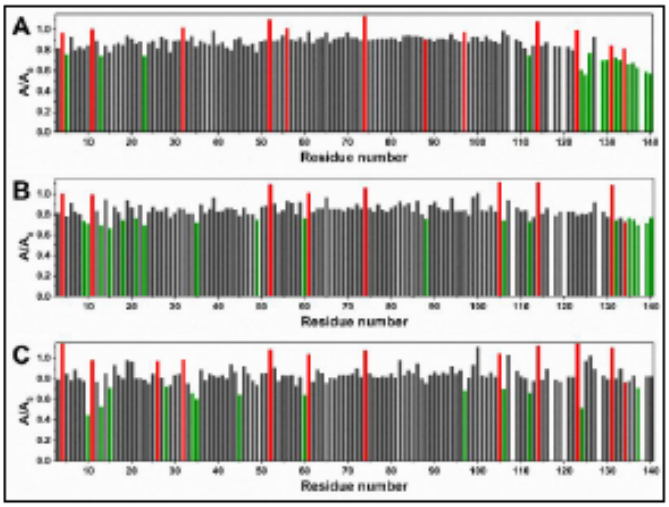

Fig. S4 Intensity ratios of peaks coming from 2D ^{15}N ^{1}H HSQC experiments performed at T = 283 K using a Bruker Avance III HD 950 MHz NMR spectrometer at different NaCl concentrations. The intensity values were computed with CARA (Computer Aided Resonance Assignment). The ratios highlighted in green are the ones which are smaller by one or more standard deviation with respect to the average value. The ratios highlighted in red correspond to peaks in overlap, their values were not used to calculate averages and standard deviations. (A) Experiment performed in 20 mM KPi, 50 mM NaCl, pH 6.0 with α-syn (100 μM) and HSA (900 μM). (B) Experiment performed in 20 mM KPi, 100 mM NaCl, pH 6.0 with α-syn (100 μM) and HSA (900 μM). (C) Experiment performed in 20 mM KPi, 50 mM NaCl, pH 6.0 with α-syn (100 μM) and HSA (900 μM).

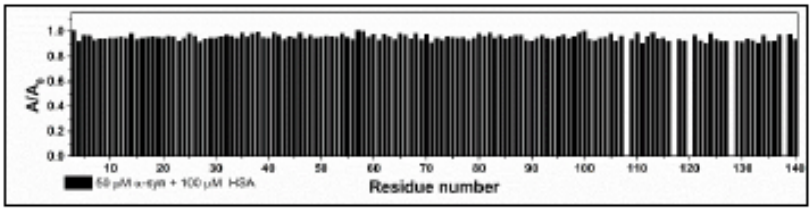

Fig. S5 Intensity ratios of peaks coming from 2D ^{15}N ^{1}H HSQC experiments performed at T = 283 K using a Bruker Avance III HD 950 MHz NMR spectrometer. The intensity values were computed with CARA (Computer Aided Resonance Assignment). The experiment was performed in 20 mM KPi, 50 mM NaCl, pH 6.0 with α-syn (100 μM) and HSA (100 μM). No relevant drops in intensity were observed with respect to the reference spectrum.

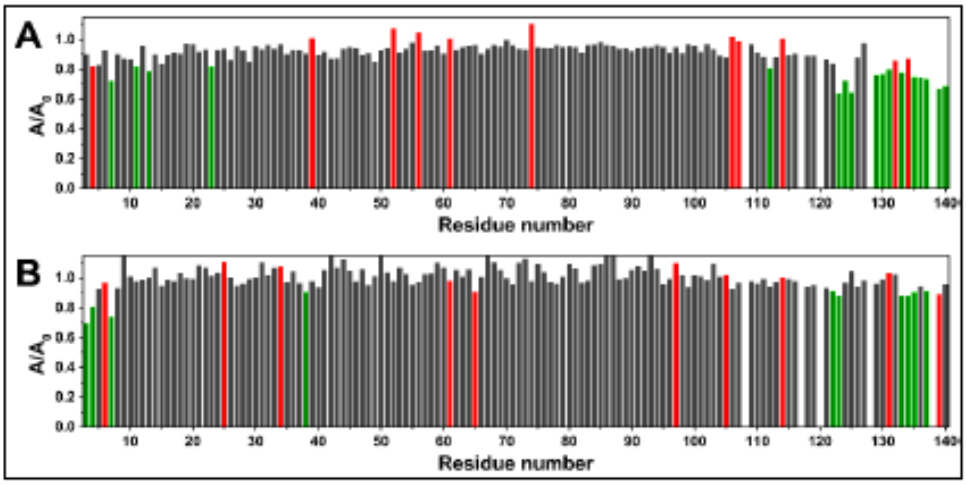

Fig. S6 Intensity ratios of peaks coming from 2D ^{15}N ^{1}H HSQC experiments performed at T = 283 K using a Bruker Avance III HD 950 MHz NMR spectrometer in different buffer conditions. The intensity values were computed with CARA (Computer Aided Resonance Assignment). The ratios highlighted in green are the ones which are smaller by one or more standard deviation with respect to the average value. The ratios highlighted

in red correspond to peaks in overlap, their values were not used to calculate averages and standard deviations. (A) Experiment performed in 20 mM KPi, 50 mM NaCl, pH 6.0 with α-syn (100 μM) and HSA (640 μM). (B) Experiment performed in PBS pH 7.4 with α-syn (100 μM) and HSA (640 μM).

Test with fatty-acid free HSA

To test if the lipids naturally included in HSA may have a role in its interaction with α-syn, we repeated the NMR interaction experiment with fatty acid free HSA in 20 mM KPi, 50 mM NaCl, pH 6.0 with α-syn (100 μM). The measured intensity ratios (Fig. S7) for fatty acid free HSA do not show significative differences with respect to the ratios obtained with native HSA. The rooted mean squared ratio difference is about 0.06 and mainly due to an almost negligible offset in intensity ratios which may be provoked by very small differences in the experimental setup (slightly different shims with respect to the reference spectrum, concentration differences, etc.).

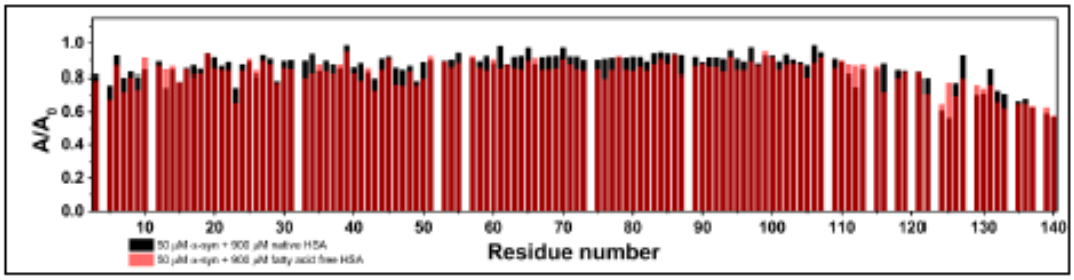

Fig. S7 Intensity ratios of peaks coming from 2D ^{15}N ^{1}H HSQC experiments performed at T = 283 K using a Bruker Avance III HD 950 MHz NMR spectrometer. The intensity values were computed with CARA (Computer Aided Resonance Assignment). The ratios corresponding to peaks in overlap, were excluded from the graph. The experiment was performed in 20 mM KPi, 50 mM NaCl, pH 6.0 with α-syn (100 μM) and native (black) and fatty-acid free (red) HSA (900 μM).

References

[1] V.E. Shevchik, G. Condemine, J. Robert-Baudouy, Characterization of DsbC, a periplasmic protein of Erwinia chrysanthemi and Escherichia coli with disulfide isomerase activity., EMBO J. 13 (1994) 2007–2012. https://www.ncbi.nlm.nih.gov/pmc/articles/PMC395043/ (accessed May 16, 2018).

[2] C. Huang, G. Ren, H. Zhou, C. Wang, A new method for purification of recombinant human alpha-synuclein in Escherichia coli, Protein Expr. Purif. 42 (2005) 173–177. doi:10.1016/j.pep.2005.02.014.

[3] S.L. Shammas, T.P.J. Knowles, A.J. Baldwin, C.E. MacPhee, M.E. Welland, C.M. Dobson, G.L. Devlin, Perturbation of the Stability of Amyloid Fibrils through Alteration of Electrostatic Interactions, Biophys. J. 100 (2011) 2783–2791. doi:10.1016/j.bpj.2011.04.039.

[4] J.A. Cohlberg, J. Li, V.N. Uversky, A.L. Fink, Heparin and other glycosaminoglycans stimulate the formation of amyloid fibrils from alpha-synuclein in vitro, Biochemistry. 41 (2002) 1502–1511.

[5] L. Giehm, D.E. Otzen, Strategies to increase the reproducibility of protein fibrillization in plate reader assays, Anal. Biochem. 400 (2010) 270–281. doi:10.1016/j.ab.2010.02.001.

[6] M. Shahnawaz, T. Tokuda, M. Waragai, N. Mendez, R. Ishii, C. Trenkwalder, B. Mollenhauer, C. Soto, Development of a Biochemical Diagnosis of Parkinson Disease by Detection of α-Synuclein Misfolded Aggregates in Cerebrospinal Fluid, JAMA Neurol. 74 (2017) 163–172. doi:10.1001/jamaneurol.2016.4547.

[7] N.R. Rovnyagina, N.N. Sluchanko, T.N. Tikhonova, V.V. Fadeev, A.Y. Litskevich, A.A. Maskevich, E.A. Shirshin, Binding of thioflavin T by albumins: An underestimated role

of protein oligomeric heterogeneity, Int. J. Biol. Macromol. 108 (2018) 284–290. doi:10.1016/j.ijbiomac.2017.12.002.
[8] R.L.J. Keller, Optimizing the process of nuclear magnetic resonance spectrum analysis and computer aided resonance assignment, Doctoral Thesis, ETH Zurich, 2005. doi:10.3929/ethz-a-005068942.

3.5 Human plasma HDL prevents the formation of α-synuclein oligomers and fibrils (manuscript in preparation)

This project, as well as the research focused on the study of the interaction between α-synuclein and HSA, was born from some unexpected observations coming from α-synuclein aggregation experiments in presence of CSF: the aggregation process was significantly and reproducibly slowed down, due to the interaction of α-synuclein with high-molecular weight compounds present in this human biofluid. The antiaggregatory effect of CSF on α-synuclein was tested by SAA by adding aliquots of CSF coming from neurological controls (see Fig. 3.3.5 A).

Since was excluded that effect observed for CSF could have been caused by HSA, an investigation of the role of lipoproteins (abundant high-molecular weight constituents of CSF and plasma), was started.

Lipoproteins are complex particles with a central hydrophobic core of non-polar lipids (primarily cholesterol esters and triglycerides), surrounded by a hydrophilic membrane consisting of phospholipids, free cholesterol and apolipoproteins. Lipoproteins are divided into seven classes based on size, lipid composition, and apolipoprotein content.

In particular, the tested compound in this work was HDL (High Density Lipoprotein).

To characterize this interaction, SAA and NMR investigations were exploited.

My role in this project mainly concerned the expression and purification of high quality samples α-synuclein both for aggregation and interaction experiments.

Introduction

Lipoproteins are complex particles composed of multiple proteins that transport lipids around the body within the aqueous environment outside the cells. High-density lipoproteins (HDL) are the smallest particles among the five major groups of lipoproteins (10–22 nm),[1–3] they are also the most dense because the high protein content with respect to the lipid part. The most characterized and most abundant protein constituents of HDL are apolipoprotein-A1 (apoA1) and apolipoprotein-E (apoE).[4] The Central Nervous System apoE is completely brain-specific, and there is no exchange between plasma-derived apoE and brain apoE because of the boundary of the Brain-Blood Barrier (BBB).[5] Also due to the different composition in terms of apolipoproteins, the CSF HDL are bigger in size than plasma HDL and smaller than Low-Density Lipoproteins (LDL), their density is between LDL and HDL.[3],[6-7] While apoE is found to be the main constituent of HDL particles in CSF, apoA1 is the main constituent of HDL in plasma.[2],[8] However, apoA1 also contributes for lipid transportation and delivery in the brain and the apoA1 levels of CSF and plasma have been shown to be correlated.[9] Since there is no evidence of apoA1 synthesis in the brain, apoA1 or apoA1 rich HDL, in contrast to apoE, is thought to be able to cross the BBB.[4] HDL are reported have an impact in many neurodegenerative disorders. apoE plays a crucial role in AD, mild cognitive impairment and Creutzfeldt-Jakob disease (CJD).[10-11] In particular, the APOE ε4 allele is strongly associated with the sporadic late-onset AD.[12-14] Conversely, no association was found between apoE and PD,[15] while lower levels of apoA1 were rather measured in the plasma of PD patients with respect to controls.[16-18] These findings were confirmed again in late 2015, when plasma apoA1 and high-density lipoprotein at baseline were measured in 254 research volunteers (154 patients with PD and 100 normal controls) enrolled in the Parkinson's Progression Markers Initiative (PPMI)[19] study (without any ongoing levodopa treatment). In this latter study, lower levels of apoA1 were found to be associated with the age of PD onset and severity of motor symptoms (p-values < 0.05),[20] suggesting that apoA1 or apoA1-rich lipoproteins may be both a protective factor and a candidate biomarker for PD. The mechanism underlying the protective role of HDL in neurodegenerative diseases remains unknown but, for AD, it seems to be intimately linked to increased risk of brain Aβ aggregation in ε4

carriers.[21] Recently, CSF HDL was shown to retard Aβ42 aggregation in an apoE ε4-dependent manner.[22-23]In this study, the addition of CSF fractions containing HDL produced an extended lag-phase of the ThT fluorescence profiles, which implies an interference with the primary nucleation of the aggregates. Although the protective role of HDL was extensively investigated for AD, few previous studies have focused on the role of HDL in the context of PD and α-synuclein aggregation.[4] In this work we investigate the effect of plasma HDL, rich in apoA1 apolipoproteins, on α-synuclein aggregation and if the inhibitory effect of human CSF on α-synuclein aggregation may be produced by HDL. Our hypothesis is that these compounds naturally prevent the formation of fibrils and oligomers by interacting with α-synuclein aggregates and not directly with α-synuclein monomers.

Fluid matrix	apo E (mg/dl)	apo A1 (mg/dl)
CSF	0.3 ± 0.2 [24]	0.3 ± 0.2 [24]
	1.0 ± 0.1 [25]	0.33 ± 0.05 [25]
	0.4 ± 0.2 [26]	0.4 ± 0.2 [26]
	0.5 ± 0.3 [27]	0.3 ± 0.2 [27]
Plasma	7 ± 5 [24]	140 ± 50 [24]
	8 ± 1[27]	270 ± 20 [27]

Table 3.5.1: Reported values of Apolipoprotein E and A1 levels in CSF and plasma of healthy individuals.

Materials and Methods

α-synuclein expression and purification

Escherichia Coli BL21(DE3)Gold were transformed with pT7-7 vector cloned with the gene encoding α-synuclein. The overnight preculture of transformed cells was diluted 100-fold in LB medium and induced at an OD_{600} value of 0.6-0.8 with 1 mM Isopropyl-β-D-thiogalactoside and, after 5 hours incubation at 37 °C, the cells were harvested at 4000 rpm (JA-10, Beckman Coulter). The extraction was carried out through osmotic shock using 100 ml of buffer TRIS 30 mM, EDTA 2 mM and sucrose 40%, at pH 7.2 according to Shevchik et al.[28] and Huang et al.[29] . The suspension was then ultracentrifuged at 20000 rpm (Type 70 Ti rotor, Beckman Coulter) for 25 min and pellet was collected and resuspended with 90 ml precooled ultrapure water additioned with 38 µL of $MgCl_2$ 1 M and then ultracentrifuged a second time. Supernatants derived from these two centrifugation steps, were

joined and dialyzed against 4 L of buffer 20 mM TRIS/HCl at pH 8.0. The protein then was loaded in the FPLC system and an anion exchange chromatography was carried out with 0-50% linear gradient NaCl 1 M (GE Healthcare HiPrep™ Q HP 16/10 Column). The collected fractions were lyophilized and resuspended in 10 mM TRIS/HCl, 1 mM EDTA and Urea 8 M at pH 8.0 for the chemical denaturation. To eliminate all the protein formed aggregates, two size-exclusion chromatographies (HiLoad™ 16/600 Superdex™ 75 pg Column) were performed with 20 mM phosphate and 0.5 mM EDTA at pH 8.0 as elution buffer. Purified α-synuclein (α-synuclein) was dialyzed against Milli-Q water and lyophilized in batches for long-term storage. Roche cOmplete™ protease inhibitor cocktail was added only during the extraction step in the quantity suggested by the producer.

α-synuclein aggregation experiments

The lyophilized aliquots α-synuclein were resuspended in NaOH 3.5 mM (pH 11.54) right before the experiments to avoid the instantaneous formation of aggregates. At high pH, the negatively charged monomers (the isoelectric point of α-synuclein is 4.67) experience an electrostatic repulsion that impedes the aggregation and favors the dissociation of small aggregates.[30],[31] The solution of α-synuclein and NaOH was brought to pH 7.4 and protein concentration of 100 μM by adding concentrated PBS buffer (e.g. 1 mL of NaOH solution with 1 mL of 2x PBS solution). Thioflavin-T was also added in a final concentration of 10 μM. To avoid the possible growth of bacteria during the experiment, a 0.08% of NaN_3 was present in the reaction buffer. We added different volumes of HDL derived from human plasma (LP3-5MG from SIGMA-ALDRICH, HDL concentration 11.64 mg/mL). Subsequently, each sample was split in 3 replicates of 200 μl each that were put in a *TECAN (REF: 30122306)* clear-bottom 96-well plate. We added 6 acid washed glass beads with a diameter of 1 mm in each well to enhance the aggregation speed and increase homogeneity among replicates.[32] The plates were always sealed with a sealing tape to minimize evaporation during the experiments. Successively, plates were inserted in a BMG LABTECH ClarioStar fluorimeter and subjected to the incubation/shaking protocol of Shahnawaz et al.[33] (T = 310 K, 29 min. incubation, 1 min. shaking at 500 rpm). Once every 30 minutes, the

fluorescence was read from the bottom using an excitation and emission wavelength of 450 nm and 480 nm, respectively.

Dot blot assays

The dot blot assay was performed using A11 anti-oligomer antibodies (ThermoFisher Scientific) and OC anti-fibril antibodies (Sigma-Aldrich) on the samples used for the fluorimetric assay, by collecting together the replicates for each concentration of HDL and HSA. Volumes of 2 µL of each sample where dropped on a nitrocellulose membrane, previously soaked with TBS-T (0.1%) and were let dry for 60 minutes. The substrate was then fixed to the membrane by soaking it in PBS with 0.4% PFA for 30 minutes. The blocking was subsequently performed by soaking the membrane in a solution of dry milk (2%) and TBS-T (0.1%) for 60 minutes at room temperature. The blocking buffer was then poured off and the membrane was incubated with A11/OC antibodies (1:1000) in a solution of dry milk (5%) and TBS-T (0.1%) at 4°C for 60 minutes. The membrane was then washed and incubated with HRP anti-rabbit secondary antibodies (1:5000) and a solution of dry milk (5%) and TBS-T (0.1%) for 30 minutes. The data were subsequently processed and analyzed using ImageJ.

NMR experiments

All the NMR spectra were acquired at 283 K with a Bruker Avance III HD NMR spectrometer operating at 950 MHz ^{1}H Larmor frequency, equipped with a cryogenically cooled probe. The spectra were processed with the Bruker TOPSPIN 4.0 software packages and analyzed by the program Computer Aided Resonance Assignment (ETH Zurich; Keller, 2004). During the NMR titration of α-synuclein with HDL, 1 aliquot (5 µL) of a concentrated 11.64 mg/mL solution of human HDL (LP3-5MG from SIGMA-ALDRICH) were added to the buffered solution containing ^{15}N isotopically enriched α-synuclein at the concentration of 100 µM in PBS (pH 7.4, 137 mM NaCl). For the NMR experiments, standard 3 mm glass tubes were used with a final sample volume of of 200 µL. We acquired a 1D ^{1}H experiment and 2D ^{1}H ^{15}N HSQC experiment[34] for both the sample containing HDL and the reference one.

Results and Discussion

To test the effects of HDL on α-synuclein aggregation we performed ThT aggregation experiments. In these kind of experiments, the ThT fluorophore reports the formation of fibril-like aggregates due to its affinity to the beta-sheet motifs typical of amyloid aggregates.[35] We applied the PMCA shaking/incubation protocol of Shahnawaz, Soto and coworkers[33] to speed-up the aggregation and added 6 glass beads (with a diameter of 1 mm) per well to further promote the aggregation process and increase the homogeneity among replicates (further details in the Materials and Methods section). The experiments were performed in well plates in triplicate (final volume of 200 µl per well), the control samples with α-synuclein alone consisted in 100 µM monomeric α-synuclein, 10 µM ThT and 0.08% of NaN_3 in PBS buffer. The samples containing HDL had the same composition except for the quantity of HDL that was of 12 mg/dL and 57 mg/dL respectively. We also prepared control samples containing 12 mg/dl and 57 mg/dL HDL without α-synuclein to subtract any possible background fluorescence. Although the background fluorescence was almost negligible, we subtracted the fluorescence data relative to samples containing only HDL (averaged on replicates) from the data relative to samples containing both α-synuclein and HDL (averaged on replicates). By looking at the ThT fluorescence profiles of Fig. 3.5.1, it is evident that the addition of increasing quantities of HDL to the solution had an impact on α-synuclein aggregation.

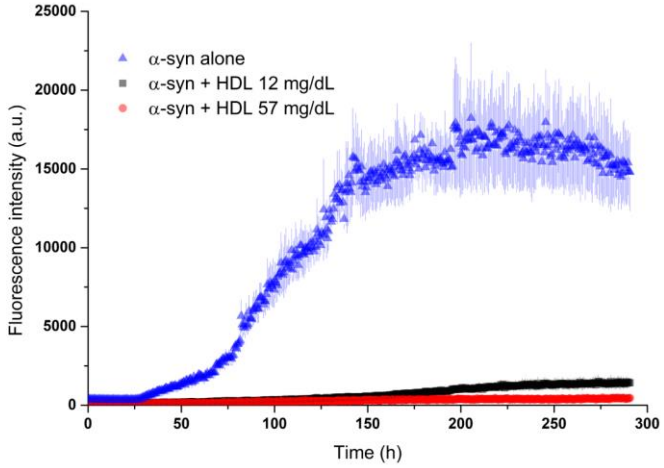

Fig. 3.5.1 Monomeric α-synuclein 100 μM was left aggregating in the presence of ThT 10 μM and increasing quantities of HDL. The experiments were performed in triplicate in a 96-wells plate in PBS pH 7.4, T = 310 K. Glass beads (6x 1mm diameter) were added to the samples. The plate was subjected to cycles of shaking (1 min. shaking 500 rpm, 29 min. rest) inside a BMG Labtech ClarioStar fluorimeter. The data shown are the averages of three replicates with background removed. The error bars were calculated as the standard deviation of the mean value calculated on the three replicates.

The kinetic profiles, which were used to produce the averaged curves depicted in Fig. 3.3.1, were fitted with Boltzmann's sigmoidal functions (Eq. 3.5.1), using *OriginPro 9*, in order to obtain an estimate of the aggregation time. In the non-linear curve fitting procedure used, the parameters A_1, A_2, t_0 and dt of Eq. 3.3.1 were let free.1111

$$y(t) = A_2 + \frac{A_1 - A_2}{1 + \exp\left(\frac{t - t_0}{dt}\right)} \tag{3.5.1}$$

The parameter t_0 corresponds to the inflection point of the sigmoidal curves used to fit the data and can be used to quantify the time necessary to produce a consistent quantity of fibrillary aggregates. Another parameter which can be useful to characterize *the speed of the aggregation is the time at which the fluorescence starts to deviate si*gnificantly from its initial value (t_{lag}). This parameter quantifies the time at which fibrils start to form. We defined it, in the same way of Paragraph 3.2, as the time at which the fluorescence (F) of a well becomes higher than the average fluorescence (on the same well) of the first 5 h ($\overline{F(t)}_{t<5\ h}$) plus 2 standard deviations (2σ) for 5 consecutive measurements:

$$F\left(t_{lag} + i\Delta t\right) \geq \overline{F(t)}_{t<5\ h} + 2\sigma\left(F(t)\right)_{t<5\ h};\ \forall\ i \in (0, 1, 2, 3, 4)$$

Where Δt is the time between two consecutive measurements. The measured t_0 and t_{lag} values, together with the A2-A1 values of the sigmoidal fitting, which report for the amplitude of the sigmoids, are reported in Table 3.5.2. In the Table, the values relative to the experiments performed in PBS with α-synuclein and HSA. Which were measured during the same acquisition, on the same plate and with the same batch of α-synuclein, are also reported for comparison.

Sample	t_{lag} (h)	t_0 (h)	A2 - A1 (a.u.)
α-synuclein alone	28.3 ± 0.5	105 ± 2	$(1.7 \pm 0.2) \cdot 10^4$
α-synuclein + 12 mg/dL HDL	44 ± 4	176 ± 6	$(1.4 \pm 0.3) \cdot 10^3$
α-synuclein + 58 mg/dL HDL	82 ± 7	119 ± 9	$(3.7 \pm 0.9) \cdot 10^2$
α-synuclein + 4.5 μM HAS	30 ± 1	116 ± 3	$(2.2 \pm 0.2) \cdot 10^4$
α-synuclein + 100 μM HSA	61 ± 1	114 ± 2	$(1.33 \pm 0.07) \cdot 10^4$
α-synuclein + 640 μM HSA	130 ± 10	141 ± 6	$(8 \pm 2) \cdot 10^3$

Table 3.5.2: Measured t_{lag}, t_0 and A1-A2 values for samples containing α-synuclein and different quantities of HDL and HSA.

While some differences on the t_0 parameters may be observed for samples containing HDL with respect for the samples containing α-synuclein alone, minor differences are present for the t_{lag} values. The most pronounced effect was rather the change of the maximum fluorescence value, quantified in Table 3.5.2 by the A2-A1 parameter. The measured amplitudes are also depicted in the column plot present in Fig. 3.5.2, which can better show the difference in the A2-A1 values of the sample containing α-synuclein and HDL from the ones containing α-synuclein and HSA or α-synuclein alone.

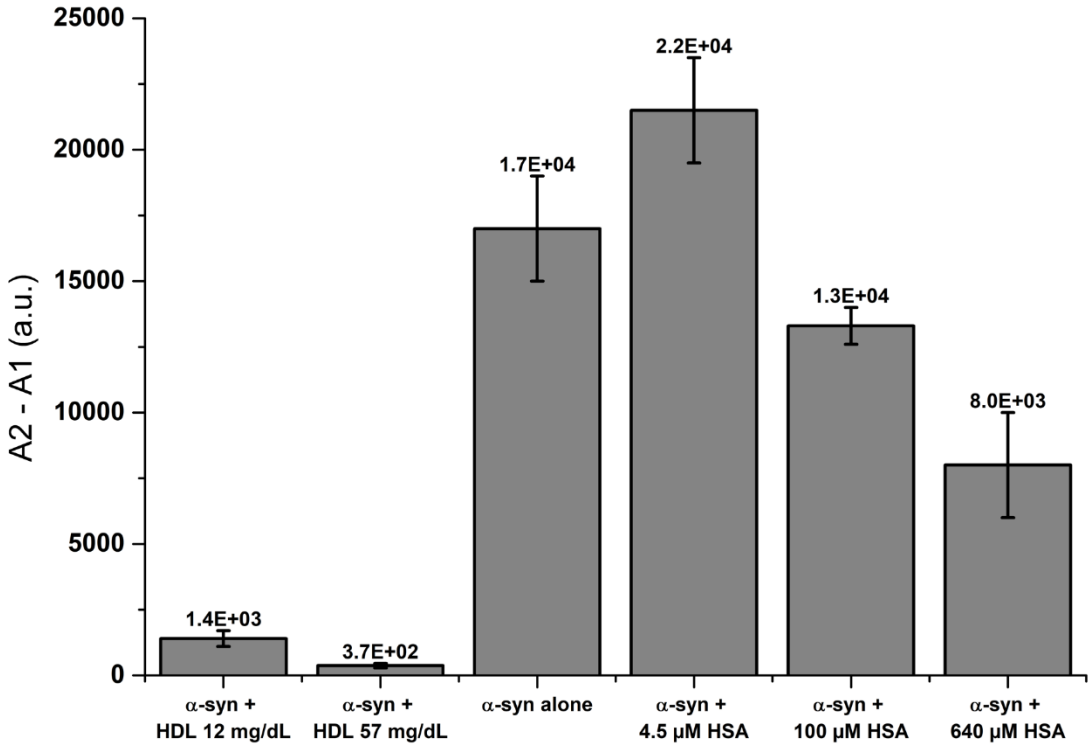

Fig. 4.5.2 Measured A1-A2 values coming from the sigmoidal fitting of the ThT profiles relative to samples containing α-synuclein and different quantities of HDL and HSA.

To better clarify if the much lower ThT intensity was produced by a lower quantity of aggregates we performed a dot blot on the samples containing HDL and HSA with OC and A11 antibodies.[36]

The OC and A11 antibodies bind to different oligomeric conformations: the OC antibody binds fibrils and fibrillary oligomers while the A11 is sensitive to more amorphous oligomeric aggregates. Particularly, A11 oligomers showed to be more toxic than the OC oligomers and recently showed the ability to impair the proteasome function[36]. As can be seen from Fig. 3.5.3 and Fig. 3.5.4, control samples without α-synuclein did not bind to any of the two antibodies, while the samples containing α-synuclein and HDL produced some OC and A11 oligomers but in a much lower quantity with respect to the samples containing α-synuclein and HSA. This result is in accord with the ThT measurements which reported a lower quantity of fibrils for samples containing α-synuclein and HDL.

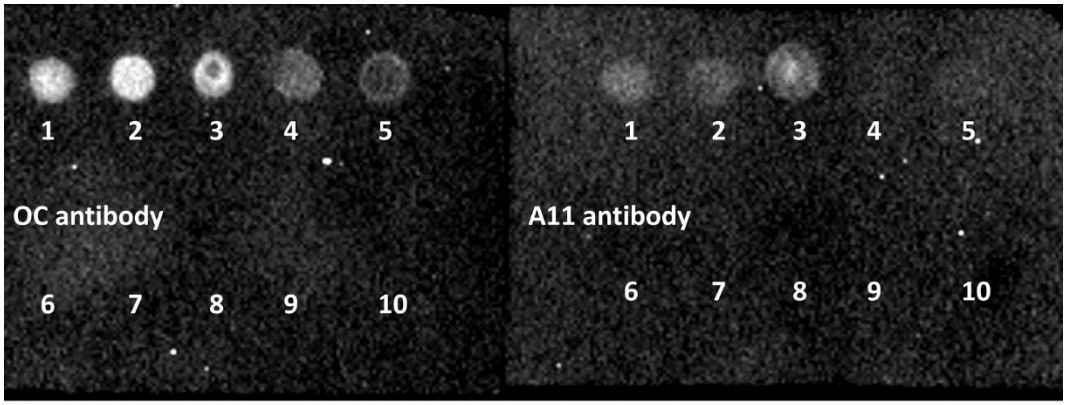

1 α-syn + 4.5 μM HSA **2** α-syn + 100 μM HSA **3** α-syn + 640 μM HSA
4 α-syn + 2 μL HDL (0.114 mg/ml) **5** α-syn + 10 μL HDL (0.57 mg/ml) **6** 4.5 μM HSA
7 100 μM HSA **8** 640 μM HSA **9** 2 μL HDL (12 mg/ml)
10 10 μL HDL (57 mg/dL)

Fig. 3.5.3 The dot blot assay was performed using A11 anti-oligomer antibodies and OC anti-fibril antibodies on the samples used for the fluorimetric assay which contained 100 μM α-synuclein and different amounts of HSA and HDL. The dot images were processed and analyzed with ImageJ. Control samples n° 6, 7, 8, 9 and 10 did not react with any of the two antibodies used.

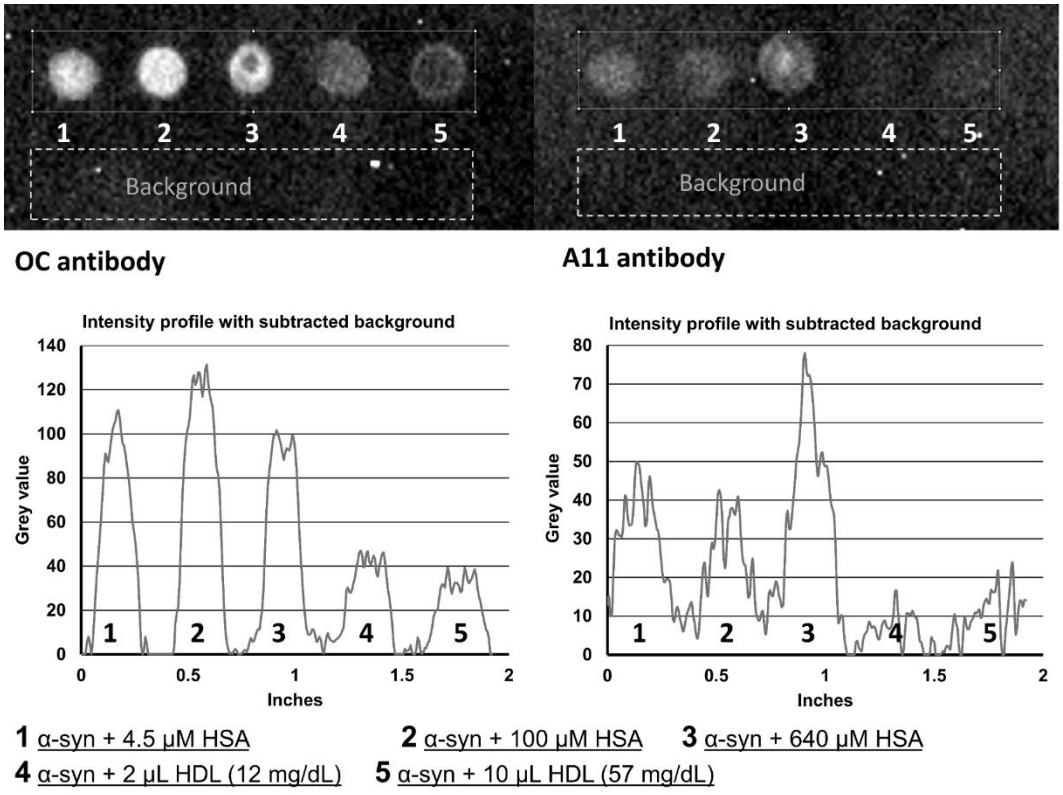

1 α-syn + 4.5 μM HSA **2** α-syn + 100 μM HSA **3** α-syn + 640 μM HSA
4 α-syn + 2 μL HDL (12 mg/dL) **5** α-syn + 10 μL HDL (57 mg/dL)

Fig. 3.5.4 The dot blot assay was performed using A11 anti-oligomer antibodies and OC anti-fibril antibodies on the samples used for the fluorimetric assay which contained 100 μM α-synuclein and different amounts of HSA and HDL. The dot images were processed (window/levels adjustments) and analyzed with ImageJ.

In 2017 Emamzadeh and Allsop[37] showed that α-synuclein, apoA1, apoJ and apoE could be detected by immunoprecipitation in plasma both with anti-α-synuclein and anti-apolipoprotein antibodies, suggesting a possible direct or indirect interaction between α-synuclein and plasma HDL. To test if the inhibitory effect of plasma HDL on α-synuclein aggregation could be produced by the direct interaction with α-synuclein monomer, we performed a 2D ^{15}N ^{1}H NMR HSQC experiment with ^{15}N isotopically enriched α-synuclein. After having acquired a reference spectrum with α-synuclein 100 μM in PBS pH 7.4 in a 3 mm diameter NMR tube (final sample volume 200 μl), we added 5 μL of human plasma HDL in the NMR tube (HDL final concentration 28.4 mg/dL, final sample volume 205 μL). No relevant shifts in the 2D ^{15}N ^{1}H NMR HSQC were observed so we evaluated the intensity ratios by dividing the amplitude of the crosspeaks relative to the experiment with HDL by the ones relative to the reference spectrum. The ratios calculated in this way (corrected for the dilution factor of α-synuclein) are shown in Fig. 4.5.5.

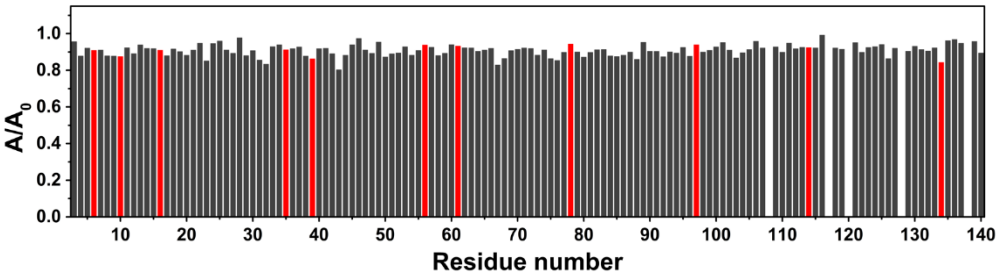

Fig. 3.5.5 Intensity decreases of the signals of 2D ^{15}N ^{1}H HSQC experiments acquired at 950 MHz on α-synuclein (100 μM) after the addition of 5 μl HDL (final concentration 28.5 mg/dL) at T = 283 K in PBS (NaCl 137 mM) pH 7.4. The intensity ratios corresponding to overlapping peaks are highlighted in red and should be not taken into account.

By considering the experimental uncertainties on the measure of the intensity of the crosspeaks, we can say, by looking at Fig. 3.5.5, that no relevant interactions were observed between the tested quantities of human plasma HDL particles and monomeric α-synuclein.

Conclusions

In our experiments human plasma HDL decreased significantly the quantity of fibrillary and oligomeric aggregates produced by α-synuclein. We did not observe any relevant interaction between monomeric α-synuclein and HDL from NMR

experiments. These findings suggest that the interaction between HDL and α-synuclein may not involve the primary nucleation of the aggregates and we hypothesize that HDL may instead interact with α-synuclein oligomers preventing them to grow and to convert into fibrillar amyloids. This observation is also in accord with the lag-time measurements, which are primarily influenced by primary nucleation effects[38] and showed lower t_{lag} values with respect to the experiments performed with HSA. ApoA1 is the main component of HDL in plasma but it is also necessary for cholesterol transportation in the central nervous system. The plasma level of apoA1 was found to be lower in PD patients than that in normal individuals, indicating a possible role for apoA1-deficency in the pathogenesis of PD.[39–41],[21] We hypothesize that apoA1-containig HDL, may have a protective role against PD, impeding the transmission and the growth of α-synuclein aggregates from cell to cell. Since from other works it was also shown that HDL particles are able to bind α-synuclein,[10] and from our data it seems that monomeric α-synuclein is not able to bind plasma HDL, apoA1 rich HDL may also be responsible for the transportation of small α-synuclein aggregates out of the brain. The antiaggregatory effect of plasma HDL on α-synuclein probably contributes to the antiaggregatory effect observed for human CSF on α-synuclein aggregation[33] . However, ApoA1 rich HDL is only one type of lipoproteins among the ones present CSF and we cannot exclude that VLDL, LDL or ApoE-rich HDL, may be involved in the antiaggregatory effect.

References

1. Feingold, K. R. & Grunfeld, C. in *Endotext* (eds. De Groot, L. J., Chrousos, G., Dungan, K., Feingold, K. R., Grossman, A., Hershman, J. M., Koch, C., Korbonits, M., McLachlan, R., New, M., Purnell, J., Rebar, R., Singer, F. & Vinik, A.) (MDText.com, Inc., 2000). at <http://www.ncbi.nlm.nih.gov/books/NBK305896/>

2. Vitali, C., Wellington, C. L. & Calabresi, L. HDL and cholesterol handling in the brain. *Cardiovasc. Res.* **103,** 405–413 (2014).

3. Bibow, S., Polyhach, Y., Eichmann, C., Chi, C. N., Kowal, J., Albiez, S., McLeod, R. A., Stahlberg, H., Jeschke, G., Güntert, P. & Riek, R. Solution structure of discoidal high-density lipoprotein particles with a shortened apolipoprotein A-I. *Nat. Struct. Mol. Biol.* **24,** 187–193 (2017).

4. Emamzadeh, F. N. Role of Apolipoproteins and α-synuclein in Parkinson's Disease. *J. Mol. Neurosci.* **62,** 344–355 (2017).

5. Bales, K. R. Brain lipid metabolism, apolipoprotein E and the pathophysiology of Alzheimer's disease. *Neuropharmacology* **59,** 295–302 (2010).

6. Orth, M. & Bellosta, S. Cholesterol: Its Regulation and Role in Central Nervous System Disorders. *Cholesterol* (2012). doi:10.1155/2012/292598

7. Pitas, R. E., Boyles, J. K., Lee, S. H., Hui, D. & Weisgraber, K. H. Lipoproteins and their receptors in the central nervous system. Characterization of the lipoproteins in cerebrospinal fluid and identification of apolipoprotein B,E(LDL) receptors in the brain. *J. Biol. Chem.* **262,** 14352–14360 (1987).

8. Mahley, R. W. Central Nervous System Lipoproteins. *Arterioscler. Thromb. Vasc. Biol.* **36,** 1305–1315 (2016).

9. Fagan, A. M., Younkin, L. H., Morris, J. C., Fryer, J. D., Cole, T. G., Younkin, S. G. & Holtzman, D. M. Differences in the Aβ40/Aβ42 ratio associated with cerebrospinal fluid lipoproteins as a function of apolipoprotein E genotype. *Ann. Neurol.* **48,** 201–210 (2000).

10. Qian, J., Wolters, F. J., Beiser, A., Haan, M., Ikram, M. A., Karlawish, J., Langbaum, J. B., Neuhaus, J. M., Reiman, E. M., Roberts, J. S., Seshadri, S., Tariot, P. N., Woods, B. M., Betensky, R. A. & Blacker, D. APOE-related risk of mild cognitive impairment and dementia for prevention trials: An analysis of four cohorts. *PLOS Med.* **14,** e1002254 (2017).

11. Perrier, V., Imberdis, T., Lafon, P.-A., Cefis, M., Wang, Y., Huetter, E., Arnaud, J.-D., Alvarez-Martinez, T., Guern, N. L., Maquart, G., Lagrost, L. & Desrumaux, C. Plasma cholesterol level determines in vivo prion propagation. *J. Lipid Res.* **58,** 1950–1961 (2017).

12. Safar, J. G., Wille, H., Geschwind, M. D., Deering, C., Latawiec, D., Serban, A., King, D. J., Legname, G., Weisgraber, K. H., Mahley, R. W., Miller, B. L., DeArmond, S. J. & Prusiner, S. B. Human prions and plasma lipoproteins. *Proc. Natl. Acad. Sci. U. S. A.* **103,** 11312–11317 (2006).

13. Corder, E. H., Saunders, A. M., Strittmatter, W. J., Schmechel, D. E., Gaskell, P. C., Small, G. W., Roses, A. D., Haines, J. L. & Pericak-Vance, M. A. Gene dose of apolipoprotein E type 4 allele and the risk of Alzheimer's disease in late onset families. *Science* **261,** 921–923 (1993).

14. Liu, C.-C., Kanekiyo, T., Xu, H. & Bu, G. Apolipoprotein E and Alzheimer disease: risk, mechanisms and therapy. *Nat. Rev. Neurol.* **9,** 106–118 (2013).

15. Poirier, J., Davignon, J., Bouthillier, D., Kogan, S., Bertrand, P. & Gauthier, S. Apolipoprotein E polymorphism and Alzheimer's disease. *Lancet Lond. Engl.* **342,** 697–699 (1993).

16. Federoff, M., Jimenez-Rolando, B., Nalls, M. A. & Singleton, A. B. A large study reveals no Association between APOE and Parkinson's disease. *Neurobiol. Dis.* **46,** 389–392 (2012).

17. Qiang, J. K., Wong, Y. C., Siderowf, A., Hurtig, H. I., Xie, S. X., Lee, V. M.-Y., Trojanowski, J. Q., Yearout, D., Leverenz, J., Montine, T. J., Stern, M., Mendick, S., Jennings, D., Zabetian, C., Marek, K. & Chen-Plotkin, A. S. Plasma Apolipoprotein A1 as a Biomarker for Parkinson's Disease. *Ann. Neurol.* **74,** 119–127 (2013).

18. Wang, E.-S., Sun, Y., Guo, J.-G., Gao, X., Hu, J.-W., Zhou, L., Hu, J. & Jiang, C.-C. Tetranectin and apolipoprotein A-I in cerebrospinal fluid as potential biomarkers for Parkinson's disease. *Acta Neurol. Scand.* **122,** 350–359 (2010).

19. Swanson, C. R., Li, K., Unger, T. L., Gallagher, M. D., Van Deerlin, V. M., Agarwal, P., Leverenz, J., Roberts, J., Samii, A., Gross, G. R., Hurtig, H., Rick, J., Weintraub, D., Trojanowski, J. Q., Zabetian, C. & Chen-Plotkin, A. S. Lower plasma ApoA1 levels are found in Parkinson's disease and associate with APOA1 genotype. *Mov. Disord. Off. J. Mov. Disord. Soc.* **30,** 805–812 (2015).

20. Marek, K., Jennings, D., Lasch, S., Siderowf, A., Tanner, C., Simuni, T., Coffey, C., Kieburtz, K., Flagg, E., Chowdhury, S., Poewe, W., Mollenhauer, B., Klinik, P.-E., Sherer, T., Frasier, M., Meunier, C., Rudolph, A., Casaceli, C., Seibyl, J., Mendick, S., Schuff, N., Zhang, Y., Toga, A., Crawford, K., Ansbach, A., De Blasio, P., Piovella, M., Trojanowski, J., Shaw, L., Singleton, A., Hawkins, K., Eberling, J., Brooks, D., Russell, D., Leary, L., Factor, S., Sommerfeld, B., Hogarth, P., Pighetti, E., Williams, K., Standaert, D., Guthrie, S., Hauser, R., Delgado, H., Jankovic, J., Hunter, C., Stern, M., Tran, B., Leverenz, J., Baca, M., Frank, S., Thomas, C.-A., Richard, I., Deeley, C., Rees, L., Sprenger, F., Lang, E., Shill, H., Obradov, S., Fernandez, H., Winters, A., Berg, D., Gauss, K., Galasko, D., Fontaine, D., Mari, Z., Gerstenhaber, M., Brooks, D., Malloy, S.,

Barone, P., Longo, K., Comery, T., Ravina, B., Grachev, I., Gallagher, K., Collins, M., Widnell, K. L., Ostrowizki, S., Fontoura, P., Ho, T., Luthman, J., Brug, M. van der, Reith, A. D. & Taylor, P. The Parkinson Progression Marker Initiative (PPMI). *Prog. Neurobiol.* **95,** 629–635 (2011).

21. Swanson, C. R., Berlyand, Y., Xie, S. X., Alcalay, R. N., Chahine, L. M. & Chen-Plotkin, A. S. Plasma ApoA1 Associates with Age at Onset and Motor Severity in Early Parkinson Disease Patients. *Mov. Disord. Off. J. Mov. Disord. Soc.* **30,** 1648–1656 (2015).

22. Padayachee, E. R., Zetterberg, H., Portelius, E., Borén, J., Molinuevo, J. L., Andreasen, N., Cukalevski, R., Linse, S., Blennow, K. & Andreasson, U. Cerebrospinal fluid-induced retardation of amyloid β aggregation correlates with Alzheimer's disease and the APOE ε4 allele. *Brain Res.* **1651,** 11–16 (2016).

23. Kim, J., Basak, J. M. & Holtzman, D. M. The Role of Apolipoprotein E in Alzheimer's Disease. *Neuron* **63,** 287–303 (2009).

24. Koch, S., Donarski, N., Goetze, K., Kreckel, M., Stuerenburg, H.-J., Buhmann, C. & Beisiegel, U. Characterization of four lipoprotein classes in human cerebrospinal fluid. *J. Lipid Res.* **42,** 1143–1151 (2001).

25. Roher, A. E., Maarouf, C. L., Sue, L. I., Hu, Y., Wilson, J. & Beach, T. G. Proteomics-Derived Cerebrospinal Fluid Markers of Autopsy-Confirmed Alzheimer's Disease. *Biomark. Biochem. Indic. Expo. Response Susceptibility Chem.* **14,** 493–501 (2009).

26. Song, H., Saito, K., Seishima, M., Noma, A., Katsuya Urakami & Nakashima, K. Cerebrospinal fluid apo E and apo A-I concentrations in early- and late-onset Alzheimer's disease. *Neurosci. Lett.* **231,** 175–178 (1997).

27. Johansson, P., Almqvist, E. G., Bjerke, M., Wallin, A., Johansson, J.-O., Andreasson, U., Blennow, K., Zetterberg, H. & Svensson, J. Reduced Cerebrospinal Fluid Concentration of Apolipoprotein A-I in Patients with Alzheimer's Disease. *J. Alzheimers Dis.* **59,** 1017–1026 (2017).

28. Shevchik, V. E., Condemine, G. & Robert-Baudouy, J. Characterization of DsbC, a periplasmic protein of Erwinia chrysanthemi and Escherichia coli with disulfide isomerase activity. *EMBO J.* **13,** 2007–2012 (1994).

29. Huang, C., Ren, G., Zhou, H. & Wang, C. A new method for purification of recombinant human alpha-synuclein in Escherichia coli. *Protein Expr. Purif.* **42,** 173–177 (2005).

30. Shammas, S. L., Knowles, T. P. J., Baldwin, A. J., MacPhee, C. E., Welland, M. E., Dobson, C. M. & Devlin, G. L. Perturbation of the Stability of Amyloid Fibrils through Alteration of Electrostatic Interactions. *Biophys. J.* **100,** 2783–2791 (2011).

31. Cohlberg, J. A., Li, J., Uversky, V. N. & Fink, A. L. Heparin and other glycosaminoglycans stimulate the formation of amyloid fibrils from alpha-synuclein in vitro. *Biochemistry* **41,** 1502–1511 (2002).

32. Giehm, L. & Otzen, D. E. Strategies to increase the reproducibility of protein fibrillization in plate reader assays. *Anal. Biochem.* **400,** 270–281 (2010).

33. Shahnawaz, M., Tokuda, T., Waragai, M., Mendez, N., Ishii, R., Trenkwalder, C., Mollenhauer, B. & Soto, C. Development of a Biochemical Diagnosis of Parkinson Disease by Detection of α-synuclein Misfolded Aggregates in Cerebrospinal Fluid. *JAMA Neurol.* **74,** 163–172 (2017).

34. Bodenhausen, G. & Ruben, D. J. Natural abundance nitrogen-15 NMR by enhanced heteronuclear spectroscopy. *Chem. Phys. Lett.* **69,** 185–189 (1980).

35. Biancalana, M. & Koide, S. Molecular Mechanism of Thioflavin-T Binding to Amyloid Fibrils. *Biochim. Biophys. Acta* **1804,** 1405–1412 (2010).

36. Glabe, C. G. Structural classification of toxic amyloid oligomers. *J. Biol. Chem.* **283,** 29639–29643 (2008).

37. Emamzadeh, F. N. & Allsop, D. α-synuclein Interacts with Lipoproteins in Plasma. *J. Mol. Neurosci.* **63,** 165–172 (2017).

38. Arosio, P., Knowles, T. P. J. & Linse, S. On the lag phase in amyloid fibril formation. *Phys. Chem. Chem. Phys.* **17,** 7606–7618 (2015).

39. Qiang, J. K., Wong, Y. C., Siderowf, A., Hurtig, H. I., Xie, S. X., Lee, V. M.-Y., Trojanowski, J. Q., Yearout, D., Leverenz, J., Montine, T. J., Stern, M., Mendick, S., Jennings, D., Zabetian, C., Marek, K. & Chen-Plotkin, A. S. Plasma Apolipoprotein A1 as a Biomarker for Parkinson's Disease. *Ann. Neurol.* **74,** 119–127 (2013).

40. Wang, E.-S., Sun, Y., Guo, J.-G., Gao, X., Hu, J.-W., Zhou, L., Hu, J. & Jiang, C.-C. Tetranectin and apolipoprotein A-I in cerebrospinal fluid as potential biomarkers for Parkinson's disease. *Acta Neurol. Scand.* **122,** 350–359 (2010).

41. Swanson, C. R., Li, K., Unger, T. L., Gallagher, M. D., Van Deerlin, V. M., Agarwal, P., Leverenz, J., Roberts, J., Samii, A., Gross, G. R., Hurtig, H., Rick, J., Weintraub, D., Trojanowski, J. Q., Zabetian, C. & Chen-Plotkin, A. S. Lower plasma ApoA1 levels are found in Parkinson's disease and associate with APOA1 genotype. *Mov. Disord. Off. J. Mov. Disord. Soc.* **30,** 805–812 (2015).

Chapter 4

Conclusions and perspectives

This PhD research project, entitled “Expression and characterization of human proteins involved in neurodegenerative diseases”, was focused on the application of molecular biology techniques and development of experimental protocols to express and purify α-synuclein and Aβ peptides. The proteins expressed during my research activity have been used to design and carry out experiments aimed to investigate i) the structural features of Aβ mixed filbrils assembly, ii) the interaction of α-synuclein with cerebrospinal fluids components, iii) the kinetics of the aggregation mechanism of Aβ1–40.

The biophysical characterization of the investigated proteins has been carried out using NMR spectroscopy and ThT fluorescence assay.

In detail, the analysis of the aggregation kinetics of Aβ1–40 has been obtained analyzing a series of 1D ^{1}H NMR spectra of the peptide under quiescent conditions. The quality of the peptide in terms of purity from contaminant proteases was crucial to obtain reliability and reproducibility of the kinetics analysis. At this regard, one important results of my research activity has been the development of a protocol to prevent/remove the contamination of the samples from bacterial proteases which dramatically degrade the protein in solution and prevent the kinetic studies

The purification of monomeric amylogenic peptides from pre-formed aggregates is another important goal for the analysis of the aggregation kinetics, for the preparation of samples of fibrils for structural studies, and for the development of new analytical methodologies. During this study, different protocols for Aβ and α-synuclein monomerization and strategies to avoid protein aggregation in the different steps of the samples preparation have been designed and successfully tested.

The back-to-back size-exclusion chromatography technique combined with the alkaline treatment of the α-synuclein and Aβ peptides samples allowed the obtainment monomeric final samples due to the fractionation capability of gel-filtration purification, which let the separation of different population of oligomers as well as relatively pure populations of monomers, dimers and trimmers.

In addition, Aβ degradation was then completely abolished by adding a protease inhibitor cocktail containing high concentration of ethylenediaminetetraacetic acid (EDTA), a divalent metal ions cheletors with a specific activity against metalloproteases, the *SigmaFast* EDTA-free complete protease inhibitor cocktail and sodium azide (NaN_3) to block the proteolysis catalyzed by the residual bacterial contamination. The common features of the amyloidogenic proteins make possible the application of these experimental conditions as general standard protocol for the preparation of final samples of any neurodegenerative-related protein.

In particular, α-synuclein, purified according the protocols developed during my PhD has been fundamental to analyze the interaction of this intrinsically disordered protein with human serum albumin. The analysis of the interaction α-synuclein with other biological fluids components (i.e. lipoparticles) is currently in progress, as well as the development of diagnostic PMCA and RT-QuIC assays for detection of misfolded α-synuclein in samples of CSF from patients suffering from neurological diseases.

On the other hand, all the implementations done to Aβ expression and purification protocols were crucial to produce pure monomers for mixed fibrils assembly and for aggregation kinetics investigation. The reliability and the reproducibility of the expression profile, despite the general improvements, could be increased taking as a template what was achieved during this PhD thesis work.

After their production, Aβ peptides and α-synuclein were the substrate of different projects focused on the investigation of the aggregation mechanism in the neurodegenerative process.

To summarize all the progress done during this PhD, the investigation of the aggregation kinetics of the AβM1-40 peptide can be performed by in solution NMR , giving a complementary point of view compared to ThT fluorescence.

Furthermore, the “mixed” fibrils of Aβ peptides obtained with 1:1 stoichiometry can be definitely and more correctly referred to as “interlaced”, as was confirmed by SSNMR analysis.

Concerning α-synuclein-related projects, we found that, HSA, at the concentration found in human serum, slows down the aggregation of α-synuclein significantly, supporting the hypothesis of the chaperone-like behavior of HSA. The interaction between HSA and α-synuclein occurred in an ionic strength and pH dependent manner, as was proved by NMR and ThT fluorescence assays. .

Finally, a stronger antiaggregatory effect was observed for Human plasma HDL (rich in apoA1), which decreased significantly the quantity of fibrillary and oligomeric aggregates produced by α-synuclein.

Among the hundreds of different neurodegenerative disorders, so far the main attention has been given only to a small group of them, including Alzheimer disease (AD) and Parkinson disease (PD). It was estimated that, over the next generations, the proportion of elderly citizens will double and, with this, the proportion of persons suffering from some kind of neurodegenerative disorder. To increase the social impact of neurological diseases there is the evidence that, several approved drugs, are only symptomatic and do not stop the progression of the degenerative process. For this reason, in this context, all the scientific community needs further efforts to deeply understand the mechanisms behind these diseases of our Century: lots of work has been done, but there is still much to be done.